



Durham E-Theses

CCD polarimetry as a probe of regions of recent star-formation

Draper, Peter Walter

How to cite:

Draper, Peter Walter (1988) *CCD polarimetry as a probe of regions of recent star-formation*, Durham theses, Durham University. Available at Durham E-Theses Online: <http://etheses.dur.ac.uk/6597/>

Use policy

The full-text may be used and/or reproduced, and given to third parties in any format or medium, without prior permission or charge, for personal research or study, educational, or not-for-profit purposes provided that:

- a full bibliographic reference is made to the original source
- a [link](#) is made to the metadata record in Durham E-Theses
- the full-text is not changed in any way

The full-text must not be sold in any format or medium without the formal permission of the copyright holders.

Please consult the [full Durham E-Theses policy](#) for further details.

CCD POLARIMETRY AS A PROBE OF
REGIONS OF RECENT STAR-FORMATION.

by
Peter Walter Draper
B.Sc. (Dunelm).

A thesis submitted for the degree of Doctor of Philosophy.
Department of Physics, University of Durham.

1988

The copyright of this thesis rests with the author.
No quotation from it should be published without
his prior written consent and information derived
from it should be acknowledged.



10 MAY 1988

Abstract

CCD POLARIMETRY AS A PROBE OF REGIONS OF RECENT STAR-FORMATION. By P.W. Draper.

Chapter 1 of this thesis details the incorporation of a Charged Coupled Device (CCD) detector system with the Durham Imaging Polarimeter. The details include the physical characteristics of the device and the electronics and software associated with the device control and data storage. The introduction of the CCD detector system has made necessary the inclusion of a super-achromatic half-wave plate in the polarimeter which has an inherent variability in its optic axis. Chapter 2 of this work describes fully how suitable corrections for this effect can be made, and derives "first order" results. The CCD performance is examined in comparison with the detector used previously and hence the veracity of the new results is established.

Chapter 3 is a relevant summary of the status of the astronomy of the immediate regions of recent star-formation. Chapter 4 describes multicolour polarimetry of NGC2261/R Mon covering the period 1979 to 1986. The data conclusively proves that the polarisation of R Mon must be due to effects close to R Mon (~ 14 astronomical units). This is evident because of the dynamic timescale of the variations of the polarisation of R Mon and the anomalous band of polarisations seen across the head of the nebula. The interpretation presented is an extension of the Elsässer and Staude (1978) method of polarising objects embedded within the confines of a nearly edge-on disk. Detailed polarisations within the main nebula body provide evidence for this extended interpretation and also for an extensive *helical* magnetic field which may extend into the disk. Also it is seen that R Mon must still be "shrouded" in material preventing light from directly reflecting in the main nebula body. It is not thought that the variations in the region close to R Mon are due to planetary bodies but to accretion from the disk. The results of this re-interpretation of the polarising mechanism are tentatively applied to other similar objects.

Contents

Declaration.	XIV
1 CCD Polarimetry.	1
1.1 The Electronographic Polarimeter.	1
1.2 A New Detector System.	3
1.3 The Control Systems.	5
1.4 The CCD.	10
1.5 Adapting the Polarimeter to the CCD.	18
1.6 The CCD Control Software.	18
1.7 Preparation of the CCD data.	23



1.8	Future Developments.	25
2	Data Correction and Verification.	27
2.1	Introduction.	27
2.2	The Comparison Data.	28
2.3	Data Correction.	39
2.3.1	Halfwave plates.	39
2.3.2	Achromatic halfwave plates.	40
2.3.3	Superachromatic halfwave plates.	41
2.3.4	The corrections.	44
2.4	Results.	46
2.5	Conclusions.	55
3	Immediate Regions of Recent Star-Formation.	57
3.1	Introduction.	57

3.1.1	T Tauri stars.	58
3.1.2	Herbig-Haro objects.	60
3.2	Outflows from Young Stars.	62
3.2.1	Morphology of the outflows.	67
3.2.2	The energetics of molecular outflows.	71
3.2.3	Frequency of occurrence.	75
3.3	Physical Structures Near Protostars: Disks, Toroids and Cavity Edges.	76
3.3.1	Inner dimensions of the disks.	86
3.3.2	Identification of physical structures within the out- flows.	86
3.4	Optical Jets from Pre-Main-Sequence Stars.	89
3.5	Optical Appearance of the Outflows.	93
3.6	Other Consequences of Outflows.	94
3.7	Summation.	100

4	Polarisation of NGC2261/R Mon.	103
4.1	Introduction.	103
4.2	Previous Studies.	105
4.2.1	The variability of NGC2261/R Mon.	105
4.2.2	Spectroscopy of NGC2261/R Mon.	106
4.2.3	Infra-red photometry of R Mon.	108
4.2.4	Visual photometry of NGC2261.	110
4.2.5	Polarimetry of NGC2261/R Mon.	111
4.2.6	Molecular line observations.	115
4.2.7	HH39.	117
4.2.8	Summary.	118
4.3	Observations.	119
4.4	Results and Discussion.	121
4.4.1	General results.	121

4.4.2	The variation of polarisation of R Mon and the <i>Polarisation Disk</i>	138
4.4.3	The wavelength dependency of the polarisation of R Mon.	168
4.4.4	The H α polarisation of NGC2261/R Mon. . . .	171
4.4.5	Variation of polarisation in the main nebula body.	175
4.5	Conclusions.	193
5	Concluding Remarks.	195
	Publications.	202
	A DORADO.	204
	B Some Retardance Theory.	212
	C Durham CCD References.	215
	References.	221

List of Figures

1.1	The relative sensitivities of a P8603/B CCD and an electronographic camera	6
1.2	The DURHAM/CAMBRIDGE CCD setup.	7
1.3	A three phase CCD	12
1.4	Plot of Signal versus Variance	16
2.1	R-band polarisation maps of R Mon/NGC2261	32
2.2	V-band polarisation maps of R Mon/NGC2261	33
2.3	R-band polarisation map of NGC2023	34
2.4	R-band polarisation map of NGC2023	35
2.5	Common data between the NGC2023 Datasets	37

2.6	Common data between the NGC2023 Datasets	38
2.7	The retardance and equivalent optic axis of the super-achromatic halfwave plate	43
2.8	The equivalent optic axis for each filter	47
2.9	Polarisation map of the data selected from the r-band R Mon/NGC2261 map	51
2.10	Polarisation map of the data selected from the v-band R Mon/NGC2261 map	52
3.1	Masses of the outflows	66
3.2	Maps of ^{12}CO emission from four molecular flows	69
3.3	Frequency distribution of collimation factors for molecular outflows	70
3.4	The flow mechanical luminosity against the stellar luminosity	73
3.5	Plot of the force against the stellar luminosity	74

3.6	Sketch of the Pudritz and Norman molecular bipolar outflow configuration	78
3.7	Unified model for outflows and disks around protostars	79
3.8	Overlay of the blue and red shifted CO emission in L1551	88
3.9	Schematic of the disk and flow system around a protostar	90
3.10	An $H\alpha$ greyscale image of the HH46/7 region	92
3.11	Greyscale image of the cometary nebula Parsamyan 21.	95
3.12	Greyscale image of the region of NGC 7129 incorporating the bipolar nebula RNO 138.	96
3.13	Greyscale image of the L1551 region	97
3.14	An $H\alpha$ greyscale image of the HH object HH100	98
4.1	Greyscale of NGC2261/R Mon	104
4.2	1979 VV band polarisation map of NGC2261/R Mon .	123
4.3	1979 R band polarisation map of NGC2261/R Mon . .	124

4.4	1981 VV band polarisation map of NGC2261/R Mon . . .	125
4.5	1985 I band polarisation map of NGC2261/R Mon . . .	126
4.6	1985 R band polarisation map of NGC2261/R Mon . . .	127
4.7	1985 I band polarisation map of NGC2261/R Mon . . .	128
4.8	1985 Z band polarisation map of NGC2261/R Mon . . .	129
4.9	1986 V band polarisation map of NGC2261/R Mon . . .	130
4.10	1986 H α band polarisation map of NGC2261/R Mon . . .	131
4.11	1986 I band polarisation map of NGC2261/R Mon . . .	132
4.12	Traces of %polarisation, the polarisation error and position angle error	133
4.13	Traces of %polarisation, the polarisation error and position angle error	134
4.14	Traces of %polarisation, the polarisation error and position angle error	135
4.15	Traces of %polarisation, the polarisation error and position angle error	136

4.16	Traces of %polarisation, the polarisation error and position angle error	137
4.17	The variation with aperture of the polarisation of R Mon	143
4.18	The variation in polarisation of R Mon with time . . .	147
4.19	The Elsässer and Staude model	149
4.20	How polarised light should scatter	152
4.21	The scattering geometry	154
4.22	How polarised light scatters	157
4.23	Deviations from the plane of symmetry	158
4.24	The ratio of the scattered polarised intensities	159
4.25	A series of scattering paths through the disk.	161
4.26	February 1985 I band Polarisation map of the head of the nebula	164
4.27	December 1985 I band Polarisation map of the head of the nebula	165

4.28	March 1986 I band Polarisation map of the nebula	166
4.29	An R-I greyscale image of NGC2261/R Mon	169
4.30	H α Elsässer and Staude model	173
4.31	The scattering of light within the nebula	177
4.32	The scattering of light within the nebula	178
4.33	Radial polarisations about R Mon	181
4.34	Radial polarisations about R Mon	182
4.35	Arc profiles of the position angle	185
4.36	Traces of position angle perpendicular to the polarisation of R Mon	187
4.37	Traces of position angle directly north from R Mon	188
4.38	A shrouded R Mon	192

List of Tables

2.1	CCD and electronographic band passes	30
2.2	First order corrections to the mean optical axis	44
2.3	R and V band corrections to the mean equivalent optical axis; based on black body spectra	46
2.4	The comparison data	50
3.1	Interstellar disks/toroids	83
4.1	Polarisation measurements of NGC2261/R Mon	121
4.2	Polarisation measurements of R Mon (other works)	141
4.3	Polarisation measurements of R Mon (this work)	142

4.4 I Band polarisation disk position angles 163

4.5 Polarisation measurements of R Mon 170

4.6 I measurements of NGC2261 position angles 183

Declaration.

The work described in this thesis was financed by a Science and Engineering Research Council studentship awarded to the author during the period 1983 to 1986, and was undertaken in the Department of Physics, University of Durham under the supervision of Dr. S.M. Scarrott.

Some of the data presented in Chapters 2 and 4 has been described in the publications:-

“Polarimetry of the NGC2261/R Monocerotis system and the faint jetlike feature to its southwest”, R.F.Warren-Smith, P.W.Draper and S.M.Scarrott, (1987). *The Astrophysical Journal*, **315**:500.

“Optical polarisation of the cometary nebula NGC2261”, M.R.Gething, R.F. Warren-Smith, S.M. Scarrott and R.G. Bingham, (1982). *Monthly Notices of the Royal Astronomical Society*, **198**:881.

All the data is fully re-analysed and re-interpreted in this work. All other work within this thesis is the work of the author except where explicitly stated in the text.

Chapter 1

CCD Polarimetry.

1.1 The Electronographic Polarimeter.

The Durham Imaging Polarimeter has been in use with the astronomy group in Durham for over a decade and has remained essentially unchanged in its basic layout and principles during this period. The polarimeter design was based on the work of Ohman (1939) and Pickering (1873). It has been well documented by various authors, Axon (1977), Warren-Smith (1979), and Scarrott *et al.* (1983). The use of this device in conjunction with an electronographic camera as the detector is also described by Warren-Smith (1979) and Scarrott *et al.* (1983). In this configuration the instrument has proven very useful, the quality of the results having allowed the investigation of many types of extended objects (see for example Scarrott *et al.* (1977), Chesterman and Pallister (1979), Gething *et al.* (1982), Warren-Smith *et al.* (1979), and Ward-Thompson *et al.* (1985)).

Although this arrangement has proven to be of considerable merit it has several handicaps which are associated with the electronographic camera. Observationally it is a quite demanding instrument to use. Before observing can begin, film has to be prepared for use by cutting from sheets (avoiding any imperfections). During each set of observations, the film has to be continually loaded and unloaded into a partially evacuated chamber and it then has to be carefully developed and stored for transportation. Sometimes during object finding, say when the object is very faint and/ or the position is not known accurately, it is necessary to wait for the film to be developed to ascertain whether the object has been found and/ or positioned correctly with respect to the image mask, this could potentially take hours because of the long exposure times required. When the film containing the data has returned from the observing site, it is then necessary to digitise the information before any further processing can be undertaken. This is usually performed on an instrument such as the RGO PDS-microdensitometer, each plate taking up to 40 minutes to process. As the nuclear emulsions which are used for detection in the electronographic camera are not totally linear in their response to the incident electron flux, corrections are necessary. The corrections themselves are not completely accurate, due to sensitivity variations between batches of film. The response of the PDS machine is not linear and corrections need to be made for this also. For instance the zero level of the microdensitometer is not stable and usually drifts as a plate is digitised; also occasional glitches in this level are produced. However, the most serious problem associated with the electronographic method is the problem of bad data itself. The plates are often covered in scratches and show pieces of dirt. The elec-

tronographic camera photocathode typically has hot and dead spots, and the mica window directly in front of the nuclear emulsion can also be contaminated. All these effects are usually seen on electronographs no matter how careful the preparation and storage. In summary these problems add up to a cosmetically poor product which needs a lot of processing to gain good results.

1.2 A New Detector System.

In view of the above considerations it was thought desirable to obtain a new detector system which could meet the increasing demands for higher quality data and greater light sensitivity, a view which was fortified by the demise of support for electronography in 1982. It was noted that all the above problems are absent, or not as pronounced, in the Charged Coupled Device (CCD) camera systems which were being developed at that time. These were becoming much more popular than other available imaging systems, as they are observationally easy to use. The images are available for inspection as soon as the exposure is taken since they are pre-digitised which, together with the decreased exposure times due to increased quantum efficiencies, makes the instrument a superb object finding device. The response of CCDs to light is extremely linear. They have very stable characteristics. Any defects in these detectors are fixed and, as such, can be removed in the same manner over and over again so that excessive detection and rejection analysis is not required.

The obvious choice of CCD would of course, be the most sensitive available. However, because these types of CCD are machined thin (so called thinned CCDs) to allow blue photon penetration and detection in the CCD substrate, they show a phenomenon known as fringing. This is caused by emission lines (particularly those of the night sky), multiply reflecting and interfering within the thinned substrate, causing an effect similar to thin films and Newtons rings in any images taken with these devices. This effect is particularly prominent because the CCD surface cannot be machined to sufficient accuracy ($< \text{one wavelength}$). The effect which fringing would have on the polarisation of any incident light is unknown, but it is expected that they would have some effect, because of the nature of their production. Obviously one avoids sources of error and confusion when possible, so the only other alternative was to obtain an unmachined *thick* CCD.

Thick CCDs have no fringing problems but as expected have little sensitivity in the blue end of the spectrum, and none at all in the ultra violet. This is a considerable disadvantage (especially since most reflection nebula are identified by their intrinsic blueness, and so are more luminous at this wavelength), but because the response of such CCDs continues into the infrared (out to about one micron) unlike the electronographic camera which cuts off in the red (see fig 1.1 for the response of a CCD and an electronographic camera), this opened the possibility of extending polarimetric studies into this previously little studied region of the electromagnetic spectrum. Taking these considerations, together with the absence of the fringing in to account, it was decided that a *thick* CCD was probably the one most suited to

the further development of Imaging Polarimetry.

1.3 The Control Systems.

The CCD system obtained was designed and built by Craig Mackay of the University of Cambridge, an outline of his original system incorporating a GEC MA357 CCD as the detector is to be found in Wright and Mackay (1981). Our system was built by Mackay in 1983/4 and incorporates a GEC P8603/B CCD as the detector. The control system is also not quite the same as Mackay's original. Due to financial constraints it was impossible to obtain an image processor: instead the Image Research Company of Cambridge has supplied a frame store to handle basic image display only.

A schematic diagram of the Durham/Cambridge CCD system setup is shown in fig 1.2. A brief description of each of the components will be attempted here, so that an appreciation of the system and its workings can be obtained.

The liquid nitrogen dewar contains the CCD, temperature sensors and temperature control devices. The CCD itself is mounted on a copper block connected to the liquid nitrogen reservoir by a copper braid. This arrangement maintains the CCD temperature at typically 120 K. The CCD is kept in an evacuated chamber, which acts to prevent heat escape from the nitrogen container and prevents the formation of

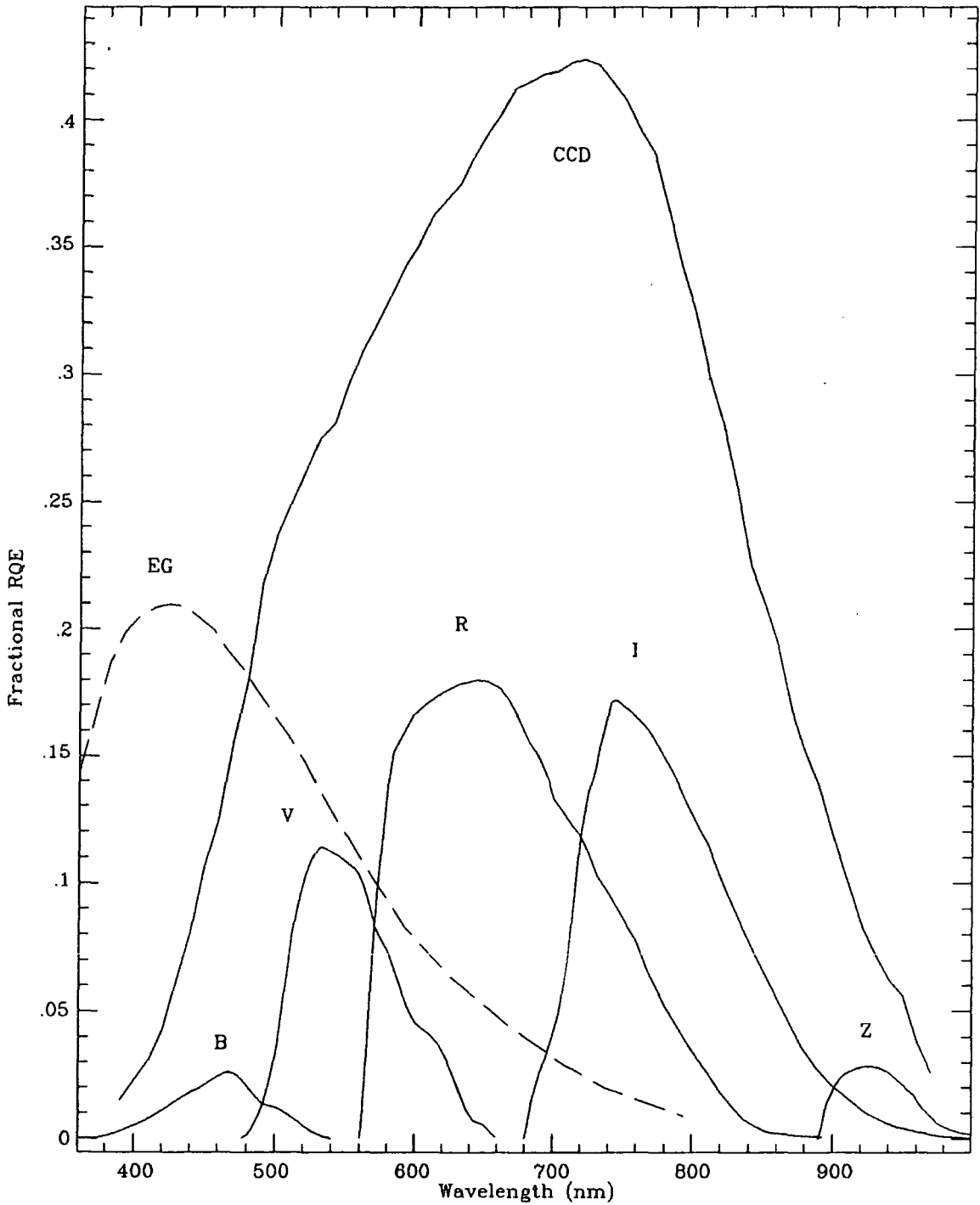


Figure 1.1: The relative sensitivities of a P8603/B CCD and an electronographic camera. Also shown are the detective sensitivities of the filter system in use with the CCD system.

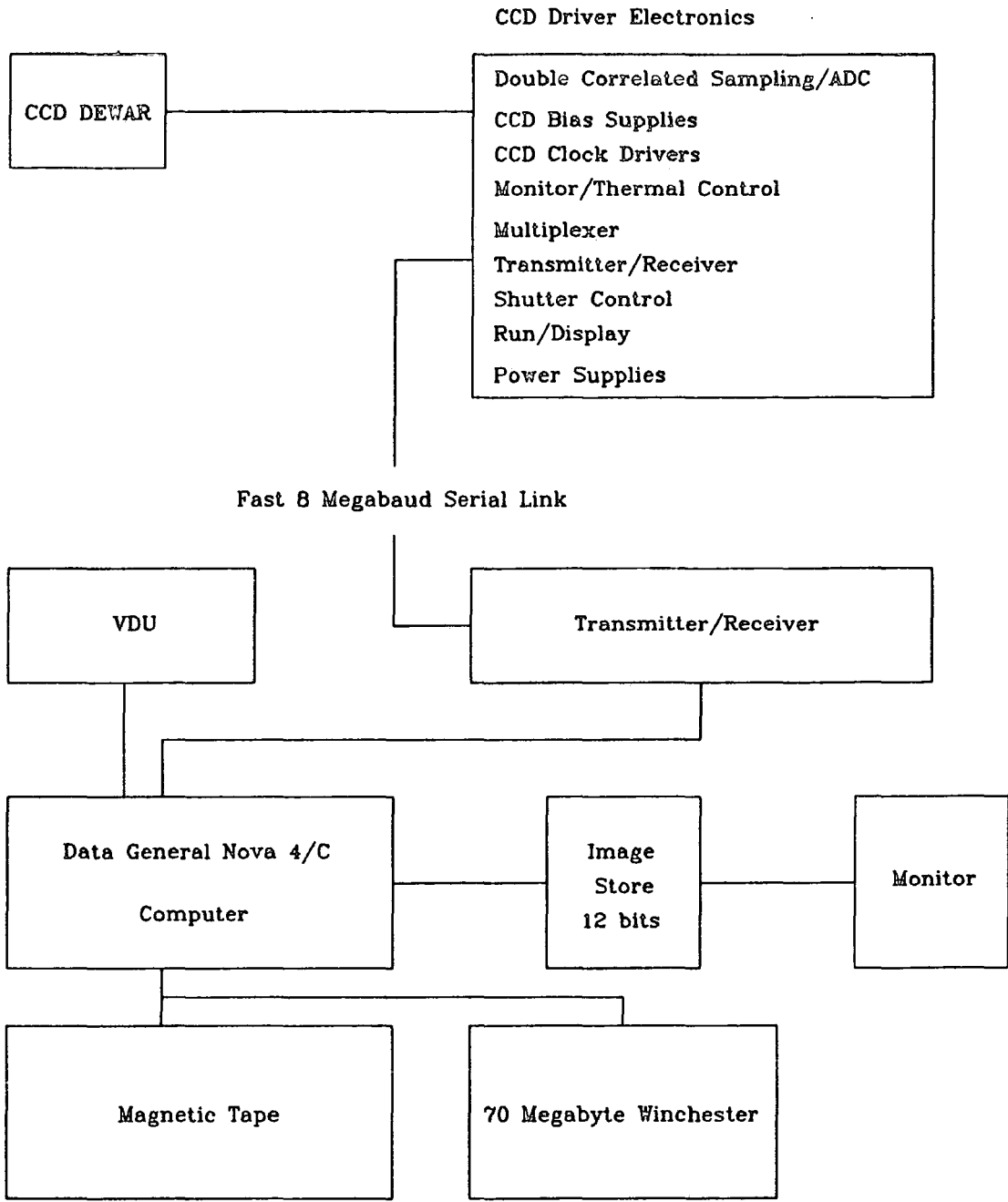


Figure 1.2: The DURHAM/CAMBRIDGE CCD setup.

condensation on the device. The liquid nitrogen dewar contains about 2 litres of liquid nitrogen when full, which is sufficient to last for around 10 hours of normal use. The vacuum chamber maintains itself well over a period of two weeks (the longest time of continuous observation attempted so far).

The CCD is connected to the driver electronics rack by a single flat cable. The electronics rack contains all the modules required; to supply the CCD bias voltages and clocking signals; to process the analogue signal output by the CCD, into a digital representation; to control and organise the communications with the host computer; to monitor the system performance and control the automatic shutter.

The Double Correlated Sampling (DCS)/ Analogue to Digital Converter (ADC) module, suppresses noise created by the on-chip amplification circuits and performs a 16 bit digitisation of this signal for return to the host computer via the transmitter/ receiver module, which handles the communications. All communication with the CCD is performed via the transmitter/ receiver module along an eight megabaud serial link (coaxial cable). This allows the control computer and peripherals to be at a considerable distance from the CCD and driver rack (up to 200m).

The thermal monitoring and temperature control module displays the temperature of various elements of the CCD system, (nitrogen, chip, mount and ambient), on the face of the electronics rack, and may also, optionally, be used to control the CCD mount temperature if

higher operating temperatures are required. All sensor functions may be displayed on the control console (to monitor the chip temperature after each exposure if necessary). The bias and power supplies of the CCD electronics rack may also be monitored similarly using a digital voltage meter installed inside the rack. The clocks module generates the signals needed to transfer (clock) charge along the CCD to the output registers (see fig 1.3(c) for an example of clocking voltages).

If necessary the CCD camera can be driven in stand-alone mode by the run/ display module which generates analogue signals which can be shown on an oscilloscope. It also displays (on LEDs) the bits of any data words which are being transmitted.

The Shutter control module allows the shutter to be opened and closed for accurately timed intervals from the control computer or from the rack. The shutter was obtained some time after the CCD camera. Unfortunately the window of the CCD dewar is now enclosed by the shutter housing which, particularly if the conditions are cold and/ or humid, causes water vapour to condense inside the enclosure, misting up the window. When this happens the dewar has to be removed and the window cleaned. The misting may not be noticed for some time, since the CCD window is necessarily enclosed, and many observations can be lost.

The control computer is a Data General Nova 4/C; a 16 bit general purpose minicomputer with a memory of 64 K, which can allow parallel process action with time sharing if required. It also accommo-

dates access to many peripheral devices.

Image display is achieved using an image store which displays images on a black and white monitor. The images can be up to 640 x 512 pixels, each pixel consisting of up to 12 bits of information. Of these 12 bits however, only 8 contiguous bits can be displayed at any one time, either directly or having been transformed through a programmable look-up-table (LUT). The image thus displayed may also be enlarged to closely inspect any portion.

The system also has a magnetic tape unit which is a streamer device which can read and write to 9 track computer tape for general data transport, it is, however, quite a slow process. The CCD frames are stored in the Flexible Image Transport System format (FITS, see Wells, Greisen and Harten (1981)) which can be read on most computers. On-line data storage is performed on a Winchester hard disk which can store up to 70 megabytes of information; this corresponds to about 70 CCD frames (plus the operating system and necessary programs) which are stored as signed word arrays (16 bits per pixel).

1.4 The CCD.

The CCD is a GEC P8603/B analogue integrated circuit consisting of 576 x 385 picture element (pixels) that are light sensitive. Each pixel is 22 microns square. More specifically the CCD is a buried channel three

phase device; a simplified diagram of the structure of such a device is shown in fig 1.3(a). Each pixel in the CCD acts as a Metal Oxide Semiconductor (MOS) capacitor, forming a potential well into which the charge carriers (electrons or holes, depending upon which form the silicon doping takes) released from the valence band in the crystal structure can accumulate. The energy band gap in the crystal has been arranged in such a way that the energy from a single photon is sufficient to liberate a charge carrier. Thus the device integrates the light incident on it during an exposure, one detected photon corresponding to one released charge carrier.

At the end of an exposure, light is stopped from activating the CCD and the frame is read out. The readout is controlled by the host computer which sends the appropriate instructions to the control electronics rack. This then transmits the potentials necessary to cause the charge to transfer across the device into the output registers (extra large pixels at the end of each row which can contain the charge of many pixels at once). The charge transfer is achieved using a three phase method. The potentials applied to the CCD electrodes and the subsequent movement of charge across the device are shown in fig1.3 (b,c). By repeating the clocking as shown, it is possible to move all the charge in the CCD into the output registers (one or more pixels at a time).

Once the charge is in the output registers it can then be similarly moved onto the on-chip amplifier from where it can then be sampled and the amount of charge converted into a digital representation. This

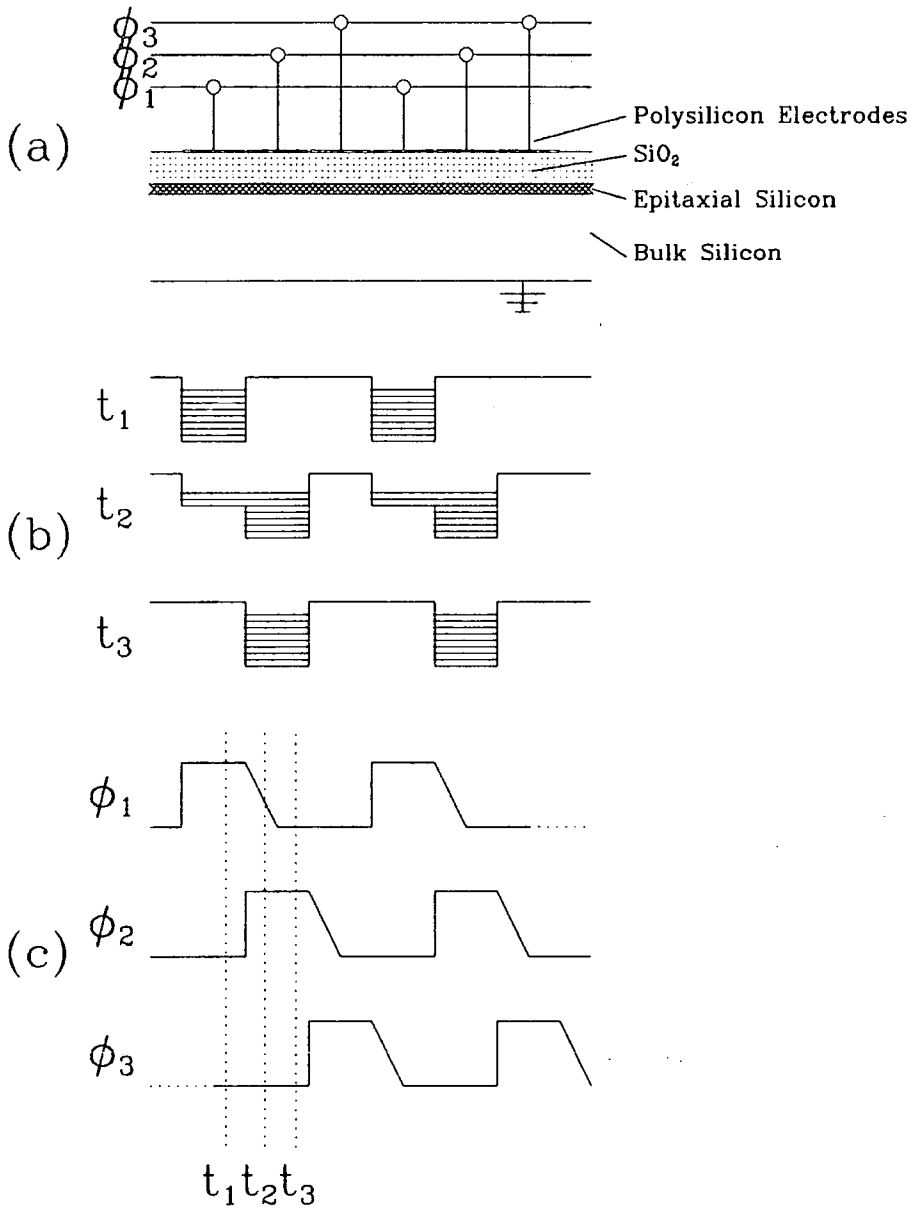


Figure 1.3: Diagrams showing; (a) the physical structure of a buried channel three phase CCD; (b) how charge transfers across the CCD; (c) the "clocking" voltages applied to the electrodes in (a) ϕ_1, ϕ_2, ϕ_3 , the charge states in (b) correspond to times when the voltages at t_1, t_2, t_3 , are applied to ϕ_1, ϕ_2, ϕ_3 .

value is then returned, on request, to the host computer which stores it on disk. The sequence of controls by which the readout is achieved is as follows: a column of charge is transferred into the last column of wells (parallel transfer) on the CCD, which are the output registers. When the charge is in the output registers it is then transferred a pixel at a time down the column (serial transfer) onto the on-chip amplifier, where it is amplified and transferred to the DCS module. The noise in the output produced by the on-chip switches is reduced by this module which then passes the signal to the ADC which digitises it. The signal is then passed back down the communications link to the host computer which stores it on disk. In this way a digital two dimensional representation of the final charge density on the CCD is stored on disk.

To achieve the noise levels required to enable integration for long periods the CCD is cooled to a temperature of typically 120 degrees K to reduce the dark current (ie. electrons which gain sufficient energy from thermal excitations to be released into the conduction band). Other sources of noise are the shot noise of the photons themselves (ie. from the poisson statistics of counting), the readout noise, which is produced by the on-chip high gain electronics, together with the noise from the electronics rack (from the ADC, the voltage supplies etc.).

The readout noise and gain of the system are usually estimated by applying the signal-variance method. Basically this technique works by noting all the sources of noise in the system as a whole, ie. photon shot noise, the readout noise itself and the spatial noise (the flatfield response, due to variations of sensitivity from place to place) and equating

all these to the total noise observed in the data values:-

$$\sigma_{t,e}^2 = \sigma_{r,e}^2 + \sigma_e^2 + \sigma_{s,e}^2$$

where,

$\sigma_{t,e}^2$ = total noise,

$\sigma_{r,e}^2$ = readout noise,

σ_e^2 = shot noise,

$\sigma_{s,e}^2$ = spatial noise,

and the subscript , e refers to electrons. If we set $g = n_e/S_{ADU}$ and use $\sigma = \sqrt{n_e}$, where ADU represents the analog-to-digital unit, and if we remove the spatial noise by dividing the values by a best estimate flat-field and finally convert electrons into ADUs we have the approximate relation:-

$$\sigma_{t,ADU}^2 = \sigma_{r,ADU}^2 + S_{ADU}/g$$

So we derive the usual relation:-

$$V = S/g + \sigma^2$$

where V is the variance in the signal S in analogue to digital units (ADUs). The factor g is the required gain in electrons per ADU. The readout noise is σ^2 . Plotting values of variance against signal allows the two quantities to be estimated by forming a least squares fit to this

line. A plot of this type is shown in fig 1.4. The plot gives a value of 1.9 electrons per ADU for the CCD in use. However, due to an inaccurate knowledge of the zero value readout level (which is not important using our method of processing - see section 2.7) the readout noise cannot be determined from this graph. Fortunately the dark current for this device is effectively negligible, which allows the readout noise to be determined by just performing an unexposed readout of the CCD. The readout noise determined by such a method is about 11 electrons with peak to peak values of about 21 electrons. Both these values are produced using the gain factor determined above (1.9 electrons/ADU). Also using this method the dark current can be checked by making no exposure readouts, from which the zero level is measured, after leaving the system for timed intervals. The dark current found using this method is less than 1 ADU for a period of half an hour.

Other sources of noise and bad data which have to be considered are cosmic rays, hot spots, dead pixels, bad columns, charge transfer inefficiencies and charge overflow and smearing. The device presently in use has three bad columns and one hot spot, all of which are routinely removed (by setting invalid), from any data before further processing takes place. Usually the exposures used are sufficiently short so that the build up of cosmic rays is negligible (there are about 5 visible events per minute in low signal exposures), and as such is usually ignored. Exposures of up to twenty minutes are feasible before the amount of cosmic rays visible become large. If any object requires longer exposures multiple exposures are taken in preference to one, which allows the cosmic rays to be removed, or diminishes their overall effect.

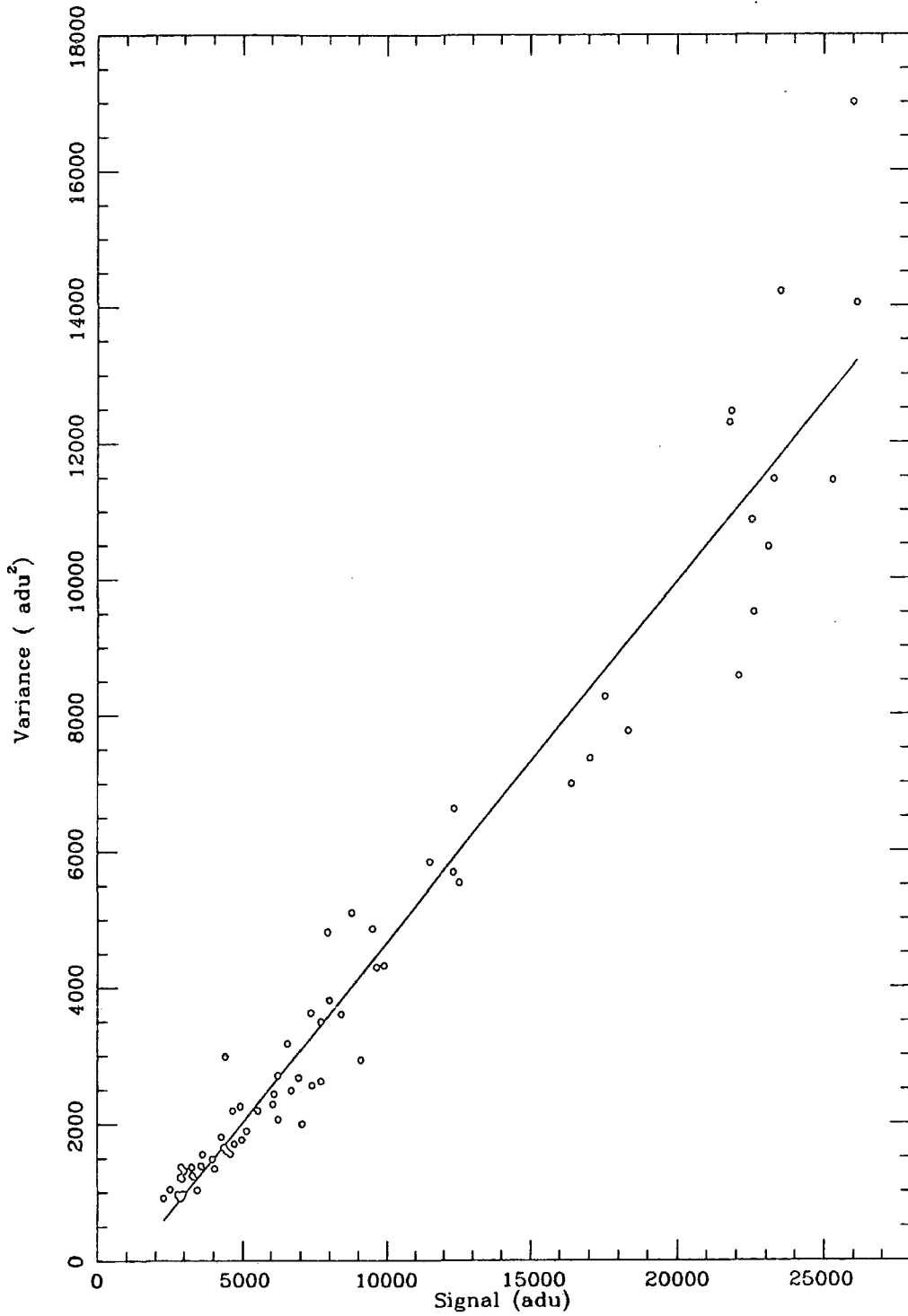


Figure 1.4: Plot of signal versus variance and the least squares fit to these values.

Charge overflow and smearing also limits the amount of time which may be profitably spent observing an object during any one exposure. This is usually set by the brightest star in the field of view.

Charge transfer inefficiencies can occur when a pixel is transferred across the whole face of the CCD. Obviously there is more chance of charge leakage and other losses, the greater the number of times a well of charge has to be moved. To combat this effect the charge is read out relatively slowly (it takes over 30 seconds to readout one CCD frame, whereas in TV applications CCDs are read out in approx 1/20 th of a second). However some inefficiencies still occur due to *surface states* which occur in the forbidden energy gap between the valence and conduction bands. These energy states are produced by the disruption of the periodic lattice structure near the silicon dioxide–bulk silicon interface. If carriers caught in these states are not transferred back into the conduction band, before or during charge transfer, the charge is lost or appears in the next well. One solution to this problem is to cause the charge to accumulate away from the silicon dioxide–bulk silicon interface; this can be effected by putting a shallow layer of oppositely doped silicon under the silicon dioxide. This is a buried channel device. Since our CCD is such a device it has very good charge transfer characteristics. Very few problems are seen even at very low signal levels.

1.15 Adapting the Polarimeter to the CCD.

The adjustments required to physically accommodate the CCD as the detector, for the Durham Imaging Polarimeter, were minimal, it being only necessary to change the detector mounting. This was changed to allow the CCD dewar to ride on the back of the polarimeter (in the same place as the electronographic camera) in such a way as to allow it to rotate and translate for optical alignment purposes. The adaptation was simplified due to the similar sizes of the electronographic camera light sensitive photocathode and the CCD detective area. In addition to this change it was also necessary to obtain a new half-wave plate to enable the measurements to be extended into the near infra-red. A super-achromatic half-wave plate was obtained which has an effective range from 400 to 1000 nm.

1.26 The CCD Control Software.

The control software for the CCD readout, image display and data storage functions, was supplied with the camera system. The software had already been developed at Cambridge by Mackay and co-workers (together with some software designed to perform basic image frame manipulation (+ - \times \div etc.)). The method of data handling employed was quite simply to read out the CCD at the end of an exposure and write the frame to disk. These frames were then stored on disk until an appropriate time arose, such as morning, or bad weather, when they

could be written to tape. This method of operation led to certain problems during an observing run. If the number of exposures made during any night exceeded about 70, it was necessary to stop observing whilst a number of the frames were written to tape. This wasted time, which is very precious on any large telescope. Also because the frames were dumped to tape during the day, the dump was unsupervised, so if any problems arose (local power supply failures, computer crashes etc.) during this time, observing time could also be wasted rectifying the situation, since the frames had to be dumped before the next nights observation could begin. All these problems were aggravated by the painfully slow frame dumping process itself. It was therefore decided that a new system which could relieve these problems was necessary.

Computer time is available when waiting for an exposure to finish or waiting while a new object is found. So if a new system could make use of this spare processor time it could probably meet all the extra requirements. The security of the system could also be improved if files containing lists of the tapes, which included the identities of each frame on each tape were kept permanently on disk. On investigation it was discovered that, with effort, the Nova computer could be made to run two programs simultaneously. So it became apparent that if a program could be written such that when it is loaded into the foreground (the portion of the computer memory reserved for running a second program is called the foreground, the other memory portion which is still available is called the background) it could write new frames to tape as they were taken, this would probably solve all the problems.

Accordingly a suite of programs was developed to achieve the aims outlined above, the system is named DORADO (Durham Overseas Recording of Astronomical Digital Observations system, for posterity) and was jointly developed by the author and Dr. Rodney Warren-Smith. The basic principles of the DORADO system will now be explained. After the system has been initialised a tape is introduced into the system. This forms the starting point of any observing session, under DORADO. A catalogue of tapes with entries containing the number of frames which have already been written to each tape is then consulted. The tape mounting routine (Tapemount) then offers this number to the user as a default for the number of frames to be kept on this tape, or allows the user to return some other number (after some protest) less than this number. If the tape is new and has not been introduced into DORADO before, a new entry is made in the tape catalogue (a protected file on disk, which is invisible to the user under normal operation), and a new tape log file is also made (also a protected file on disk). The tape log file is unique to this tape and will contain the identifications of the frames written to this tape.

When the tape mounting routine has gained all the necessary information about this tape it then loads a program, (Tapedump) into the foreground of the computer memory. Tapedump then continually runs in the foreground throughout any other permissible operation in the background (ie. at the computer console). The tape dumping routine actually performs the copying of frames from disk file to tape file. The tape files are stored in FITS format (Wells, Greisen and Harten (1981)), which is a standard format for transporting n dimensional data

arrays, and can be read on most applications computers, or for which a suitable reading/ writing routine can be readily produced. The frame dumping program also updates the catalogue of tapes after each frame is successfully dumped; note that if some problem occurs whilst a frame is being written to tape the system behaves as if no attempt were made to write this frame to tape, since the catalogues and log files are updated only on successful completion of the transfer of each frame. Thus the data is safe and will be written to tape when the situation is recovered. If any errors do occur which force the foreground process to exit they are reported by any of the tape and file inspection routines. Such errors are caused if the tape is full, or a file which is to be dumped has been deleted, etc.

The foreground frame dumping process identifies which frames are ready to be dumped by inspecting a communications file which contains a list of all the frames to be written to tape, plus some other information about each frame which is to be written into the header of the tape file (it usually contains the frame exposure time, any comments, object name, the time and date and others). If the communications file is empty the foreground process waits until an entry is made, usually by one of the exposure routines or by the frame submission routine which can submit any frames to this frame dumping queue. If any file, such as the frame dumping queue, or one of the catalogues, is being accessed by any routine, a status flag is first set in a common area which the computer defines for communications between programs. Suitable action is taken by all other routines, which usually wait until the status flag is reset before attempting to access the file themselves

(after of course re-setting the status flag to busy). This stops any problems arising from two programs say trying to write into the same file at the same time. Also if any background routine requires the complete attention of the central processor it can write into this area, instructing the foreground process to stop its current activity and wait for a specified time, a command which can be repeated to extend the wait indefinitely if required. This ability is essential when the CCD is being read out, because timing problems can arise if the processor does not give its full attention, also similar problems can arise when images are being transferred to the image display unit. Thus the foreground process takes lowest priority using only the time which is unused by the other routines, which control the CCD and allow image display. Access to the communications file, catalogues and logfiles takes place on a first come basis.

When the foreground process is loaded any other of the suite of DORADO routines may be run in the background. Thus exposures can be made, images displayed, information can be displayed, the tape queue and catalogues can be inspected, and the status of the frame dumping process can be monitored; all while the foreground process processes and writes any frames to tape. Unfortunately the memory of the Nova computer is somewhat limited, there being only 64K of RAM available to contain the operating system (Data General's Real time Disk Operating System RDOS), and both the foreground and background processes. Thus when the foreground process is loaded, severe restrictions are placed on the memory available to the background process. This makes it necessary not only to optimise all the code in the

DORADO routines (making most very efficient, but not easy to read, understand, and correct), but also made it necessary to convert many more of the originally available routines than was first thought. A full listing of all the DORADO-compatible routines in the CCD system is given, together with a description of their functions, in appendix A.

1.7 Preparation of the CCD data.

When the CCD data has been taken and written to tape, it must now be converted on the Durham node of STARLINK into a standard format before it can be analysed to produce the final polarisation maps and intensity images, by the Durham Imaging Polarimetry System (DIPS) suite of programs (written by Dr. Rodney Warren-Smith). Accordingly a sequence of necessary pre-processing programs were produced by the author and Dr. Warren-Smith.

The CCD data is in the form of an array of 16 bit words (integers) in the range 32767 to -32768, which corresponds to the Fortran data type `integer*2`. The sense of the values is negative (ie. an image which is displayed looks like a photographic negative). To prepare the data it is necessary to convert the integers into a positive image whose values correspond to the number of electrons in each pixel.

First the data range is corrected into a positive image, then the integer values are changed into number of electrons, rather than the

analogue to digital units, by scaling the integers so that when the values are corrected by a scale and zero factor, the number returned is the number of electrons ie. $(\text{number of electrons}) = (\text{integer value}) \times (\text{scale factor}) + (\text{zero factor})$. This is the standard method of storing polarimetry images, as integer*2 images together with descriptors containing the scale and zero factors. This method of storage uses half the memory of real (equivalent to integer*4) images, which is very useful when dealing with large datasets. The bias offset of the CCD and electronics is removed by reading out before and after each sequence of serial transfers (ie. each line). This is achieved by reading the lines from the CCD without sending the data transfer word/ instruction. This has the effect of defining a region around each CCD frame which contains the "zero" subtraction. It is then simply necessary to determine which lines in the frame contain the bias value, which after some noise rejection and smoothing can be interpolated across each line and subtracted. This method allows the zero value to be monitored during *each* line read-out so that any variations can be subtracted correctly, unlike the usual method of using an average bias frame to perform the correction.

After these essential corrections have been made, it is now possible to remove any areas which contain bad data from the frame. This is achieved by resetting the integer values of bad pixels to a fixed value (usually the lowest possible integer*2 value), which is stored as a descriptor (together with the scale and zero). Thus when any further processing is done it is only necessary to check that a value does not correspond to this invalid value, before using it. Because the CCD is such a stable device, all of its intrinsic defects tend to be spatially

fixed, thus a standard "mask" of areas which are probably in error, such as bad lines, and hot spots, can be made and applied routinely to all frames.

Charge overflow in each pixel can also be found automatically (at least in the source pixels), since it only occurs when the number of electrons in a well exceeds a critical value, which is determined by the CCD type and can be estimated by observation. These pixels can also be invalidated. All these processes stop bad data from entering the final data set and producing bad results. Finally the data is also rotated to correspond to the DIPS standard, and further descriptors are added containing such information as halfwave plate position. The data is then ready for processing in the DIPS package.

1.8 Future Developments.

The future of the CCD system lies mainly with the development of an *Automated* Polarimeter, currently nearing completion, and hopefully undergoing field tests sometime early in 1988. The automated polarimeter is operated by a dedicated micro-processor, which will eventually enslave the the Nova minicomputer and take over all user interfacing, with the polarimeter system. It is the intention to make this system sufficiently versatile to make whole series of exposures, under complete automation, thus the observer will only have the responsibility of telescope setting and guidance (if the telescope does not auto-track), and

focussing etc. No doubt this system will serve well until the next generation of detectors arises.

There is also the possibility of extending the wavelength range which it is possible to observe back into the blue end of the spectrum, so that the wavelength coverage which can be achieved will extend well over a factor of two (400nm to 1 micron), this has been achieved with thick CCDs by coating them with materials which absorb blue photons and then (proportionally) fluoresce in the red (Cullum *et al.* (1985)).

Chapter 2

Data Correction and Verification.

2.1 Introduction.

In this chapter the numerical results acquired using the Durham Imaging Polarimeter in conjunction with the new CCD detector system will be verified and compared with values obtained using the electronographic camera as the detector. It is known that the results obtained with the electronographic camera are reliable, within the errors of their measurement (Axon (1977)). Thus such a comparison should provide a sufficiently satisfactory check that the new system does indeed measure the true polarisation and contrast the improvements in the data quality.

Also within this chapter the corrections which need to be made to the measured position angle of polarisation in data taken with the

new polarimeter setup will be detailed. These corrections are necessary because the equivalent optic axis of the new superachromatic halfwave plate shows some variability with wavelength. The method for deriving corrections for these variations will be described and applied to the data on a “first order” level. Finally the results obtained to date will be summarised, presenting a large volume of data which is directly attributable to the improved applicability and efficiency of the new system.

2.2 The Comparison Data.

For a comparison of the two data types (electronograph and CCD), objects were selected from the lists of those observed with the electronographic camera, and those which had been observed with the CCD camera system. It was found that the object R Monocerotis with its associated nebulosity NGC2261 and the reflection nebula NGC2023 had been observed with both systems, and also that the resultant datasets were in similar band passes, so that any wavelength dependency in the polarisation of these objects would not effect any measurements too adversely. Consequently the data available for these two objects was used for the following analyses.

NGC2023 is classical reflection nebula in Orion which is almost fully illuminated by the star HD37903. Mannion (1987) has fully analysed the data used here and other data in all the available passbands.

The reader is directed to this work for any further information about this object. NGC2261 and R Mon will be fully examined later in this work.

To ensure that the comparison was made using unbiased samples of both data types, an equal number of exposures of each object in each bandpass were used. For data from NGC2261 taken in both the R and broadband V (VV) bandpasses only three of the usual four plates taken during an electronographic study were available. These two datasets were taken on the same telescope as the CCD data. Consequently the CCD data used was also restricted to three frames; in the CCD R and V bandpasses. A comparison of the two different sets of filter responses, convolved with the detector response is made in table 2.1. Note that the two different R filters are quite similar in properties, but that there is some considerable wavelength change between the V filters; it is therefore expected that the R measurements should be more reliable.

More data has been taken of NGC2261 using a electronographic camera and the VV filter. This was taken on a different telescope (the AAT) and comprises two complete sets of four plates, but unfortunately (for this study) these were taken at a much increased image scale. Because of this it was necessary to resample this data down to the resolution of the other datasets, to allow easy direct comparisons. The NGC2023 data consists solely of two R band datasets, comprised of four plates/ frames each taken on the same telescope.

Table 2.1:

CCD band passes(nm).			
Filter	Mean	Peak	Band Width
V	555.5	532.3	90
R	668.9	646.6	172
Electronographic band passes(nm).			
Filter	Mean	Peak	Band Width
VV	521.3	480.6	116
R	669.9	631.5	111

Fortunately it was possible to select a region within the scope of the NGC2261 data, which has an area in common with the electronographic data nearly equal to a full grid width. Thus a comparison could be made over almost all of the electronographic data. A grid is the width of one part of the image mask placed at the focal plane of the telescope which blocks out half the object (in strips). This allows the object to be re-imaged by the Polarimeter into two orthogonal polarisation states, thus allowing the polarisation to be calculated without the requirement of photometricity.

Unfortunately the NGC2023 data was taken with the grids running perpendicularly between each set of observations. In the electronographic data the grids ran east-west, and in the CCD data north-south, so only those areas of common overlap in this lattice of data were available for comparison.

The original polarisation measurements extracted from the data-

sets for both objects are shown in figures 2.1 to 2.4. Obviously the new setup of the Durham Imaging Polarimeter and CCD camera measures quantities which appear to be the same as the polarisations measured by the Polarimeter and electronographic camera, as can immediately be appreciated by inspecting these figures. The NGC2261 data has a contoured image, shown to give an appreciation of the dimension and shape of the object. No similar image is shown for the NGC2023 data because the sparsity of data precludes an intelligible contour effect, however, a cross is shown to mark the position of the illuminating star HD37903. The integration bins used in all these maps is 5 pixels square, each pixel corresponding to about 1.2 arcseconds.

Note that the CCD data for NGC2023 appears to go much further from the illuminating star before the polarisations randomise, lending credence to the view that the CCD data goes much deeper than the electronographic data. The relative exposure times for this data are 5 minutes and 30 minutes per plate, for the CCD and electronographic data respectively. Both datasets were taken on the 1 metre George and Florence Wise observatory telescope, Israel. This gives total exposure times of 2 hours for the electronographic data and 20 minutes for the CCD data. However, it is usual for the atmospheric transparency to differ between separate observations so that any integration of signal, and subsequent comparison of noise levels, is only approximate. Even so, it is apparent, even from a cursory glance at the raw data, that the CCD in conjunction with its R filter is a much more sensitive device than the electronographic camera and its R filter; 5 minutes exposure time with the CCD system being at least equivalent to half an hour

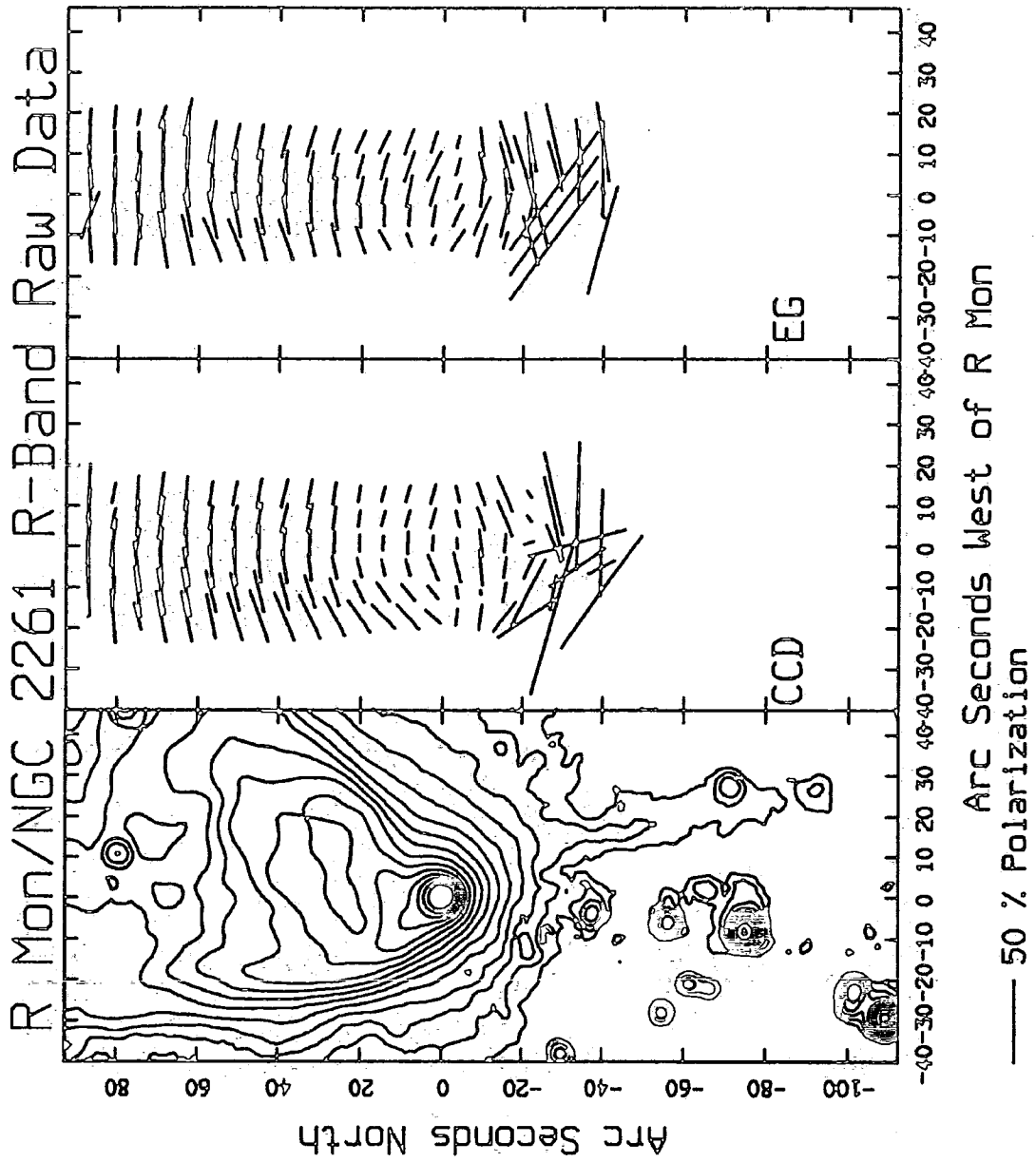


Figure 2.1: Original R-band polarisation maps of R Mon/NGC2261, from datasets taken with the CCD camera (CCD) and the electronographic camera (EG). Also shown is an contoured intensity image of NGC2261. The integration bins are 5 pixels square (6").

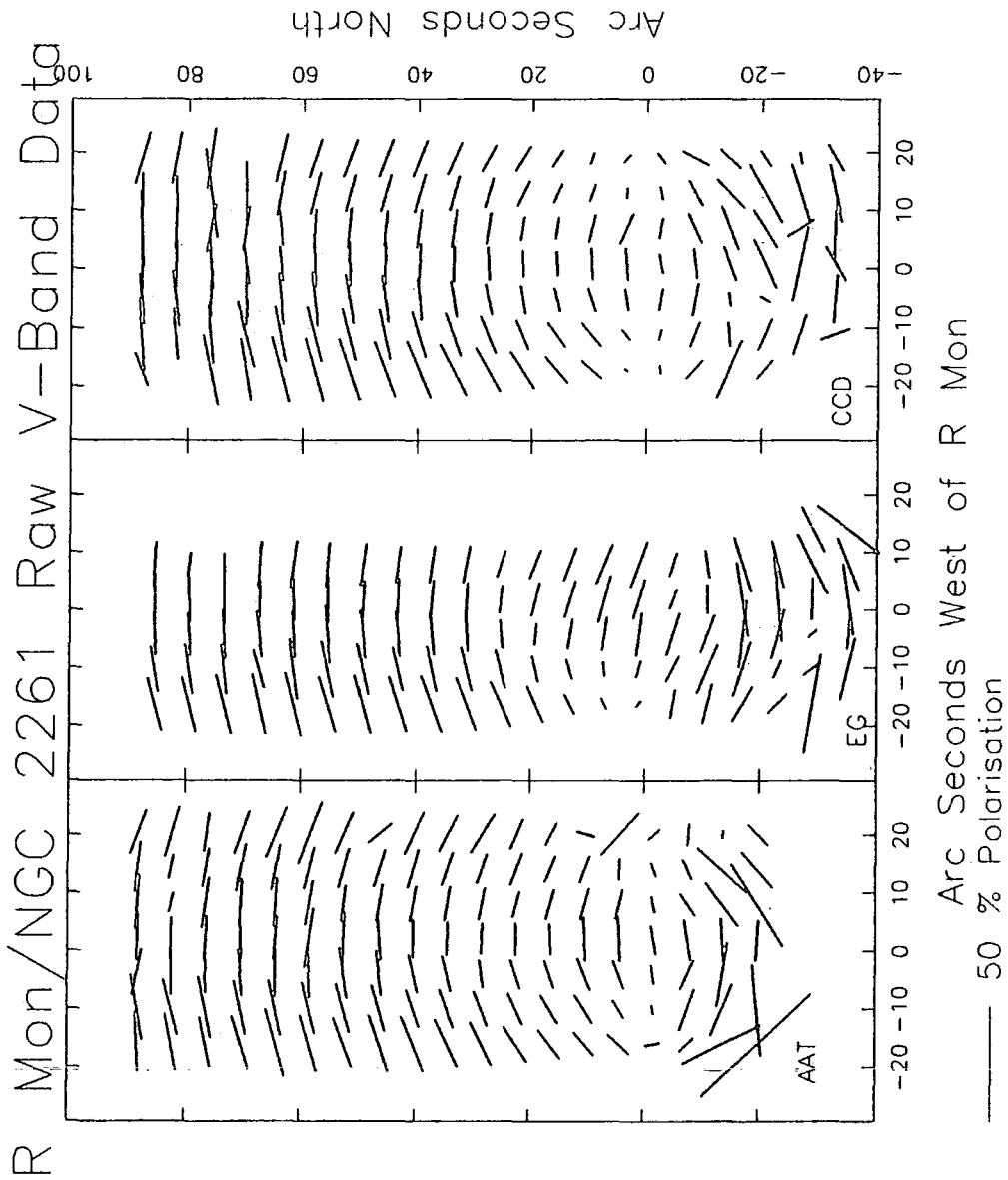


Figure 2.2: Original V-band polarisation maps of R Mon/NGC2261, from datasets taken with the CCD camera (CCD), the electronographic camera (EG) and the electronographic camera on the AAT (AAT). The integration bins are 5 pixels square (6").

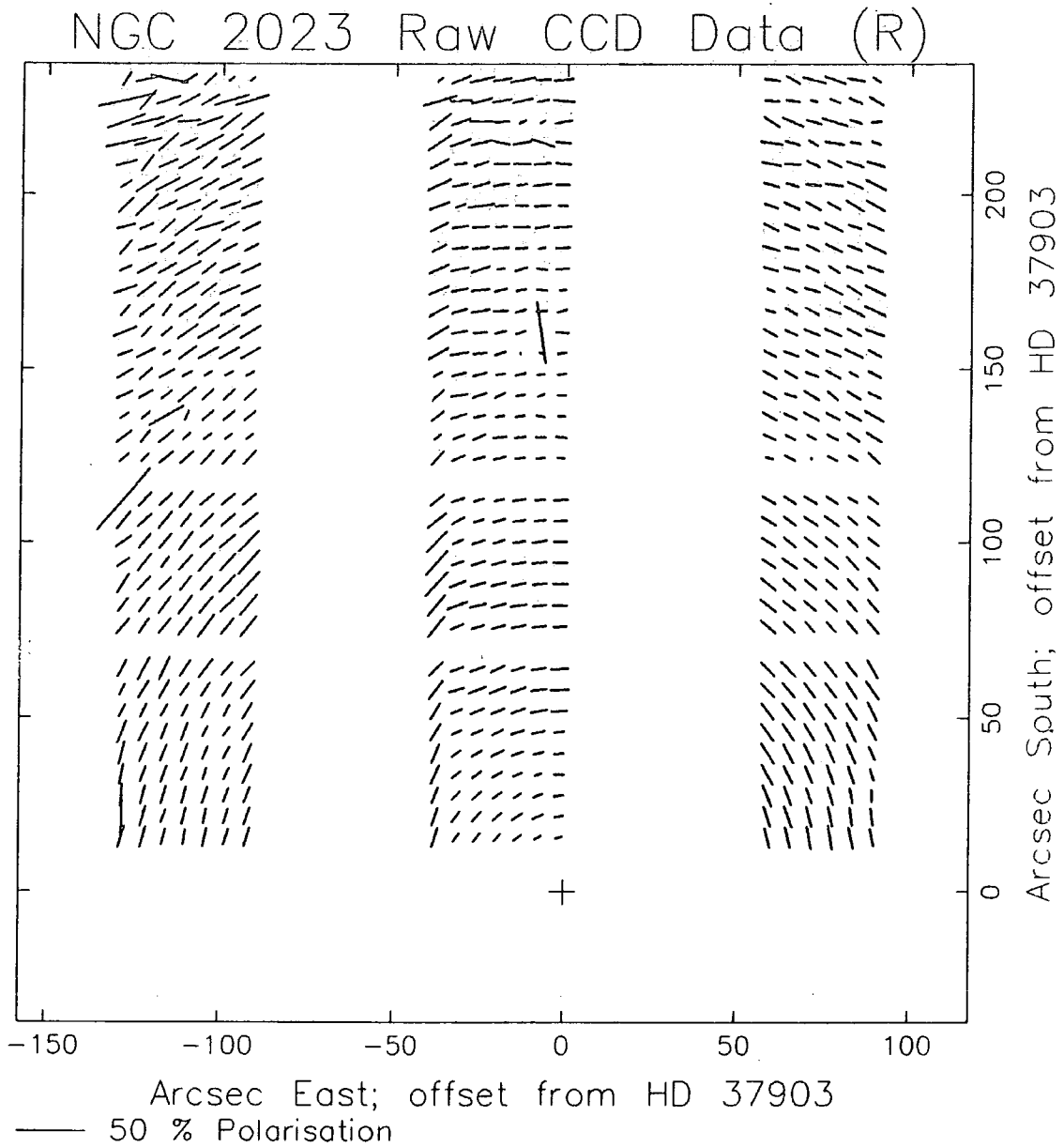


Figure 2.3: Original R-band polarisation map of NGC2023, taken with the CCD camera. The cross denotes the position of the illuminating source HD37903. The integration bins are 5 pixels square ($6''$).

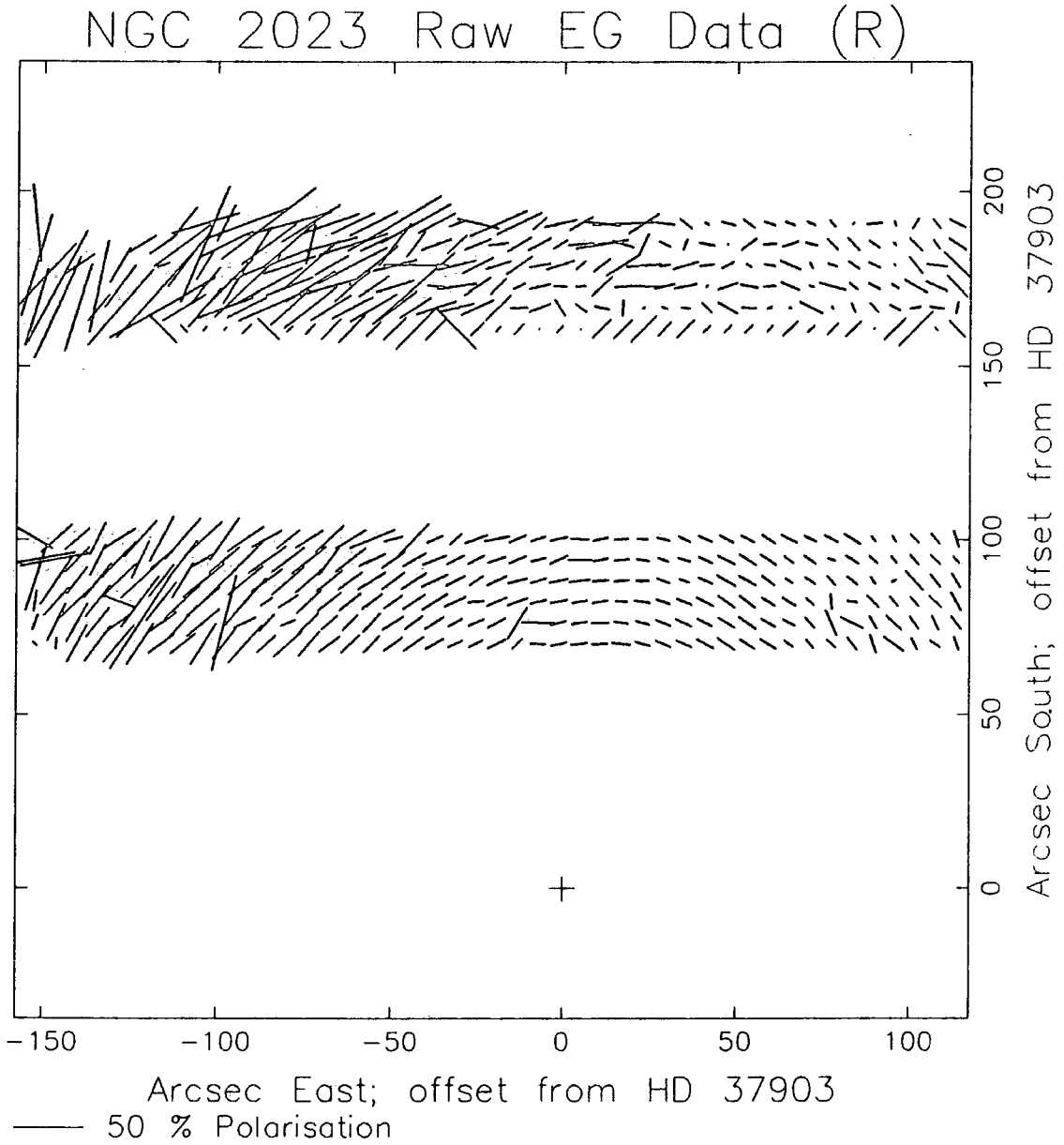


Figure 2.4: Original R-band polarisation map of NGC2023, taken with the electronographic camera. The cross denotes the position of the illuminating source HD37903. The integration bins are 5 pixels square (6").

exposure with the electronograph plus its R filter. This represents an improvement in sensitivity of at least a factor of 6. Note also the contrast in number of spurious vector events between the two maps; the CCD data appears cosmetically cleaner, except for one line of vectors effected by a “grid edge”. This effect is due to the data analysis and is not due to any data error. The data which is available for comparison from these two datasets is shown in fig 2.5 and 2.6. Obviously in the case of the electronographic data, only data in the areas marked 1 and 2 are going to give reasonable results.

A similar contrast between the five NGC2261 datasets is not so readily apparent as the object is much more well defined and the signal does not tail off smoothly into noise. Two of the three electronographic datasets were obtained at the Wise observatory in January 1979. The exposure times for this data were 30 minutes per plate in both the R and VV filters. The third electronographic dataset was obtained at the prime focus of the Anglo Australian Telescope in 1980, and thus is at a considerably enlarged image scale of about 0.33 arc seconds per pixel, compared with the image scale of the Wise data which is about 1.2 arc seconds per pixel. The exposure time for the AAT data is 15 minutes per plate. The CCD data was also obtained at the Wise observatory in December 1985 and January 1986. The R band data has an exposure time of 30 seconds, and the V band data 3 minutes, per plate.

An apparent difference between the datasets is the region of anomalous polarisations (first noted by Gething *et al.* (1982)) about the head of the nebula. This varies between the 1979, 1981 and 1985/6

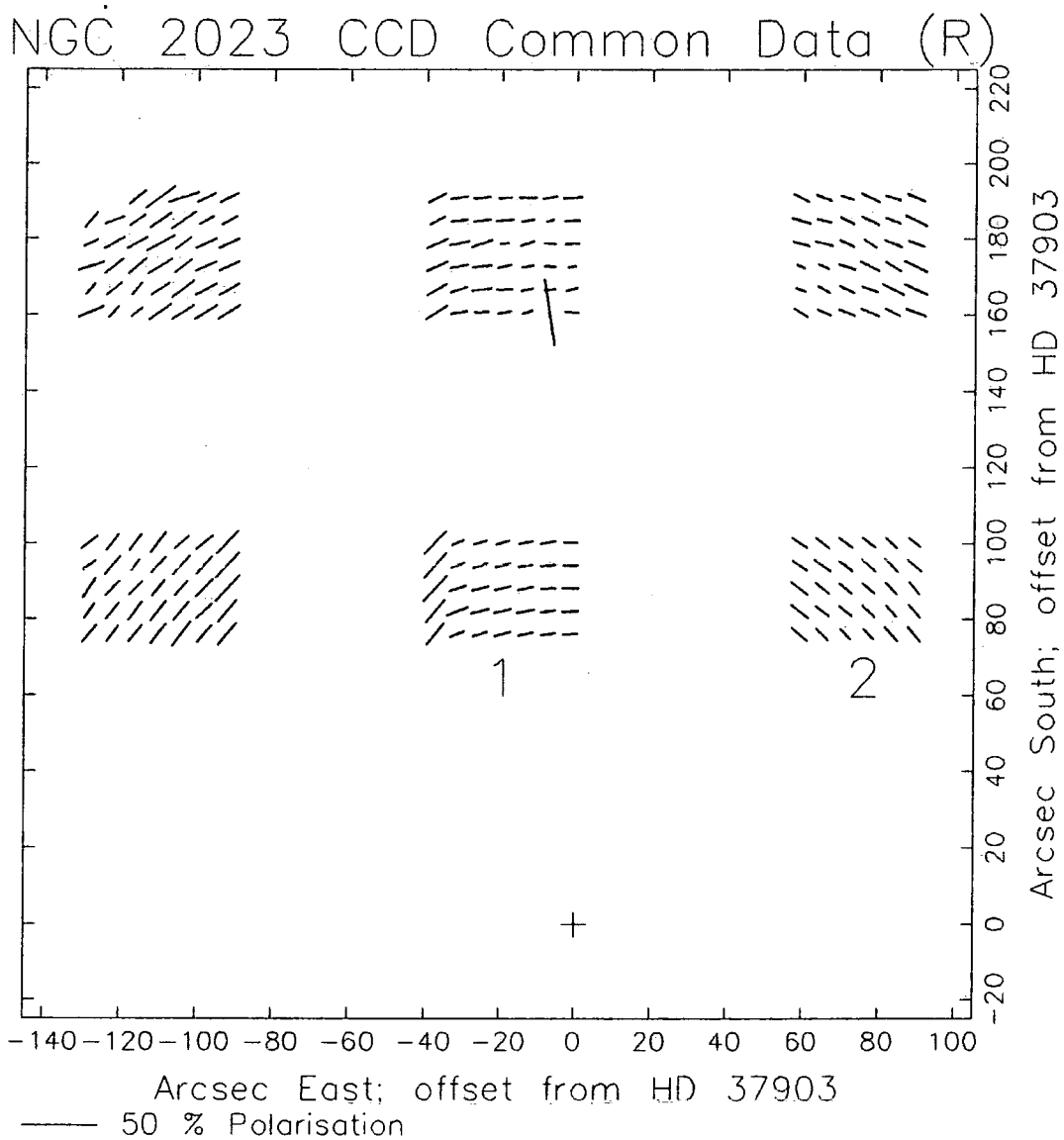


Figure 2.5: CCD data common between figures 2.3 and 2.4.

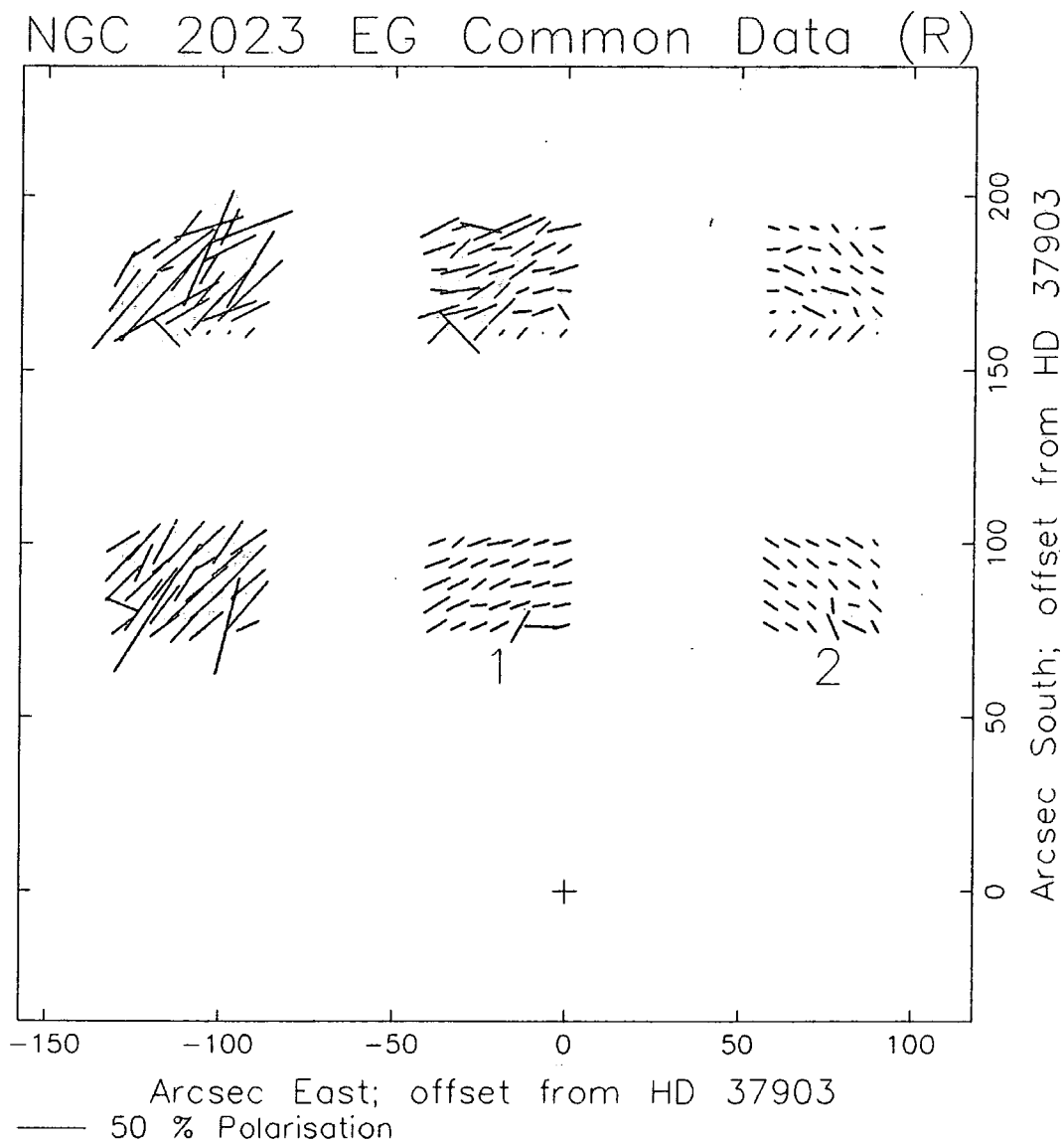


Figure 2.6: Electronographic data common between figures 2.3 and 2.4.

datasets. Clearly this region cannot be used for any comparison and needs to be removed before any further analysis can take place (see Chapter 4 for further discussion concerning these variations). It is not expected that these effects should propagate significantly into the predominantly reflection part of the nebula, where the vectors appear mostly centrosymmetric (ie. where all the vectors are normal to the radius vector from the illuminating star) so only this region will be used for the comparison.

2.3 Data Correction.

2.3.1 Halfwave plates.

A halfwave plate can be defined as the specific condition of a plane section of a birefringent material, cut parallel to the material's optic axis, which splits the incident radiation into two orthogonally polarised Ordinary and Extraordinary ray components and introduces a phase difference of 180 degrees between the two components. Generally such a plate is called a retarder. The O and E rays have different velocities in the material, but providing that the incident light is normal to the face of the retarding plate the rays are not deviated and emerge with a net phase difference, given by:-

$$\delta = 2\pi d(n_o - n_e) * 1/\lambda - (2.1)$$

where λ is the wavelength, d the thickness, and n_o and n_e are the refractive indices of the ordinary and extraordinary rays. If the condition $\delta = (2m + 1) * \pi$, is satisfied, where m is an integer (positive), the two rays emerge 180 degrees out of phase and the retarder is called a halfwave plate. However, this condition is wavelength dependent and any single value of d (the thickness) makes the condition true only at one *specific* wavelength. Note that if the halfwave plate is rotated between, say, two consecutive measurements, the angle of the plane of polarisation is rotated through twice the angle the plane of polarisation makes with the direction of the optic axis.

2.3.2 Achromatic halfwave plates.

Achromatic wave plates can be produced which are approximately half-wave over a small range in wavelength. This is achieved by combining two plates which are halfwave plates at two different, but close, wavelengths.

This limitation in the range over which a specific halfwave plate can be used, enforced the use of the following method used in conjunction with the electronographic camera. A series of halfwave plates cut to be perfectly achromatic at two near wavelengths, which when combined gave a nearly perfectly achromatic halfwave responses in the range in between, were used to give full coverage in steps of approximately 100 nm (in actual fact only two halfwave plates were used since the wavelength range over which the electronographic camera was sensitive

was small). Thus to take full advantage of the complete range of the new polarimeter setup many more halfwave plates would be necessary. However, each time a different halfwave plate is used a recalibration of the polarisation position angle is necessary, requiring some additional observing time either to set up or determine by observation.

2..1 Superachromatic halfwave plates.

To overcome these problems, thus aiding simplicity, a superachromatic halfwave plate was obtained from the Bernard Halle Nachff workshop, Germany. This halfwave plate is achromatic (± 1 per cent) over the range 310-1100 nm ie. about 800 nm in total. It consists of three identical pairs of quartz and magnesium fluoride (MgF_2) plates, each pair of which is an achromatic halfwave plate in its own right. The two outer plates have their optical axes parallel, the inner one has its optical axis at an angle with respect to the others.

The feasibility of combining three halfwave plates in this manner to produce a superachromatic halfwave plate (or similarly producing a general superachromatic retarder), was first discussed by Pancharatnam, a full description of his methods is undertaken by Serkowski (1973). The theoretical retardance of the halfwave plate is shown in fig 2.7(a), the halfwave plate is seen to be achromatic to within 3 degrees over the full range, and as Serkowski has noted this means that the measured polarisation is correct to a term in $\cos(180\pm 3)$, (see Appendix B for the relevant details); an insignificant depolarisation, unless the ob-

servations are at the extremes of those possible in measuring stellar polarisations.

Unfortunately using this combination of three halfwave plates produces a *wavelength dependent equivalent optical axis*, which varies by ± 2 degrees over the full range. This problem is also seen in normal achromatic plates, because quartz shows some circular birefringence altering the equivalent optic axis, but only by an angle at worst of the order 0.2 degrees over the equivalent wavelength, Serkowski (1973).

The theoretical variation of the equivalent optic axis of the superachromatic halfwave plate with wavelength is shown in figure 2.7(b). The size of these variations can be calculated from the retardances of the individual quartz-MgF₂ plates, which in our case are identical, by the equations derived by Pancharatnam. For the apparent retardance τ and equivalent optic axis ω we have the relations:-

$$\cos(\tau) = \cos(\tau_1)\cos(\tau_2/2) - \sin(\tau_2/2)\sin(\tau_1)\cos(2c) \quad (2.2)$$

$$\cot(2\omega) = [\sin(\tau_1)\cot(\tau_2/2) + \cos(\tau_1)\cos(2c)]/\sin(2c) \quad (2.3)$$

where τ_1 is the retardance of the first and last quartz-MgF₂ pair, and τ_2 that of the central pair, c is the angle between their optic axes.

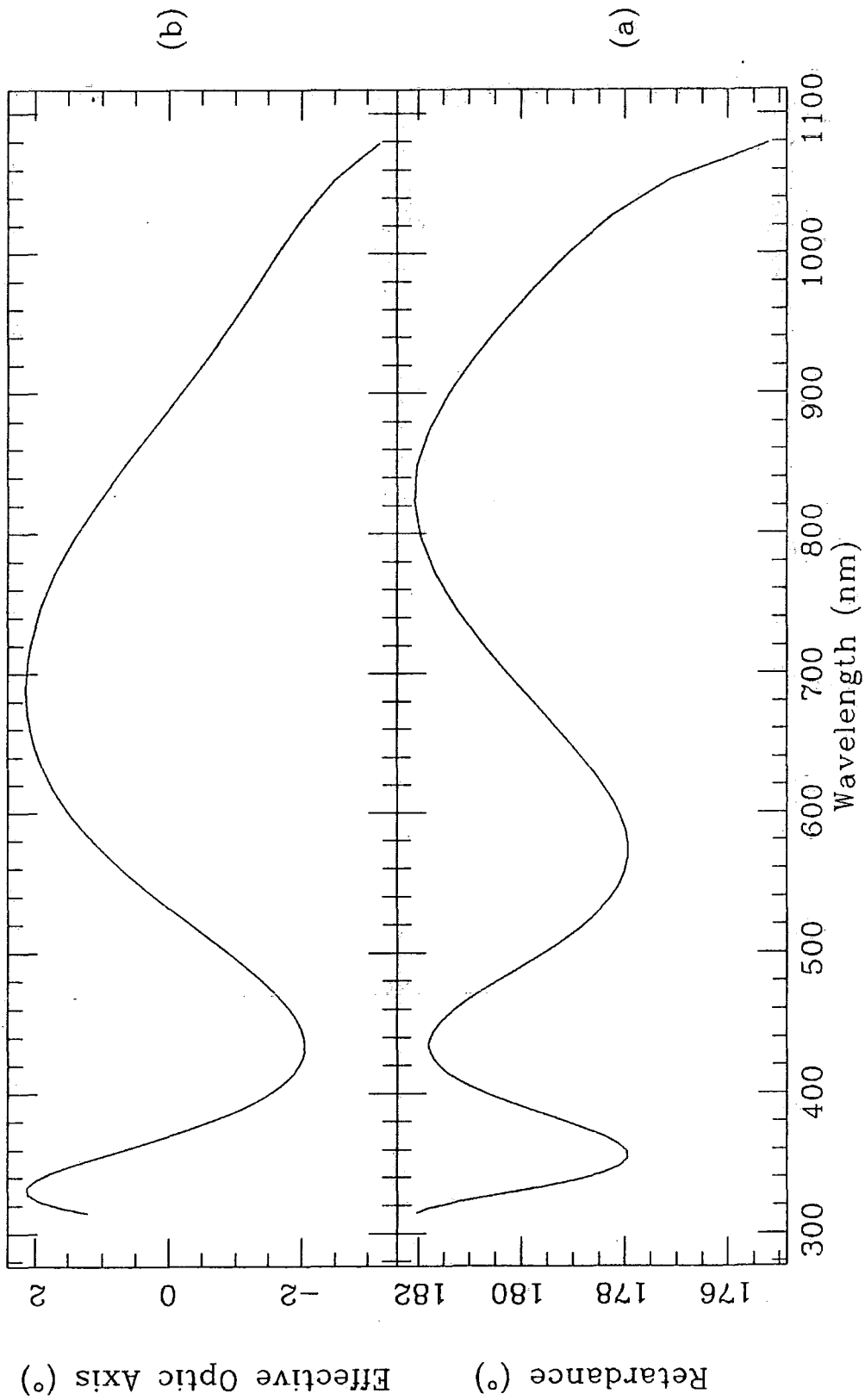


Figure 2.7: The variation with wavelength of the retardance and equivalent optic axis (relative to the mean optic axis) of the superachromatic halfwave plate

Table 2.2:

First order corrections to the mean optical Axis.	
Filter	Correction (deg)
B	-1.56
V	0.51
R	1.80
I	1.44
Z	-0.69
NF	1.09

NF=No Filter CCD response.

2.3.4 The corrections.

Because of the variation of the equivalent optic axis it is necessary to correct the position angle of any polarisation measurements if accuracy to better than plus or minus twice the mean optic axis over the selected band pass is to be achieved. Twice because the plane of polarisation is rotated through an angle twice its angle with the direction of the optic axis. Hence the real effect of the variations shown in fig 2.7(b) is twice as large.

Applying a normalised weighting function equivalent to the band-passes of the CCD filter system, it is possible to produce first order correction terms with respect to the position of the mean equivalent optic axis. The equivalent optic axis of the halfwave plate, after being convolved with each of the normalised filter functions and with a nor-

malised CCD response, are shown in fig 2.8. The mean values (ie. the integral under these curves) for the responses are presented in table 2.2. The means are the usual values:-

$$Mean = \frac{\int \Psi(\lambda)F(\lambda)d\lambda}{\int F(\lambda)d\lambda} \quad -(2.4)$$

with optical axis function Ψ , and filter function F , or:-

$$Mean = \int \Psi(\lambda)F(\lambda)d\lambda \quad -(2.5)$$

if $\int F(\lambda)d\lambda = 1$. Additional (filter, object) functions are simply introduced:-

$$Mean = \int \Psi(\lambda)F_1(\lambda)F_2(\lambda)\dots F_n(\lambda)d\lambda \quad -(2.6)$$

with normalised functions $F_1, F_2, \dots F_n$. It must be emphasised that these corrections are only first order, since the mean optic axis will also be a function of the power spectrum of the object under observation. Where possible, to achieve maximum accuracy, a weighting function in respect of this must also be applied before finding the mean value. This effect may be significant when making very accurate observations of objects with steep power law-type spectrums. The magnitude of the corrections are quite similar at high temperatures for blackbody spectra, compared with the uniform source values, and the results of some such calculations for the change in position angle in V and R are

Table 2.3:

R and V band corrections to the mean equivalent optical axis; based on black body spectra.				
Peak Wavelength (nm)	Temp (K)	V	R	Corrections (deg)
300	9666	0.40	1.77	
400	7250	0.44	1.78	
500	5800	0.46	1.79	
600	4833	0.52	1.80	
700	4143	0.56	1.81	
800	3625	0.61	1.82	
900	3222	0.65	1.83	
1000	2960	0.69	1.83	
uniform	—	0.51	1.80	

shown in table 2.3.

2.4 Results.

After selecting the data as described in section 2.2 and correcting with the approximated corrections derived in section 2.3, the actual values themselves can be inter-compared between the various datasets. To achieve a compromise between the intrinsic variability of the functions under consideration, and the requirement that the signal to noise ratio in any integration bin remains as high as possible, various integration bins were tried until the two effects seemed to reach a satisfactory compromise. This occurred at about an integration size of 10 pixels square.

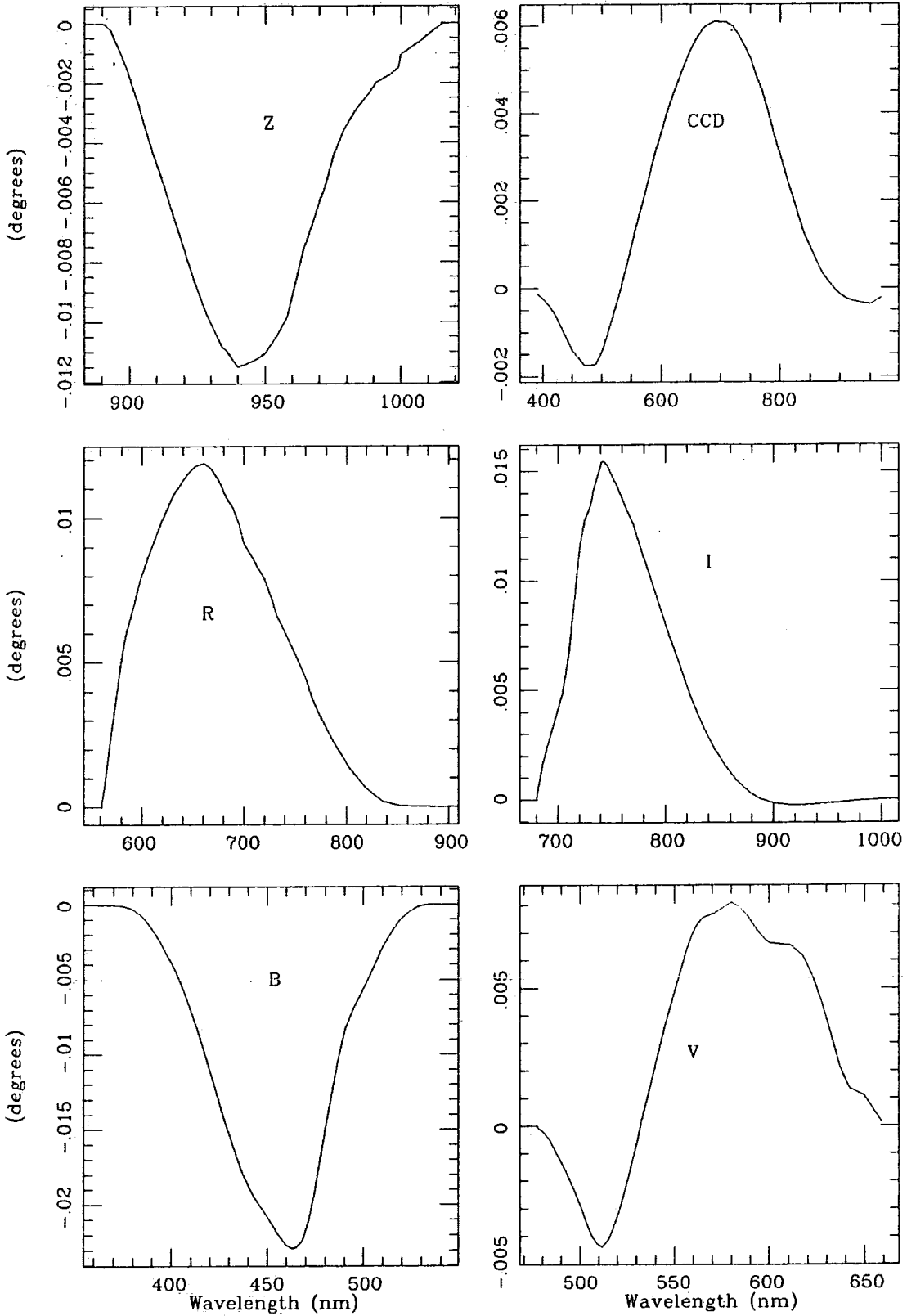


Figure 2.8: Plots showing the convolution of the equivalent optic axis with the indicated normalised (filter) functions. Note that the integral under each curve is the "first" order correction to the optic axis

Accordingly each of the datasets under consideration was analysed using this integration size.

Because the polarisation parameters are variable in the field (ie. the percentage polarisation genuinely varies as does the position angle) it is not totally satisfactory to just take the means of the values over the whole field, each individual measurement needs to be paired against a measurement made in exactly the same integration bin in the comparison dataset, before a global mean can be taken. Also because each measurement made can be genuinely variant from the mean, the standard deviation does not give a measure of the accuracy of the means. This is because it assumes that the population of observed values is distributed normally about the mean, clearly not true here. However, it is true that the distribution function of the compared datasets should be the same, if we are measuring the same variation. A more satisfactory measure of the consistency of the mean values should therefore be given by the function:-

$$\sum_{\text{all pairs}} (\text{value1} - \text{value2})^2 / n - (2.7)$$

the mean squared difference, between the datasets. This will be zero for perfect consistency (unlike the standard deviation, the mean squared deviation from the mean, of the considered datasets which will always be non-zero, but will assume the same value for datasets in perfect agreement), and should hopefully give a measure of how trustworthy the means are, and consequently show how well they agree.

Before going ahead with the procedure outlined above the polarisation maps themselves were visually inspected and any obviously spurious vectors were removed: spurious vectors being those which do not follow the general trend of the polarisation pattern, either in position angle or in percentage polarisation. They are usually caused by blemishes, dirt, scratches, defects, etc. These bad vectors were much more evident in the electronographic data than in the CCD data. The data selected from the NGC2261 datasets is shown in figures 2.9 and 2.10, the data used for NGC2023 is the obvious re-binning of the data marked in the regions 1 and 2 in figures 2.5 and 2.6. Almost no vectors were removed from the CCD data once they had been paired against their equivalent electronographic vectors. If the reverse procedure was attempted this was certainly not true. With these carefully selected datasets the comparison was made. The results of this are shown in table 2.4. Table 2.4 also shows some values from the *complete* NGC2261 CCD V band dataset (consisting of 16 plates across almost the whole object) which have been made at the same points in the nebula and with the same apertures as those made photoelectrically by Hall (1964).

From table 2.4 it is apparent that the polarisation measurements, although not in perfect agreement with the electronographic measurements, are in good general agreement in both the percentage measures and position angles measures, all variations being well within their estimated deviations. The correlation in the case of NGC2023, being very good indeed for both these values, although the Root Mean Square Difference (RMSD) makes the agreement seem fortuitous. There is also encouragingly good correlation with the photoelectric measurements

Table 2.4:

NGC2261, EG=Wise 1979 electronographic data, CCD=Wise 1985/6 CCD data.						
Filt	Detect	N Points	M Poln(%)	RMSD	Pos Ang	RMSD
R	EG	14	23.5	3.6	94.9	6.1
R	CCD	14	22.3		92.3	
VV	EG	14	19.1	3.2	92.9	3.6
V	CCD	14	20.8		95.1	
NGC2261, AAT=AAT 1980 electronographic data, CCD=Wise 1985/6 CCD data.						
Filt	Detect	N Points	M Poln(%)	RMSD	Pos Ang	RMSD
VV	AAT	14	19.96	2.2	93.6	4.2
V	CCD	14	20.6		95.8	
NGC2023, EG=Wise 1980 electronographic data, CCD=Wise 1984 CCD data.						
Filt	Detect	N Points	M Poln(%)	RMSD	Pos Ang	RMSD
R	CCD	24	12.09	1.83	76.13	5.5
R	EG	24	12.04		76.81	
NGC2261, HALL=Hall (1964) data, CCD=equivalent positions in Wise 1986 CCD data.						
Filt	Detect	N Points	M Poln(%)	RMSD	Pos Ang	RMSD
B/V	HALL	13	19.2	3.8	89.9	4.0
V	CCD	13	19.9		91.4	

RMSD=Root Mean Square Difference

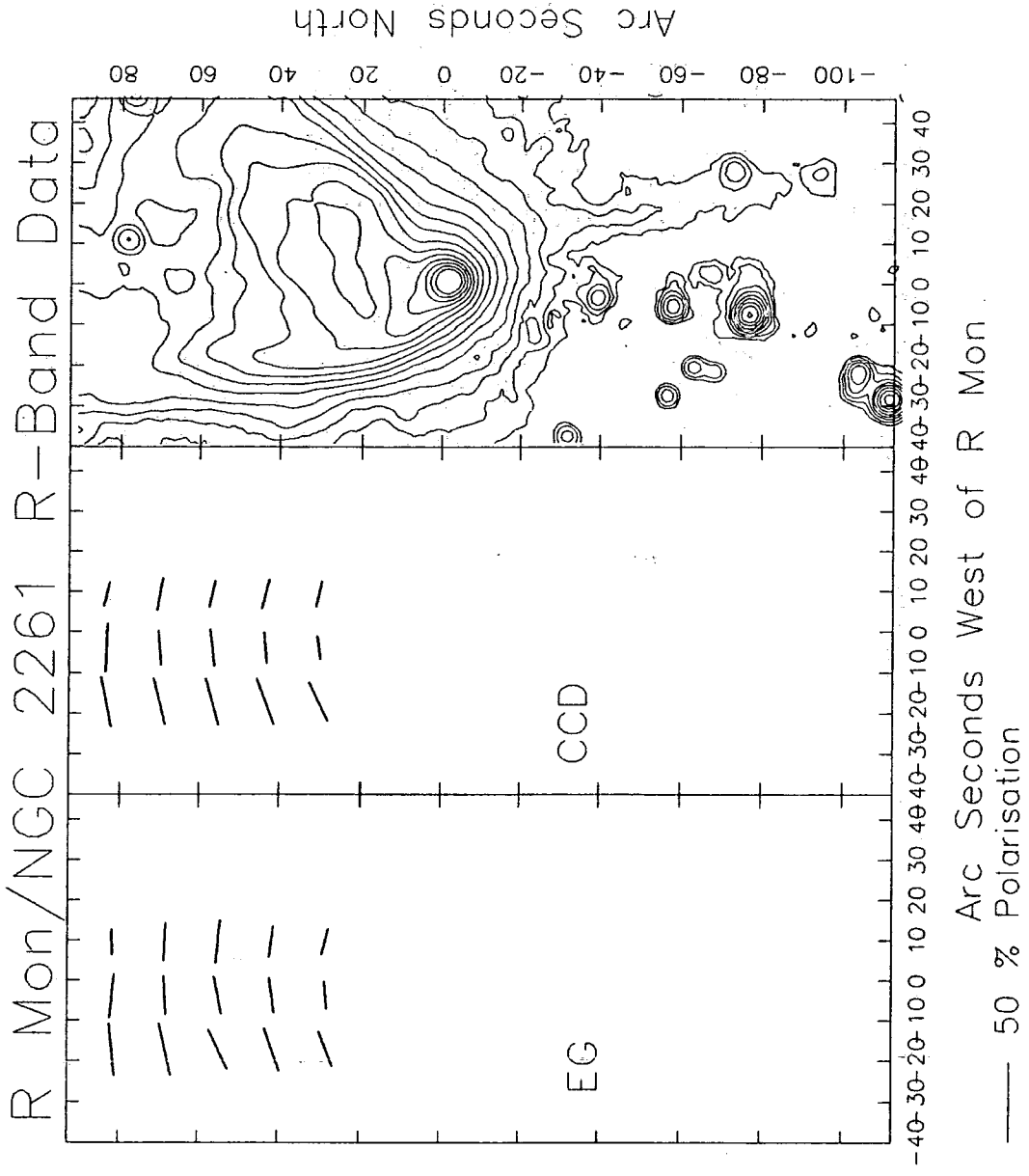


Figure 2.9: Polarisation map of the data selected from the r-band R Mon/NGC2261 map

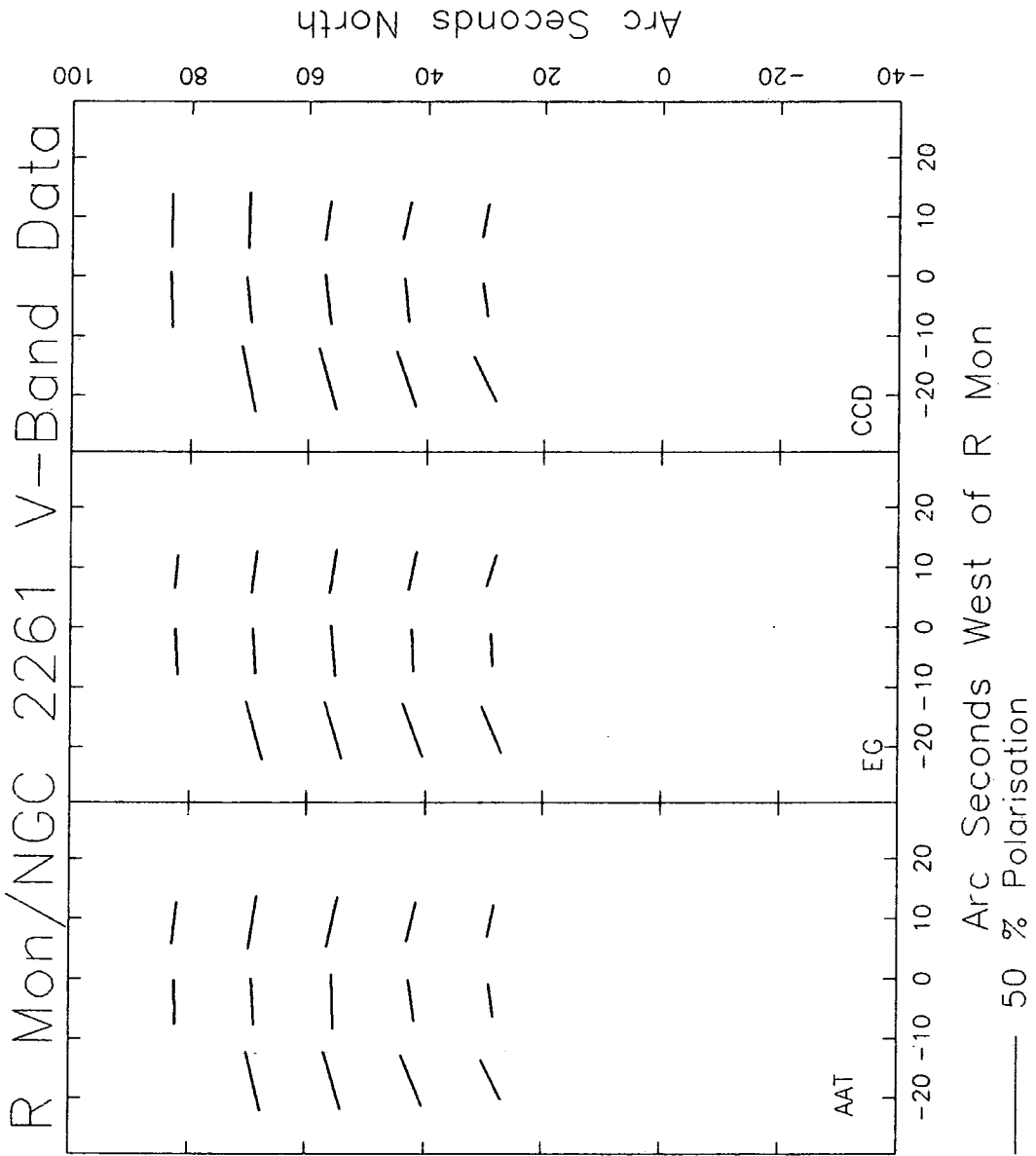


Figure 2.10: Polarisation map of the data selected from the v-band R Mon/NGC2261 map

made by Hall (1964).

On the evidence of the values shown in table 2.4, it is evident that the present set up of the Durham Imaging Polarimeter, incorporating a CCD camera system, measures the polarisation of objects reasonably reliably. Absolute accuracy, however, is not determined, and is not likely to be because there is a sparsity of reliably calibrated sources at higher polarisations and in addition, the Polarimeter is not designed to easily measure stellar polarisations to great accuracy. However, it is evident that the absolute accuracy must be better than 10 per cent of the measured polarisation.

Using the error estimates of Warren-Smith (1979), now incorporated within the Durham Imaging Polarimetry System (DIPS) and implemented on the Durham node of STARLINK by Warren-Smith, the internal accuracy of the CCD results seems to be limited mostly by the photon statistics and the flatfielding errors. Estimates of the signal to noise ratios in these results also show that in all cases, the electronographic and CCD values are similar, thus showing that the CCD is a much improved device for integrating light signals over the electronographic camera. This is because, as has been noted above, the exposure times used in obtaining the CCD measurements were much less than those used for the electronographic results. For the V band measurements, the improvement seems to be of the order 10, and for the R filter somewhat better still; a very satisfactory improvement.

It may be asked if the values obtained for the position angle cor-

rections are accurate. Although it is difficult to doubt the measurements and claims of the manufacturer of the halfwave plate, it is possible that a error in analysis may have been made. To check this simply a polaroid was placed in the beam of the polarimeter and measurements were made in the V and R bands for which it was expected that the polaroid characteristics would be fairly constant. The position angle difference between these bands was found to be about 1.8 degrees, somewhat different from the constant spectrum source value of 2.6 degrees. However after the value was corrected with the transmission response of the polaroid, a reasonably good agreement was found; 1.5 degrees. It is probable that the discrepancy can be accounted for if the power spectrum of the light source was known. There is therefore no reason to doubt the values obtained from the procedures outlined above. Further laboratory checking would be prohibitively difficult since polaroids are not readily available to cover the whole range of the halfwave plate.

The Imaging Polarimeter in Durham has been in use with the CCD detector system since May 1984, and has been successfully used in numerous observing schedules at various telescopes around the world. The data now amounts to a very large collection indeed, some of which has been successfully analysed and interpreted in papers and articles in many journals, in which the author has been involved in many cases. The main areas of interest arising from studies undertaken are; nebulae (bipolar and cometary), jets from young stars, Herbig-Haro objects, faint structures in dark clouds, magnetic fields in nebulae and dark structures, and also polarisation in external galaxies. Studies in these areas has proved fruitful as evidenced by the volume of work which has

already been published, which is listed in Appendix C.

2.5 Conclusions.

In conclusion, the results obtained with the adapted polarimetry system are consistent with those acquired with the older, now outdated, system. However, the variation of the equivalent optic axis of the new superachromatic halfwave plate needs to be taken into account if good accuracy is required in the position angle of polarisation, particularly in any series of multicolour datasets. This accuracy of polarisation position angle measurement being in turn dependent on how well the transmission functions of the filter system in use are known, and possibly how well the *observed* power spectrum of the object under consideration is known (a 2 dimensional function in an extended object!). However, from the black body data presented in table 2.3 and the uniform source data in table 2.2, it is seen that these corrections in the visible are usually small, and unless the accuracy required is greater than about 5 degrees, may be ignored.

Finally, it may be noted with some optimism for increased accuracy without increased complexity that a method discussed by Serkowski (1974) exists for overcoming the problem of this variation of the optic axis in Pancharatnam type halfwave plates. Simply, the solution is to take a second identical halfwave plate and fix it in position, with respect to the wollaston prism, after the rotating halfwave plate. This

configuration makes the intensity of the transmitted light dependent on the angle between the two halfwave plates (see Appendix B), which is independent of the wavelength (provided the plates are truly identical). This may provide a method of eliminating the above problems, finally providing a properly superachromatic arrangement.

Chapter 3

Immediate Regions of Recent Star-Formation.

3.1 Introduction.

This chapter is intended to provide a concise, and for the most part, relevant summary of the observational features and properties of the immediate regions of recent star-formation, together with some description of the various theoretical models which have been forwarded to account for the observations of these regions.

Most workers in the field of star formation now accept that almost all stars go through a period of energetic mass loss, which is perhaps most characterised by the bipolar cold molecular outflows, observed in some sources (eg. L1551, NGC2071, etc. Bally and Lada (1983)). These bipolar outflows are the phenomenon which is probably the most

interesting and startling of the many primary markers of regions of recent star formation, which include rapidly moving Herbig-Haro objects; optically visible jets which appear to originate at the pre-main-sequence stars and high velocity H_2O masers. All these phenomena appear, at least in principle, to be the consequence of the outflows whose estimated kinetic energies are very large 10^{43} to 10^{47} ergs. The mechanism/ structure/ origin of the outflows are consequently of extreme interest. The energy produced by the outflows represents a large proportion of the energy input into molecular gas in the Galaxy and may have some important consequences for subsequent star formation in molecular clouds.

3.1.1 T Tauri stars.

The earliest evidence in favour of an outflow phase from pre-main-sequence stars arose from studies of T Tauri stars. T Tauri stars are emission line variable stars, whose masses are similar to solar values ($\leq 2.5M_\odot$). More massive counterparts of the T Tauri stars are the Herbig emission Ae and Be stars (Herbig (1960), Finkenzeller and Mundt (1984)). The position of T Tauri stars in the Hertzsprung-Russell diagram is above the main sequence, indicating that they are young protostars still undergoing some contraction. Optical spectra of emission lines from these objects show broad, asymmetric, double peaked profiles. Often there is a double peaked structure which shows an absorption feature on blue side of the emission profile, it is this feature which has often been interpreted as evidence in favour of mass outflow for extended periods, from these objects (Kuhi (1978)). Some

Tauri stars (approx 5 per cent) also exhibit a classical P Cygni type profile, which is accepted as an unequivocal indication that mass outflow is occurring.

However, it is also true that 5 per cent of T Tauri stars also show inverse P Cygni profiles (the so called YY Orionis stars), indicating mass inflow, and that some show signs of both inflow and outflow (Kuhi (1978), Ulrich (1978), Appenzeller (1983)), although the inverse profile is not seen in $H\alpha$ (Kuhi (1983)). Other evidence of winds emanating from T Tauri stars has been found in studies of radio continuum emission (Cohen, Bieging and Schwartz, (1982)). The observed emission intensities are consistent with electron densities decreasing with the inverse square of the distance from the source, suggesting continuous outflow.

Mass loss estimates from T Tauri stars vary from around 10^{-7} to $10^{-9} M_{\odot}/yr$ with a mean of about $3 \times 10^{-8} M_{\odot}/yr$ (Kuhi (1964)). Understanding of the mechanisms producing these outflows still remains uncertain. However, it seems that models which are powered by Alfvénic wave propagation, producing the desired wind acceleration, are now being favoured over the models of thermally driven winds that were first suggested. This re-emphasis of the type of model preferred has arisen because thermally driven winds imply very high radiation losses and x-ray fluxes from the solar coronae, which are not observed (Appenzeller (1983)). The overall picture of how accretion and outflow change with time and why is not so clearly defined, scenarios including both outflow and inflow, sometimes at the same time, or by catastrophic changes,

are still being postulated and refined.

3.1.2 Herbig-Haro objects.

Herbig-Haro (HH) objects are usually observed as small semistellar nebulous knots, whose characteristic spectra are dominated by strong low excitation emission lines in OI, [NII], [SII], and the hydrogen lines. The prototypical examples of these objects (HH1,2 and 3) were discovered independently by Herbig and Haro in the early fifties, in a dark cloud within the vicinity of Orion. Since this time the number of objects in this class has increased to more than 70, all of which are located within star forming regions. This strong association with star formation regions has led to the great interest in these objects as potential markers of some stage of proto-stellar evolution.

It has been shown that some of the more extended of these objects, classified as HH objects mainly by their spectral characteristics, are predominantly seen in reflected light (HH100: Vrba, Strom and Strom (1975), HH24: Strom, Strom and Kinman (1974), HH102: Draper, Warren-Smith and Scarrott, 1985(c) for example). This phenomenon usually allows an unambiguous identification of the source of the scattered light, which is seen to be not in the HH objects as was first thought, but from embedded infra-red sources displaced some distance from the HH objects. However, it remains true that the smaller more condensed HH nebulae are not usually highly polarised. HH1 and 2 appear to be mostly illuminated by intrinsic emission (Schmidt and

Vrba (1975), confirmed by Scarrott *et al.* (1985)). HH29, which is near HH102 in the L1551 dark cloud, is certainly not as highly polarised as its surrounds (Draper, Warren-Smith and Scarrott (1985(c))). Interestingly HH24 is highly polarised (approx 24 per cent), but spectropolarimetry shows its spectral lines are not (Schmidt and Miller (1979)) confirming that the spectral lines are emitted intrinsically to the HH object, and that the continuum light is reflected from the illuminating/ powering source. So it appears that spectra in HH objects must accordingly be interpreted mainly in terms of intrinsic emission within the objects themselves.

Initial attempts to manufacture mechanisms to account for the emission spectra of the HH objects by photoionisation and particle streaming methods failed, and so because evidence was now mounting that the HH objects show supersonic radial velocities (Strom, Grasdalen, Strom (1974)) it was postulated that the energy source producing the HH phenomenon was a strong stellar wind which was shocking into the interstellar medium. The spectra observed would then be produced in the cooling region of a fast shock wave. Models of this scenario produce a reasonable fit to the spectral observations (see the reviews of Schwartz (1983) and Mundt (1987)).

Models of the mechanisms proposed which supply the shock wave necessary to these models can be classified in two groups:-

1. those with a single eruptive event from the central source, such as a bullet like ejection of clumps of circumstellar material (Norman

- and Silk (1979)), or perhaps an FU orionis type phenomenon,
2. and those with the continuous action of a stellar wind onto a working surface, although the energy requirements for this mechanism dictates considerable anisotropy in the flow. This is presumably caused either by a collimation mechanism (Schwartz (1983)) or some focussing mechanism (Cantò (1983), Cantò and Rodriguez (1981)).

This view of HH objects is reinforced by proper motion measurements showing inferred tangential velocities up to 350 Km/sec (See Jones (1983) for a summary of the HH objects with measured proper motions to that time). The driving sources for these objects appear to be low to intermediate mass T Tauri like stars, which are quite often deeply embedded. The proper motions and apparent spectral velocities of HH objects can also be interpreted as providing direct evidence for an outflow period in the early phase of stellar evolution.

3.2 Outflows from Young Stars.

Perhaps the most incontrovertible evidence in favour of an outflow phase during stellar evolution is provided by the various radiometric millimeter wave measurements made of the transitions of cold simple molecules in the areas of dark clouds associated with star formation. Usually the regions of interest are indicated by the presence of strong infra-red sources, HH objects, reflection nebula etc., which are commonly taken

as indicators of star formation activity.

Initially molecular clouds were observed in some of the rotational transitions of carbon monoxide (CO), and surprisingly it was discovered that the widths of the emission lines indicated that bulk motions within the clouds of around 1 to 3 km/sec were occurring. This compares with the temperature measurements made of these same clouds which gave values around 10 K, in turn implying that the sound speed within the gas is actually around a few tenths of a km/sec. So the molecular clouds appeared to be in sustained supersonic motion. The origins of this motion remains obscure.

During these studies it was also found that localised areas within the clouds had motions as high as 6 to 8 km/sec. At first these were thought to be due to collapse onto protostars, however, more sensitive measurements of the Orion region showed that CO emission in actual fact was being emitted at considerably larger velocities, up to 150 km/sec (Zuckerman, Kuiper and Kuiper (1976)). Clearly motions at this speed were impossible by any gravitationally bound motion (rotation or collapse; the enclosed mass required to restrain matter moving at 100 km/sec at say one parsec is around $10^6 M_{\odot}$!). It was therefore suggested that outflow was taking place. Since this discovery many high velocity molecular flows have been found around embedded protostars; 36 are listed by Bally and Lada (1983), and more recently Lada (1985) has increased this to 68 sources.

Estimates of the various physical parameters of the molecular

flows can be made by observing a range of the transitions of a molecular species. These measurements are specifically used to determine the optical depth, temperature, and abundance (at least in theory), so that the masses of the outflows can be estimated. More often values are derived assuming that the optical depth is small and that the abundance and excitation temperature are the same as those of the ambient gas. This usually leads to an underestimate of the mass (see Lada (1985) for a more thorough analysis of all these considerations). To correct for the optical depth it is usual to observe CO and its isotopic molecule ^{13}CO . By measuring the line strengths of these two molecules it is possible to evaluate the relative isotopic abundances as they appear. Assuming that the ratio of ^{12}CO to ^{13}CO is the same as that observed in the solar neighbourhood (about 90), this gives an estimator of the optical depth (assuming the ^{13}CO line is optically thin). Studies of this ratio have shown that CO is optically thick in most sources (1 to 5 nepers). Snell (1987) also notes that the optical depth can be strongly dependent on the radial velocity of the high velocity emission. The optical depth is seen to decrease at higher velocities, which, it is suggested, implies that most of the mass of gas is to be found at low velocity.

The excitation temperature can be derived from observations of two or more transitions of CO, which determines the ratio of the populations in the energy levels. Observations suggest that the temperature of the high velocity gas is comparable to the ambient gas and is in the range 10 to 90 K (Lada (1985), Snell *et al.* (1984)). This implies that the gas in these flows is cold. The abundance of CO, relative to the other components in the gas, is poorly known, and so the ratio has

to be assumed to be that of the ambient gas, but it is thought that these approximations do not account for an uncertainty of greater than a factor of two (Lada (1985)). The filling factors for these measurements have been estimated to be in the range 0.1 to around unity, the lower filling factor being associated with the highest velocity material, indicating that perhaps the high velocity material is less clumpy than the lower velocity material. It certainly suggests that the clumps of material are distributed with velocity, there being many more clumps at lower velocities (Snell *et al.* (1984)).

Using corrections for all these factors it is then possible to derive estimates of the mass of gas in any outflow (and hence the momentum and energy). The range of mass estimates is found to be from 0.01 to $100M_{\odot}$ (Snell (1987)), a histogram of the (46) masses derived so far are shown in fig 3.1. The median mass of the distribution is around $3M_{\odot}$ (note that the masses are usually lower limits, because corrections are typically not made). The main result from this analysis is that the material seen in the flow cannot derive from a stellar wind of the size of mass loss seen, and therefore must be accelerated by some interaction mechanism between the wind and ambient material, or indeed by some other mechanism.

To determine the density of the high velocity gas it is customary to observe other molecular species, whose excitation thresholds require higher densities. However, the weakness of signals from these molecules requires prohibitively long integration times. A survey (Thronson and Lada (1984)) for CS (J=2-1) emission detected only 3 out of 9 sources,

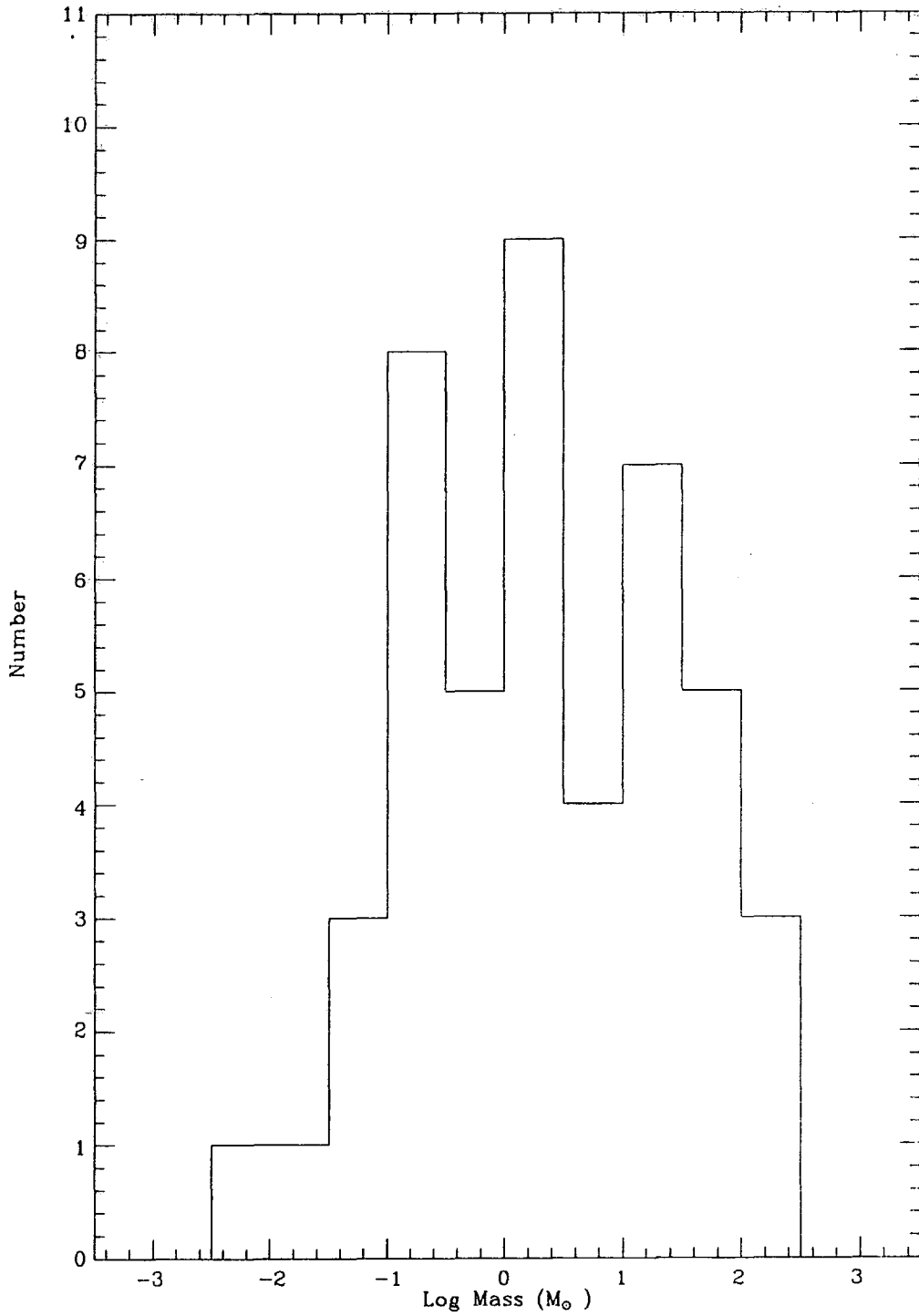


Figure 3.1: Plot showing a histogram of the range of masses in 46 molecular outflows. Data from Snell (1987).

CS (J=2-1) requires densities of around 10^4 hydrogen molecules per cm^3 . Other searches of specific objects have detected another 3 sources (Bally (1982), Kawabe *et al.* (1984), Kaifu *et al.* (1984)). The CS emission is much smaller in extent than the CO observations and much weaker, indicating that the high density component has a much smaller filling factor and hence must represent only a small portion of the outflow material.

3.2.1 Morphology of the outflows.

The morphology of the high velocity flows has a predisposition to be bipolar, that is a tendency for there to be two apparent components equally displaced from the source, one component showing only red shifted gas, and one component showing only blue shifted gas. Often the lobes appear to be collimated, that is they seem to be elongated in opposite directions. The directions of the flow in such cases is well correlated with the proper motions of H_2O masers (eg. Genzè *et al.* (1981)), and HH objects (eg. Cudworth and Herbig (1979)), providing direct evidence in some objects for the outflow picture of how the material is moving. In general Lada (1985) has noted that there are three basic morphological types:-

1. isotropic outflows,
2. monopolar outflows, and
3. bipolar outflows,

he also notes that out of 41 mapped sources 75 per cent are bipolar, 15 per cent are monopolar (ie. show only one lobe of red or blue shifted gas), and 10 per cent are isotropic (ie. the red and blue shifted lobes appear mostly symmetric about the source). Examples of these basic types are shown in fig 3.2.

Although most flows are bipolar, the degree of collimation they show varies considerably from source to source. Some sources are highly collimated (ie. L1551 and NGC2071) while others are poorly collimated (ie. AFGL490), but on the whole most sources appear to be poorly collimated (Bally and Lada (1983)). It might be supposed that such an apparently poorly collimated set of objects may be due to the projection effects found in a randomly-orientated sample of reasonably well collimated sources, or even due to some poor resolution effects, which would tend to smear out the images of the objects. Lada (1985) uses the ratio $R_{coll} = R_{max}/R_{min}$, where R_{max} is the major, and R_{min} the minor axes of the flow, as an estimator of the collimation factor. Fig 3.3 shows Lada's frequency distribution of the collimation factors in 26 sources. If it is assumed that the distribution represents a randomly orientated set of objects, Lada shows that there are far more poorly collimated objects than would be predicted from this analysis. Thus it appears that the poor collimation factors probably represent an intrinsic property of the flows, even if the resolution of the measurements is improved (Snell (1987)).

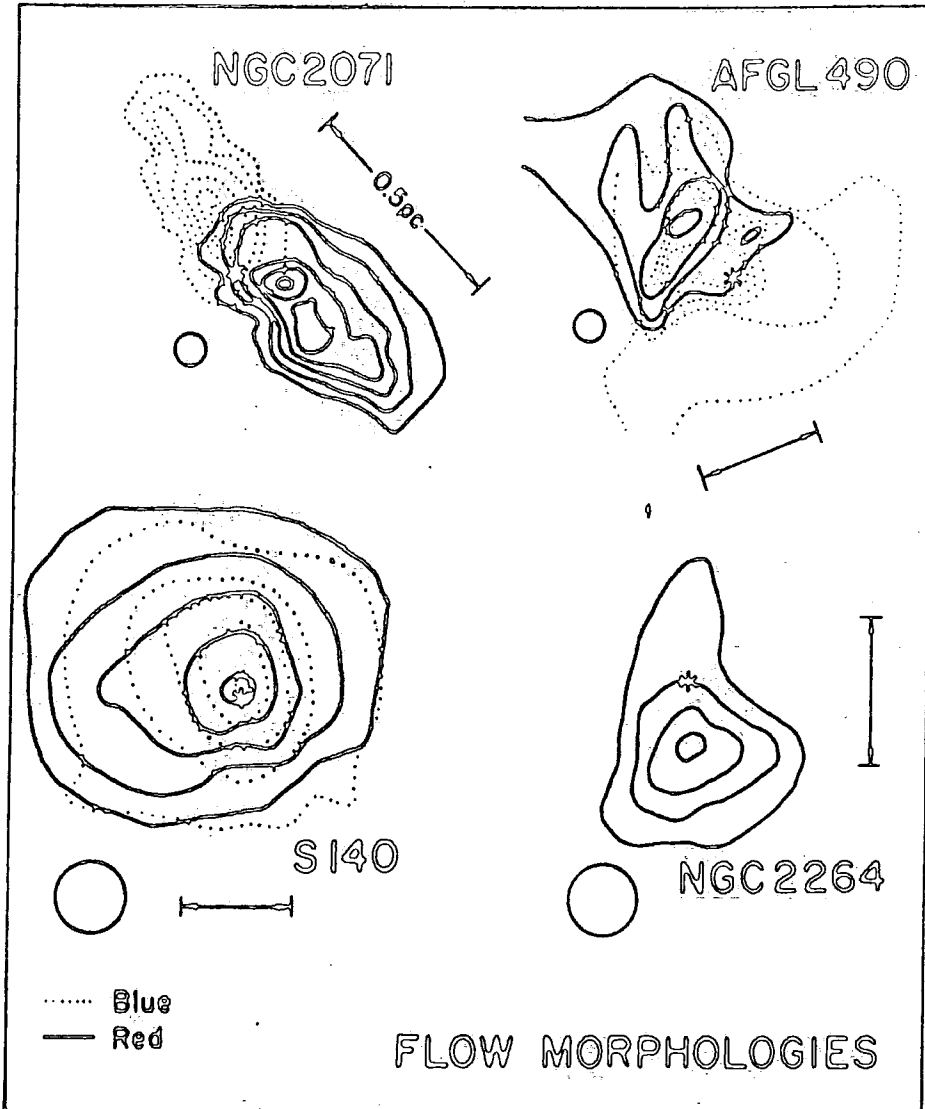


Figure 3.2: Maps of ^{12}CO emission from four molecular flows with differing spatial morphology. NGC 2071 is an example of a well collimated bipolar flow. AFGL 490 is an example of a poorly collimated bipolar flow. S140 is an example of an isotropic bipolar flow and NGC 2264 is an example of a monopolar source. Figure taken from Lada (1985).

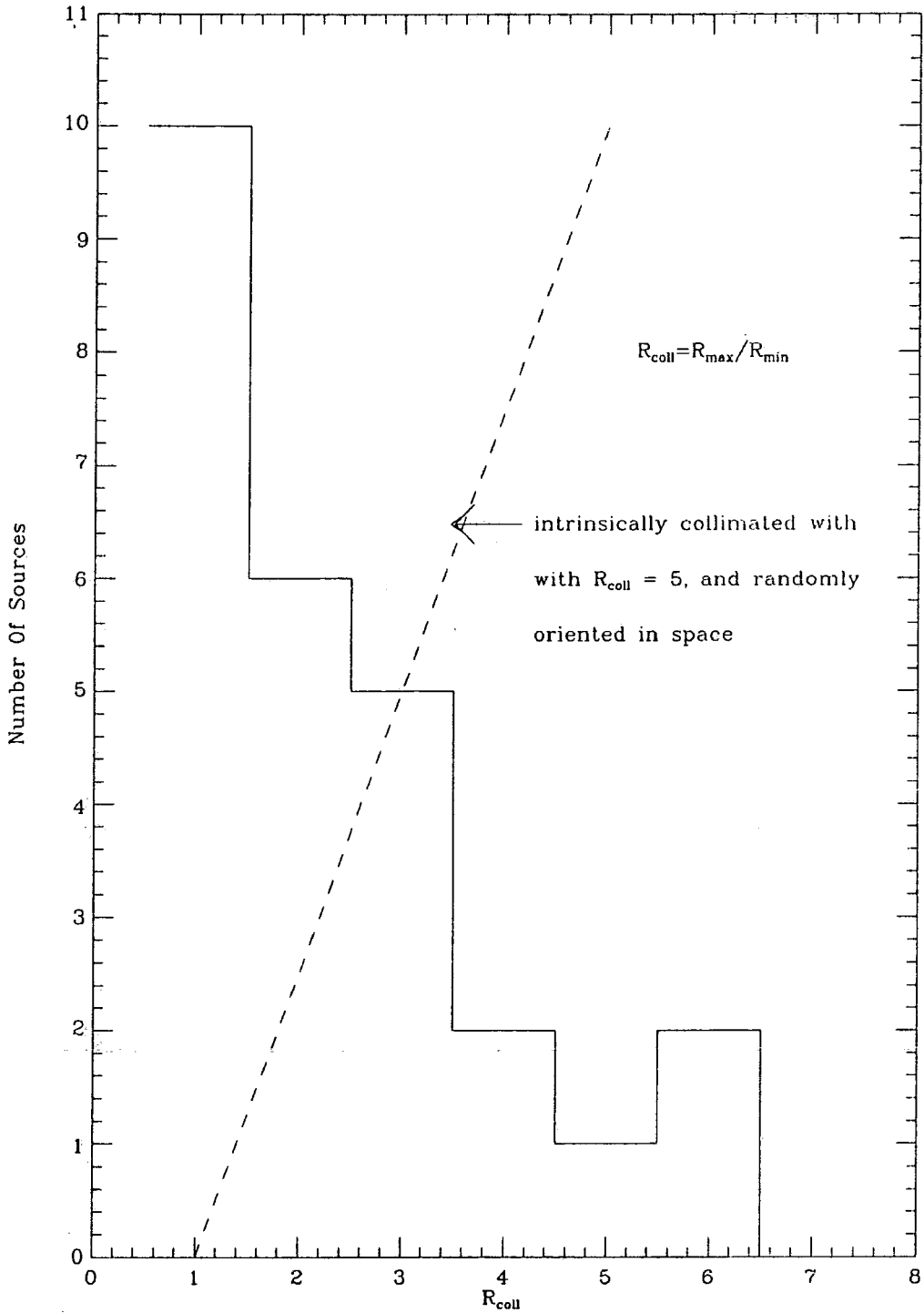


Figure 3.3: Frequency distribution of collimation factors for hypersonic molecular flows. This distribution suggests that there is a wide range in intrinsic collimations of the observed flows. Data from Lada (1985).

3.2.2 The energetics of molecular outflows.

The momentum and energy content of the molecular outflows can be derived from the observed velocities and estimated masses, but these are usually lower limits because the optical depth corrections are usually not known or not applied and also because the orientation and geometry are not well known, and thus cannot be corrected for accurately.

The rate of supply of momentum and energy can be determined if the dynamical timescale of the flows is known. Simply, the dynamical timescale can be determined by the ratio of the size of the flow (which is strongly dependent on the geometry) and the velocity of the outflow. The range of the timescales derived by this method is found to be approximately 10^3 to 10^5 years, with a strong median value in the range 10^4 . Hence using the derived timescale, the measured momentum and energy, the momentum and energy fluxes of the outflow may be found. Usually it is assumed that the momentum and energy fluxes are related by conservation to the properties of the stellar wind, which, it is assumed is sweeping up the cold molecular gas.

Bally and Lada (1983) first carried out a comparison of the mechanical luminosity (ie. the energy supply rate) with the total radiant luminosity of the source, and the photon momentum flux (of the source) with the momentum flux in the flow. Lada (1985) has extended this analysis to his larger group of high velocity flows. Plotting (fig 3.4) the mechanical luminosity against the total radiant energy of the source

(usually derived from far infra-red luminosities), there appears to be a general correlation between the two quantities. All the measurements in this plot lie below the line drawn which indicates equality between the two quantities (ie. when all the energy of the source is converted into energy in the flow), showing that over the dynamical timescales of the flows, the central sources have radiated considerably more luminous energy than is now seen in the kinetic energy of the flow, ie. the energy in the radiation fields is sufficient to drive the flows, if they have maintained reasonably stable outputs over the estimated lifetimes. However, high values of the ratio of mechanical to radiant luminosity (about 0.002-0.02) imply an extremely efficient conversion mechanism assuming of course that the source of energy is indeed the radiation field of the central object.

Plotting (fig 3.5) the photon momentum flux against the flow momentum flux, it is seen that the momentum supplied by the source photon flux is much too small, unless the radiation is scattered something like 100-1000 times before escaping. So it seems that the radiation pressure supplied by the central source cannot drive the observed flows. The points plotted in figures (3.4 and 3.5) show significant correlation with the ideal lines which suggests that the energetics of an outflow are determined by some mechanism related to either the mass or luminosity of the central source, as might be expected if the stars are the driving sources, or that the actual driving mechanism is the consequence of some phenomenon which is directly correlated to these parameters.

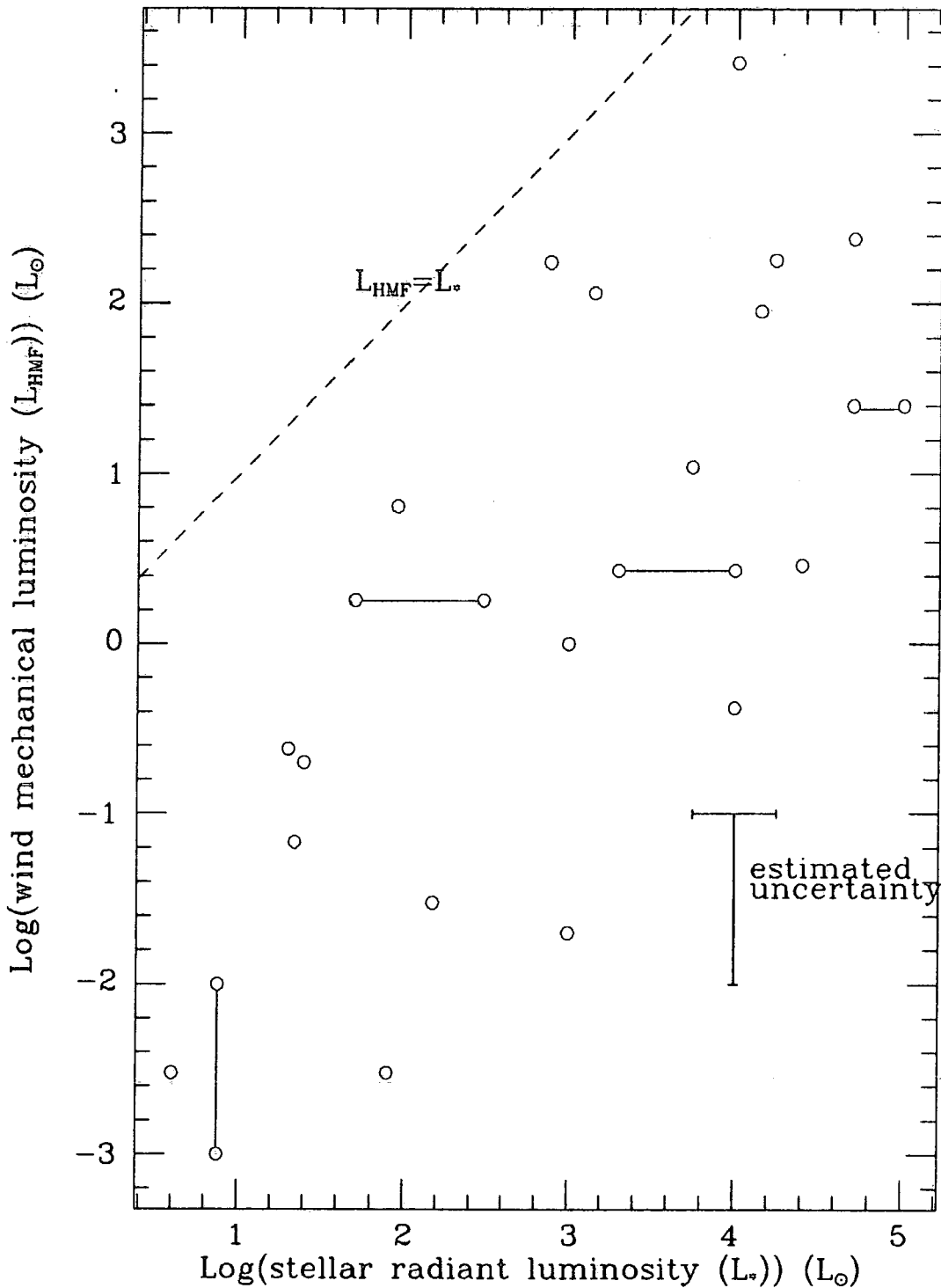


Figure 3.4: The mechanical luminosity of high-velocity molecular outflows plotted against the total radiant luminosity of the embedded central objects. The two quantities appear to be correlated although the scatter is large. All sources fall below the relation $L_{HMF} = L_*$. The estimated uncertainties in the determination of L_{HMF} and L_* for a typical source are indicated. Data taken from Lada (1985).

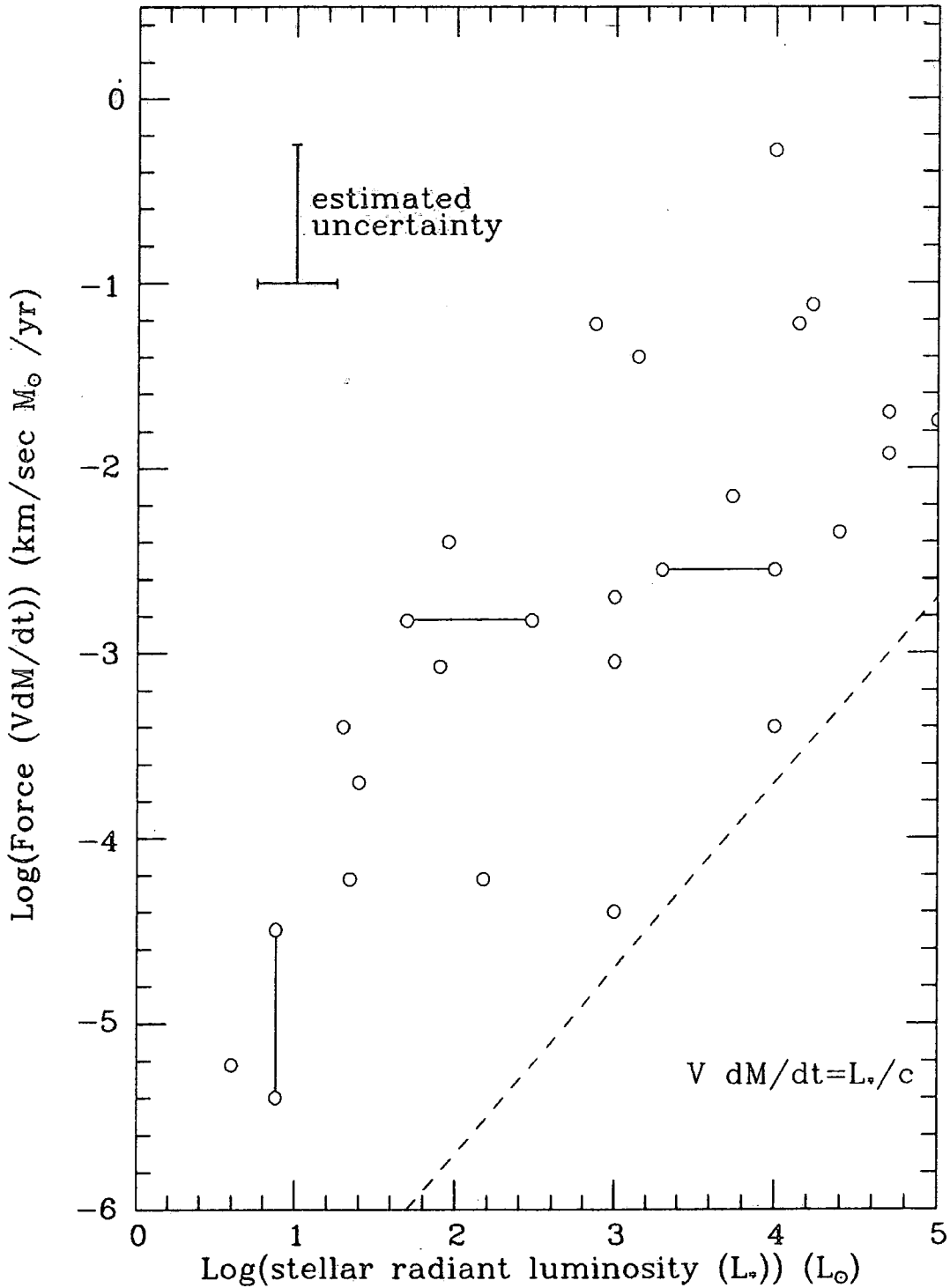


Figure 3.5: The force needed to accelerate the molecular outflows plotted against the total radiant luminosity of the embedded central objects. The two quantities appear weakly correlated. All sources fall above the relation $VdM/dt = L_{*}/c$, which suggests that radiation pressure from the central objects is not sufficient to drive the flows. Estimated uncertainties in the derived parameters are indicated. Data taken from Lada (1985).

3.2.3 Frequency of occurrence.

Lada (1985) and Snell (1987) have attempted to make estimates of the rate of occurrence of molecular outflows, within a kiloparsec of the solar system. Using a mean dynamical timescale of 2×10^4 years, Snell (1987) and Lada (1985) estimate that the formation rate of flows ($8 \times 10^{-4}/yr/kpc^2$ and $1.1 \times 10^{-3}/yr/kpc^2$ respectively) is equal to the rate of formation of stars of a solar mass or more within this volume. Apparently molecular flows are quite common, perhaps very common. These statistics imply that unless this phenomenon is recurrent on timescales greater than the dynamic timescale, the outflow phenomenon represents a fundamentally important stage of early stellar evolution.

Lada (1985) also points out that the outflow phase appears much more common in surveys of embedded, obscured sources (with about an 80 per cent success rate for detections, as opposed to a 10 per cent success rate in T Tauri and Herbig Ae/Be stars), he therefore suggests that the "molecular outflow phase may be the earliest observationally identifiable stage of stellar evolution", associated with the first 10^5 years of stellar life. He also suggests that perhaps the molecular outflow phase represents the end of star formation and the beginning of true stellar evolution.

3.3 Physical Structures Near Protostars: Disks, Toroids and Cavity Edges.

The mechanism responsible for the high degree of collimation observed in molecular outflows is yet to be absolutely identified. The earliest set of models proposed involved the collimation of a stellar wind by a high density gaseous structure, which was either in the form of a disk or a toroid, situated at right angles to the direction of the molecular flow. The size of this structure depends upon the particular model presented, there being the so called circumstellar disks (Snell, Loren and Plambeck (1980), Strom *et al.* (1985) probably best described by the Königl (1982) model), and the somewhat larger interstellar disks (Cantò *et al.* (1981), Torrelles *et al.* (1983)). In addition to these models more recent attempts to explain the collimation of the outflows (and energetics) use an interaction between the disk material, which is assumed to be rotating, and the magnetic field threading through the environ (Pudritz and Norman (1983,1986), Pudritz (1985), Shibata and Uchida (1987)).

The Pudritz and Norman model accounts for the acceleration of the molecular material from the disk itself, by centrifugally driven winds which are initiated by the thermal pressure of the disk envelope. The envelope is heated by Lyman continuum and UV radiation. The Lyman continuum ionises an inner envelope out to a radius of the order a few astronomical units, from which it is assumed that the VLA continuum and optical emission line measurements originate. Radiation is then

postulated to warm the disk out to much larger radii, which is the area of origination of the molecular flow. The flows are coupled to the magnetic field which threads the disk. This field is assumed to be generally open, with the direction of flux being mainly parallel to the rotation axis. It is this coupling which removes angular momentum from the disk, using the long lever arms thus available. This removal of momentum allows accretion onto the protostellar core, thus the luminosity of the flow is correlated to the luminosity of the protostellar object. Also the problem of the momentum source of the flow is resolved, since this is now the momentum of the disk and not the photon flux. The magnetic field collimates the outflow, becoming more toroidal at larger distances due to the inertia of the flow, which pinches and keeps the flow collimated at larger distances. The hot inner region which is ionized by the UV flux also has an associated flow, which is central to the molecular flow and which has a higher resultant velocity. Pudritz and Norman use this phenomenon to account for HH objects, which are then due to a shear between the two components, tearing off clumps of material into the faster flow, in which they are then shocked by the higher velocity flow. This model is probably the most fully described of all attempts to explain the molecular outflow phenomenon (figs 3.6 and 3.7).

Shibata and Uchida (see Shibata and Uchida 1987 and references therein) have proposed what they call the "Sweeping-Magnetic-Twist" mechanism for the formation of astrophysical jets, which are in association with accretion disks. In this model a jet is accelerated by the $\mathbf{J} \times \mathbf{B}$ force in the relaxing magnetic twist created by the winding up of the poloidal magnetic field, during the rotation and collapse of the

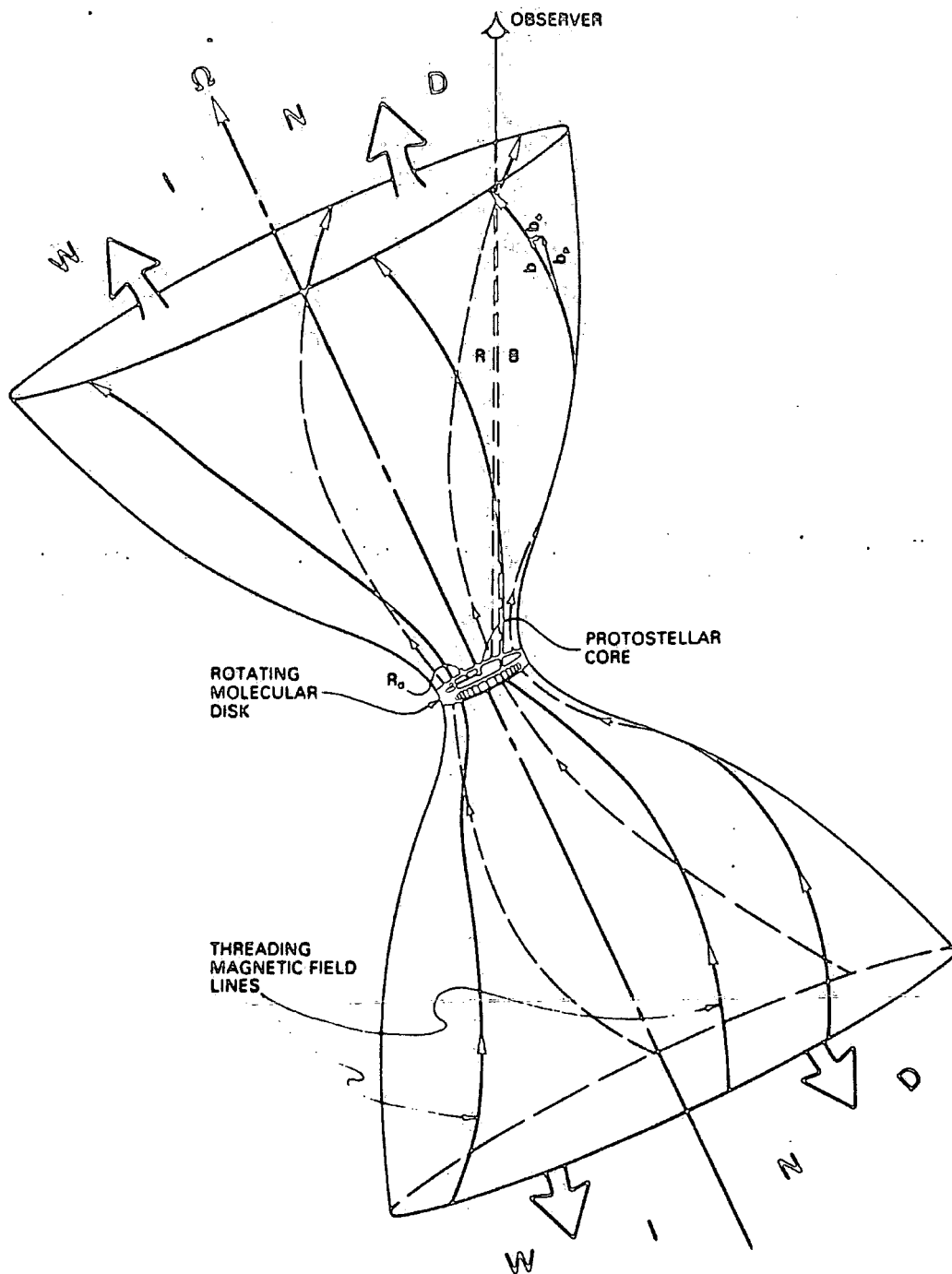


Figure 3.6: Sketch of the Pudritz and Norman molecular bipolar outflow configuration. Figure from Pudritz and Norman (1986).

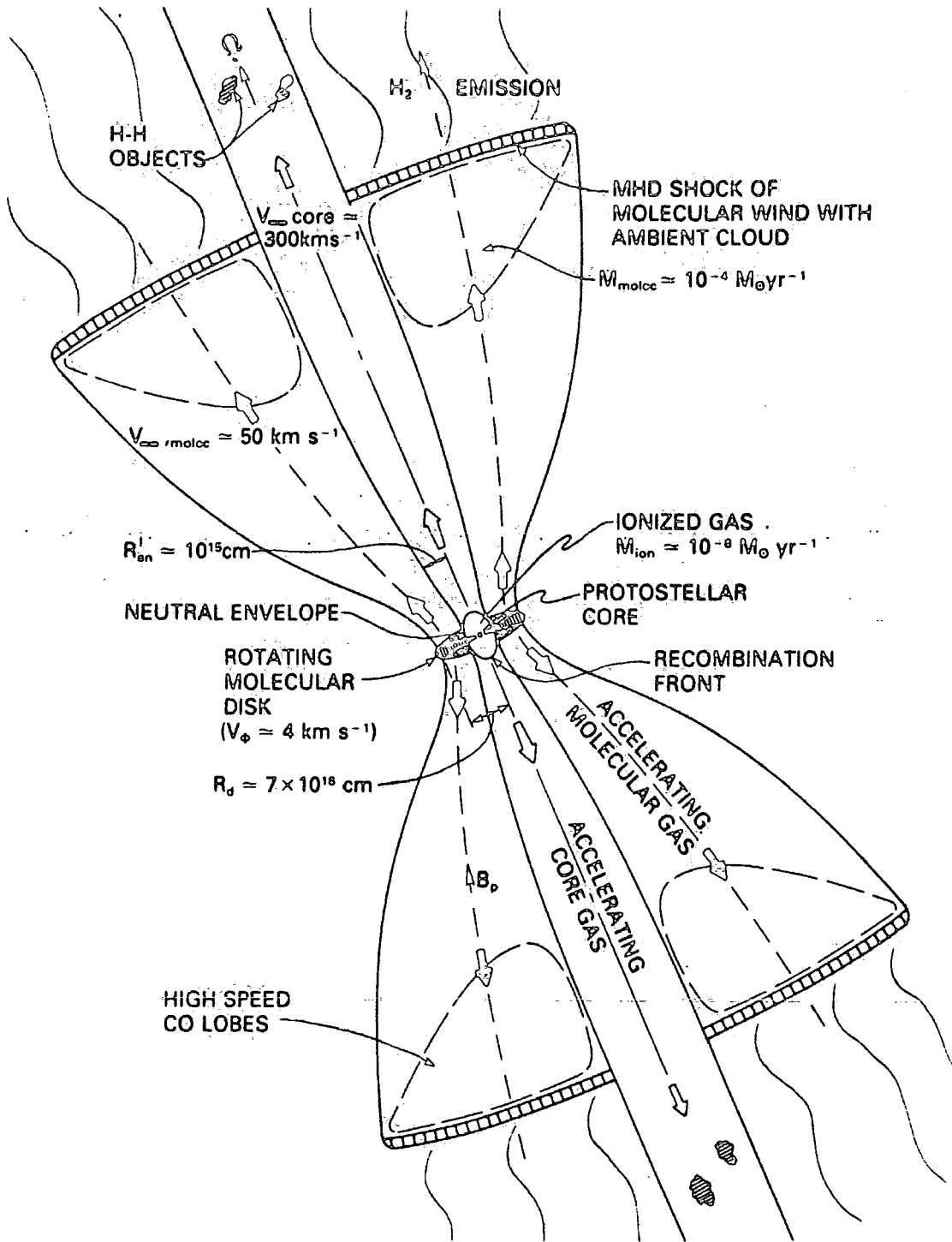


Figure 3.7: The Pudritz and Norman unified model for outflows and disks around protostars. Figure taken from Pudritz and Norman (1986).

disk. The main mechanism is different from the Pudritz and Norman centrifugal models, but incorporates the centrifugal effects naturally. The winding up of an originally poloidal field with direction parallel to the rotation axis of the system, eventually produces a toroidal field configuration in the disk (unlike the Pudritz and Norman model). The torsional Alfvén waves produced by this winding up propagate along the poloidal field. Consequently the disk loses angular momentum and contracts, accreting material onto the protostar leading to the consequences noted in the last model. As the disk contracts the field is wound even more tightly, which eventually forces the gas in the surface layers to be accelerated perpendicularly to the disk by the resultant $\mathbf{J} \times \mathbf{B}$ force producing a helically driven jet with a hollow cylindrical shape.

Other attempts include efforts by Draine (1983), who suggests a mechanism in which just the protostar, which is rotating and threaded by a magnetic field, builds up a magnetic pressure bubble above its poles by winding up the field, driving off the surrounding gas; and by Torbett (1984), whose model incorporates mass loss perpendicular to the surface, defined by the disk, by energy released in the boundary shock layer formed when matter accretes onto the protostar, matter which had previously been in vertical hydrostatic equilibrium. The energy release thermalises the disk material which expands the boundary layer. Thus the surface layers are driven off perpendicularly to the plane of the disk, resulting in a collimated flow.

The first evidence that T Tauri type stars were actually embedded in dusty material was found in infra-red photometry. The pho-

tometry showed that some T Tauri type stars exhibited a very strong infra-red excess i.e. the stars were much more luminous in the infra-red than would be expected on the basis of their approximate spectral types. This effect was first noted by Low and Smith (1966), Mendoza (1966,68) and Johnson (1967). Low and Smith associated this effect with the existence of a shell of circumstellar dust around the observed object (R Mon). Johnson (1967) confirmed the view that the observed excess was due to dust, which was re-radiating light absorbed at visual wavelengths in the infra-red. Mendoza's (1968) photometry of 32 suspected T Tauri stars showed that most had an infra-red excess, however, only a few still had a substantial excess after correcting for the interstellar extinction to the stars. The infra-red excess has since been the study of many papers Cohen (1973), Allen (1973) for example. Recently Lorenzetti, Saraceno and Strafella (1983) have attempted to fit the infra-red excesses of some objects by bremsstrahlung emission from H^{2-} . Although this gave some success in fitting the excesses of the observed Herbig Ae/Be stars, they were still forced to conclude that some objects had excesses due to dusty envelopes.

Perhaps the most convincing evidence in favour of disks or toroids around the pre-main-sequence stars, is the molecular transition observations made in CS and NH_3 , which trace out high density gas ($N_h \geq 10^7/cm^3$), although the (first) observations of a disk/ toroid were in low velocity CO measurements made by Cantò *et al.* (1981) of NGC2261. Higher velocity measurements had shown that a bipolar flow from this source ran perpendicularly to the axis defined by the apparent toroid. As a result of their observations Cantò *et al.* (1981) proposed

that an originally isotropic wind was being focussed into a bipolar outflow (Barral and Cantò (1981)). A similar situation was shown to exist in NGC2071 by Bally (1982), except that he detected a structure orthogonal to the CO outflow in CS, exhibiting a velocity gradient which may indicate a rotation of the disk-like structure. A more extensive search for high density structures in high velocity molecular flows was undertaken by Torrelles *et al.* (1983) using a transition of NH_3 . This search found that out of 9 sources for which a structure was found (structures which could also be said to have a definite direction) 7 were orientated perpendicularly to the outflow direction. These observations led these authors to confirm that the interstellar toroids were responsible for the focussing of the stellar winds into a bipolar outflow as in the models described by Barral and Cantò (1981) and Königl (1982).

Further searches for high density structures have revealed other examples of this phenomenon (see Rodriguez (1987) for a summary of 11 of these, and table 3.1). Kaifu *et al.* (1984) have detected a toroid in CS around the prototypical bipolar outflow object L1551, which is clearly defined as orthogonal to the CO outflow. Kaifu *et al.* (1984) also claim that it is rotating, but this is not confirmed by other more recent observations made by Bartla and Menten (1985), and Walmsey and Menten (1987).

Other evidence in favour of disks/ toroids has been found in optical polarisation studies of bipolar and cometary nebulae, in which it has been noted that "bands" of apparently anomalous polarisation are seen across the heads of the cometary nebulae or centres of the bipo-

Table 3.1:

Interstellar disks/toroids aligned approximately perpendicular to bipolar outflows.		
Source	Radius of Disk	References
R Mon	0.2	Cantò <i>et al.</i> (1981)
NGC2071	0.1	Bally (1982)
HH26 IR	0.2	Torrelles <i>et al.</i> (1983)
Mon R2	0.5	Torrelles <i>et al.</i> (1983)
S106	0.05	Bieging (1984)
Orion KL	0.02	Plambeck <i>et al.</i> (1982)
L1551	0.01	Kaifu <i>et al.</i> (1984)
B335	0.05	Menten <i>et al.</i> (1984)
HH1-2	0.3	Torrelles <i>et al.</i> (1985)
G35.2-0.74	0.2	Little <i>et al.</i> (1985)
GL490	0.2	Kawabe <i>et al.</i> (1984)

lar nebulae (ie. L1551: Draper, Warren-Smith and Scarrott (1985(c)). Parsamyan 21: Draper, Warren-Smith and Scarrott (1985(a)). NGC-2261: Warren-Smith, Draper and Scarrott (1987(a)), Gething, Warren-Smith and Scarrott (1982), Aspin, McLean and Coyne (1985). R and T Cra: Ward-Thompson *et al.* (1985). RNO 138: Draper, Warren-Smith and Scarrott (1985(b)). LKH α 233: Aspin, McLean and McCaughrean (1985). Haro 6-5: Gledhill, Warren-Smith and Scarrott (1986) and many other examples). The bands of polarisation are found in the areas in which one would expect to find the disks/ toroids of these systems (although not all these systems have been identified with high velocity molecular outflows). The consensus of opinion of these authors is that the anomalous polarisations are the result of preferential absorption of the emitted/ scattered light from the sources due to a system of elongated grains aligned by some method with respect to the magnetic field (see Greenberg (1978) and/ or Cugnon (1985) and references therein), which has then to assume the form of a toroid around the source. This is presented as evidence in favour of high density structures around the pre-main-sequence stars, in which the magnetic field has been "frozen in", to some extent, during the process of the collapse of the initiating cloud to the present form. This is the magnetic field configuration proposed by Shibata and Uchida in their "Sweeping-Magnetic-Twist" model (see above). The bands of polarisation are found to be always orientated approximately perpendicular to outflows.

Further evidence from polarisation measurements in favour of disks has been revealed in infra-red polarisations studies of the central stars of bipolar outflows. Sato *et al.* (1985) and Hodapp (1984) have

shown that in these sources, there is a strong tendency for the infra-red polarisation position angles to run perpendicularly to the outflow direction, and also perpendicularly to the local interstellar magnetic field (as determined by the apparent interstellar polarisation of stars seen in the periphery of the cloud, see for example Vrba, Strom and Strom (1976)). Sato *et al.* and Hodapp interpret the large polarisations observed as the result of a scattering geometry, first described by Elsässer and Staude (1978), in which the direct unpolarised light of the central source is heavily obscured towards the observer by an equatorial dust torus seen nearly edge-on, while the light observed is scattered from one or two polar lobes, resulting in the observed polarisation. This analysis is at variance with the interpretation of the authors of the spatially resolved optical polarisation measurements mentioned above, but also favours a disk/ torus interpretation of the polarisation measurements.

Direct evidence of disks/ toroids has also been found in near infra-red studies by two methods. Strom *et al.* (1985) have reported the existence of a disk of diameter approximately 500 astronomical units, seen by scattered light surrounding L1551 IRS5. The method used by Strom *et al.* (1985) involved a maximum entropy reconstruction of a heavily oversampled 2 micron image. They postulate a "two cusp" shape for the disk, which they claim is not consistent with the Elsässer and Staude model of polarisation. Beckwith *et al.* (1984) using a speckle interferometric method in the infra-red, show that a disk-like structure surrounds R Mon (NGC2261) and HL Tau (of size 1300x1300 and 320x200 astronomical units respectively). Also in far infra-red studies, Cohen, Harvey and Schwartz (1985) have resolved somewhat larger

disks of size 10^4 astronomical units around SVS 13 and HH57. In all these cases the disk is orientated orthogonally to the outflow direction.

3.3.1 Inner dimensions of the disks.

Rodriguez (1987) has pointed out that two independent measurements exist for setting a potential limit on the interior size of the disks surrounding pre-main-sequence stars. Rodriguez *et al.* (1986) observed L1551 IRS5, using the VLA, and have observed two peaks in the radio continuum, which they now interpret as the inner edges of a confining toroid which has a scale size of around 25 astronomical units. The main sequence star β Pictorus (Smith and Terrile (1985)), has recently been found to have a thin dusty disk around it (as have other main sequence stars with infra-red excesses, discovered by IRAS), which is relatively thick only to within 30 astronomical units of the central star, inside of which it becomes relatively clear. It thus seems as if it may be tentatively possible to associate these relatively clear inner regions with the planetary forming regions of these stars.

3.3.2 Identification of physical structures within the outflows.

Recently more highly resolved molecular line observations have been made of L1551 (Uchida *et al.* (1987), Rainey *et al.* (1987)). These measurements show a clear hollow cylindrical structure, in which the material is concentrated in the cavity edges. The material appears to

be rotating in the same direction as the disk as reported by Kaifu *et al.* (1984). Thus it seems that the molecular gas is expanding in a shell-like structure (fig 3.8, 3.9). The data also shows that higher velocity gas is not present near to the source, suggesting that acceleration is still occurring out to some considerable distance.

Uchida *et al.* (1987) point out that if the material is accelerated from the surface of the disk out to some considerable distance, and is mostly confined to the cavity edges, these are exactly those properties predicted by the "Sweeping-Magnetic-Twist" models of Shibata and Uchida (1987). Rainey *et al.* (1987) confirm this opinion, and also note that these effects are not explicitly predicted by the (competing) Pudritz and Norman (1983,1986) model.

A unified picture of the disk and flow system implied by these results and others is described by Kaifu (1987), he summarises the main observational features as:-

1. the observed disks commonly show a double peaked structure with a thin central part, suggesting the existence of cavities in the polar sides of the disk.
2. The inner regions of the molecular flows with low flow velocities ($\Delta V_r=1-2$ Km/sec) fit very well with the edges of the disks. In the case of L1551 they show very smooth shapes instead of the nozzle-like feature which is expected for the collimated stellar wind hypothesis.

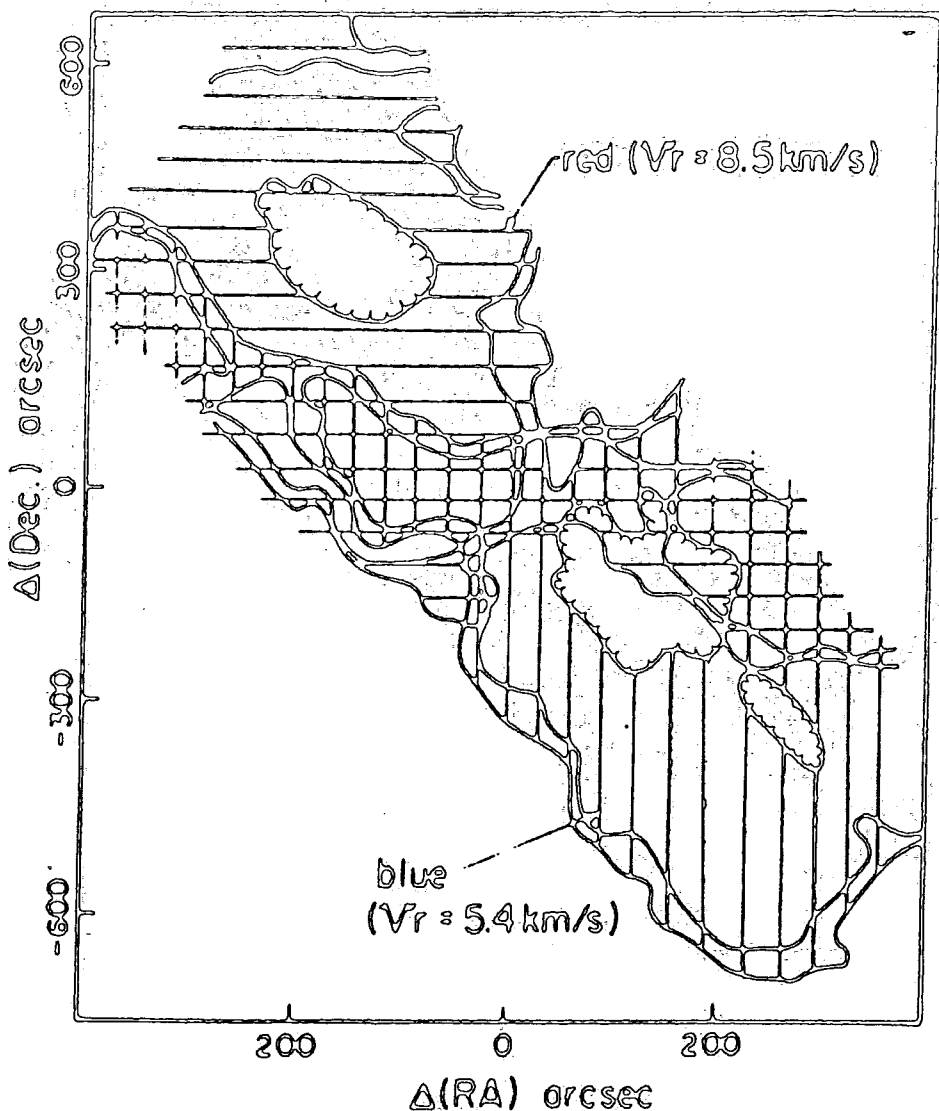


Figure 3.8: Overlay of two sketches of the blue (vertical lines $\Delta V_r = 1.5 \pm 0.5$ km/s) and red shifted (horizontal lines $\Delta V_r = -1.5 \pm 0.5$ km/s) components about the source L1551 IRS5. The cross hatched areas correspond to regions showing emission at both these velocities. Note the skew structure between the two components. Uchida *et al.* (1987) explain these maps in terms of a general rotation of both lobes of the flow in the same direction as the rotating disk of Kaifu *et al.* (1984). Figure taken from Uchida *et al.* (1987).

3. The inner regions of blue shifted flows also fit well the optical reflection nebulae, thus the light is scattered from the cavity walls, corresponding to the inner regions of the molecular flows, and can be seen through the cavities.
4. The molecular flows are likely to be accelerated along the walls of the cavities, at least in the vicinity of the disks.

The inferred model of the main observational features of a molecular flow is shown in fig 3.9.

3.4 Optical Jets from Pre-Main-Sequence Stars.

Optical observations of young stars have revealed the presence of elongated emission features which apparently emanate from the stars themselves (Mundt and Fried (1983), Mundt *et al.* (1984)). The observational properties of these so called "jets" are basically spectra similar to HH objects, high velocities (a few 100 km/sec), densities around $10 - 100 N_h/cm^3$, and mass fluxes of 10^{-10} to $10^{-7} M_o/yr$. They have accordingly been interpreted as highly collimated streams of supersonic material, presumably collimated by disks/ mechanisms of circumstellar dimensions (~ 100 astronomical units or less).

One of the most striking of the optically visible jets is the flow associated with the HH46/7 in the Gum nebula. The two HH objects appear as knots in a narrowly confined jet of material, which appears

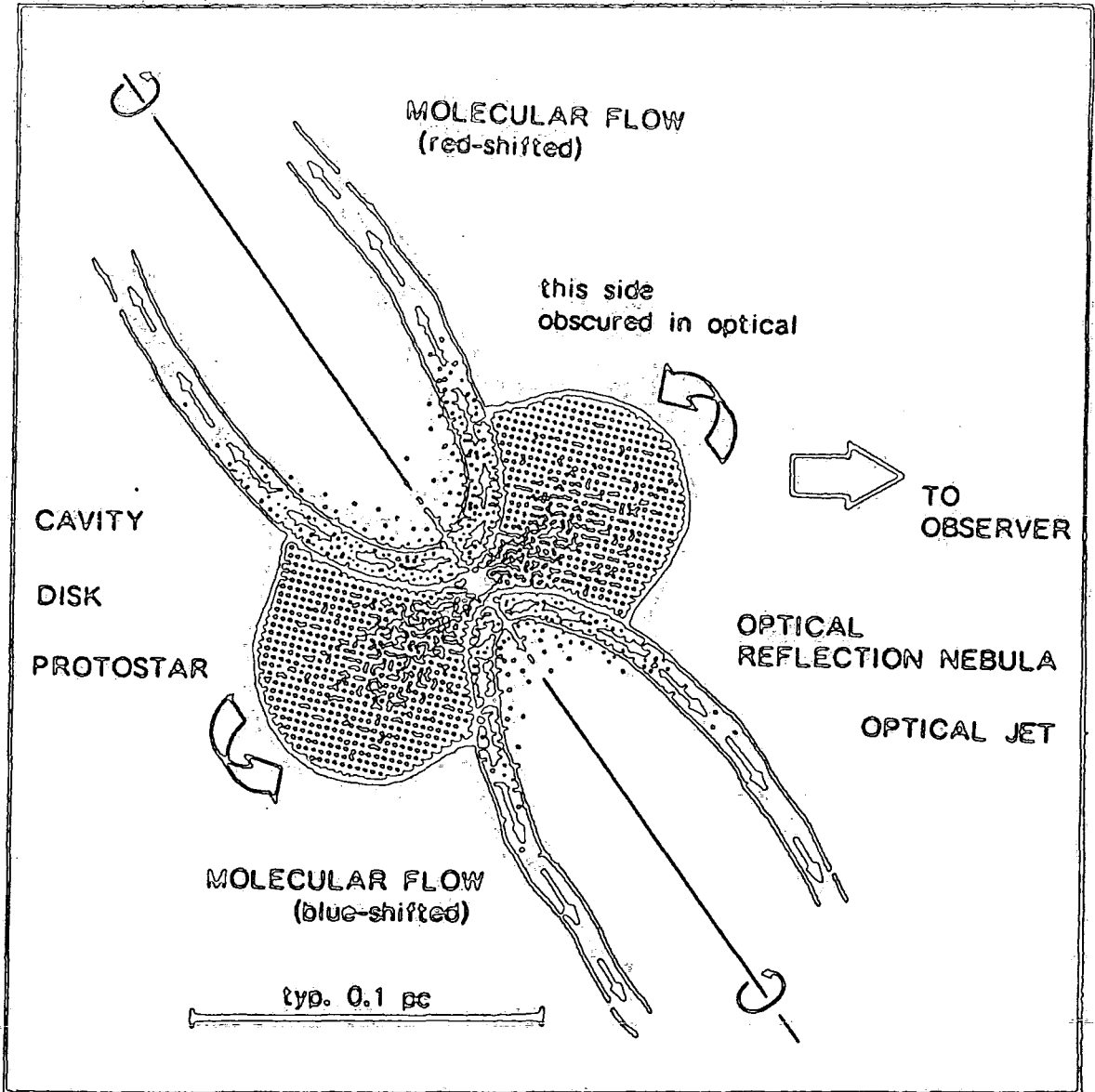


Figure 3.9: A schematic model of the disk and flow system around a protostar. Figure taken from Rodriguez (1987).

to originate from a dark rimmed globule. South-west of this jet feature are two fainter knots (HH 47c), which fall almost exactly on the line through the other HH objects. It appears that an imbedded object has produced these phenomena. Fig 3.10 shows an $H\alpha$ image of this region. A polarimetric study of this object has recently been performed by Scarrott and Warren-Smith (1988) who show that HH46 is part of an optical bipolar illuminated by an obscured star (HH46IRS), identifying the source of the highly collimated outflow.

In contrast it has also been argued by some workers (Cantò, Sarmiento and Rodriguez (1987)), that a few of these features are in fact projection effects, as a result of stellar wind interaction with the surrounding medium, specifically the cavity walls of the outflows, or as a result of the interaction of two winds, which would explain why some jets are bent at the source (ie. HL Tau).

The source for the driving mechanism of the jets is mainly considered as in the molecular case, to be a collimation of a stellar wind by some high density disk-like structure (eg. Wilson, Falle and Innes (1987)). However, electro-dynamical models in which the jets are driven by accretion onto the protostellar core, are now postulated. The magnetic field configuration supplying the mechanism by which the resultant outflow is collimated into the observed jet (Kaburaki and Itoh (1987), Uchida and Shibata (1984)).

The connection between the means of collimating the jets and the larger much more energetic molecular flows is not known, but it seems

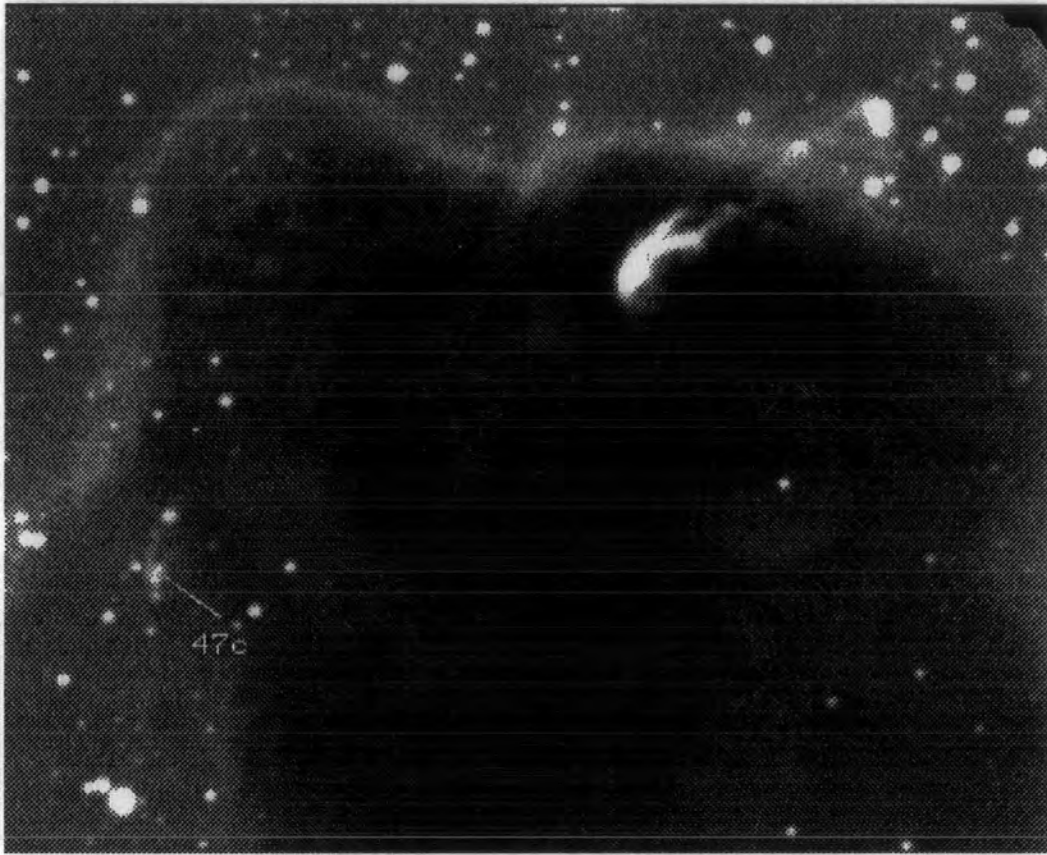


Figure 3.11: An $H\alpha$ greyscale image of the HH46/7 region. Data was taken by the author and co-workers on the SAAO 1.9m telescope in May 1985.

reasonable to suppose that they are related. Certainly these jets, if the current interpretation is correct, provide evidence for the existence of disk-like structures around pre-main-sequence stars.

3.5 Optical Appearance of the Outflows.

The most obvious optical manifestation of outflows is as cometary, bipolar or amorphous nebulae, which may be seen in conjunction with stellar jets and HH objects. The optical manifestations of these objects show a range of properties, summarised by K.M Strom *et al.* (1986), among which are:-

1. optical outflows are often highly collimated, in some instances even more highly collimated than the molecular flows (ie. L1551, fig-3.11);
2. optical outflows are often seen to be bipolar (ie. LkH α 233, LkH α 208, PV Cephei, HH 1 and 2, RNO 138 (fig3.12), the Serpens red reflection nebula, R Mon (fig4.1));
3. in some cases optical jets and HH objects are not accompanied with a detected molecular flow; in some the optical and molecular flows are not aligned (ie. R and T Cra);
4. indications of helical structures are seen in the optical morphology of some objects;

5. the momentum in the ionized component of the optical outflow is about 0.1 times the momentum of the molecular flow;
6. the observed velocities in the optical components are usually ten times the velocities observed in the molecular flow;
7. there is a strong tendency for optical outflows to be aligned with the magnetic field as seen in the outer parts of the cloud (ie. Strom and Strom (1987) show 6 aligned outflows in the L1641 cloud.)

Some questions arise from the consideration of these observations: are the optical and molecular outflows a consequence of the same phenomenon? The mechanical luminosity of the objects is estimated to be a considerable fraction of the bolometric luminosity, this raises the same questions as in the molecular example and again forces the question is the mechanism behind the energetics some other mechanism than the radiant energy of the protostar (ie. accretion driven)? It also needs to be established if the mechanism of collimation is the same as in the molecular flows. Finally, models of outflows need to naturally explain why the outflows align with the external magnetic field.

3.6 Other Consequences of Outflows.

Before making a final summary of the observational characteristics of the outflows, it seems pertinent to comment on some other questions which have been posed with respect to the consequences of the outflows on more general considerations of star formation. This interest

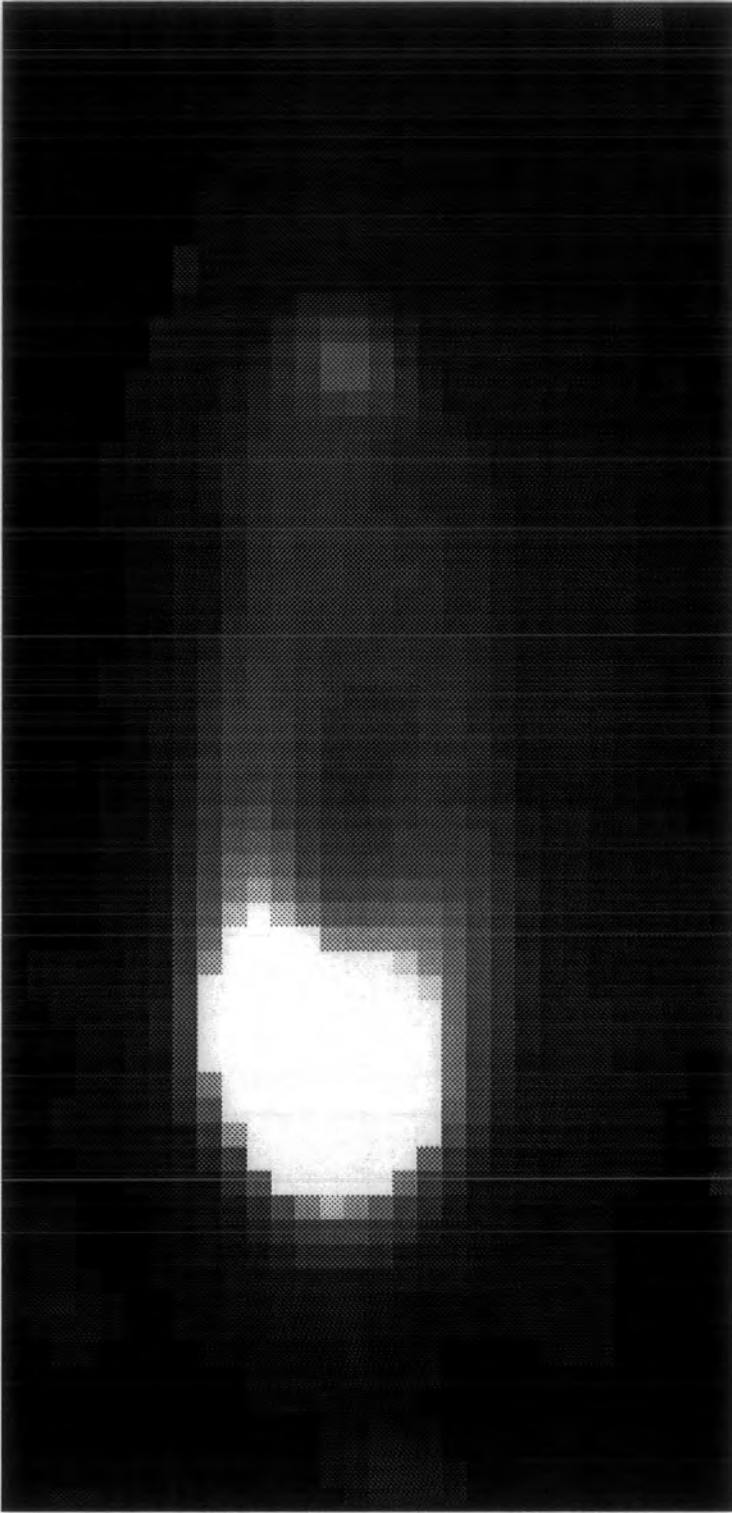


Figure 3.12: Greyscale image of the cometary nebula Parsamyan 21. Notice the bifurcated structure.

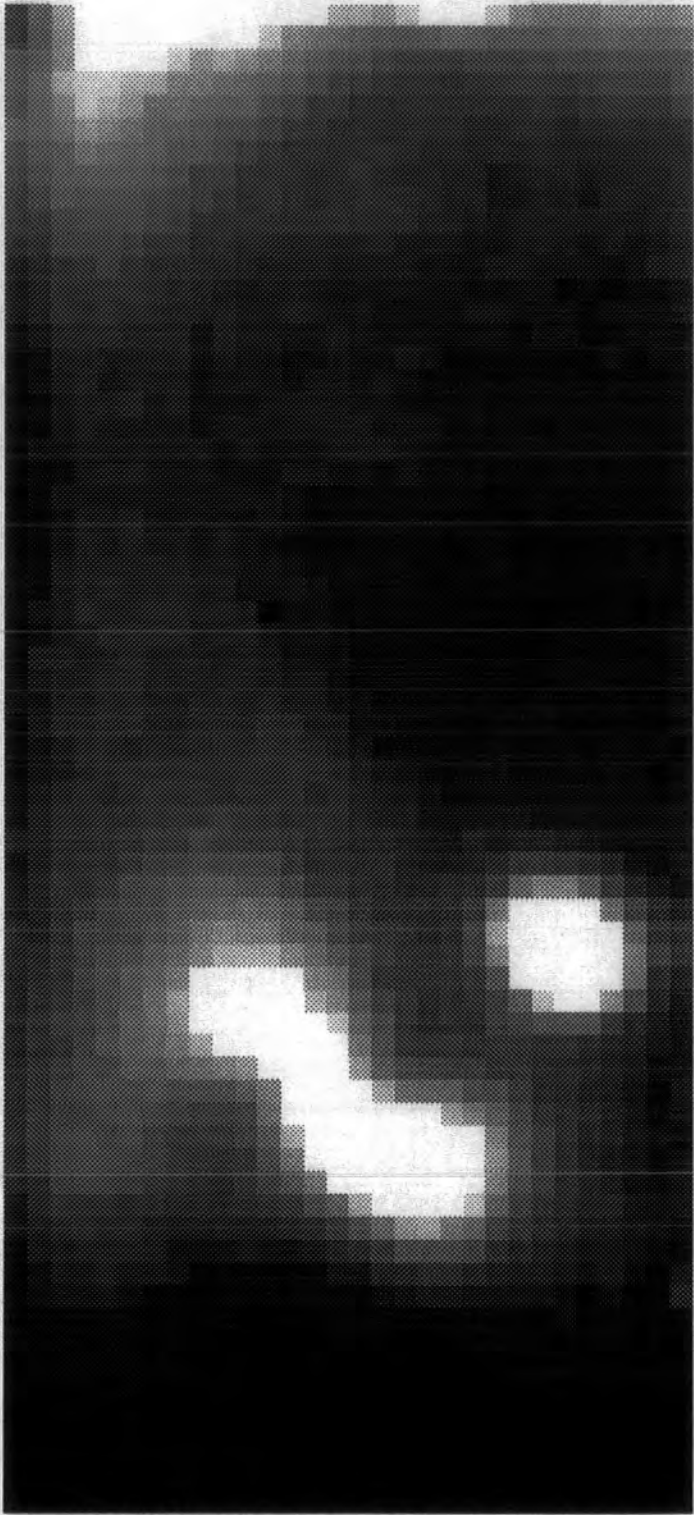


Figure 3.13: Greyscale image of the region of NGC 7129 incorporating the bipolar nebula RNO 138.

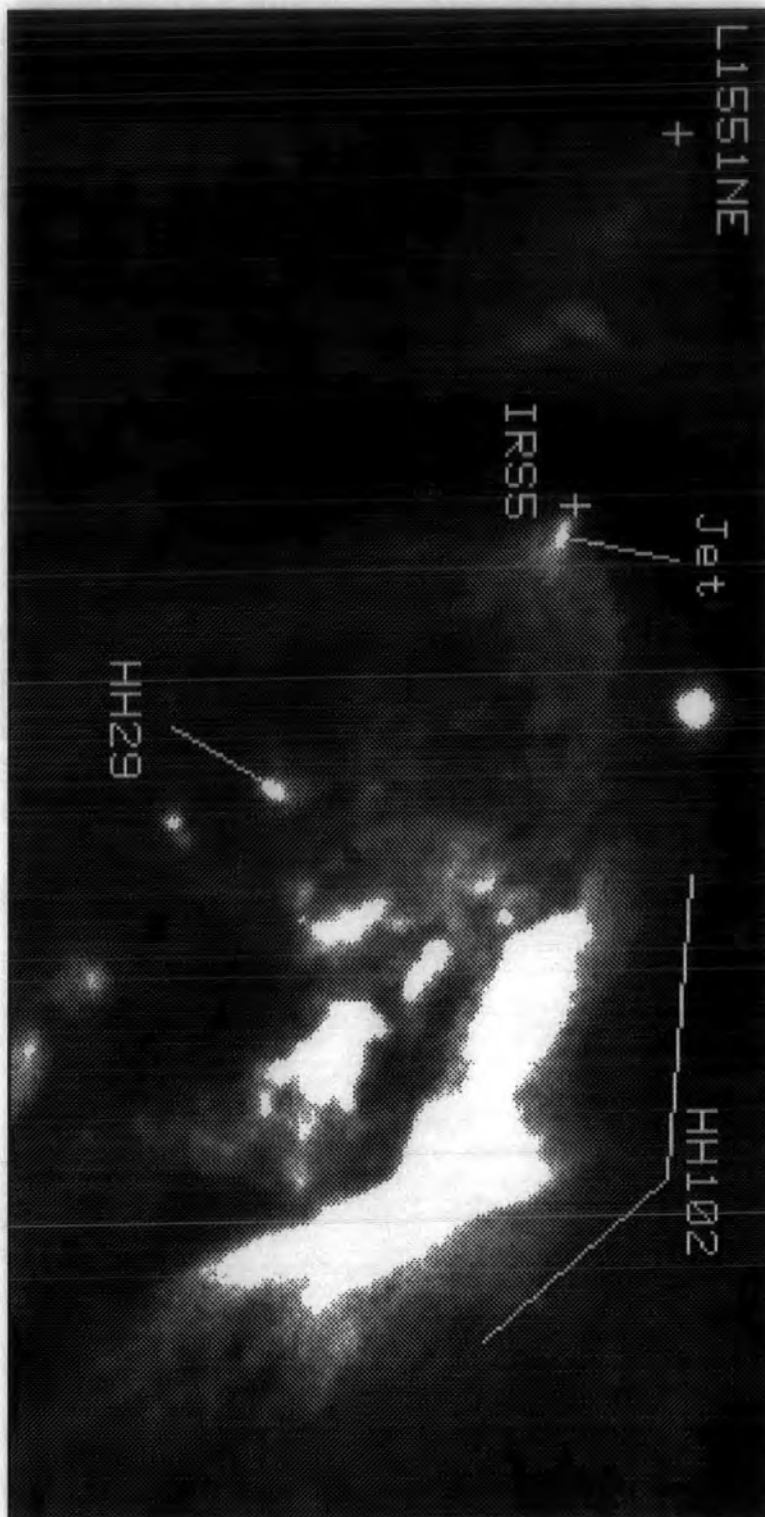


Figure 3.14: Greyscale image of the L1551 region showing the HH102 nebula, HH29 and the L1551NE reflection nebula.



Figure 3.15: An $H\alpha$ greyscale image of the HH object HH100. Data was taken by the author and co-workers on the SAAO 1.9m telescope in May 1985.

mainly arises because the molecular flows are so large and very energetic, and also because their formation rates are so high. It is thought that this could make molecular outflows an important source of energy in molecular clouds, possibly affecting the resultant star formation rate.

Certainly it is true that the inner turbulence of the molecular clouds has been of some interest and consternation to astronomers since it was discovered that the motions within the gas were supersonic, the source of these motions was unknown, but could not be “natural” because supersonic motions should dissipate in not too large a timescale. The shocks resulting from the dissipation of the supersonic motions, should produce a global collapse of the cloud and hence a very high star formation rate. Consequently it has been proposed that molecular outflows could be the source of the energy perpetuation in the support of the molecular clouds against global collapse (Franco and Cox (1983), Norman and Silk (1980)). This is an appealing solution to the problem, because this would also relate the star formation rate at any time to the evolution of the stars already formed, producing a feedback mechanism to limit the star formation efficiency to the low values observed.

However, another possible (concurrent ?) mechanism for producing a similar effect has been put forward by Pudritz and Silk (1987), which incorporates the magnetic field of the cloud, and its interaction with the ionised component of the cloud to account for the angular momentum loss. This analysis consequently predicts the star formation mass spectrum (ie. how many stars of what mass are forming at any time) depends upon the fraction of ionised material within the cloud

and predicts how this this fraction evolves with time as stars are formed which increases the ionisation levels. The theory seems to predict an evolution of the mass of the stars forming from low to intermediary to high mass, simply because more ionisation leads to better coupling with the neutral mass of material (reducing field slip, ambipolar diffusion), which leads to better braking of the material for an increased mass, so that fragmentation need not occur to resolve the angular momentum problem.

3.7 Summation.

In summation the main characteristics of regions closely associated with protostars are the presence of optical nebulae of many types (cometary, bipolar and amorphous) which have associated with them; HH objects of two types; semistellar, and amorphous, which seem to have two different mechanisms for producing their spectra (and continua); intrinsic (excited) emission and reflected light. Also at optical wavelengths the stellar "jets" are seen apparently emanating from the protostellar sources, and also exhibit emission spectra. Their opening angles suggest very strong collimation on circumstellar scales.

Also of great importance are the observations of the various rotational transitions of molecular species which are found in quantity within these regions. The study of these emissions reveals the motions of gas close to protostars and the presence of other structures of vary-

ing densities. The motions of the gas are shown to be very energetic and directed away from the sources, flowing into cavities created in the interstellar medium in these directions. Physically dense structures are observed about the protostars perpendicular to the outflows, which are taken to indicate disks or toroids about the protostars. Detailed studies in the molecular transitions also show that the outflows are *massively* confined to the cavity walls. The energetics of these flows are impossible to explain within any momentum driven scenario which involves the stellar wind flowing from the protostar sweeping up material.

Infra-red and optical polarimetry of the protostars and their associated nebulae support the existence of disks about the protostars, although they differ in the exact mechanism producing the observed polarisation. Speckle infra-red interferometry directly observes the disks on the scale of $10^3 - 10^2$ astronomical units. The evidence for disks seems to be present on all scales (eg. see Strom *et al.* (1985) and Snell *et al.* (1985))

Of considerable interest to studies of these regions are the models recently proposed to account for the energetics of the outflows, the most interesting of which are the hydromagnetic models of the type proposed by Shibata and Uchida (1987, and references therein), Pudritz and Norman (1983,86 and Pudritz (1985)) and Draine (1983). However, which type of model or admixture of models will ultimately provide the correct solution is not determined. Perhaps it may be suggested that the Uchida and Shibata model is marginally favoured at present, on the basis of its prediction of the flow of material up the cavity edges, but



this is not explicitly denied by the Pudritz and Norman model. These models are certainly not accepted as even applicable by all workers (see Shu, Adams and Lizano (1987)).

Chapter 4

Polarisation of NGC2261/R Mon.

4.1 Introduction.

The prototypical cometary reflection nebula NGC2261 (fig 4.1) and the semi-stellar brightness peak at its apex, R Monocerotis (R Mon, RA. 6:33.7, Dec +8:50 (1900)), have been the centre of numerous astronomical investigations. The aim of these investigations has always been to gain insight into the processes in action within the system, in the hope of gaining a proper understanding of what the system represents and how it came to its present configuration. In this chapter multicolour imaging polarimetry of this object will be described and an interpretation of the data will be undertaken, with the intent of further investigating the properties of this object and also hopefully providing resolution of some of the outstanding issues, which have been raised with respect to

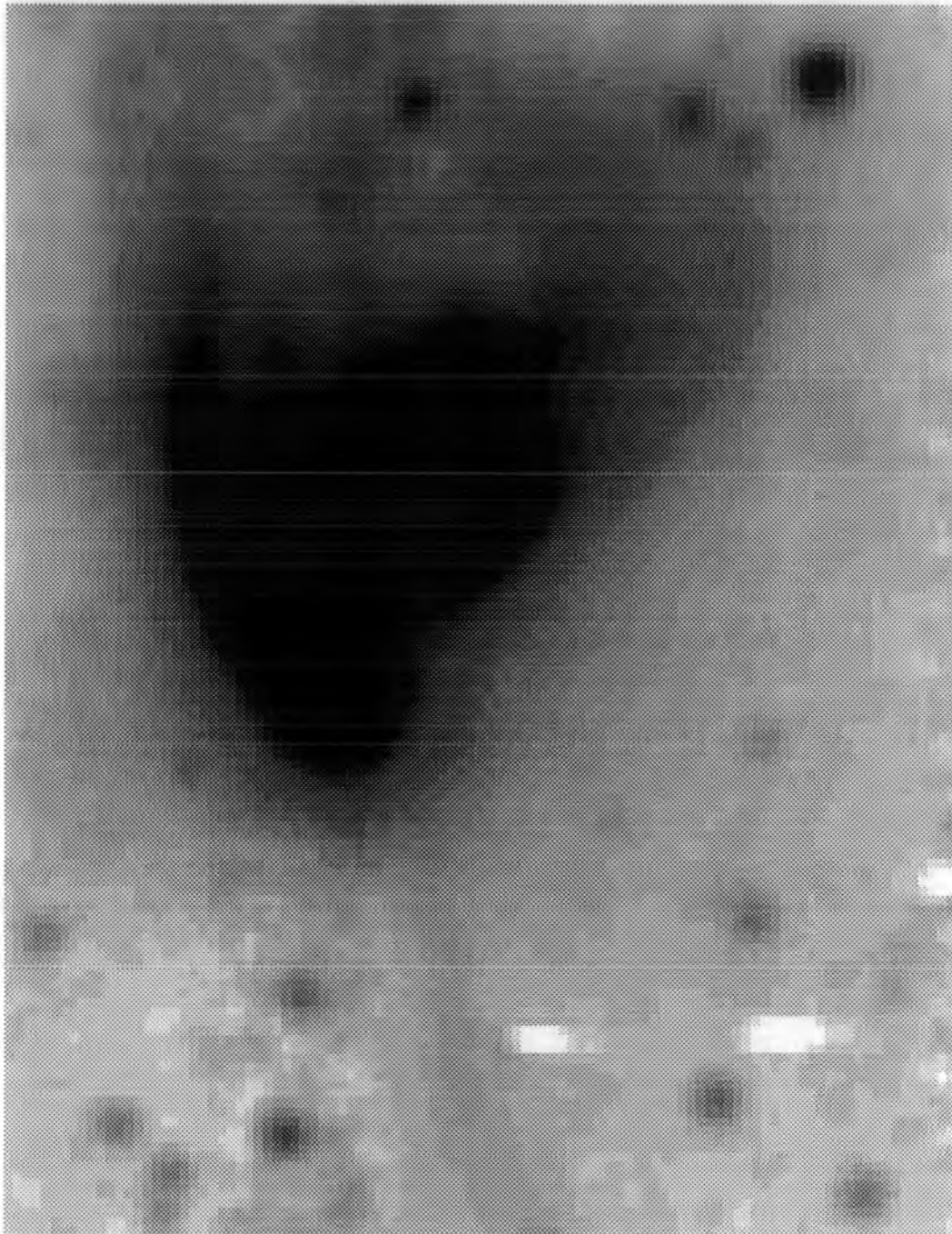


Figure 4.1: A composite greyscale image of NGC2261/R Mon. The intensity range has been modified to show the main features of the nebula.

this and other similar systems.

4.2 Previous Studies.

The amount of work which has been undertaken by various astronomers, of the NGC2261/R Mon system is considerable. In this section a summary of the more pertinent work will be given in order to give an appreciation of the current status of understanding of the NGC2261/R Mon system, and to relate the observations which have relevance to the later discussion.

4.2.1 The variability of NGC2261/R Mon.

In 1916 Hubble published a study of NGC2261, he noted that in several photographic plates, taken by himself and other workers in the period 1900 to 1916, the main body of the nebula was observed to undergo quite striking structural variations. Hubble also noted that the semi-stellar knot R Mon had been observed to show variations from 9th to 13th magnitude. Since this time NGC2261 has been known as Hubble's variable nebula.

The variability within the cometary nebula has been noted on many photographic plates taken of the nebula after 1916 (Johnson (1966), Joy (1945)). The mutability of structure within the nebula and the change in the magnitude of R Mon have been investigated to deter-

mine if any correlation exists between the fluctuations; to date no such relationship has been found (Johnson (1966)). Lampland noted in 1926 that all parts of the nebula undergo some structural change, either dimming or total obliteration, which appear not to be due to changes in the structure or organisation of the nebula, because they reappear in the same places at later times. He thus suggests that the changes are due to variations of illumination of the nebula by the nucleus (R Mon). Johnson (1966) observed that the apparent proper motions of features within the main body of the nebula measured in plates taken by Lampland were around $1/4$ of an arc second per day, and furthermore the motions were always away from R Mon, indicating that the fluctuations were due to apparent light changes in R Mon. If it is assumed that these features were propagating at the speed of light this gives an estimated distance of around 700pc to the nebula, this is in very good agreement with the estimated distance of 690pc (Johnson (1968)) to the NGC2264 region, with which it is assumed that NGC2261 is associated.

4.2.2 Spectroscopy of NGC2261/R Mon.

As expected from observations of a star which is still approaching the main sequence, the spectral type of R Mon remains ambiguous. Joy (1945) classified R Mon within a group of T Tauri stars as being in the range F5–G5 with emission lines resembling those of a solar chromosphere. Herbig (1960) describes the spectra of R Mon as a strong emission spectra consisting of lines of H, CaII, and FeII, when observed near to its minimum in intensity. Sharp, rather weak absorption rever-

sals appear in the early Balmer lines, which become more conspicuous with increasing quantum number. Herbig also points out that the K line of CaII is very strong, and says that the overall impression from the spectra of R Mon is of a low excitation emission spectrum, superimposed with a weaker absorption shell. At maximum light, Herbig reports that the emission spectrum is much weaker, the K emission line has disappeared and the spectrum is now dominated by very strong deep narrow Balmer absorption lines, which are visible far into the ultra-violet. It thus seemed to Herbig (1960) that the spectral variations represent an interplay between the emission spectra and absorption shell features, whose intrinsic strengths were apparently inversely correlated. At this time he did not specify a spectral type, he did, however, provisionally classify it within a group which were B or early A, having weak absorption shells, no strong emission lines, except those of hydrogen, and also exhibiting a conflict in spectral criteria (such as between the HeI and CaII lines) that probably arose from the shell, but he added that R Mon definitely had a stronger emission spectrum than was normal for this group.

In a later paper on the structure and spectrum of NGC2261 Herbig (1968) says that he now considers it doubtful that R Mon had ever been observed without including a significant contamination of light from NGC2261. He then identified R Mon as a triangular nebula about 5 arc seconds across, from which an appreciable fraction of the light (in the infra-red) originated. Herbig went on to point out that there is no convincing evidence of the presence of a G or K type star, and also that in 1946 when R Mon rose to 10th magnitude, it exhibited a spec-

trum which was superficially like that of an A-type supergiant, with a possible suggestion of a shell. This suggestion is backed by Imhoff and Mendoza (1974) who assign a spectral type of an A5 supergiant to R Mon, and also by Greenstein (1948) who observed R Mon in 1947 and also noted the effects observed by Hubble at that time.

Stockton, Chesley and Chesley (1975) have made spectroscopic observations of NGC2261, the main nebula body. They observed unexpected variations in the tangential velocity of the reflected absorption spectrum as a function of distance from R Mon. This, they noted, could not be due to differential motions within the nebula, because the emission lines showed no equivalent variation. Stockton, Chesley and Chesley, consequently attributed the effect to time variations in the absorption shell around R Mon, in conjunction with the differences in light travel times for light scattered into the same beam from different parts of the nebula. They also reported the detection of spectral lines which were in actual fact associated with the HII region surrounding the nearby star S Mon, in the light apparently received from NGC2261. This confirmed the association of NGC2261 with the NGC2264 region and the lower limit imposed upon the distance estimate to NGC2261.

4.2.3 Infra-red photometry of R Mon.

The first infra-red photometry of R Mon revealed a very interesting feature which was later found to be typical of objects of its type. In the infra-red, the fluxes observed to emanate from the nucleus of the

nebula showed a very large excess, ie. the star was much more luminous in the infra-red than would be expected on the basis of its approximate spectral type. This effect was noted by Low and Smith (1966), Mendoza (1966,68) and Johnson (1967). Low and Smith associated this effect with the existence of a shell of circumstellar dust around R Mon, which they proposed might even be a pre-planetary system on the basis that the excess was fitted out to around 20 microns by a dust model consisting solely of 10 micron grains. Johnson confirmed the view that the excess was due to dust which was re-radiating light absorbed at visual wavelengths in the infra-red, and not due, as some first supposed, to an infra-red companion star. Mendoza's more complete analysis in 1968 confirmed that no companion existed on the basis of an infra-red spectrum of the object.

Mendoza (1968) also took 0.36 to 5 micron photometry of 32 other suspected T Tauri stars. He noted that nearly all of these stars displayed some infra-red excess, however, only a few (R Mon included) still had substantial excess after correction for the interstellar extinction to the stars. From his photometry, Mendoza estimated the total luminosity of R Mon to be about $800 L_o$, and from its placement in the H-R diagram (well above the main sequence) he estimated its mass to be $7.3 M_o$ and its age, from Iben's (1965) evolutionary tracks, to be 16,000 years. However, he also noted that if the spectral type is earlier than the one used (he assumed K1 for R Mon, so it is almost certainly true that its type is earlier) then the star is probably older and of greater total luminosity, but of similar mass.

Mendoza (1968) also speculated that R Mon is part of a group of objects whose evolutionary status is earlier than those of objects similar to T Tauri, on the basis of its very large infra-red excess. This categorisation, Mendoza says, suggests that the dust envelopes around T Tauri type stars are more disrupted or form disks. The infra-red excess of R Mon and other objects has since been the study of many papers Cohen (1973), Allen (1973). Recently Lorenzetti, Saraceno and Strafella (1983) have attempted to fit the infra-red of some objects excess by bremsstrahlung emission from H^{2-} . Although this gave some success in fitting the excesses of the observed Herbig Ae/Be stars, R Mon maintained a considerable excess, which the authors were forced to conclude was due to a dusty envelope. In summary it seems that infra-red photometry of R Mon concludes that R Mon is probably a very young object, probably younger than the T Tauri stars, and is still enshrouded by some of the original material of the cloud from which it condensed.

4.2.4 Visual photometry of NGC2261.

In a reflection nebula, the light scattered towards the observer is usually bluer than that of the illuminating star, but shows essentially the same spectrum. Visual photometry of NGC2261 and R Mon show that the main nebula body is increasingly bluer than R Mon (Hall (1964,65), Bruck (1974), Aspin, McLean and Coyne (1985)), out to a distance of about 60 arc seconds, at which point the nebula colour starts to redden. These results confirm the reflection nature of the light emanating from

NGC2261.

4.2.5 Polarimetry of NGC2261/R Mon.

There have been many polarimetric studies of R Mon and NGC2261; Hall (1964,65), Zellner (1970), Jones and Dyck (1978), Garrison and Anderson (1978), Gething *et al.* (1982), Sato *et al.* (1985), Aspin, McLean and Coyne (1985) and Warren-Smith, Draper and Scarrott (1987(a)). Hall (1964,65) studied the wavelength dependence of polarisation of R Mon and the spatial polarisation of NGC2261. He found the polarisation of NGC2261 to be as high as 34 per cent in some regions. Hall also noted that the polarisation increased with distance from R Mon, and that the normals to the electric vector pointed, approximately, directly to R Mon. These factors combined with his determination of a linear relationship between the inverse wavelength and percentage polarisation in NGC2261 (whose percentage polarisation increased with increasing wavelength), enabled Hall to conclude that NGC2261 was a reflection nebula, not a synchrotron source. Hall found that polarisation of R Mon was about 10 to 12 percent over the range 0.36 nm to 0.58 nm, which makes it one of the most intrinsically polarised objects of this type.

Zellner (1970) found that the very high polarisation of R Mon was variable, and also that its degree of polarisation dependency with wavelength changed with time. At one stage, the degree of polarisation wavelength dependency was approximately flat, but later appeared to

increase into the near infra-red. Zellner also proposed that the polarisation properties of R Mon were compatible with scattering from large grains, ruling out electron scattering and Rayleigh scattering.

The first infra-red polarisation measurements of NGC2261/R Mon were made by Jones and Dyck (1978) at a wavelength of 2.2 microns. They found the polarisation of R Mon to be around 4 percent at 102 degrees, indicating that the polarisation of R Mon was decreasing into the infra-red (from around 12 percent in the visual). They also found that the position angle of polarisation increased smoothly by 10-15 degrees over the full range of their measurements (0.35 to 2.2 microns). Jones and Dyck's measurements of NGC2261 showed that the percentage and position angle of polarisation are roughly independent of wavelength. From their polarisation measurements of R Mon, they concluded that the reduction in polarisation of R Mon is due to dilution of the scattered component of intensity, by an increase in the flux direct from the embedded source (R Mon). They also suggested that the wavelength independency of polarisation of the main nebula body, NGC2261, implies scattering from relatively small particles (at a wavelength of 2.2 microns), similar to Rayleigh scattering.

In a study of Herbig Ae/Be stars, Garrison and Anderson (1978) have measured the polarisation of R Mon in the U, B, V, R, and H α wavebands. Within this set of objects R Mon is by far the most polarised. Comparing their results with those of Zellner (1970) and Hall (1965), Garrison and Anderson find some corroboration for Zellner's finding that R Mon shows variable polarisation, but note that the di-

aperture sizes used in the measurements were different and that this could account for at least some of the observed variations, since the component due to the polarised flux from the surrounding nebula was not known. They also found that again, as had been noted before, that the position angle of polarisation increased with increasing wavelength, and thus suggested that this was probably due to some geometric effect(s). Garrison and Anderson's measurement also showed that the $H\alpha$ polarisation of R Mon was less than the polarisation of the continuum.

The first detailed two dimensional optical polarisation mapping of the NGC2261/R Mon region was performed by Gething *et al.* (1982), who made measurements in two wavebands (R and V). These measurements confirmed that NGC2261 is a reflection nebula, illuminated by a source whose position was coincident with R Mon. More interestingly, their maps also revealed for the first time, a band of anomalously orientated (from the expected centrosymmetric pattern of a normal reflection nebula) polarisation vectors across the head of the nebula, including R Mon. They provisionally interpreted these as due to the effects of preferential extinction produced by a screen of aligned grains, in a similar fashion to that proposed to explain the polarisation of stars by the interstellar medium. The dust grains, they speculated could be orientated by a toroidal magnetic field trapped in the equatorial disk which surrounds R Mon.

Aspin, McLean and Coyne (1985) have extended the study of Gething *et al.* to encompass a larger wavelength range (B, V, R) with better resolution, and have also performed some photometry and spec-

tropolarimetry of R Mon. They observe the general trends in colour and polarisation seen by the earlier workers and favoured the Gething *et al.* analysis of the origin of the band of polarisation seen across the head of the nebula. In their maps they also find evidence for the existence of “mini-lobes” of polarisation close to the north and south of R Mon. Their spectropolarimetry of R Mon shows that (like Garrison and Anderson (1978)) the $H\alpha$ polarisation is reduced with respect to the continuum polarisation. Within their interpretation of the polarisation mechanism for R Mon they were forced to interpret this effect as the consequence of a superposition of two or more polarising mechanisms.

Further infra-red polarimetry of R Mon was performed by Sato *et al.* (1985) whose measurements agreed with those made by Jones and Dyck (1978). Sato *et al.* note that in R Mon (as in other nebulae which they have studied) the position angle of polarisation is perpendicular to the major axis of the nebula. They also note that the nebula axis is roughly parallel to the direction of the local interstellar magnetic field as defined by nearby field star polarisations. They conclude that the polarisation of R Mon is due to scattering in the lobes of the disk surrounding R Mon as in the model of Elsässer and Staude (1978).

Most recently, imaging polarimetry of the NGC2261/R Mon system was performed by Warren-Smith, Draper and Scarrott (1987(a)), who have used the polarimeter system described in Chapter 1 of this thesis to enable very deep imaging of this object. In their polarisation maps they have detected one of the very faint features to the south of R Mon (in the opposite direction from the bright nebula), which

was noted as present by Walsh and Malin (1985), in their description of a very deep optical study of this object. Warren-Smith, Draper, and Scarrott have presented polarisation measurements of this feature which conclusively prove that it is actually the south western edge of the obscured southern cavity. The study of Warren-Smith, Draper and Scarrott has also allowed greater accuracy than previously obtained in any of the above observations, consequently allowing these authors to interpret small scale variations in the polarisation position angle of these maps with some degree of confidence. They interpret the small scale variations as being due to the influence of a large scale magnetic field present throughout the nebula, which may be of the type proposed to accelerate bipolar outflows (see Chapter 3).

4.2.6 Molecular line observations.

Observations of the NGC2261/R Mon system in the ^{12}CO ($J=1-0$) rotational transition were first made in 1980 by Cantò *et al.* (1981). Cantò *et al.* found that R Mon lay at the centre of a disk-shaped molecular cloud, in which cavities existed to the north and south, containing blue and red-shifted gas respectively. They thus proposed a model of NGC2261/R Mon which was in reality bipolar in geometry, not cometary as might be supposed from the optical morphology; the southern lobe of the bipolar geometry being highly obscured by the tilting of the disk. On the basis of these results, Cantò *et al.* also proposed an interpretation of the positioning and excitation of HH39, a series of HH objects which lie on the axis of symmetry of the nebula, about 7.5

arc minutes to the north. They proposed that a wind emanating from R Mon is channelled by the cavity to the north and then re-focussed to interact at the position of HH39, thus producing a region of shocked material. The details of this model are found in Barral and Cantò (1981), and form the basis of the so-called interstellar disk models. Using their CO measurements, Cantò *et al.* made an estimate of the mass loss rate from R Mon, which they estimated to be $1.4 \times 10^{-8} M_o/yr$, using a wind velocity of 200 Km/sec.

Near infra-red speckle interferometric measurements of R Mon by Beckwith *et al.* (1984) have shown the presence of a core-halo structure of size 1300x1300 astronomical units, which they interpret as direct evidence of a disk around R Mon of solar-system size, which may therefore be in the early stage of planetary formation. Further to these measurements, Beckwith *et al.* (1986) have made interferometric measurements of CO (J=1-0) emission of R Mon and NGC2261 which reveal small scale structure around R Mon of size ≈ 6 arcsec. These structures are apparently bound to R Mon and of approximate mass $7 \times 10^{-3} M_o$, which confirms the results of Beckwith *et al.* (1984).

Kaifu (1987) has presented CO Data of an area 160x140 arcseconds around R Mon with 15 arcseconds resolution, he confirms the results of Cantò *et al.* (1981) ie. he finds clear evidence for a bipolar flow from R Mon and evidence for the presence of a disk around R Mon. Kaifu also notes that the blue shifted flow from R Mon fits the northern optical nebula (NGC2261) very well. He also claims that the NGC2261 CO observations show similarities with the flows of L1551, GL490 and

S106, which have the general characteristics:-

1. double peaked appearance with a thin central part,
2. cavities on both sides of the disk in which the low velocity molecular flow fits well, and finally
3. the flows seem to be gradually accelerated along the walls of the cavities,

all of which are strong evidence in favour of a magnetically accelerated outflow as in the models of Pudritz and Norman (1983,86) and Shibata and Uchida (1987).

4.2.7 HH39.

HH39 is a series of HH-like knots which are found on the symmetry axis of the NGC2261/R Mon system, some 7.5 arc minutes to the north. Cantò *et al.* (1981) proposed an interstellar disk and cavity focussed wind as the mechanism for exciting the region, thus producing the characteristic low-excitation emission spectra of HH objects. Brugel, Mundt and Bührke (1984) contrary to this model, have proposed on the basis of emission lines detected in the nebula, that a collimated “jet” of high speed material flows directly up the axis of the nebula, shocking into clumps of material at the position of HH39, thus producing the HH objects. K.M. Strom *et al.* (1986) claim to have found an SII emission knot to the south of this flow, identifying this as a (complementary) red-shifted HH object.

Walsh and Malin (1985) in a deep prime focus AAT plate of the NGC2261/R Mon region, have shown that some of the brightness knots within HH39 vary in brightness, and that the region is connected to the NGC2261 nebula by a very faint loop of material extending from HH39. Jones and Herbig (1982) have measured the proper motions of four of the brighter knots in HH39, and find that the proper motions are generally pointed away from R Mon, one knot has a tangential velocity of 60 Km/sec, and the others have velocities grouped around 290 Km/sec.

4.2.8 Summary.

The overall impression of the NGC2261/R Mon system is that of a system which is apparently in continual change and flux. The optical morphology of NGC2261 and the brightness and polarisation of R Mon have been observed to be constantly fluctuating for quite some time. The geometry of the actual system is almost certainly bipolar, with material flowing from the central source, in both the north and south directions. The disk/ torus around R Mon is amongst the best defined and observed. The northern cavity contains the reflection nebula NGC2261, which contains polarisations indicative of effects other than simple scattering. R Mon appears to be a reasonably massive star at around $7M_{\odot}$, and has an immense bolometric luminosity of $800L_{\odot}$. The disk surrounding R Mon is observed from scales of 0.5 parsecs to 1200 astronomical units. R Mon is a very young object and may well be in the process of planetary formation.

4.3 Observations.

The sets of polarimetric observations which are to be discussed in this chapter were made on three distinct occasions. Chronologically, the first observations were made in 1979, on the Wise telescope at the F13.5 focus, using the Durham Imaging Polarimeter and an electronographic camera as the detector. The initial interpretation of this dataset formed the basis of the paper by Gething *et al.* (1982). The next set of data was taken on the Anglo-Australian Telescope in 1981, again with the Durham Imaging Polarimeter and an electronographic camera as the detector. This data has not been previously analysed or interpreted. The third and by far the most accurate and large dataset to be discussed, was taken using the CCD camera system outlined in Chapter 1 of this work, together with the Durham Polarimeter on the Wise telescope during the period February 1985 to March 1986. A subset of this data has previously been interpreted in the paper on the faint linear feature to the south west of R Mon, by Warren-Smith, Draper and Scarrott (1987(a)).

The first dataset includes measurements taken in the electronographic camera R and broadband V filters (see ^{table 2.1 and} fig 1.1 for the response of these filters and the CCD filter system), comprising of two sets of three plates of data with total exposure times of 90 minutes for each set. The second dataset is a series of measurements made in the broadband electronographic V filter, consisting of eight separate plates with a total exposure time of 120 minutes. The image scale on these mea-

surements was much larger than for the other sets, being about 0.33 arcseconds per pixel as opposed to 1.2 for the Wise datasets. For the purpose of this chapter the AAT data was resampled to the same image scale as the other datasets, so that direct comparisons could be made. The third dataset consists of a collation of data covering the V,R,I,Z and $H\alpha$ wavebands. The amount of data in each set is shown in table 4.1. The image scale of the measurements and the orientation was corroborated by comparison with the astrometry performed by K.M. Strom *et al.* (1986) for the NGC2261/R Mon region. All the above data has been analysed or re-analysed using the routines now available on the Durham node of STARLINK for analysing two channel imaging polarimetry (which is partly described in chapter 1, and for which the philosophy of application is described by Scarrott *et al.* (1983)) and represents some of the data used in Chapter 2 of this work.

The zero point calibration of the R-band CCD dataset polarisation position angle was performed by analysing accurate R-band polarimetry of Halley's comet obtained in December 1985. The zero point was determined through knowledge of the orbit of Halley and the solar and terrestrial positions at this time, from which the scattering angle was known. The corrections described in Chapter 2 were applied using terms relative to the R-band zero term.

Table 4.1:

Polarisation measurements of NGC2261/R Mon.				
Date	Filter	Detector	Total Exposure Time	No. of Plates
Jan 79	VV	EG	90 Minutes	3
Jan 79	R	EG	90 Minutes	3
Jan 81	VV	EG	120 Minutes	8
Feb 85	I	CCD	12 Minutes	12
Dec 85	R	CCD	28 Minutes	16
Dec 85	I	CCD	48 Minutes	16
Dec 85	Z	CCD	60 Minutes	12
Jan 86	V	CCD	69 Minutes	16
Feb 86	H α	CCD	180 Minutes	12
Mar 86	I	CCD	107 Minutes	20

4.4 Results and Discussion.

4.4.1 General results.

Inspecting figures 4.2 through 4.11, which display the polarisation maps produced from all of the datasets described above, an immediate conclusion may be drawn. As seen in the other polarimetric investigations of the object NGC2261, the main body of nebulosity directly to the north of R Mon is a reflection nebula, whose illuminating source is most likely to be co-incident with the apical brightness peak, R Mon. The levels of polarisation observed are typically 20 percent in V, and increase with wavelength, becoming as high as 40 percent in the Z band. The highest

levels of polarisation are observed on the north eastern edge of the nebula, and range from 30 percent to 60 percent over the full wavelength range. The range of errors of the measurements presented in the polarisation maps are shown in figs 4.12 to 4.16, which display measurements made along a line running directly north from R Mon. These traces are intended to show the range of errors and values found in the polarisation maps.

To the south west of R Mon, the linear feature described by Walsh and Malin (1985), is present and measurably polarised in the 1979 electronographic R and V datasets, a result which was not expanded upon by Gething *et al.* (1982). The linear feature is polarised at a level of around 30-40 percent in these maps, slightly less so in the V than in the R band. This feature is also present in some of the later 1985/6 CCD datasets as reported by Warren-Smith, Draper and Scarrott (1987(a)) for the V, R and March 1986 I Datasets. It is also present to some extent in the December 1985 I and February 1985 I datasets shown here, which adds yet more weight to the argument that the south west feature is a reflection phenomenon, and furthermore that it represents a physical structure, identified as the edge of the southern, usually obscured, counter lobe. This conclusion is further strengthened by photographs published by Joy (1945), whose plate XV also shows a similar feature on the south eastern edge, which gives the appearance of a properly bipolar geometry to the nebula. However, no coincident feature can be found in the data which is presented here, and hence confirmation of this notion must await further observations of this object at some future time, when it seems reasonable to suppose

NGC2261/R Mon V-Band 1979 EG Data

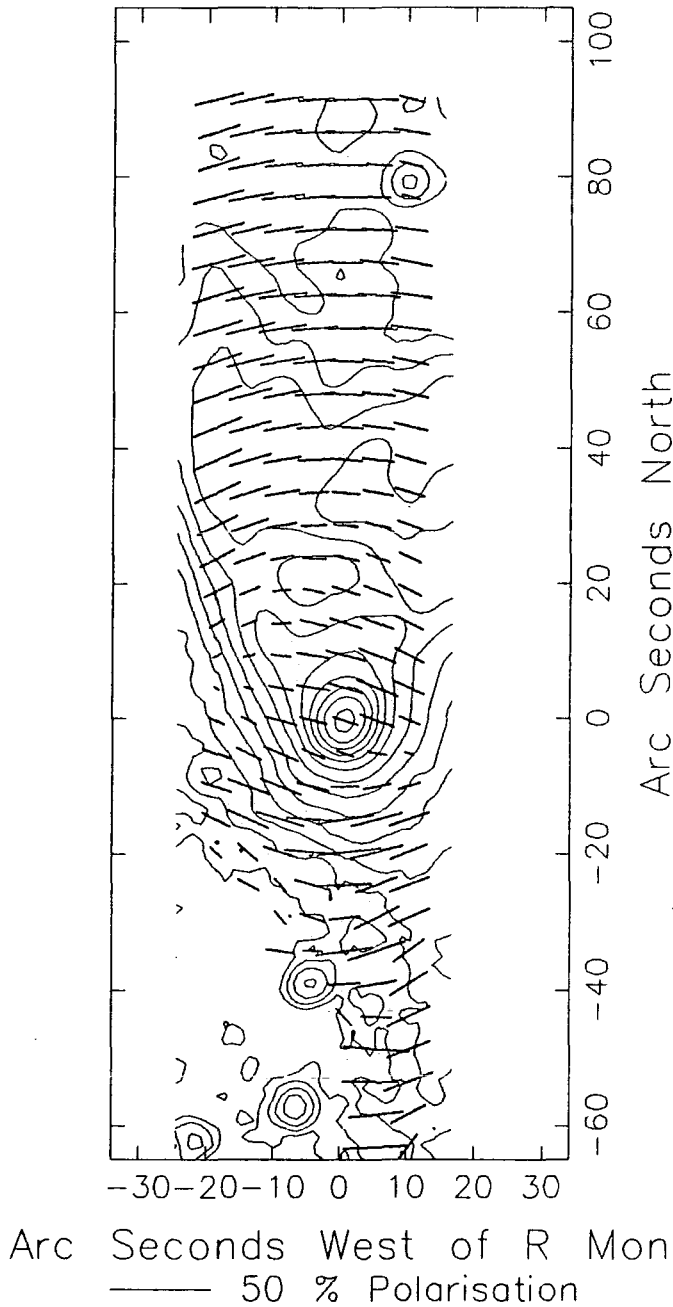


Figure 4.2: An electronographic VV band polarisation map of NGC2261/R Mon, superimposed on an intensity contour map. The contour intervals are 0.5 magnitudes. The integration bins for the polarisation measurements are 7 pixels square (8.5")

NGC2261/R Mon R-Band 1979 EG Data

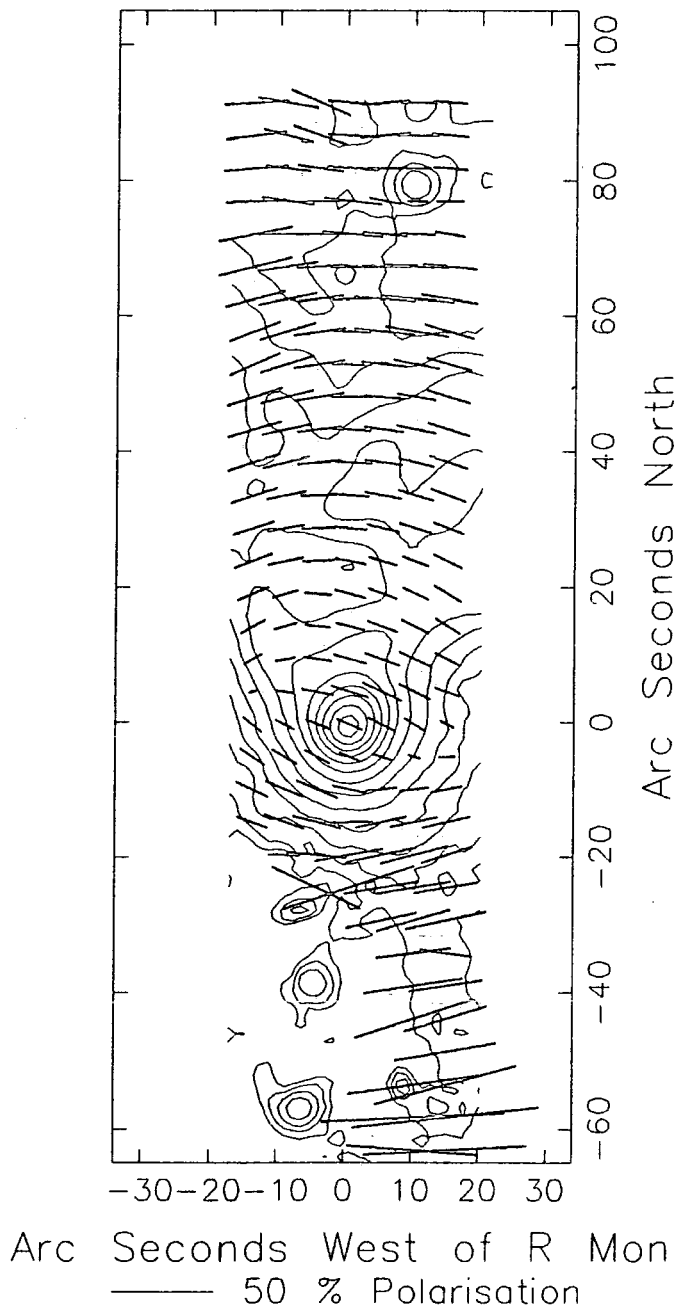


Figure 4.3: An electronographic R band polarisation map of NGC2261/R Mon, superimposed on an intensity contour map. The contour intervals are 0.5 magnitudes. The integration bins for the polarisation measurements are 7 pixels square (8.5")

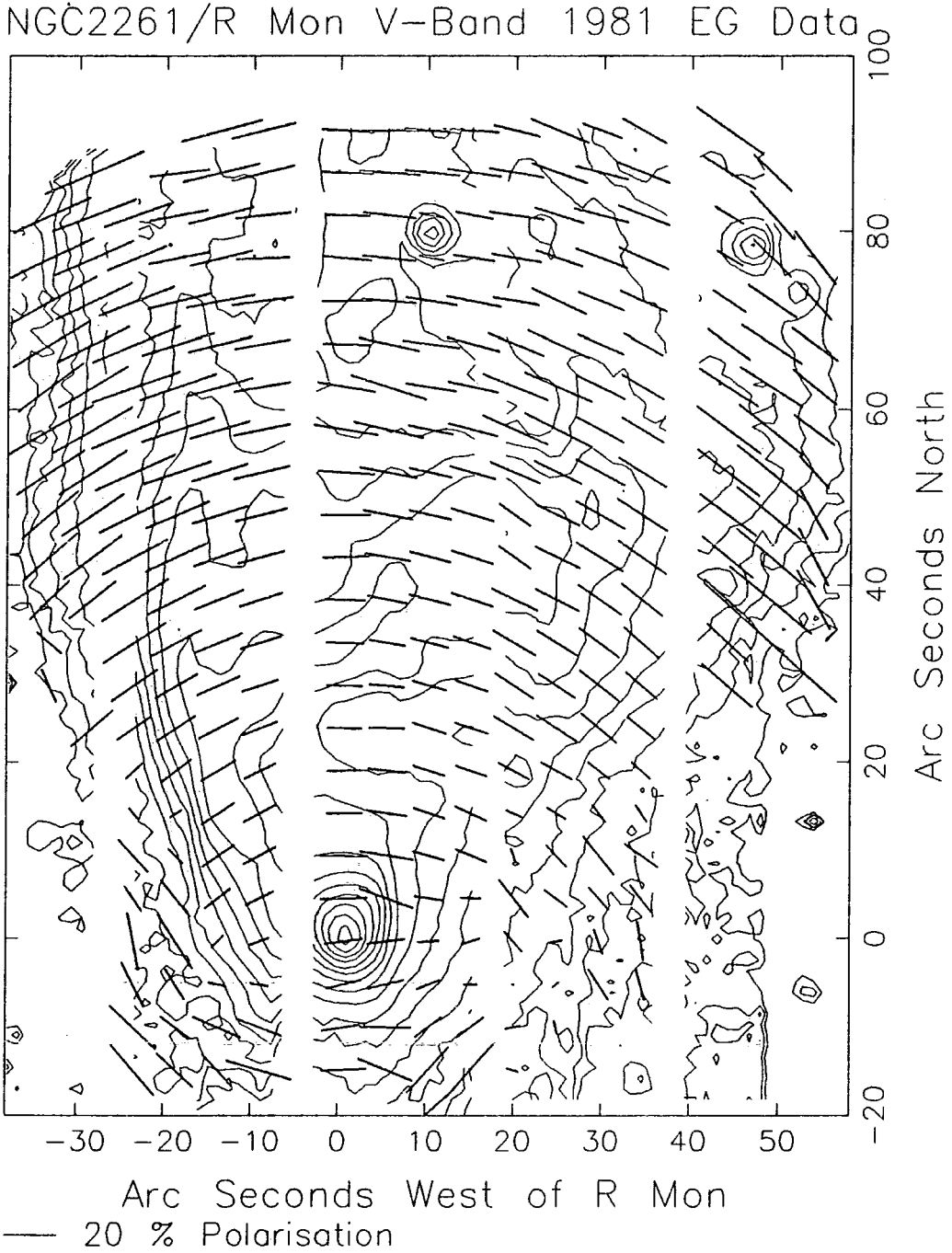


Figure 4.4: An electronographic VV band polarisation map of NGC2261/R Mon, superimposed on an intensity contour map. The contour intervals are 0.5 magnitudes. The integration bins for the polarisation measurements are 7 pixels square ($8.5''$)

NGC2261/R Mon I-Band Feb85 Data

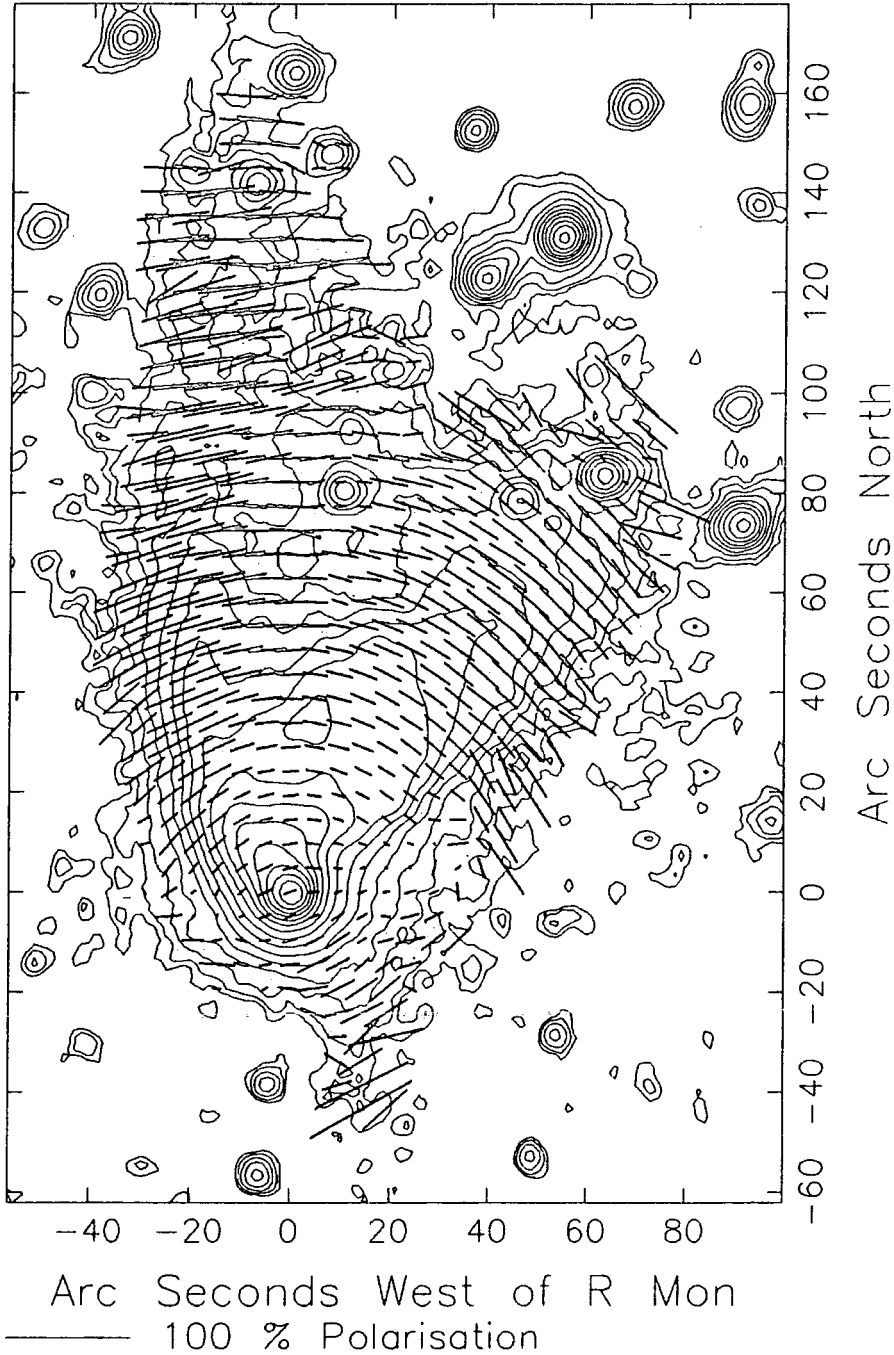


Figure 4.5: A CCD I band polarisation map of NGC2261/R Mon, superimposed on an intensity contour map. The contour intervals are 0.5 magnitudes. The integration bins for the polarisation measurements are 7 pixels square ($8.5''$)

NGC2261/R Mon R-Band Dec85 Data

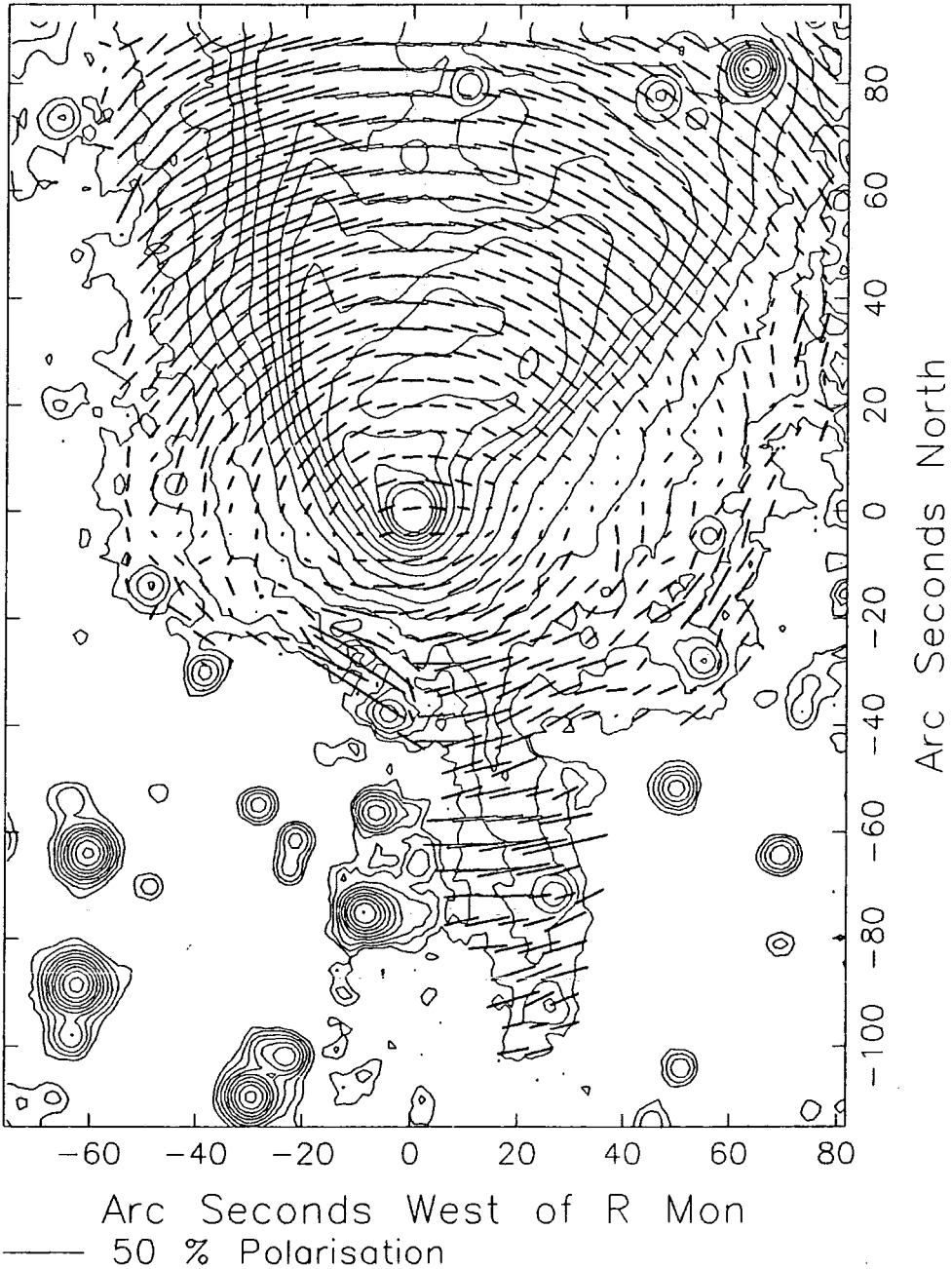


Figure 4.6: A CCD R band polarisation map of NGC2261/R Mon, superimposed on an intensity contour map. The contour intervals are 0.5 magnitudes. The integration bins for the polarisation measurements are 7 pixels square ($8.5''$)

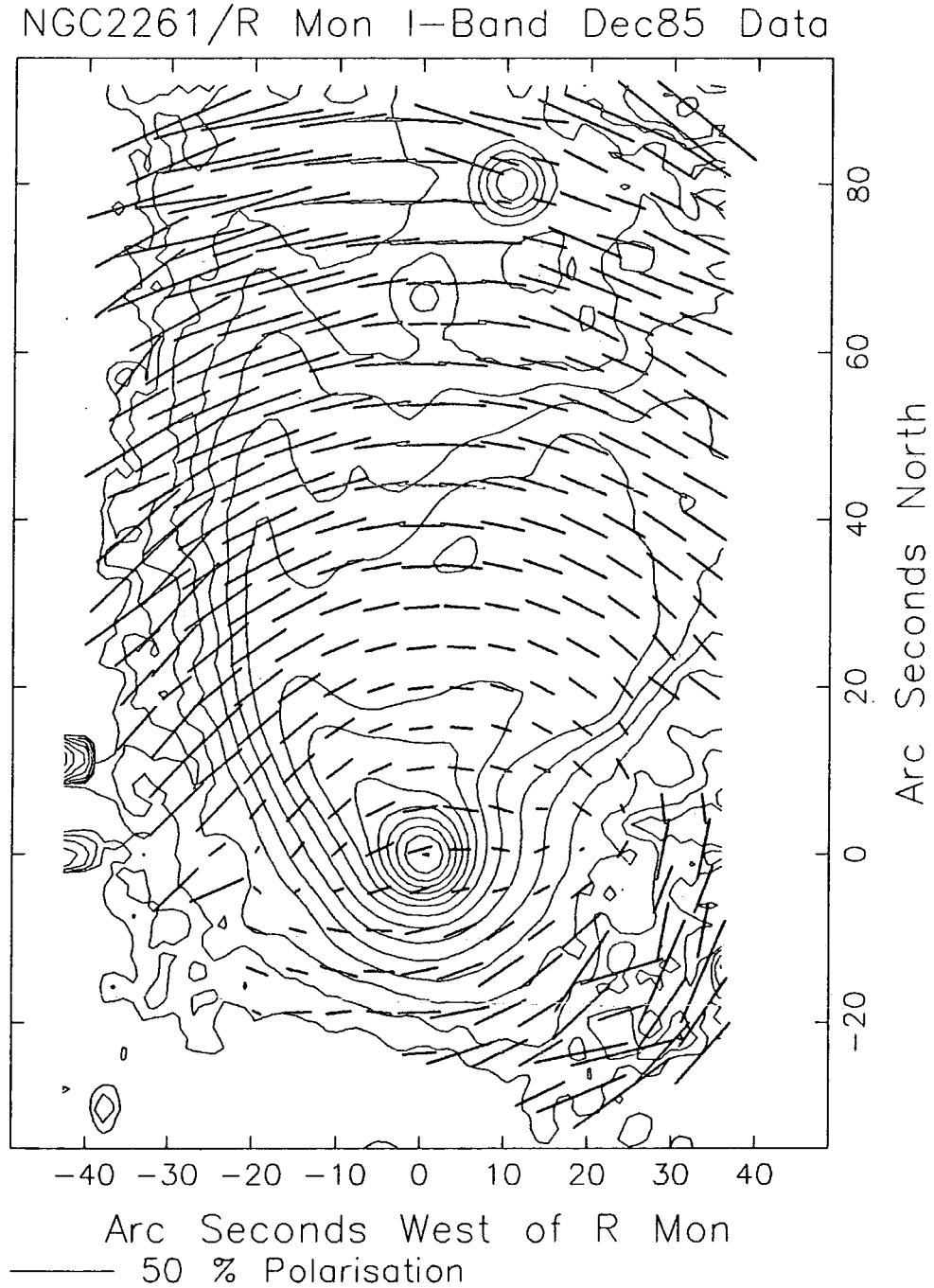


Figure 4.7: A CCD I band polarisation map of NGC2261/R Mon, superimposed on an intensity contour map. The contour intervals are 0.5 magnitudes. The integration bins for the polarisation measurements are 7 pixels square ($8.5''$)

NGC2261/R Mon Z-Band Dec85 Data

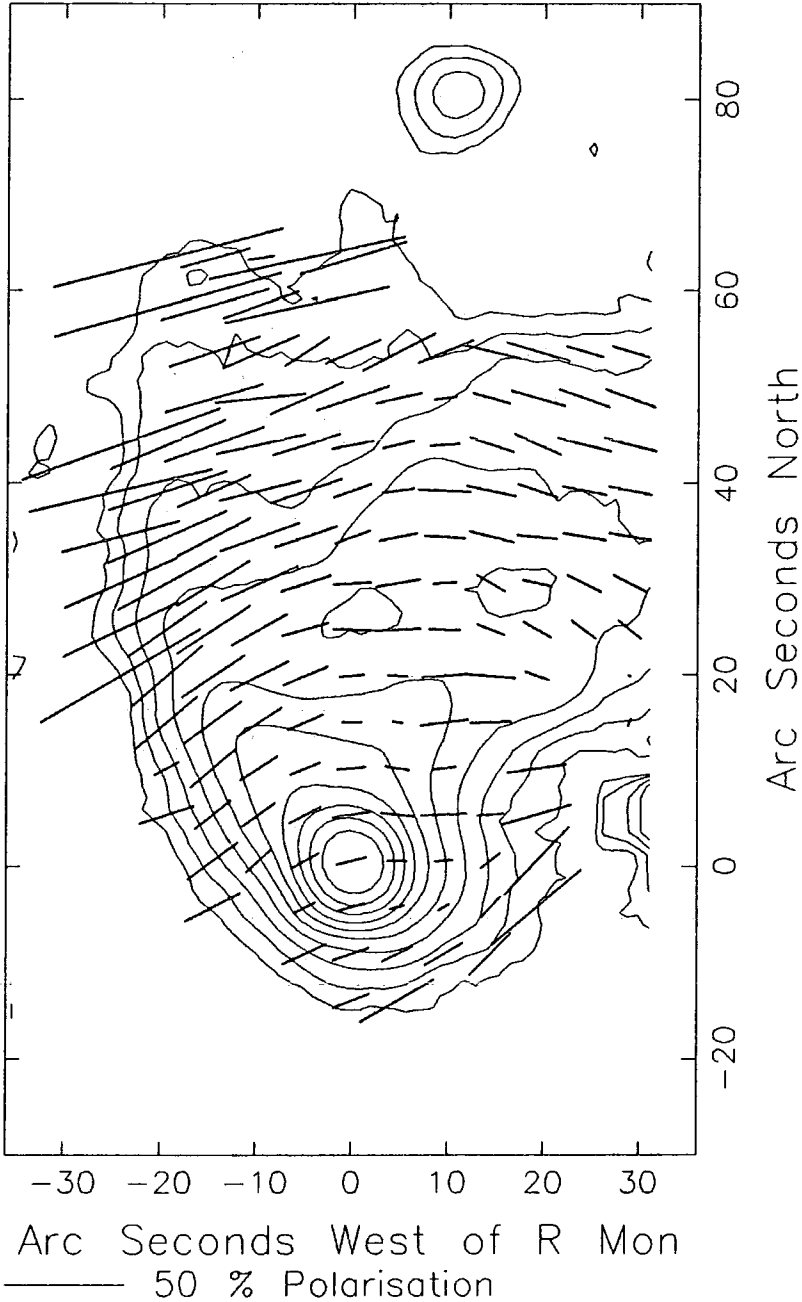


Figure 4.8: A CCD Z band polarisation map of NGC2261/R Mon, superimposed on an intensity contour map. The contour intervals are 0.5 magnitudes. The integration bins for the polarisation measurements are 7 pixels square (8.5")

NGC2261/R Mon V-Band Jan86 Data

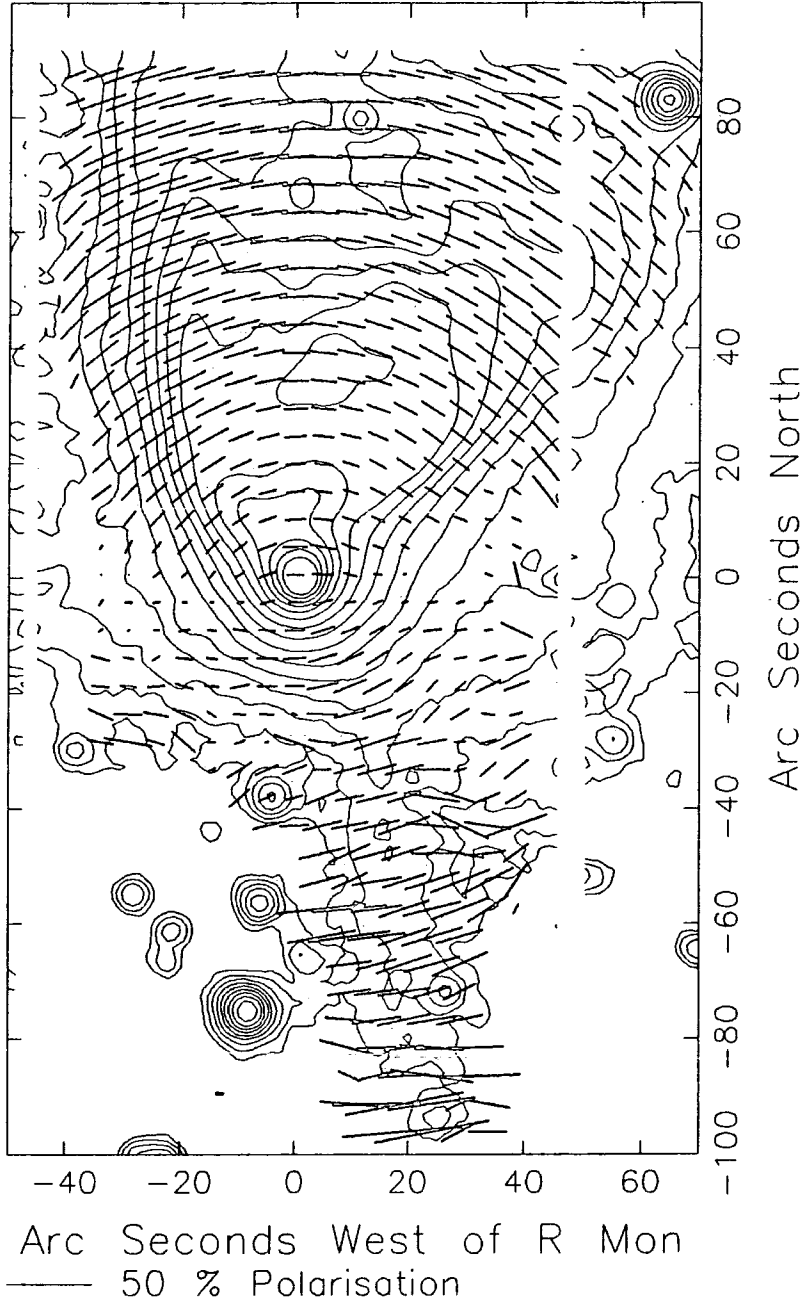


Figure 4.9: A CCD V band polarisation map of NGC2261/R Mon, superimposed on an intensity contour map. The contour intervals are 0.5 magnitudes. The integration bins for the polarisation measurements are 7 pixels square ($8.5''$)

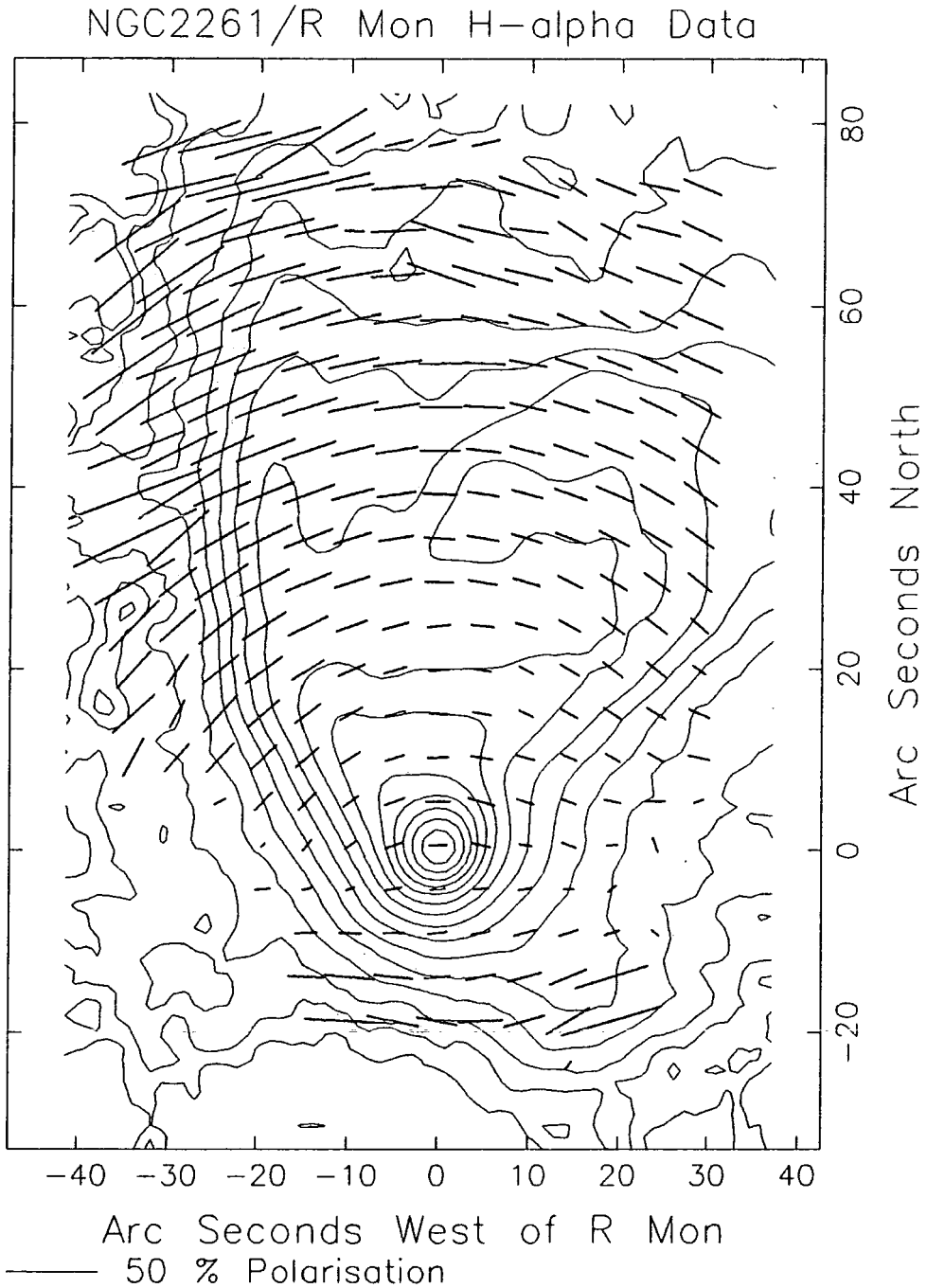


Figure 4.10: A CCD $H\alpha$ band polarisation map of NGC2261/R Mon, superimposed on an intensity contour map. The contour intervals are 0.5 magnitudes. The integration bins for the polarisation measurements are 7 pixels square ($8.5''$)

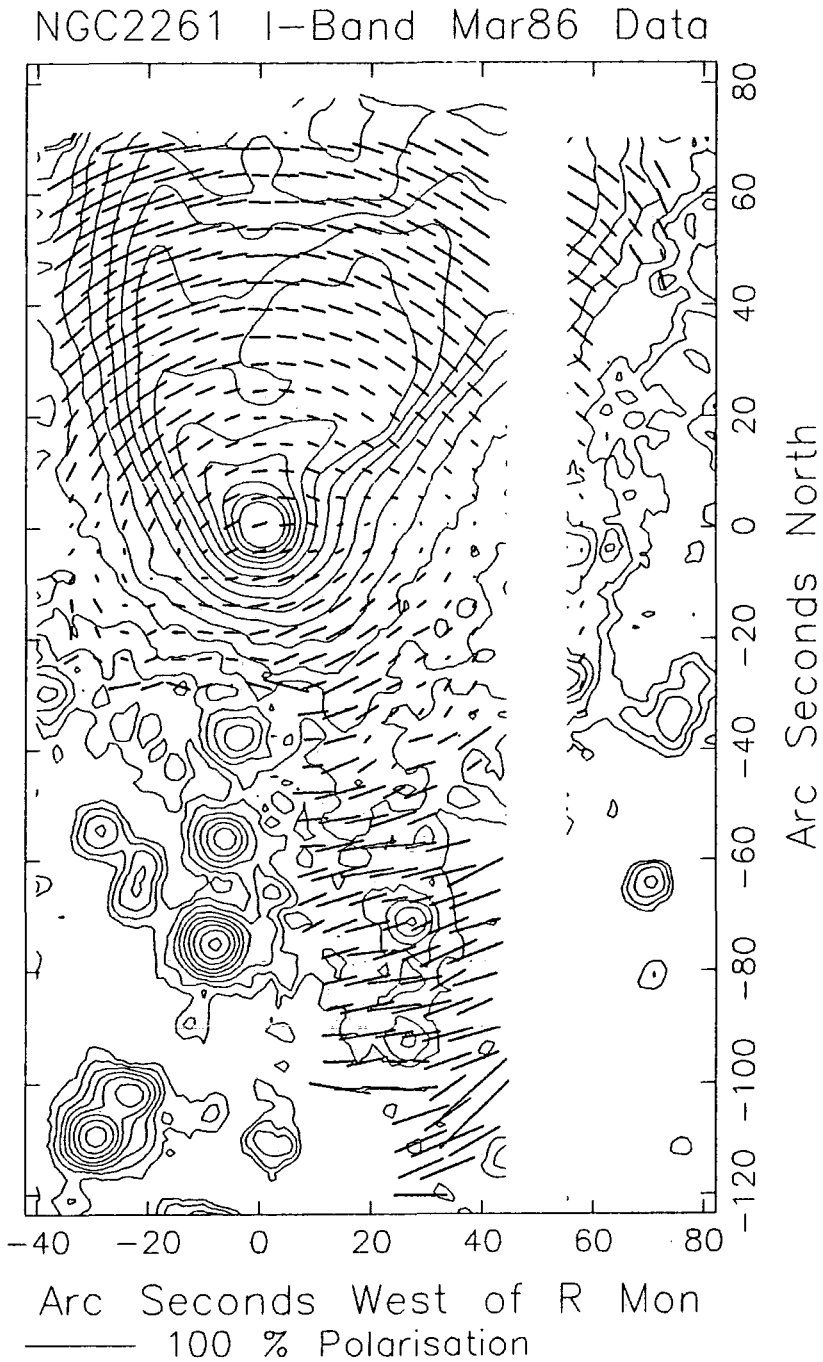


Figure 4.11: A CCD I band polarisation map of NGC2261/R Mon, superimposed on an intensity contour map. The contour intervals are 0.5 magnitudes. The integration bins for the polarisation measurements are 7 pixels square ($8.5''$)

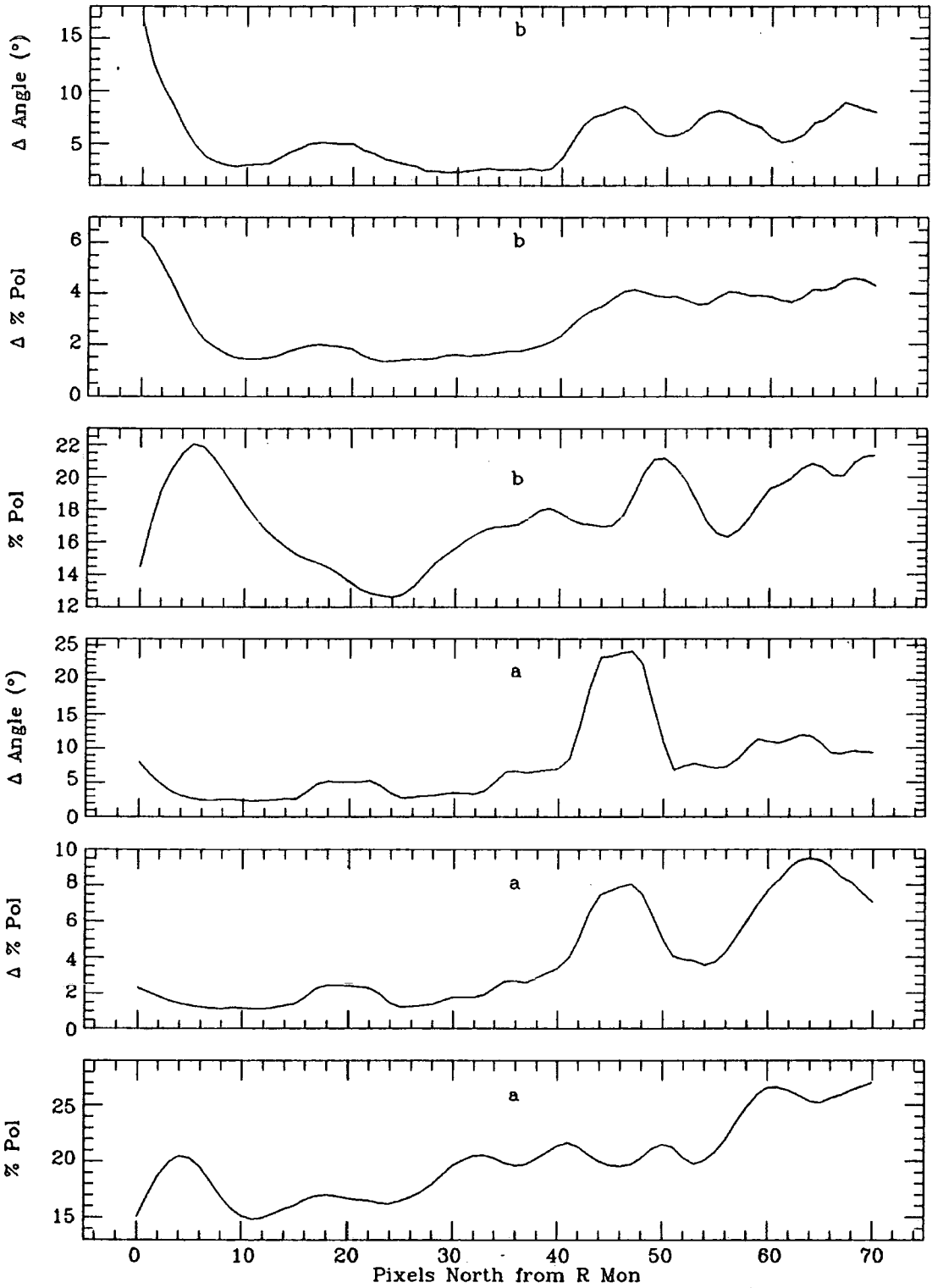


Figure 4.12: Traces of % polarisation, the error in the % polarisation (%) and the error in the position angle, taken along a line extending 70 pixels (85") directly north from R Mon. The traces are for the datasets; (a) fig 4.2 (1979 electronographic VV) and (b) fig 4.3 (1979 electronographic R).

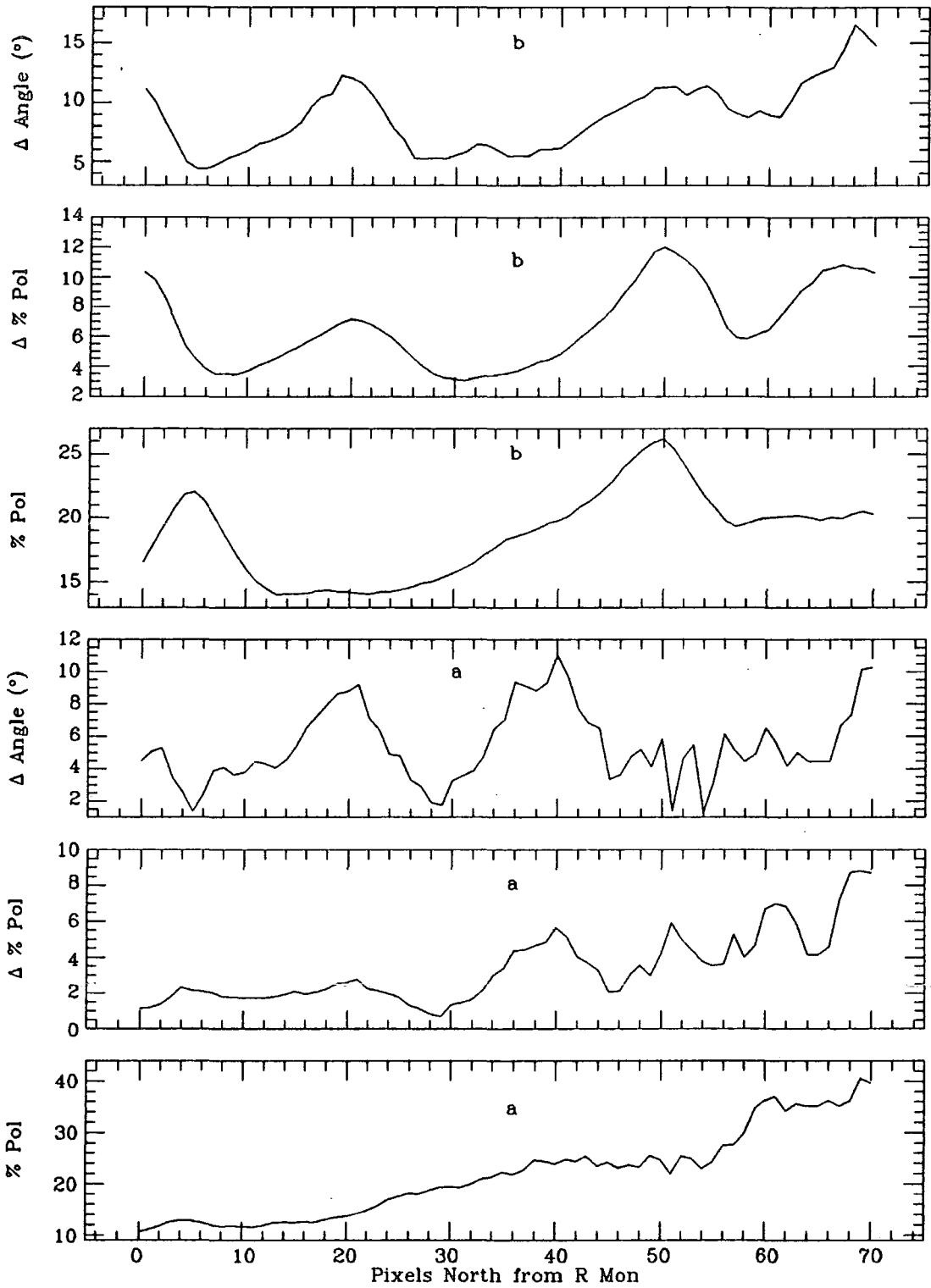


Figure 4.13: Traces of % polarisation, the error in the % polarisation (%) and the error in the position angle, taken along a line extending 70 pixels ($85''$) directly north from R Mon. The traces are for the datasets; (a) fig 4.4 (1981 electronographic VV) and (b) fig 4.5 (February 1985 I).

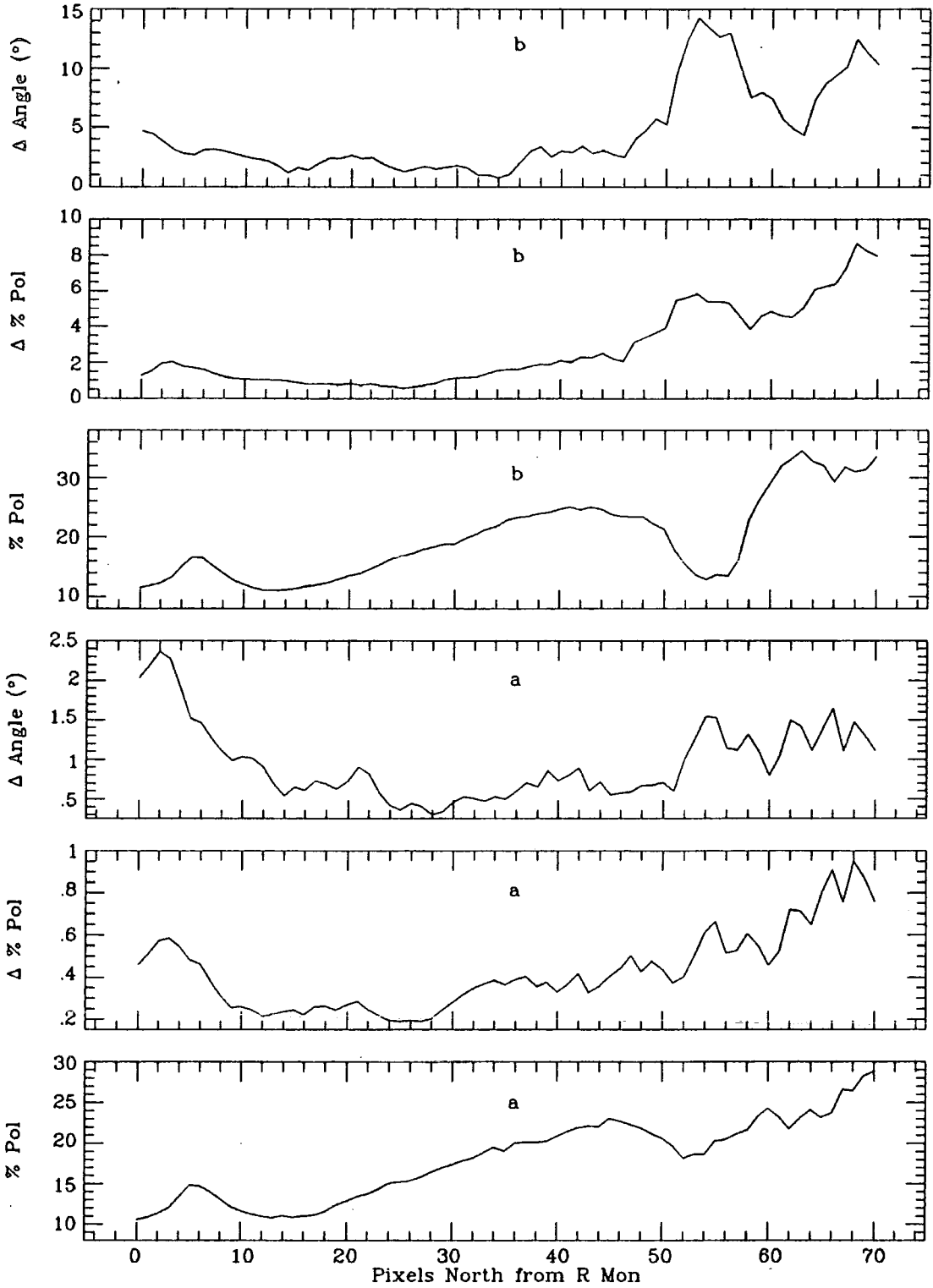


Figure 4.14: Traces of % polarisation, the error in the % polarisation (%) and the error in the position angle, taken along a line extending 70 pixels (85'') directly north from R Mon. The traces are for the datasets; (a) fig 4.6 (December 1985 R) and (b) fig 4.7 (December 1985 I).

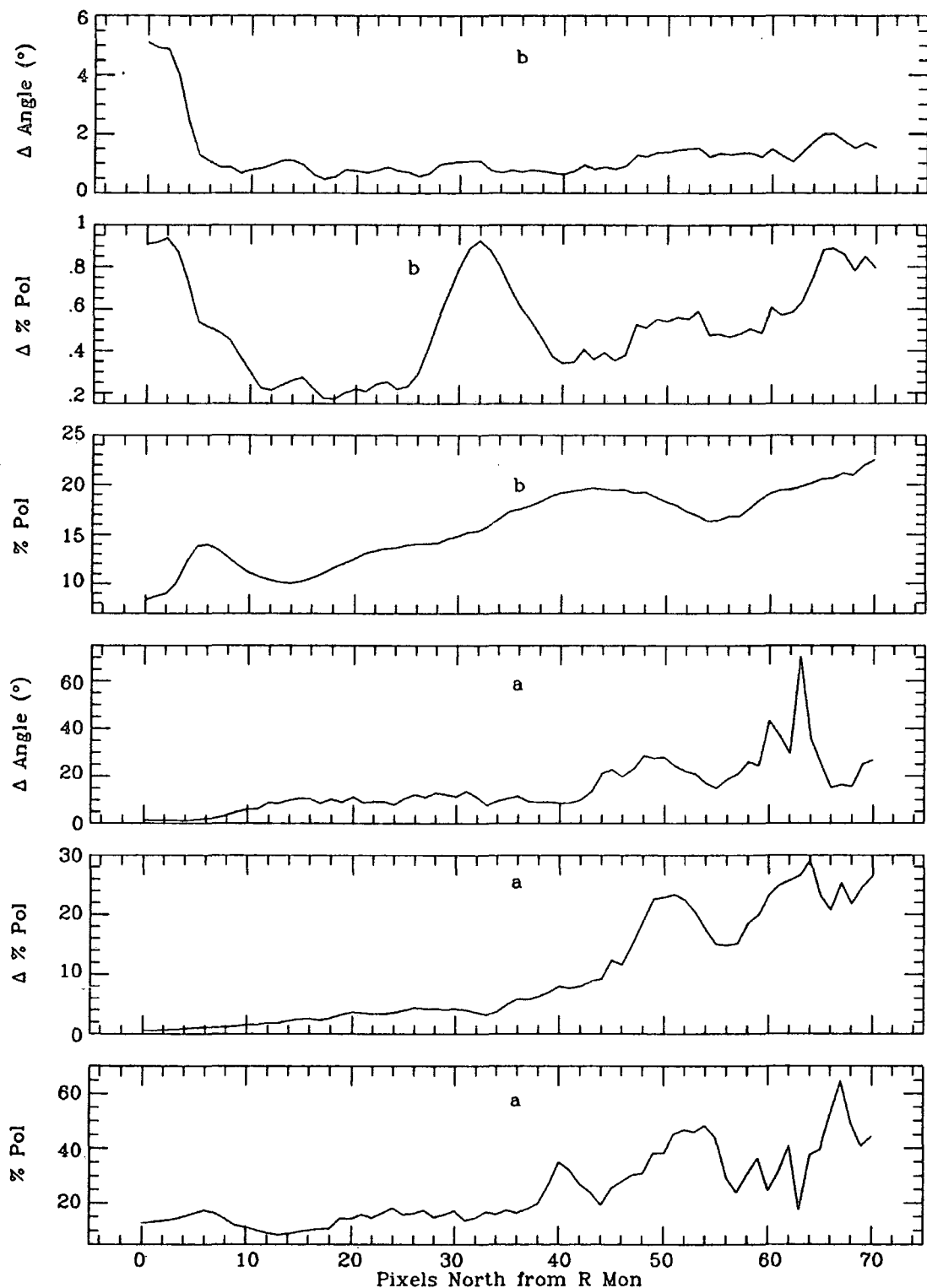


Figure 4.15: Traces of % polarisation, the error in the % polarisation (%) and the error in the position angle, taken along a line extending 70 pixels ($85''$) directly north from R Mon. The traces are for the datasets; (a) fig 4.8 (December 1985 Z) and (b) fig 4.9 (January 1986 V).

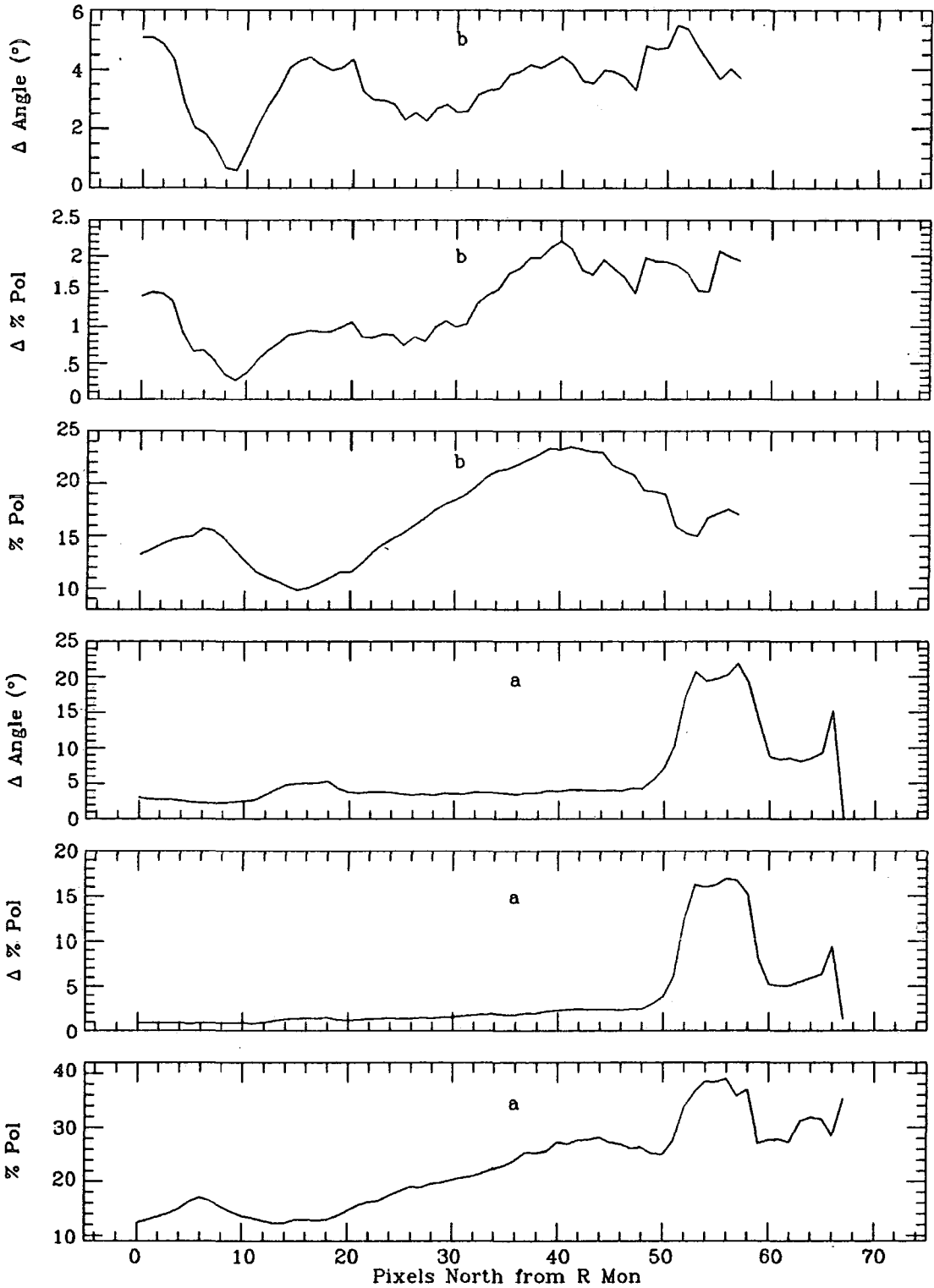


Figure 4.16: Traces of % polarisation, the error in the % polarisation (%) and the error in the position angle, taken along a line extending 70 pixels ($85''$) directly north from R Mon. The traces are for the datasets; (a) fig 4.10 (February 1986 $H\alpha$) and (b) fig 4.11 (March 1986 I).

the south eastern feature may become relatively brighter, as it has been in the past.

4.4.2 The variation of polarisation of R Mon and the *Polarisation Disk*.

On closer inspection the maps presented in figures 4.2 to 4.11 also show one other easily discernable feature, of great relevance to this work. Each map shows a band of “anomalously” orientated polarisations across the head of the nebula including R Mon. This effect was first described by Gething *et al.* (1982), whose datasets are represented by figures 4.2 and 4.3. The polarisations are described as anomalous because they deviate from the normal pattern of centrosymmetric polarisation vectors expected from a reflection nebula with a single point-like illuminator. Centrosymmetric describes a pattern of vectors whose normals have a common centre and thus the vectors describe circular patterns about this centre.

In the data, the orientation of the anomalous band of polarisations is defined by the line joining the two so called “null points”; the regions to east and west of R Mon in which the degree of polarisation seems to fall approximately to zero. The position angle of what we might call the “polarisation disk” of the 1979 data has been estimated by the author to be around 74 degrees. Although the null points are not shown, the extrapolation to their approximate positions is obvious. The position angle correlates with the position angle of the polarisation

of R Mon which is around 70 degrees in the 1979 data. This is in direct conflict with the position angle of polarisation of R Mon as reported by Gething *et al.* (1982) who say the polarisation of R Mon has a position angle of 97 degrees in the V band. The polarisation maps presented in this thesis agree with those shown in Gething *et al.* and on inspection of the Gething *et al.* maps, it is clear that the polarisation of R Mon must have a position angle (always measured *north through east*) substantially less than 90 degrees. Presumably Gething *et al.* (1982) were mistaken in their original measurement of the position angle of R Mon.

Realising the error of this measurement has a somewhat profound implication when comparing the position angle of polarisation of R Mon and the polarisation disk position angle, with the measurements made by the author and other workers, which are presented in figures 4.4 through 4.11. The position angle of the polarisation of R Mon and the polarisation disk are all found on the opposite side of the 90 degrees eastern line, *for all datasets*, to the 1979 measurements, *clearly the position angle of polarisation of R Mon and the polarisation disk have rotated through more than 20 degrees in a period of two years*, the time interval between the 1979 and 1981 datasets. This effect has never been noted in any study of cometary or bipolar nebulae before. However, having said this, it is a well established fact that the polarisation of R Mon itself is variable in both percentage polarisation and position angle (Zellner 1970).

The range of variations of polarisation observed in R Mon are

shown in tables 4.2 and 4.3 which present a summary of all the measurements which the author has been able to obtain. It could possibly be argued that the variations observed are due to the various aperture sizes used which must include a unknown nebula contribution, but as was noted by Aspin, McLean and Coyne (1985), and is shown in fig 4.17 for one of the CCD datasets, the actual variation of polarisation with aperture is not strong and so it seems that most of the observed variations are intrinsic to R Mon.

The large change in position angle of polarisation of R Mon noted here also resolves the apparent discrepancy between the measurements made by Jones and Dyck (1978), who found the polarisation of R Mon to be at a position angle of 86 degrees at 0.55 microns, and the grouping of other measurements all found to be greater than 90 degrees at this wavelength, as commented upon by Aspin, McLean and Coyne (1985). The Jones and Dyck measurements were made in 1976 and 1977 at least 6 months, possibly 14 months after the measurements of Garrison and Anderson (1978), who measured the position angle of polarisation of R Mon to be about 103 degrees at 0.55 microns. Thus a change in polarisation of over 4 percent and a position angle change of 17 degrees at least at 0.55 microns, is possible over about a period of around one year. The 1979 and 1981 measurements presented here show a variation of 2 percent and a position angle change of 21 degrees over two years, it therefore seems that a change in the polarisation position angle of R Mon of this magnitude is not the first to be observed, and hence seems perfectly reasonable. This conclusion is reinforced by the measurements made by Zellner (1970), who observed a change of over 4 percent and

Table 4.2:

Polarisation measurements of R Mon (other works).					
Ref	Wave-length (μm)	Date	% Polarisation (error)	Position Angle($^{\circ}$) (error)	Aper- ture ($''$)
Hall (1964)	0.48	12/62- 1/63	12.0	104.0	13.3
Hall (1965)	0.58	8/12/64	11.6	99.0	26.0
	0.44	8/12/64	9.3	97.0	26.0
	0.36	8/12/64	10.0	94.0	26.0
Zellner (1970)	0.83	24/12/68	10.5(0.4)	98.4(1.0)	8.0
	0.83	4/11/69	14.8(0.2)	105.7(0.4)	8.0
	0.52	30/10/69	11.0(0.2)	96.4(0.4)	8.0
	0.43	5/11/69	11.7(0.2)	96.8(0.4)	8.0
	0.36	18/11/68	9.0(0.5)	89.2(1.6)	8.0
	0.36	3-5/11/69	12.2(0.4)	93.6(1.0)	8.0
Garrison and Anderson (1978)	0.36	26/1/76	13.5(0.4)	97.0(1)	
	0.43	24/1/76	15.3(0.2)	102.0(1)	
	0.43	25/1/76	15.1(0.3)	101.0(1)	
	0.43	26/1/76	14.4(0.2)	99.0(1)	
	0.55	24/1/76	16.7(0.2)	104.0(1)	
	0.55	25/1/76	16.2(0.25)	102.0(1)	
	0.71	27/1/76	16.45(0.3)	103.0(1)	
	H α	26/1/76	13.12(0.6)	106(1)	
Jones and Dyck (1978)	0.55	7/76-	12.2(0.3)	86.0(1)	10.0
	0.65	3/77	11.8(0.4)	87.0(1)	10.0
	0.82		12.2(0.4)	90.0(1)	10.0
	1.25		6.2(0.7)	105.0(3)	9.0
Aspin, Mclean and Coyne (1985)	0.46	11-12	13.3	98.0	10.0
	0.54	/11/83	14.4	100.0	10.0
	0.76		12.7	103.0	10.0
	H α		9.6(0.5)	110	
Sato <i>et al.</i> (1985)	2.3	4/12/83	4.6(0.6)	101(4)	25 60

Table 4.3:

Polarisation measurements of R Mon (this work).					
Detector	Filter	Date	% Polarisation (error)	Position Angle($^{\circ}$) (error)	Aper- ture (")
Electrono- graphic Camera	VV	3/1/79	13.4(0.5)	72.0(1.5)	10.0
	R	5/1/79	14.9(0.5)	67.0(1.5)	10.0
	VV	1/81	15.7(0.5)	93.0(1.1)	10.0
CCD	I	18/2/85	10.6(0.3)	109.6(1)	10.0
	R	16/12/85	10.6(0.3)	96.5(1)	10.0
	I	13/12/85	11.6(0.3)	104.5(1)	10.0
	Z	14/12/85	12.4(0.4)	106.5(1.5)	10.0
	V	1/86	10.5(0.3)	94.0(1.5)	10.0
	H α	5/2/86	9.9(0.3)	91.7(1)	10.0
	I	12/3/86	12.7(0.3)	105.7(1)	10.0

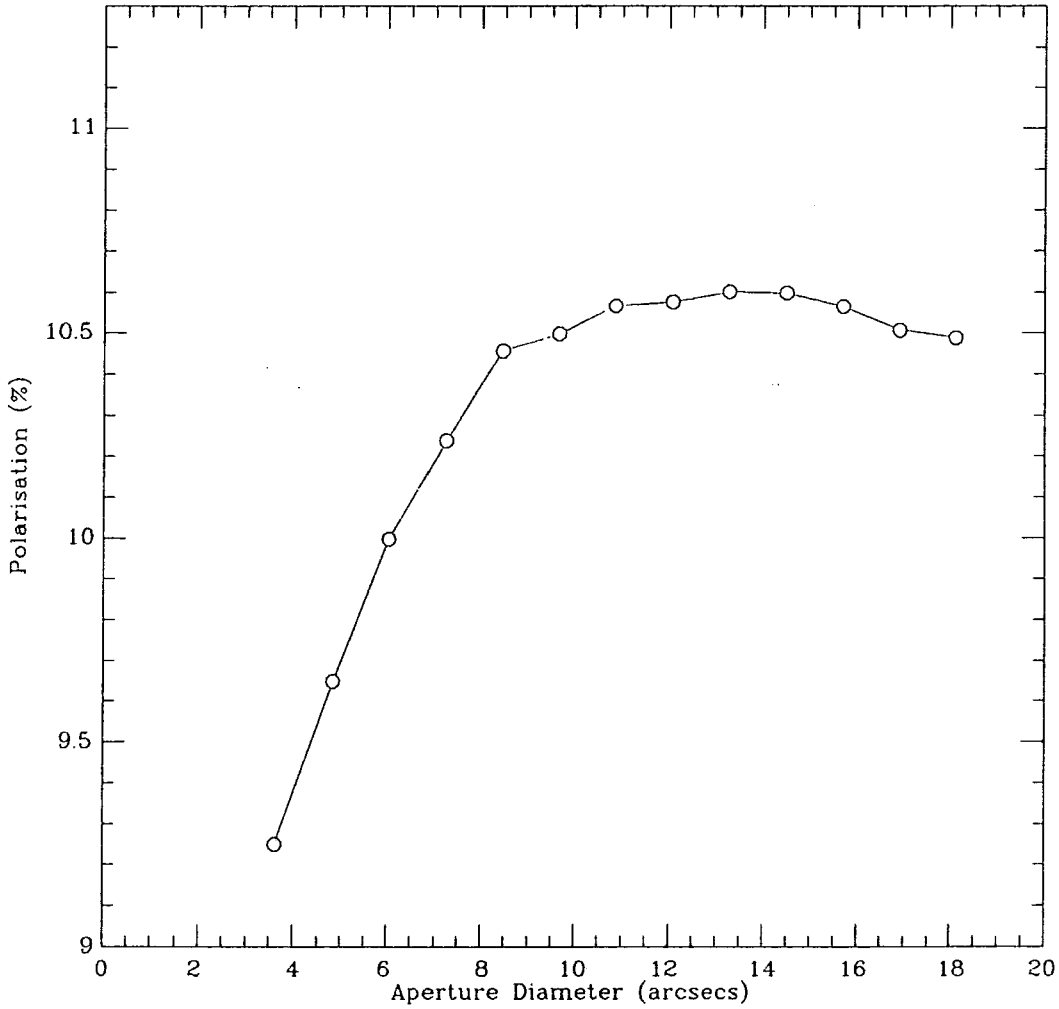


Figure 4.17: The variation with aperture of the polarisation of R Mon. The measurements were made using the January a 1986 V dataset (fig4.9).

8 degrees in a period of 11 months, in approximately the I band, which compares with a variation of 2 percent and an angle change of 6 degrees shown in the I band observations presented here over a period of 13 months. The fact that the position angle of the polarisation disk varies with time and that it also appears to be correlated to the position angle of the polarisation of R Mon, suggests that whatever mechanism is responsible for producing the polarisation of R Mon, must also be, at least in part, responsible for the appearance of the polarisation disk or vice-versa.

The hypothesis which has been in most favour for the production of the polarisation of R Mon and the anomalous band, has been that the disk surrounding R Mon contains a magnetic field which has been essentially “frozen” to the material from which the presently observed system originated. During the collapse of the material down the field lines, the proto-disk rotates to conserve angular momentum and the field wraps up into the toroidal configuration. Elongated grains of material in such a magnetic field would tend to align with the magnetic field as the component of their spin angular momentum perpendicular to the field is dissipated by paramagnetic coupling, such as in the Davis-Greenstein mechanism or one of the similar enhancing mechanisms (See Cugnon (1985), Greenberg (1978), Warren-Smith, Draper and Scarrott (1987(b))). The end result is that a component of any light travelling through such an assembly of aligned, elongated, grains would be absorbed; the component which is perpendicular to the magnetic field. Resulting in the E vector of the polarised light lying along the field direction. This is in accordance with the mechanism proposed, and

generally accepted, for the polarisation of star light by the interstellar medium.

However, this mechanism implies that the magnetic field producing the polarisation of R Mon, and the light scattered in the disk, is coupled to the material in the disk surrounding R Mon. So if it is to be possible to change the apparent position angle of the polarisation disk, it is necessary to assume that the projected magnetic field geometry must change, implying that the real magnetic field geometry is not symmetric and is somewhat skew and furthermore is rotating with a period of the order two years. The polarisation position angle of R Mon would also be affected by this mechanism since it is within the confines of the disk. If we assume that the disk is rotating in a Keplerian fashion and that R Mon is at a distance of 700 parsecs, which is a good lower limit on its distance, and also that the mass of R Mon is about $10M_{\odot}$, which is a good upper limit (note that if the mass of the central object is decreased then the Keplerian period will increase), and finally estimate the distance of a “null” point from R Mon to be about 30 arc seconds then we derive an orbital period of almost 1 million years for the disk at this radius. Obviously changes on the timescale of those observed here are impossible under this scenario. For this reason, at least, the *variations* in polarisation of R Mon and the polarisation disk cannot be due to the effect of preferential absorption from grains aligned in a magnetic field as supposed in the model outlined above.

The actual mechanism which produces the variations in polarisation of R Mon and the polarisation disk, must be due to some phe-

nomenon which is on a much smaller scale than that of the polarisation disk itself. Considerable changes can occur on the timescale of a year or two, which must give a lower limit on the size of the region producing these effects. This turns out to be about 3 or 4 astronomical units radius about the star. Deriving an upper limit on the size of the region producing the changes requires an estimate of the period of large scale changes. No study has found a definite period in the variation of luminosity of R Mon or NGC2261. One might attempt a simple approach to estimate the period of the variations (if there is one) by plotting the polarisations measured against time. Such a plot is shown in fig 4.18 for polarisations measured in approximately the wavelength range of a V filter (≈ 0.55 microns), for which most measurements are available. The graph appears to show a periodicity of around 8 years per cycle from minima to minima, although this estimate may not be completely accurate due to the small number of sampling points available; the true periodicity could be much smaller. For a period of 16 years, using the above assumptions, a radius scale of about 14 astronomical units is obtained. So the area within which the changes producing the observed variations in polarisation in this system occur is probably within the region of about 14 astronomical units of R Mon. This is certainly on a much smaller scale than has been resolved at any wavelength to date, corresponding to a region less than 1/100 th of an arcsecond across at the distance of R Mon.

An alternative method for polarising objects embedded within a circumstellar disk was proposed by Elsässer and Staude (1978). The Elsässer and Staude model is said to work when the disk is seen nearly

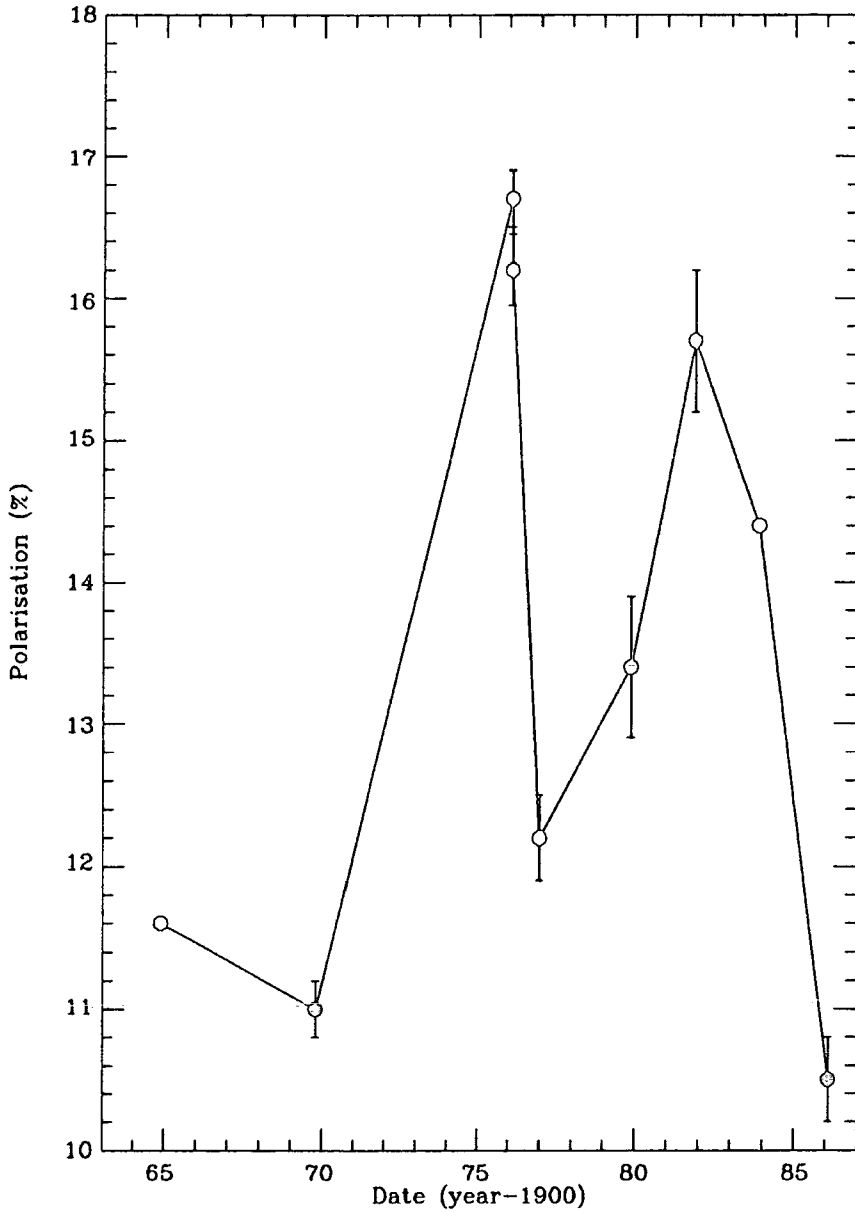


Figure 4.18: Figure showing the variation in polarisation of R Mon, in the range of a V filter ($\approx 0.55\mu$), over the period 1964 to 1986. The values are taken from tables 4.2 and 4.3.

edge-on in such a way that the central object, which is the main source of light, is almost totally obscured from direct view. When this situation occurs the light (or radiation) which is then observed is scattered into the beam of the observer from the poles above and below the central object. Because the scattering geometry is incomplete (ie. does not allow light to scatter into the observers beam from all around the object), the light exhibits a net polarisation, parallel to the disk (fig 4.19). It is this method which is favoured by workers in the infra-red range (see Hodapp (1984), Sato *et al.*(1985)) who have great difficulty in explaining the levels of polarisation they observe in some objects of the same type as R Mon using an aligned grain mechanism.

At least in principle it now seems sensible to use the Elsässer and Staude model for explaining the polarisations which are observed in R Mon. This is because the scale upon which the variations, in obscuration to the polarising lobes above and below the object, have to occur to explain the observation of the variation of polarisation is the inner radius of the disk surrounding R Mon. This dimension may be as small as 30 astronomical units across, as reported by Rodriguez (1987) for both L1551 and β -Pictorus. The mechanism for producing the variations (ie. variable, non-uniform illumination of the polarising lobes) could be episodes of large non-homogeneous accretion from the inner disk onto the protostellar core, which would have a natural timescale of the same order as those seen; simply the orbital period or free-fall time at that distance.

To explain the exact variations of polarisation seen in R Mon

Elsasser and Staude Model

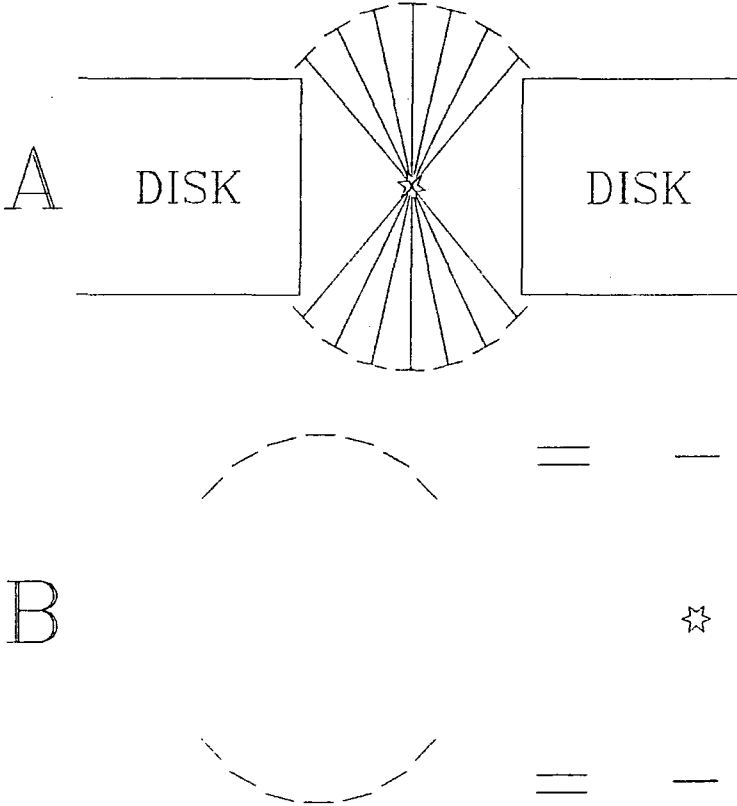


Figure 4.19: A pictorial representation of the Elsässer and Staude model for producing the polarisation of objects embedded within a disk. In A the object is viewed edge-on and light scattered in the areas above and below the disk is only seen. B shows how the resultant of the incomplete scattering geometry in A has a net polarisation parallel to the disk, if it is summed within an aperture enclosing the whole area. Normally only one lobe would be visible.

requires an explanation of the dominant source of light in the inner system, be it from the protostar itself, through energy released by gravitational contraction, or possibly the beginning of thermonuclear processes, or as seems more likely considering the present direction of models to explain the source of energy driving the molecular bipolar outflows, (chapter 3), accretion from the disk onto the protostellar core. However, whatever the actual source of the radiant energy, it is possible to explain the change of polarisation of R Mon by changing the distribution of the light source within the region defined by the inner disk, say by obscuring parts of the protostar or brightening parts as energy is released, possibly by clumpy accretion. Such a scenario of variability of structure close to R Mon has long been considered possible as the only satisfactory mechanism to explain the variations in apparent structure of NGC2261 as seen by Hubble (1917), Johnson (1966) and many others.

An explanation of the variability of the position angle of the polarisation disk follows naturally from such a model of the polarisation of R Mon. Regions to the east and west of R Mon cannot now see the source of light directly, the light which now reaches them is the light which has been scattered in one polar (polarising) lobe of the disk. Therefore any light which is subsequently scattered into the beam of any observer is already partially polarised approximately in the plane of the disk, and thus when it is scattered the resultant observed polarisation is simply a superposition of the polarisation in the plane of the disk with the polarisation in the scattering plane (ie. the normal centrosymmetric pattern of polarisations). This could, in principle, result in a pattern of

polarisations similar to that observed.

At second glance, however, such a scenario is not as obvious as it might seem. If we consider a particle at the edge of the disk the light which is incident upon it is polarised in the plane of the disk (as it would be if the particle were at the front of the nebula), but to achieve the desired result, that the incident polarisation is superimposed upon the scattered polarisation (perhaps producing a null point), we must assume that the incident plane polarised light scatters into the observers beam in the same plane as the incident light, ie. as in fig 4.20. This is not an obvious conclusion to draw and becomes less clear if one considers a particle *not* in the plane of the disk, where it is not readily apparent how a incident plane polarised wave will scatter and how its incident plane of polarisation will effect the outgoing wave.

To get a “feeling” for these processes it is necessary to approach the details of the phenomenon of scattering. Notni (1985) has attempted such a basic analysis of the scattering of polarised light, and his results will be re-interpreted here. To enable his interpretation Notni has used a parameterisation of the properties of scattering by interstellar grains which is described by White (1979). Basically White has used the grain types (graphite and silicates $\sim 50 - 50$) and size distribution ($N(a)=Ca^{-3.5}$ for $0.005 \leq a \leq 0.25$ microns, $N(a)=0$ otherwise), which Mathis, Rumpl and Nordsieck (1977) found gave the best fit to the extinction properties of the interstellar medium. For this grain distribution and type, White has calculated the matrix parameters (and other values) which describe the scattering of light. After calculating

the matrix parameters at a range of wavelengths White has found a set of functions which fit the parameters sufficiently well to allow simple analyses to be made. Using the parameterisations which White has described for scattering at 110 nm, Notni has calculated how the incident polarised light is expressed in the outgoing wave (in particular which direction it scatters into) and thus how its effects are shown in the resultant observed polarisation.

The scattering geometry is shown in fig 4.21. The particle is at point P. The incident light is polarised in the plane yz which will be referred to as the symmetry plane, in which the disk lies. The angle ϕ is the angle as viewed by the observer, θ is the scattering angle. Also fig 4.21(b) shows how the incident light polarisation is projected onto the directions l and r , the angle α being the projection angle. To help clarity Notni has divided the incident light into two components, an unpolarised part ($I_1 = (I', 0, 0, 0), I' = I(1 - p_o)$) and a completely linearly polarised part ($I_2 = (I'', I'' \cos 2\alpha, I'' \sin 2\alpha, 0), I'' = Ip_o$), which are subscripted 1 and 2 respectively in the following equations. The scattered intensity is I_s and the linear polarisation parameters, Stokes Q and U (for the purposes of this argument circular polarisation will be ignored). So we have:-

$$I_{s1} = H(\theta)I(1 - p_o)(1 + \cos^2(\theta))$$

$$Q_{s1} = -pH(\theta)I(1 - p_o)(\sin^2(\theta))$$

$$U_{s1} = 0$$

where:-

$$H(\theta) = P1/(1 + \cos^2(\theta)) \text{ with } P1 = (1 - g)/(1 + g^2 - 2g\cos(\theta))^{3/2}.$$

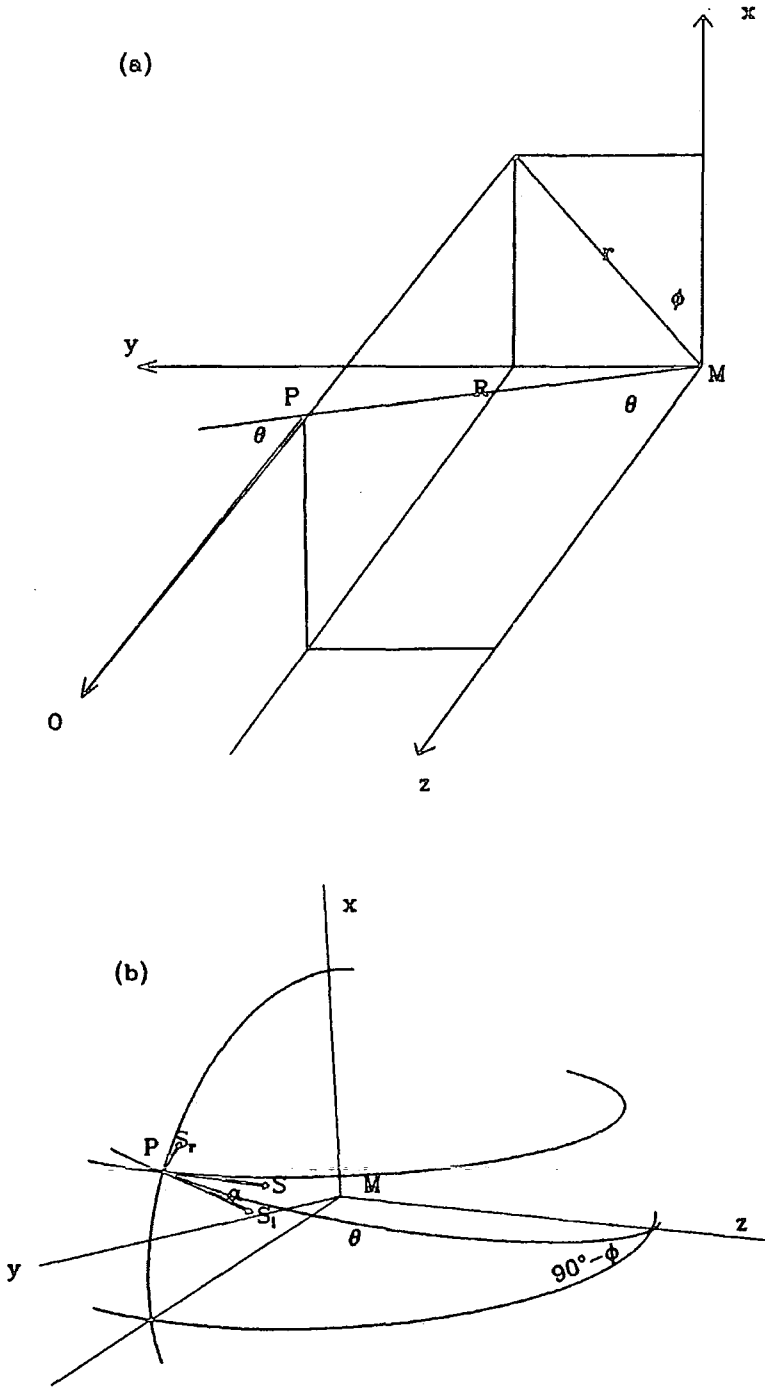


Figure 4.21: The scattering geometry, vector S is the incident polarisation.

g is the mean cosine of the scattering angle, which determines how forward-scattering the phase function is, I is the incident intensity, p_o is the degree of the incident polarisation, θ is as defined in fig 4.21, p is the peak polarisation of the grain mixture (usually at about $\theta = 90$ degrees). So we have:-

$$\begin{aligned} \tan(2\alpha_{s1}) &= (U_{s1}/Q_{s1}) = 0 \\ \Rightarrow \alpha_{s1} &= \pi/2 \end{aligned}$$

and we see that the unpolarised component is scattered and polarised by degree $|Q_{s1}|$ in a direction perpendicular to the plane of scattering (defined by MPO) which would produce the normal centrosymmetric pattern of a reflection nebula ie. the polarisation would be directed normal to the radius vectors from the star (source). For the scattering of the polarised component we have:-

$$\begin{aligned} I_{s2} &= H(\theta)Ip_o(1 + \cos^2(\theta) - p\cos(2\alpha)\sin^2(\theta)) \\ Q_{s2} &= H(\theta)Ip_o(\cos(2\alpha)(1 + \cos^2(\theta)) - p\sin^2(\theta)) \\ U_{s2} &= H(\theta)Ip_o2\sin(2\alpha)\cos(\theta) \end{aligned}$$

where:-

$$\begin{aligned} \sin(2\alpha) &= (2\cos(\theta)\tan(\phi))/(\tan^2(\phi) + \cos^2(\theta)) \\ \cos(2\alpha) &= (\tan^2(\phi) - \cos^2(\theta))/(\tan^2(\phi) + \cos^2(\theta)) \end{aligned}$$

therefore:-

$$\begin{aligned} \tan(2\alpha_{s2}) &= U_{s2}/Q_{s2} \\ &= \frac{2\sin(2\alpha)\cos(\theta)}{\cos(2\alpha)(1 + \cos^2(\theta)) - p\sin^2(\theta)} \\ &= \frac{4\cos^2(\theta)\tan(\phi)}{(\tan^2(\phi) - \cos^2(\theta))(1 + \cos^2(\theta)) - p(\tan^2(\phi) + \cos^2(\theta))(1 - \cos^2(\theta))} \end{aligned}$$

for Rayleigh scattering we have that the peak polarisation p is unity and we find that:-

$$\begin{aligned} \tan(2\alpha_{s2}) &= -\tan(2\phi) \\ \Rightarrow \alpha_{s2} &= \pi/2 - \phi \end{aligned}$$

which implies that the polarised component remains 100 percent polarised in the symmetry plane (ie. yz), as it was before scattering. In such a situation the polarised light from a central source scatters as shown on fig 4.22. This represents a good starting point from which it is possible to get a feel for how the polarised component of light will scatter and hence effect the resultant (observed) polarisation.

For non-Rayleigh scattering $p < 1$, the change in the position angle of polarisation of the polarised component is towards the plane of scattering ie. towards the radius vector from the source, which is away from the direction in which the polarisation induced in the unpolarised component lies. This is shown in fig 4.23; a series of curves for values of p and different ϕ 's for each θ from 0 to 180, of the polarisation angle of the polarised component referred to the symmetry plane (defined by 90 degrees- ϕ). The largest discrepancies occur near scattering angles of 90 degrees and intermediary ϕ 's. The polarised intensities of the two scattered components actually determines how the incident polarisation is seen in the final polarisation. Fig 4.24 shows the ratio of the two polarised components. It appears that for small scattering angles that the polarised intensity of the 2nd component is very nearly dominant.

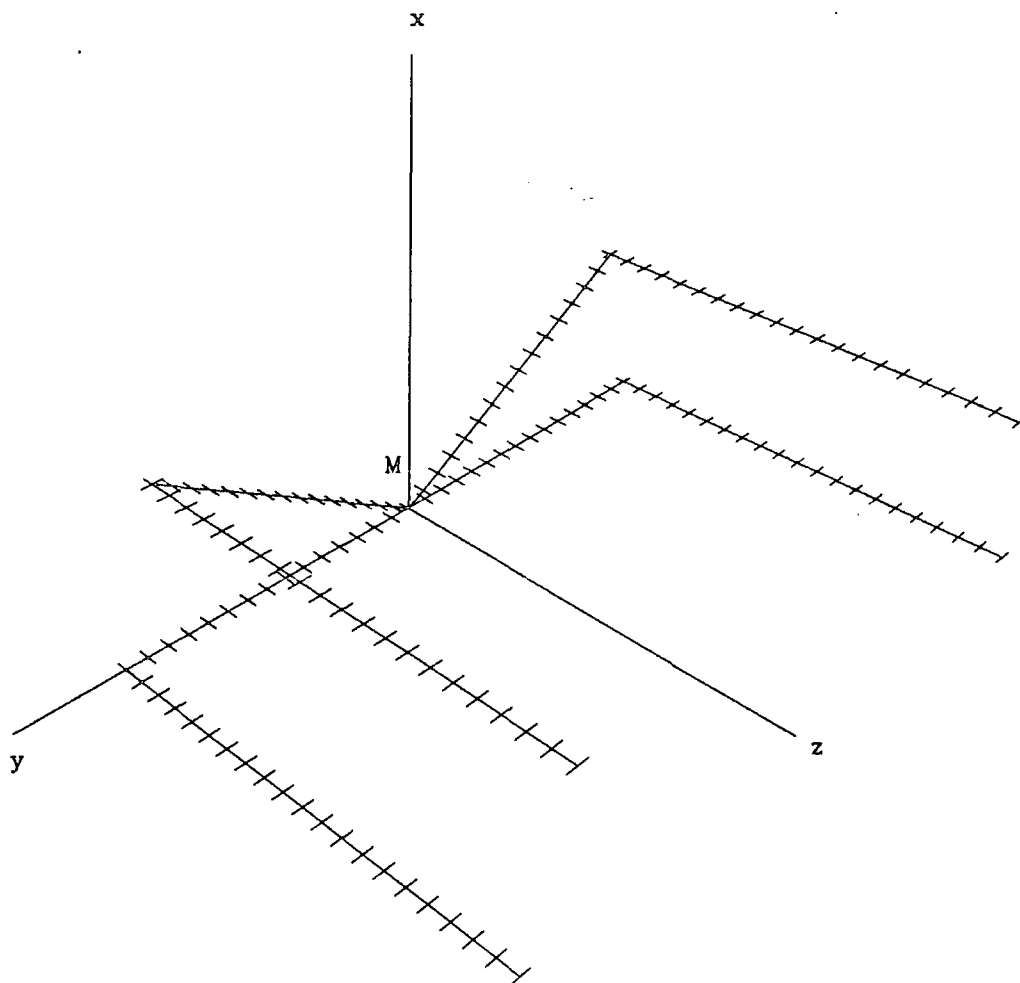


Figure 4.22: Representation of how incidently polarised light scatters in and above the plane of the disk, the outgoing polarisations are parallel for both examples (note that for Rayleigh scattering the outgoing polarised intensity is zero).

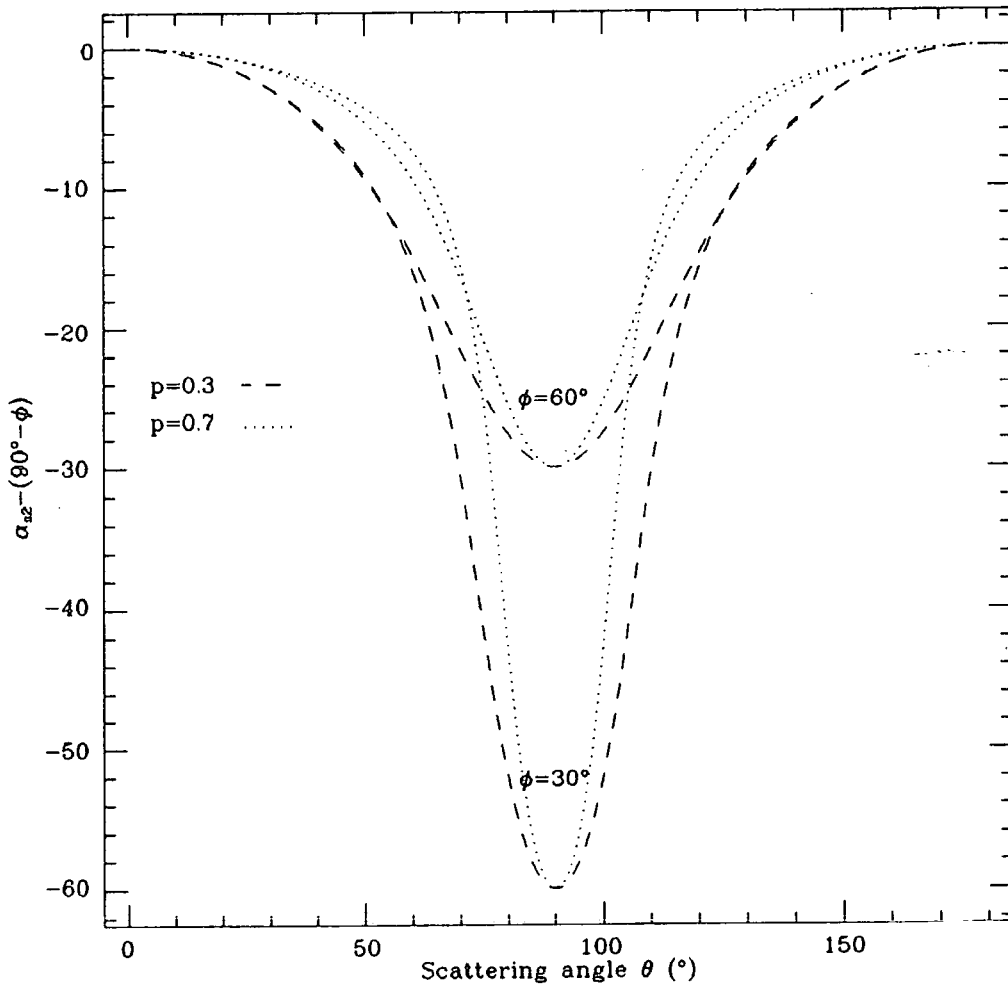


Figure 4.23: The deviations of the polarisation angle of the scattered polarised component (α_{s2}) from the plane of symmetry ($90^\circ - \phi$), for the range of scattering angles (θ).

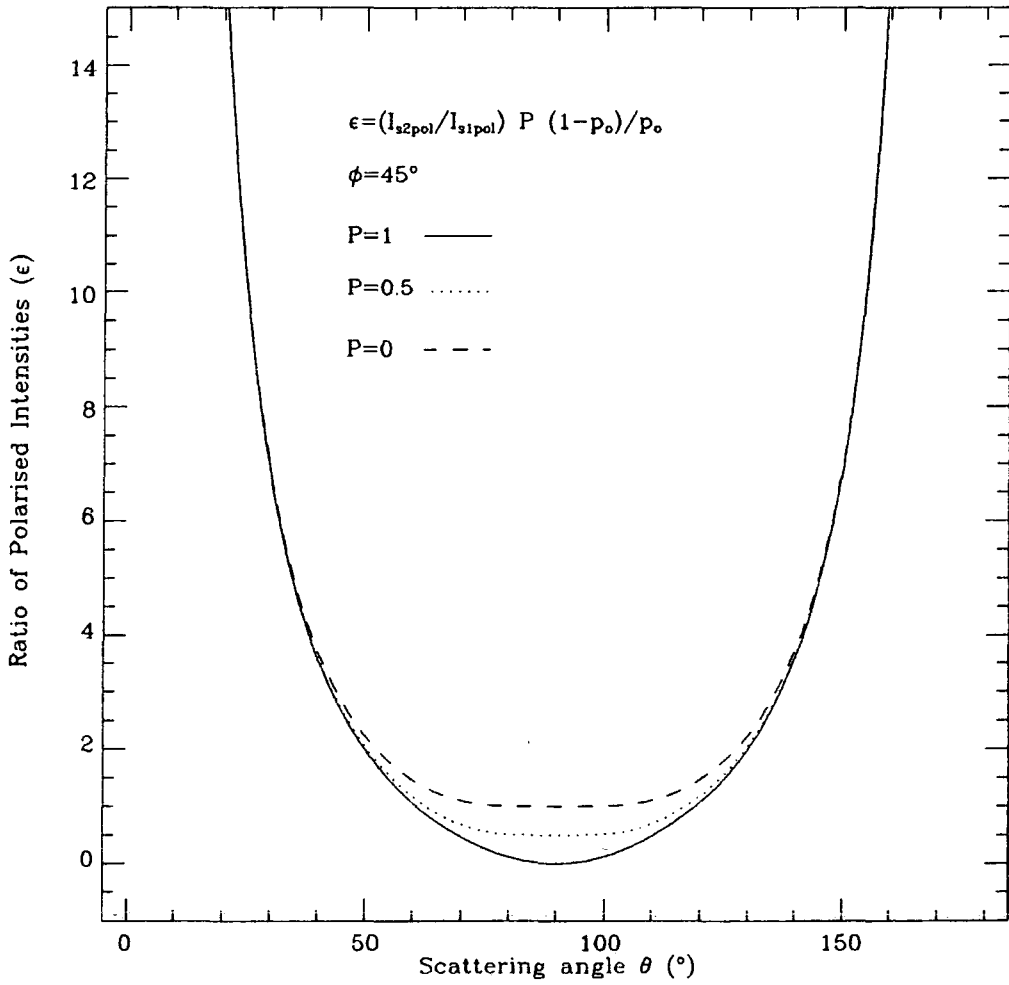


Figure 4.24: The ratio (ϵ) of the scattered polarised intensities, I_{s2pol} and I_{s1pol} .

Notni (1985) goes on further to show that it is possible to produce a polarisation pattern which is elliptical about the source if a spherical dust density is used. The elliptical pattern is particularly pronounced if the scattering is forward biased or non-Rayleigh, both effects expected to be observed in a nebula model such as that outlined here. He further shows that if a geometry is imposed (ie. the range of scattering angles is limited), which has a toroidal configuration then the polarisation vectors tend to run parallel to the source polarisation in a considerable portion of the nebula.

In conclusion the main points concerned with the scattering of polarised light are that:-

1. it mainly scatters into the observers beam in the plane of symmetry;
2. it scatters towards the radial vectors from the source at intermediary scattering angles and ϕ 's;
3. that the incident polarisation scatters with the largest polarised intensity for small scattering angles.

All this is, however, only true for wavelengths near 110 nm and extrapolation into the range of wavelengths used here cannot be made without some justification. Support for this extrapolation being reasonable is found in the polarisation maps shown here covering the range 0.55 to 1 micron approximately, which do not show any discontinuous changes in the structure of the disk, and so one would not expect any similar effects in the extrapolation. Also, other works concerning similar objects

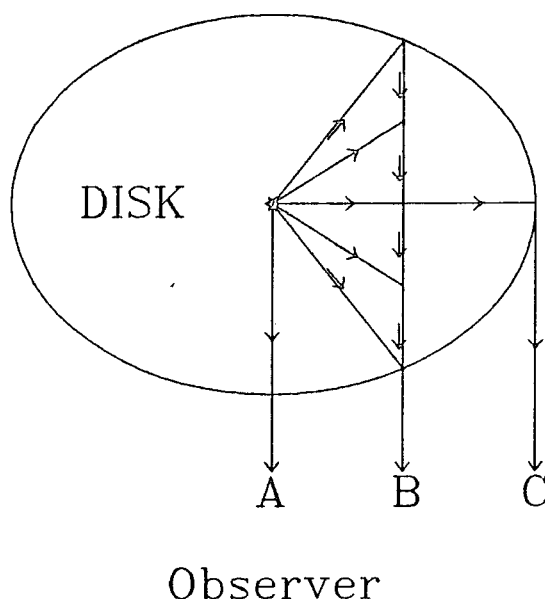


Figure 4.25: A series of scattering paths through the disk.

showing evidence for polarisation disks which are taken into the blue do not show any such irregular effects either. White (1979) also notes that incident polarised light which is not in, or perpendicular to, the scattering plane (skew polarisation) does not show any marked change in scattering properties from 100nm to 346 nm supporting the supposition that the above arguments can be naturally extended into larger wavelengths, at least for this component.

A schematic of the proposed scattering mechanism for producing the polarisation disk seen across the head of the nebula is displayed in fig 4.25. It shows the propagation of a series of light paths from the polarising regions through the disk. Consider path A; initially any light

travelling this path shows the polarisation as produced in the polarising region. Path B shows a series of light paths each of which arrive in the observers beam as originating from the same point on the surface of the disk. However, in this case the polarisation observed is changed from that of path A. A summation of the polarisations produced through the range of scattering angles along this path produces a smaller polarisation, particularly since the intensity of the scattered light is biased towards the forward scattering angles (ie. in this case light scattered near the front of the disk). Combining this small polarisation with the polarisation of the light originating in the polarising regions produces an end polarisation which is non-zero and is directed the same as the incident polarised light ie. parallel to the source polarisation. In path C only light which is scattered through 90 degrees, at which angle the induced polarisation is at a maximum, is seen. This high polarisation, when combined with the scattered polarisation of the incident flux, will produce either a polarisation at right angles to the incident polarisation, if the polarised intensity produced by scattering is a larger value than that which the incident polarisation has when scattered, or even a “null” point if the polarised intensities are equal. Certainly one would expect a “null” point somewhere between B and C, provided the maximum polarisation which can be produced by scattering is larger than the polarisation of the source.

More detailed evidence that the position angle of the polarisation disk is dependent on the polarisation of R Mon is found on more careful examination of the I band polarisation data, which covers a period of 13 months. The results from measuring the position angle of the polar-

Table 4.4:

I band polarisation disk position angles		
Dataset	Disk Position Angle	Star Polarisation Position Angle
Feb 85	109(± 2)	109.6(± 1)
Dec 85	102(± 4)	104.5(± 1)
Mar 86	105(± 1)	105.7(± 1)

isation disk, as accurately as possible, show that this value is directly correlated to the position angle of the R Mon polarisation (table 4.4 and figs 4.26, 4.27 and 4.28) . At a distance of 700 pc, the approximate radius of the polarisation disk (~ 30 arcsecs) corresponds to about $1/3$ of a light year, so it seems that these changes must propagate at a considerable fraction of the speed of light.

Figures 4.26, 4.27 and 4.28 show close up polarisation maps of the head of the nebula together with a line giving the position angle of the polarisation disk. The variation of the polarisation disk is visible particularly between the February 1985 I and December 1985 I datasets in which the change in position of the eastern null point is very clear (it changes by about 5 arcseconds east and 2 arcseconds north during this time), although as might be expected from the relative exposure times (table 4.1) the March 1986 I map is by far the least noisy. These maps also allow the examination of the detailed variation of polarisation in the polarisation disk. Above each map a “vector flow diagram” is shown. Simply, this represents a series of lines which, from the same

R Mon/NGC2261 Feb85 I Data

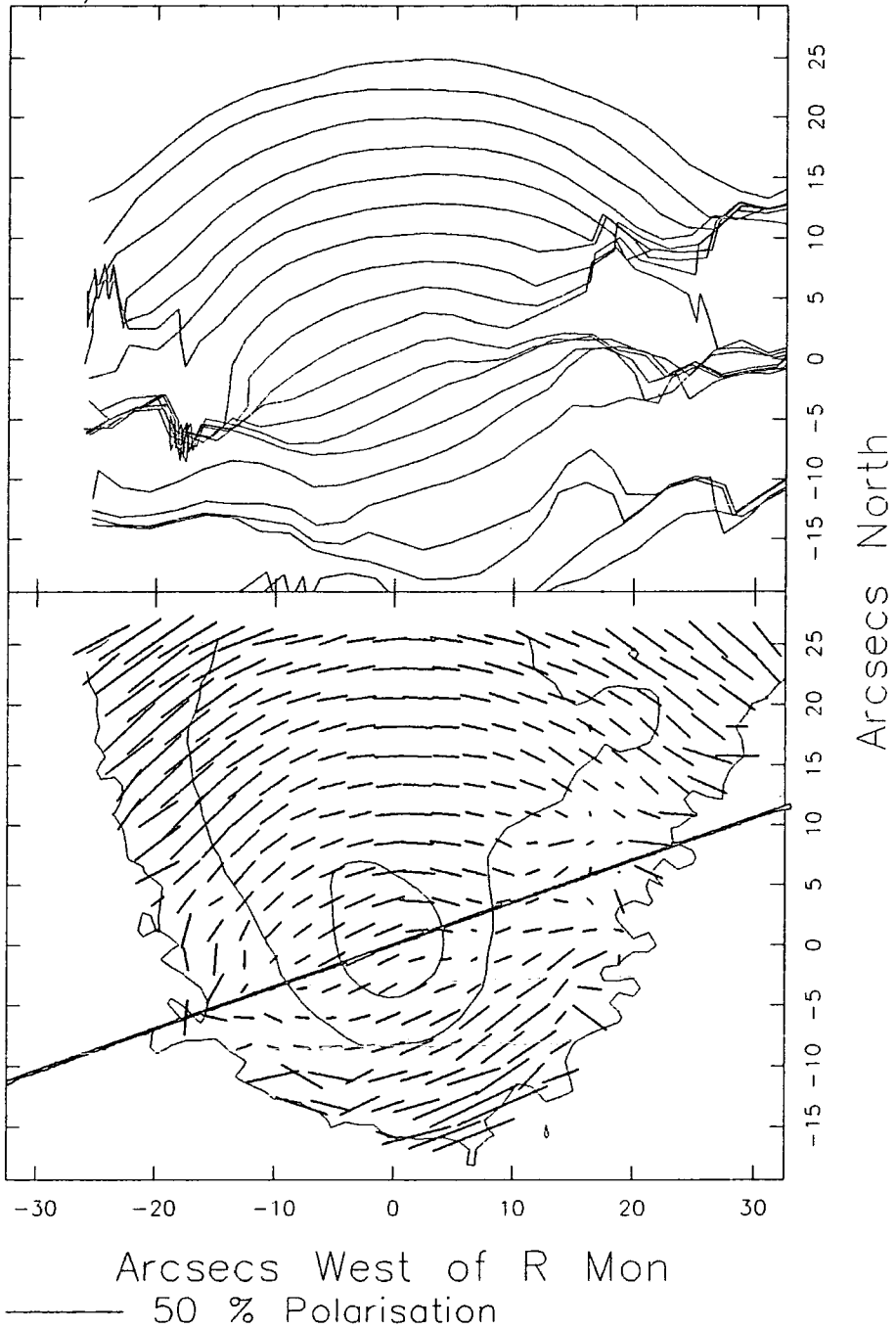


Figure 4.26: An I band polarisation map of the head of NGC2261. The polarisation integration bins are 3 pixels square ($3.6''$). The line drawn indicates the position angle of the polarisation disk, it is centered on R Mon (brightness peak). Above the polarisation map a vector flow diagram is shown.

R Mon/NGC2261 Dec85 I Data

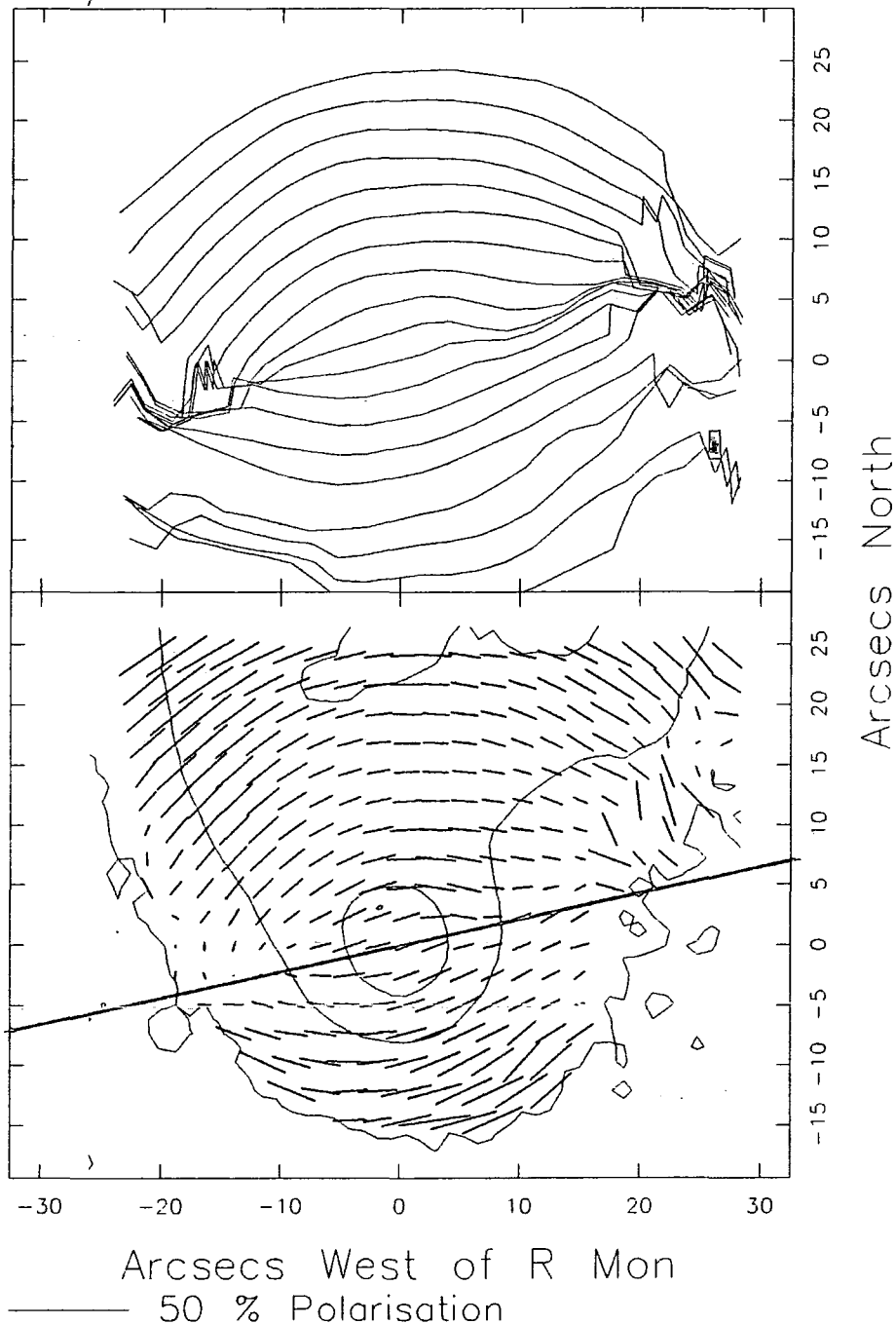


Figure 4.27: An I band polarisation map of the head of NGC2261. The polarisation integration bins are 3 pixels square (3.6"). The line drawn indicates the position angle of the polarisation disk, it is centered on R Mon (brightness peak). Above the polarisation map a vector flow diagram is shown.

R Mon/NGC2261 Mar86 I Data

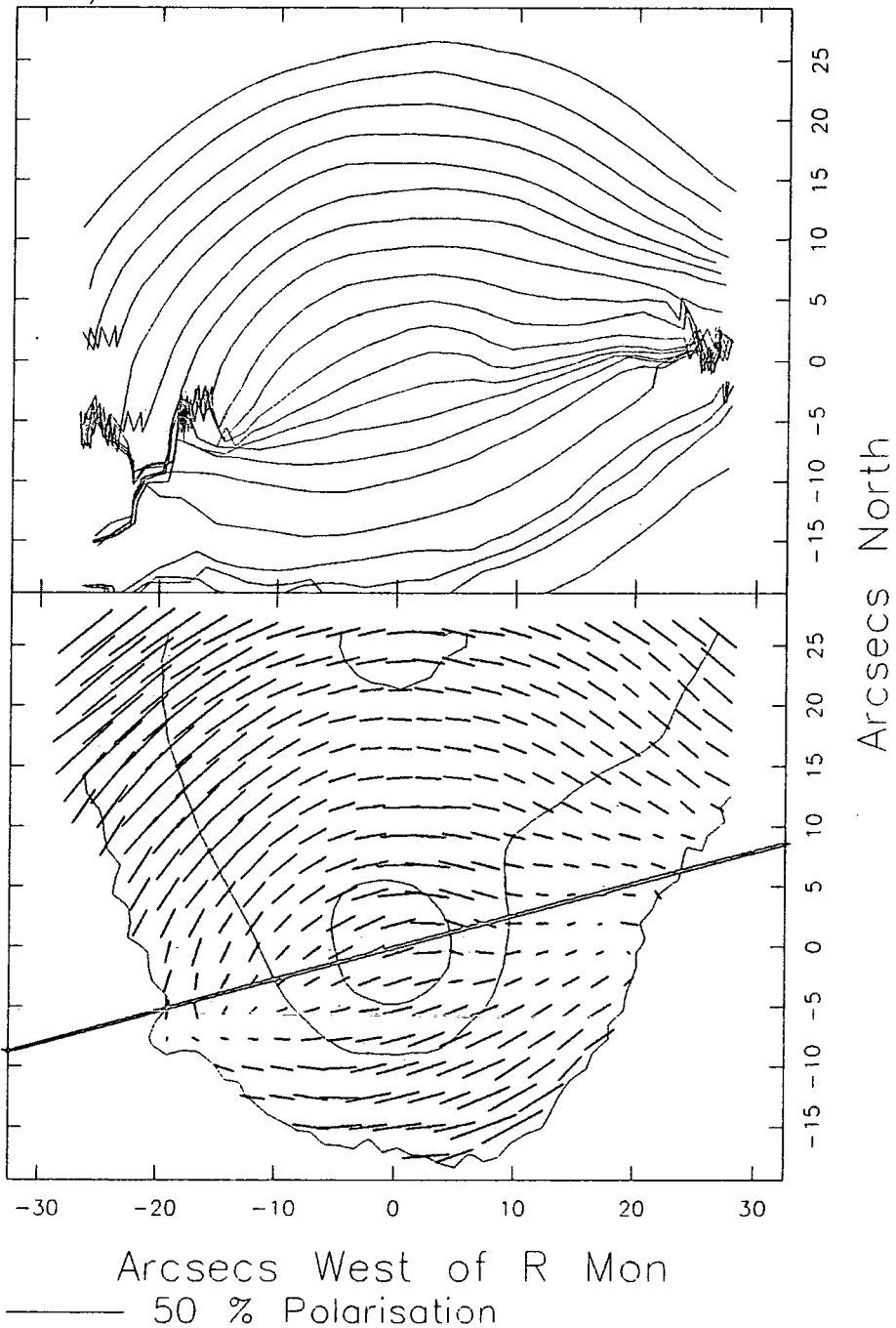


Figure 4.28: An I band polarisation map of the head of NGC2261. The polarisation integration bins are 3 pixels square ($3.6''$). The line drawn indicates the position angle of the polarisation disk, it is centered on R Mon (brightness peak). Above the polarisation map a vector flow diagram is shown.

starting points, travel a specified distance along the directions defined by the polarisation position angle at each point and then step the same distance again in the direction defined at the new point. Such a trace of the vector flow should be a circle in a centrosymmetric pattern. In an elliptical pattern such a trace should enable the definition of the ellipticity of the pattern.

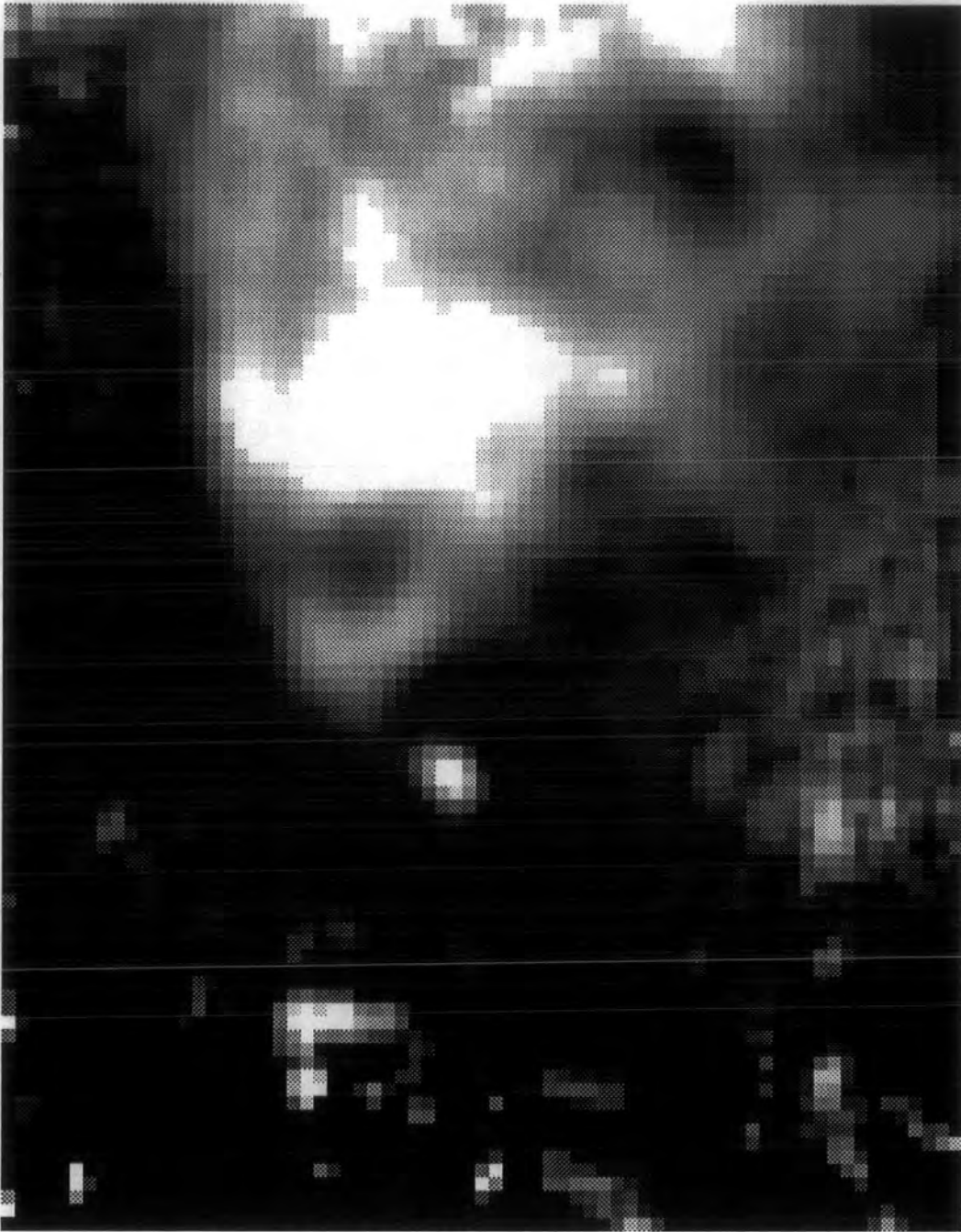
If the patterns of polarisation observed in the maps were as in the simple symmetric case outlined above for the scattering of light from an essentially polarised source, they would be expected to be elliptical patterns. Clearly the patterns shown in figs 4.26, 4.27 and 4.28 are not so. Hence to properly justify the model just described we need to explain the differences. In the north western quadrant of the figures the pattern flattens much more than would be expected, this is shown in how the vector flow traces pinch together instead of running parallel as in the north eastern quadrant. Within the proposed model it is possible to explain these effects as due to a very different scattering geometry between the two quadrants. The north eastern quadrant has a much higher polarisation suggesting that the range of scattering angles is more restricted than in the north western quadrant and also that the scattering is probably less forward than the north western quadrant. So we might expect less effect due to the polarisation of the incident light. Conversely, in the north western quadrant the low(er) polarisations indicate that the range of polarisation scattering angles is larger and/or that the scattering is limited to forward scattering angles, which would dominate in either case. Hence we would expect the polarisation of the incident light to have a large effect, so we would have an increased

flattening of the pattern in this quadrant. These conclusions are in accordance with the relative colour measures (R-I) shown in image form in fig 4.29, which clearly shows an apparent break in the extinction in the area of higher polarisations. It thus seems as if the details of the variations in polarisation disk can be explained in terms of the geometry and distribution of material within the disk, assuming the model outlined.

Unfortunately, for such a simplistic interpretation, it is clear that the null points in figs 4.27 and 4.28 are not along the line defined through the brightness peak, associated with R Mon (although this is certainly not R Mon in actuality). This is not predicted by the simple model used here, but the null points are along the line in the February 1985 data (fig 4.26). It seems impossible to conceive of a modification of the model, either using the time variability of the polarisation of R Mon, as it propagates through the nebula (disk), or by including a second polarising mechanism (such as a magnetic field). Perhaps this problem can be clarified by a proper rigorous scattering model of a nebula of this type.

4.4.3 The wavelength dependency of the polarisation of R Mon.

The wavelength dependency of polarisation of R Mon is known to be variable (Zellner (1970)), the general trend has been observed to be flat or increasing into the infra-red with increasing position angle of polarisation (ie. anti-clockwise rotation) also into the infra-red. This



↑
R Mon

Figure 4.29: An R-I greyscale image of NGC2261/R Mon.

Table 4.5:

Polarisation measurements of R Mon				
Filter	V	R	I	Z
Polarisation (%)	10.6	10.7	11.6	12.4
Position Angle	92.3	96.5	104.3	106.5

is confirmed by an assembly of the data presented here with the least time between measurements, which is found in table 4.5. The range in time between measurements being from December 1985 to January 1986. The trend of measurements is definitely up, with percentage polarisation increasing from 10.6 in the V and R bands to 12.4 in the Z band. The position angle rotates anti-clockwise by some 14 degrees over this range.

These variations in themselves tell us very little about the mechanism of polarisation of R Mon. A suitable variation of the many parameters in both the scattering (Elsässer and Staude) model and in the preferential absorption model (Davis-Greenstein), or indeed an admixture of both could easily account for these variations.

If the range of measurements is extended well into the infrared, various authors (Jones and Dyck (1978), Sato *et al.* (1985)) have noted that the polarisation of R Mon decreases to as little as 4 per cent at 2.2 microns. Their subsequent interpretation of the cause of this reduction is that as the wavelength of the emitted radiation increases, the amount of unpolarised radiation which can be seen from the central

source increases as the optical depth of the disk decreases, thus diluting the scattered flux. In principle this effect could also be explained by the aligned grain theory using a modified Serkowski law such as those proposed by Wilking *et al.* (1980), but Hodapp (1984) has attempted this analysis on other similar systems and finds that the form of the Wilking *et al.* law does not fit the data. Perhaps more significantly Hodapp and Sato *et al.* (1985) both find examples of similar objects whose degree of polarisation is increased well into the infra-red; this observation is very difficult to reconcile with the aligned grain theory.

4.4.4 The $H\alpha$ polarisation of NGC2261/R Mon.

The $H\alpha$ map (fig 4.10) of polarisation taken by the author has a nature almost identical to that of the much broader band R measurements, except for a spurious reflection effect which unfortunately coincides with the position of the south western linear feature. This result supports the reflection nature of the nebula, eliminating any sources of significant $H\alpha$ emission within the main nebula body. Closer inspection of the polarisation of R Mon itself poses some interesting questions, which have some very relevant but speculative answers, mainly in favour of the polarising mechanism described above.

Simply the $H\alpha$ polarisation of R Mon is measured to be depolarised with respect to the continuum measurement. This result is not new and has been noted by both Garrison and Anderson (1978) and Aspin, McLean and Coyne (1985). Their results show that the

$H\alpha$ polarisation is some 3 percent less than the the continuum (a 3 percent difference is seen in both examples, even though the degree of polarisation is different, ie. Garrison and Anderson find the R band to be polarised at 16.4 percent at 103 degrees and Aspin, McLean and Coyne find R to be polarised at a level of 12.7 percent at 103 degrees, but their $H\alpha$ measurements are 13.19 percent at 106 degrees and 9.6 percent at 110 degrees respectively) and slightly rotated. This compares with the $H\alpha$ measurements presented here of 9.9 percent at 92 degrees and R band value of 10.6 percent at 96.5 degrees, but there is a time interval between the two measurements of about 2 months, and they may not be representative of the actual difference at a specific time, in view of the variations in the broadband measurements of R Mon.

Aspin, McLean and Coyne (1985) were forced to conclude that the $H\alpha$ polarisation of R Mon could only be explained in terms of a multiple superposition of polarising mechanisms. However, in view of the arguments presented above, a rather more simplistic solution to these problems becomes apparent. Consider the situation shown in fig 4.30, in which two extremes of the Elsässer and Staude model of polarisation are shown together with a crude representation of the recombination front near the protostellar core, from within which the $H\alpha$ line emission originates.

In case 1, one can see that the $H\alpha$ flux polarisation must be approximately the same as the continuum, a situation which is not observed. In case 2 a completely different situation exists. The polarising regions lie within the recombination front, and thus the $H\alpha$ polarisation

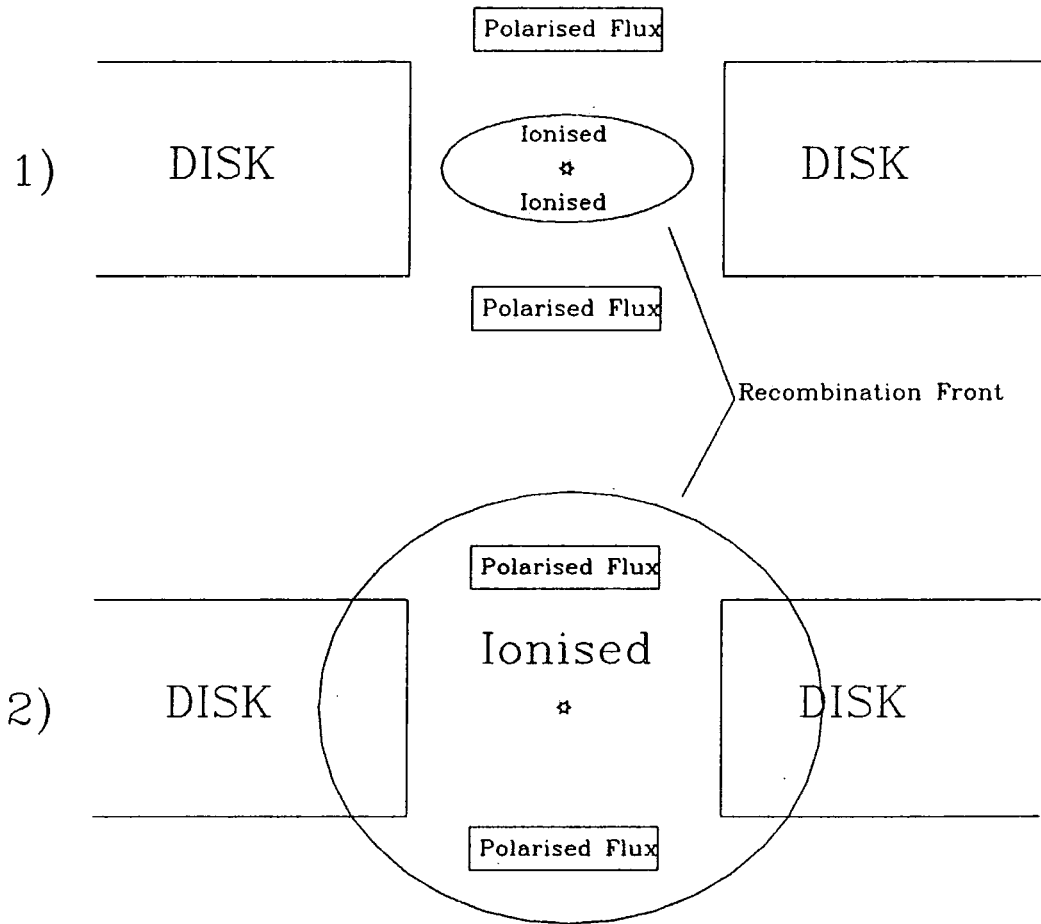


Figure 4.30: Representation of the Elsässer and Staude model showing two extremes for the position of the recombination front.

would be due only in part to the polarising effects of the Elsässer and Staude model. This then allows the $H\alpha$ polarisation to have a multiple origin if the flux subsequently passes through a screen of aligned grains. Furthermore this interpretation also allows an upper limit to be imposed on the interior size of the disk, since it now must lie within the recombination front, or nearly so, and an estimate of the size of the polarisation source. Pudritz and Norman (1986) use a recombination front diameter of size 10^{15} cm, about 66 astronomical units ($\approx 1/100$ arc second at 700 parsecs), so it seems reasonable to suppose that the polarisation source is of this order of magnitude also. This corresponds well with the inner scale of disks proposed by Rodriguez (1987), about 30 astronomical units radius. This is the inner region associated with possible planetary formation, and also correlates with the size of 14 astronomical units for the size of the inner scale of the disk on the basis of the timescale of variations of polarisation, proposed earlier in this work.

As a final word on the $H\alpha$ polarisation of R Mon, a somewhat curious interpretation of the $H\alpha$ measurements of Aspin, McLean and Coyne suggests itself to the author. Aspin, McLean and Coyne, claim to have separated the polarisation of the $H\alpha$ spectral line itself from the continuum by their spectropolarimetry. They derive a polarisation for the spectral line of 5.6 percent at 168 degrees, which they attempt to interpret in terms of the extinction to R Mon and in other unsuccessful ways. The extinction to R Mon is estimated to be 2-3 magnitudes in V (Aspin, McLean and Coyne (1985) and Cantò *et al.* (1981)), which would give an apparent polarisation of 6-9 percent using the average

relationship of 3 percent per magnitude of extinction in V, if it were polarised via aligned grains as in the interstellar medium. The position angle of interstellar polarisation near R Mon is about 170 degrees, and thus, as noted by Aspin, McLean and Coyne, the H α polarisation bears an interesting correlation to the interstellar field direction. Say if the H α flux is originally *unpolarised*, the polarisation after it passes through 2-3 magnitudes of aligned grains could easily be 6 percent, which would account for the degree of polarisation of the H α spectral line. But what about the position angle? If the field direction in the disk surrounding R Mon was pretty much parallel to the interstellar field direction then that could possibly account for the degree of polarisation *and* the position angle of the H α spectral line. This field direction would be the same as those in the models of Pudritz and Norman (1986) (see figures 3.6 and 3.7) and not the toroidal field proposed in the corresponding Shibata and Uchida (1987) model.

4.4.5 Variation of polarisation in the main nebula body.

As was originally noted by Warren-Smith, Draper and Scarrott (1987(a)), the polarisation within the main nebula body of NGC2261 shows considerable, consistent, variations from centrosymmetry, which these authors interpreted as due to the presence of a large scale magnetic field within the nebula. They also noted that the polarisation vectors within the nebula rotated in the opposite sense to that of R Mon, and on this evidence ruled out a polarised source as the cause of the large scale variations.

Given the evidence outlined in the discussion of the polarisation of R Mon and the polarisation disk above, it now seems unlikely that the nebula will not exhibit some effects due to the effective polarisation of R Mon as viewed from within the nebula. However, before inspecting the nebula polarisations for any such effects it may be informative to predict the effects that might be observed.

Within the model proposed it is expected that the polarisation of the source as seen within the nebula will vary with azimuthal distance (see fig 4.31) as the scattering angle θ varies and the polarisation of the incident light increases as θ increases. Additionally there must be an angle θ such that the source of light (ie. the real R Mon) becomes visible to the nebula, in an extreme case this would of course be only on the nebula axis.

Consider a point such as B (fig 4.31) on the front edge of the nebula which is receiving light scattered in the polar regions above R Mon. In the symmetric case the plane of polarisation of the incident light will be parallel to the polarisation expected from any unpolarised light scattered at this point. Therefore a first prediction that can be made on the basis of this model is that there must be a line through the nebula perpendicular to the polarisation vector of R Mon (as viewed from any direction), along which the polarisation vectors are all perpendicular to this radius. This effect will not be changed by varying the scattering geometry, ie. if the light is scattered from the front or back edge of the nebula, as this would only change the degree of polarisation, not its orientation.

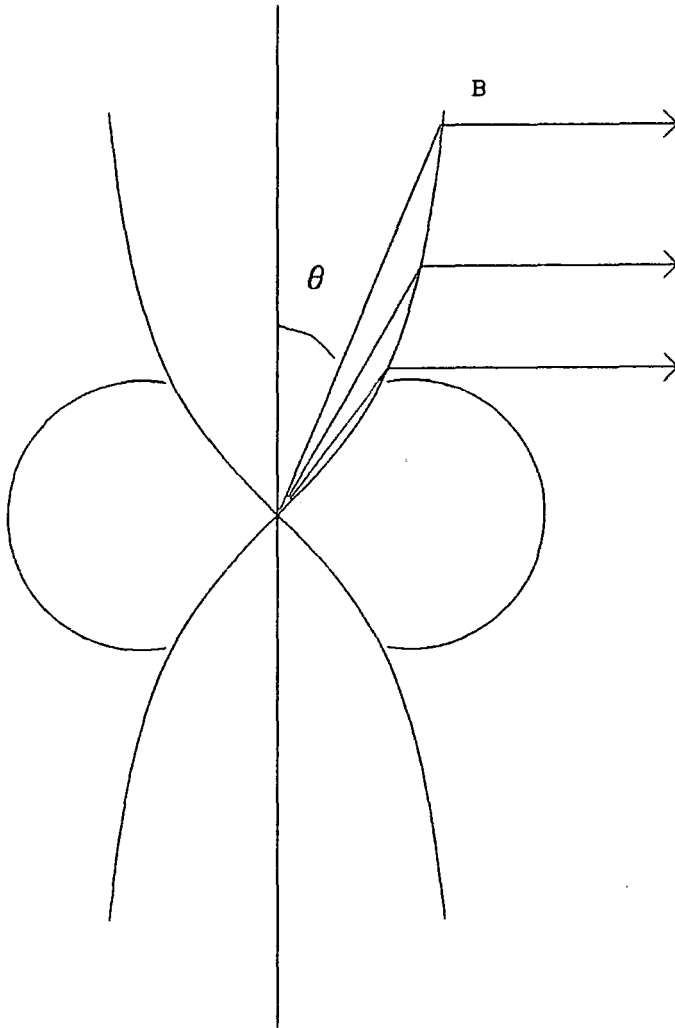


Figure 4.31: The scattering of light within the nebula. As θ increases the degree of incident polarisation increases.

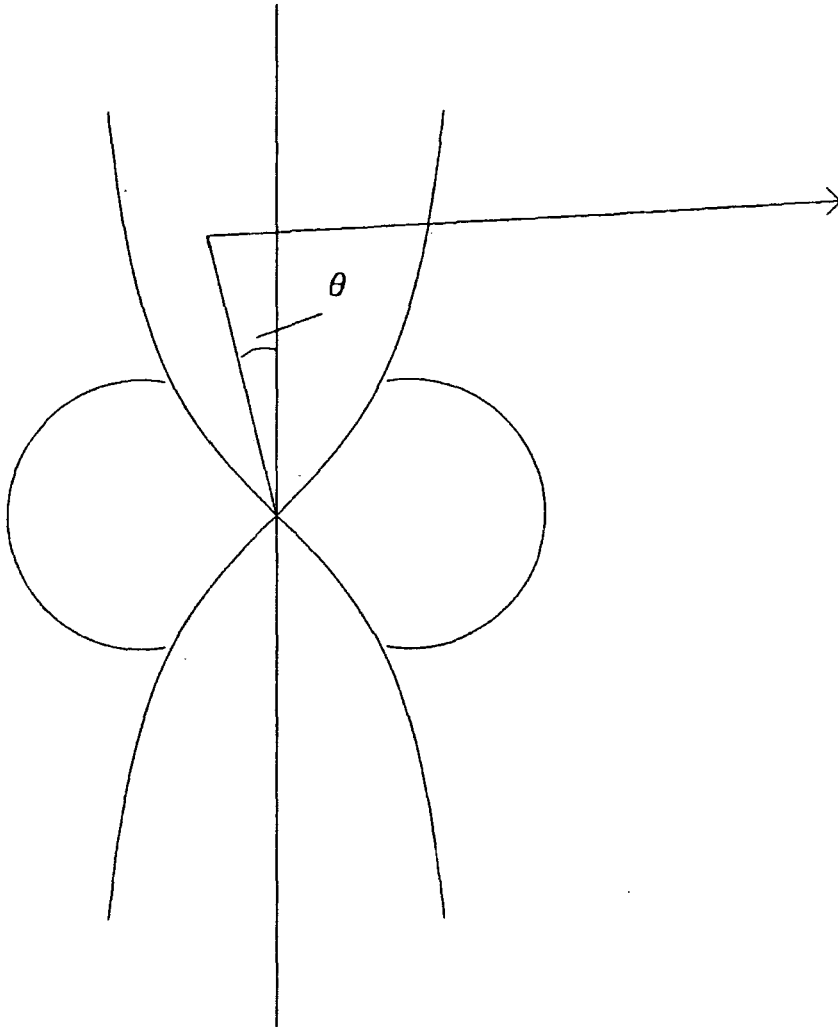


Figure 4.32: The scattering of light within the nebula. As θ increases the degree of incident polarisation increases.

In fig 4.32, light is scattered from the edge of the nebula. The incident light is polarised in the same plane as the disk (or the light observed from R Mon) and when it is scattered into the observers beam we have a situation similar to that discussed for the polarisation disk where the polarised light is scattered nearly in the plane of symmetry (ie. the plane defined by the incident polarisation vector and the line joining to the observer). In the symmetric case (and with Rayleigh scattering) this will be parallel to the polarisation of R Mon. The resultant polarisation would therefore be a superposition of the scattered incident light changed by its scattering, which may include a rotation towards the radial direction, and the normally scattered component. This superposition will tend to produce a flattening of the centrosymmetric pattern, a flattening in the sense of the polarisation of the source.

In summary the effects expected in the change of nebula polarisation due to a polarised source of the type outlined here, are a general flattening of the polarisation pattern, which should be symmetric about the line perpendicular to the polarisation vector of R Mon.

Figures 4.33 and 4.34 show a pattern of polarisation vectors around R Mon, which are calculated from the December 1985 R Band and February 1985 I Band datasets, chosen because they had the largest complete spatial coverage. The measurements were made along radii extending from R Mon. The vectors are drawn on a web of radii and circles which would define directions perpendicular and parallel to any polarisation vectors in a perfectly centrosymmetric pattern. The purpose of this web is to give a reference pattern upon which the centrosymmetry

of a particular vector can be directly assessed. Looking closely at the patterns it is apparent that the polarisation vectors on the edges of the nebula are flattened and as such, seem to deviate from centrosymmetry in a fashion similar to the model just described. So a cursory glance at the data seems to indicate that the deviations from centrosymmetry are in fact due to the effects of a polarised source on the light scattered in the nebula.

This is contrary to the interpretation of Warren-Smith, Draper and Scarrott (1987(a)), who ruled out a polarised source on the basis that the vectors in a specified area within the nebula body rotated in a sense opposite to the polarisation change of R Mon. However, this change was noted between their V and R band measurements (fig 4.9 and 4.6) and thus did not take into account the variation of the size of the relative effects as the wavelength changed, ie. the incident polarised light scattering efficiency, and the increase in the degree of polarisation of the scattered unpolarised component. Hence such an interpretation, although strong when unopposed by any other evidence now seems somewhat weaker.

A better method of analysing an effect of this manner within the nebula would be to measure the changes of the nebula polarisations if the polarisation of R Mon changed position angle in data taken using the same bandpass. The three I band datasets presented here represent such a collection of data, although the changes in position angle of R Mon are relatively small and measurements will accordingly have to be very accurate when looking for what should be even smaller effects in

R Mon/NGC2261 Feb85 I Data

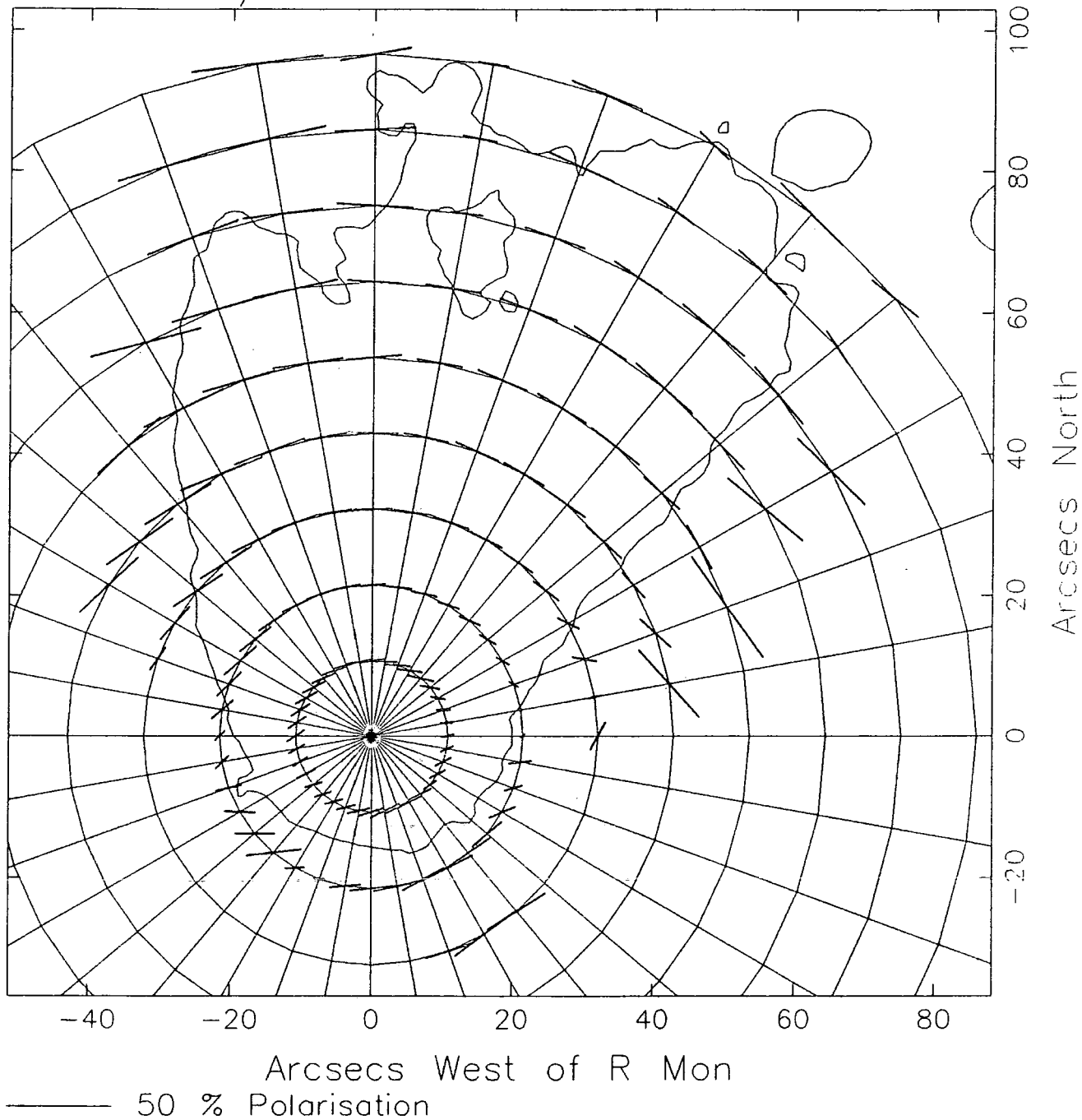


Figure 4.33: Polarisation measurements of NGC2261/R Mon made at the positions shown. The integration bins are 10 pixels square (12").

R Mon/NGC2261 Dec85 R Data

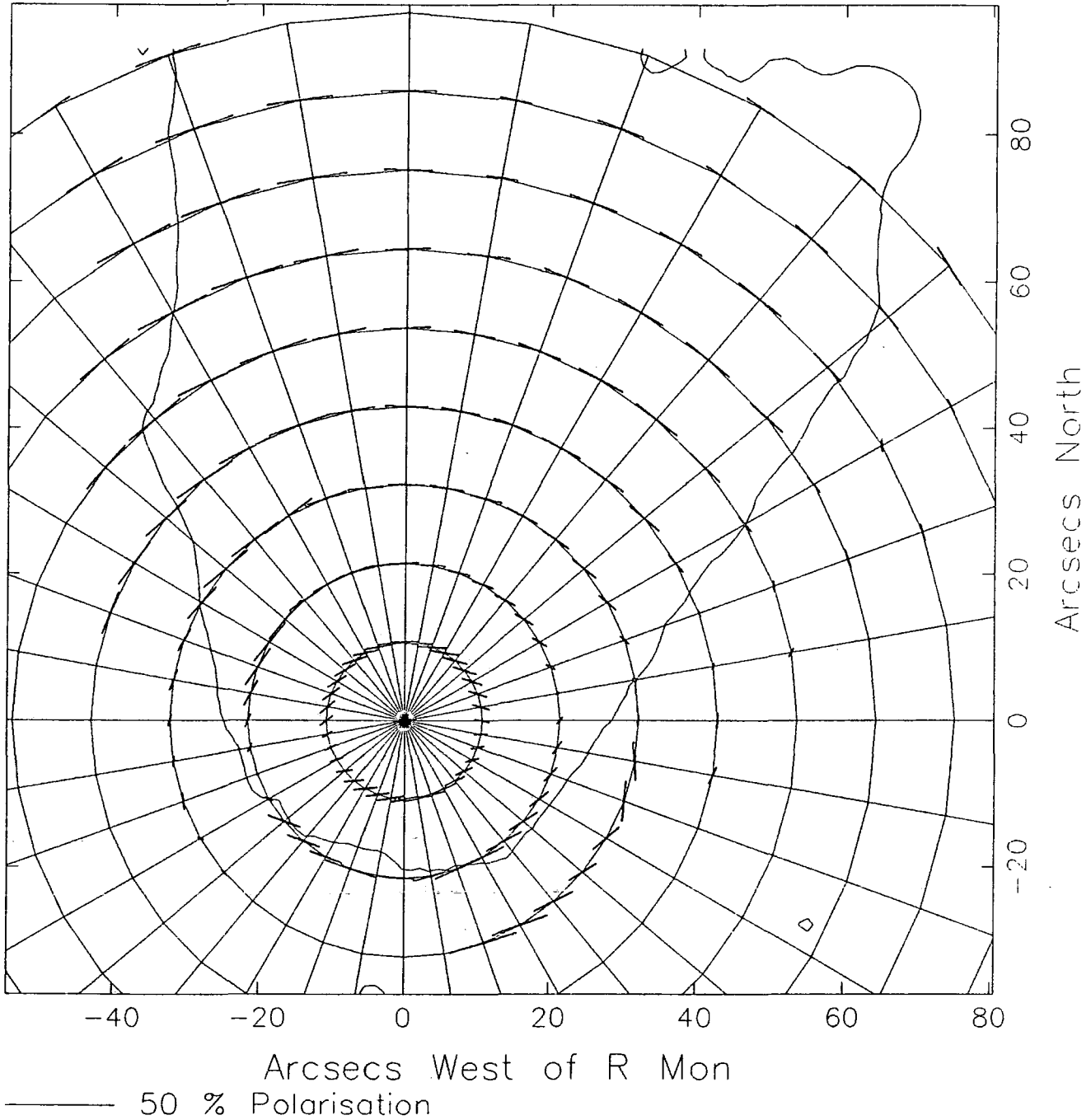


Figure 4.34: Polarisation measurements of NGC2261/R Mon made at the positions shown. The integration bins are 10 pixels square ($12''$).

Table 4.6:

I measurements of NGC2261 position angles.				
Feb85	Dec85	Mar86	$\Delta(\text{Feb85-Dec85})$	$\Delta(\text{Feb85-Mar86})$
66.95	61.63	61.94	5.32	5.01
80.82	79.12	78.81	1.7	2.01
101.44	98.81	101.6	2.63	-0.16
121.00	118.84	118.83	2.16	2.17
109.6	104.5	105.7	5.1	3.9 (R Mon)

the nebula. To this end four positions were selected within NGC2261 at a radius of 40 pixels (≈ 50 arcsecs) from R Mon. The position angle at these points was averaged within 10 pixel (square) bins. The values determined by averaging the position angle within these apertures is listed in table 4.6 for all three sets of I data. Also shown in this table are the position angles of polarisation of R Mon in each of these datasets. The last two columns show the change in position angle between the February and December and March values. Clearly the change in the nebula position angle is positively correlated with the change in position angle of R Mon. The magnitude of the change seems to be around half that of the change in position angle of R Mon.

The results from the three I datasets now seem to confirm that the global changes in the NGC2261 nebula polarisations are due to the effects of a polarised source upon scattering within the the nebula. The general trend, visible in figs 4.33 and 4.34, is shown in profile in fig 4.35(a) which is taken along an arc of radius 40 pixels for all the I

datasets. The values displayed are actually the difference between the measured value and the value which a vector would have had at that point if the pattern were truly centrosymmetric. The deviations, which show themselves as a flattening of the pattern, are clearly seen at the edges of these profiled arcs. Fig 4.35(b) is a smoothed average of the three I datasets.

Looking at figs 4.33 and 4.34 it is possible to see that the deviations from centrosymmetry are increased from the R to I band. This effect is even more pronounced in the Z band polarisation map of R Mon (fig 4.8), which although noisy seems to be very flattened. It therefore seems that the scattered incident polarised light must be increasing its resultant polarised intensity more quickly than the relative polarised intensity from normal scattering is increasing. This is contrary to the results expected from the equations describing the scattering of polarised light in which this effect might simply be described by increasing the value of P the maximum polarisation. However, the parameterisation used to derive these equations is only properly valid for wavelengths around 110 nm and for the grain mixture and size distribution used. Clearly these need to be re-assessed in the light of this observational data, before re-examining the detailed variations observed.

In fig 4.36 there are shown profiles of the position angle taken along radius vectors perpendicular to the polarisation vector of R Mon. The position angle along such a radius vector should be a constant as has been noted above, because the position angle of the resultant polarisation of an scattered unpolarised component and the position

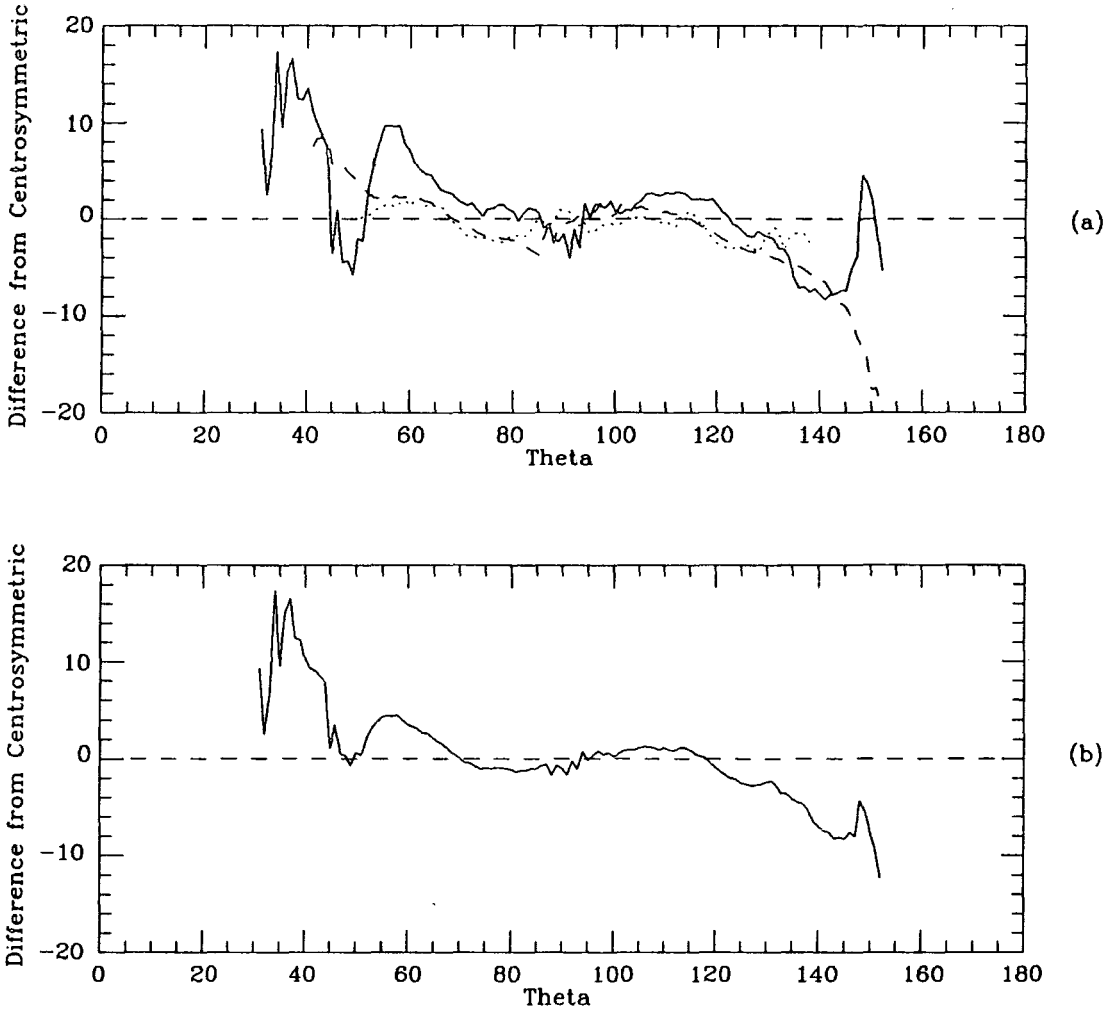


Figure 4.35: (a) Profiles of the difference from perfect centrosymmetry of the polarisation position angle along an arc of 40 pixels radius about R Mon, for the three I band datasets. (b) Smoothed mean of (a).

angle of the incident polarisation should be the same. Even if the scattering is non-Rayleigh, the incident polarised light will still scatter in the same plane. Unsurprisingly the traces show variations about an approximately constant value, which one might expect and normally attribute to noise. However, careful examination reveals some interesting correlations between the various profiles. On each profile a series of numbers have been placed identifying a region of some “feature” of the profiles, which show a certain persistence between most of the datasets. This repetition of the variations suggests that these variations are real and represent some phenomenon in the nebula which is affecting the polarisation in a persistent, repetitive, consistent, fashion. This would seem to suggest that some geometrical mechanism is at work within the nebula, which is not an effect due to a polarised source. Furthermore the effects must be large scale because not all the traces are through the same parts of the nebula as the polarisation of R Mon changes between each dataset. The traces only approximately pass through the same parts.

Before accepting this observation there are two other possible mechanisms which could also produce these effects, without resorting to magnetic fields and aligned grains. One is due to an instrumental effect which is described in Chapter 2, ie. the variation of the effective optic axis of the superachromatic halfwave plate, which could be expected to produce apparent rotations of the position angle of polarisation if the power spectrum of the object varies considerably from point to point. This objection can be simply refuted without resorting to complex calculation. The argument is that the $H\alpha$ polarisation

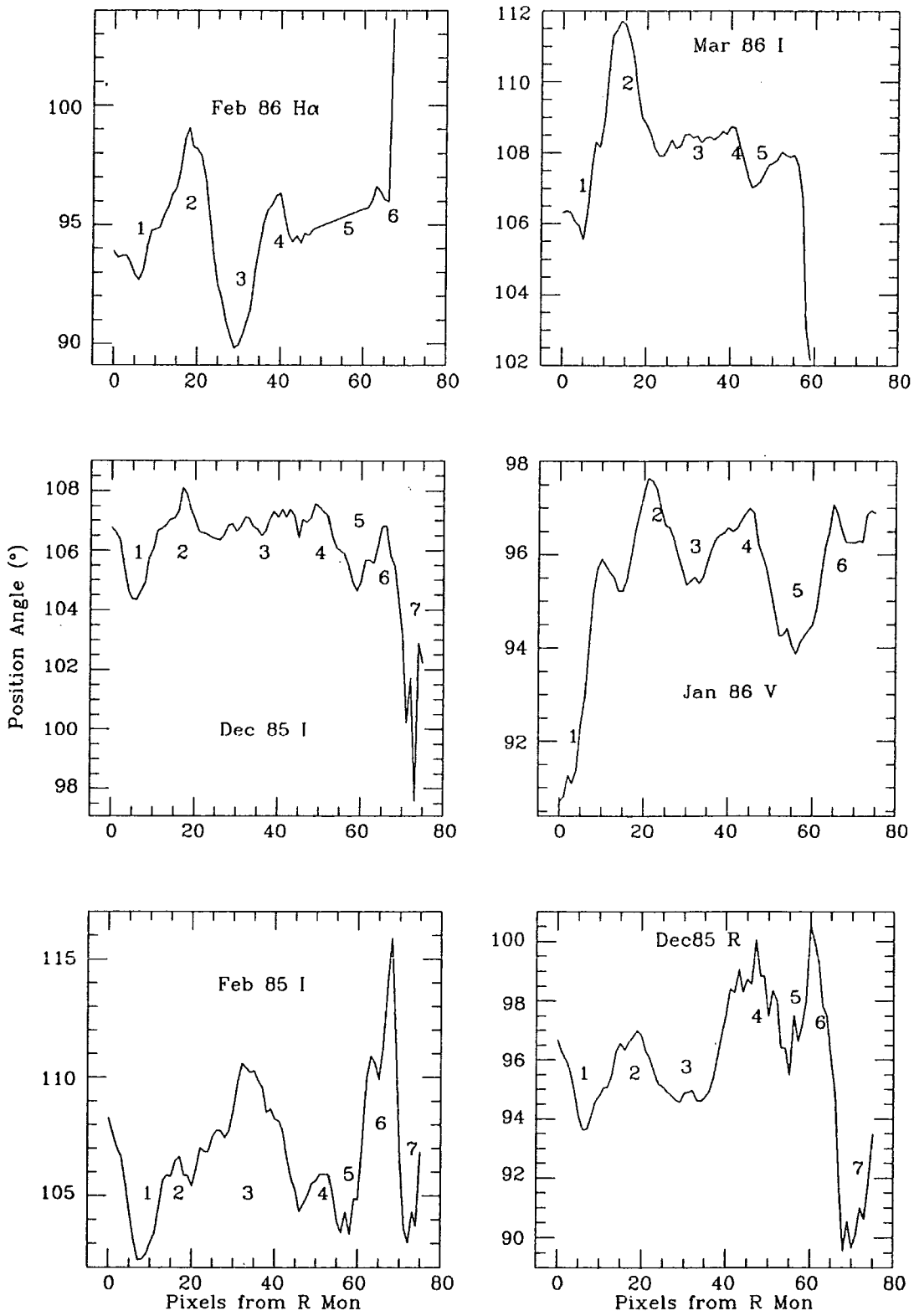


Figure 4.36: Traces of position angle along lines perpendicular to the polarisation of R Mon, for the datasets shown.

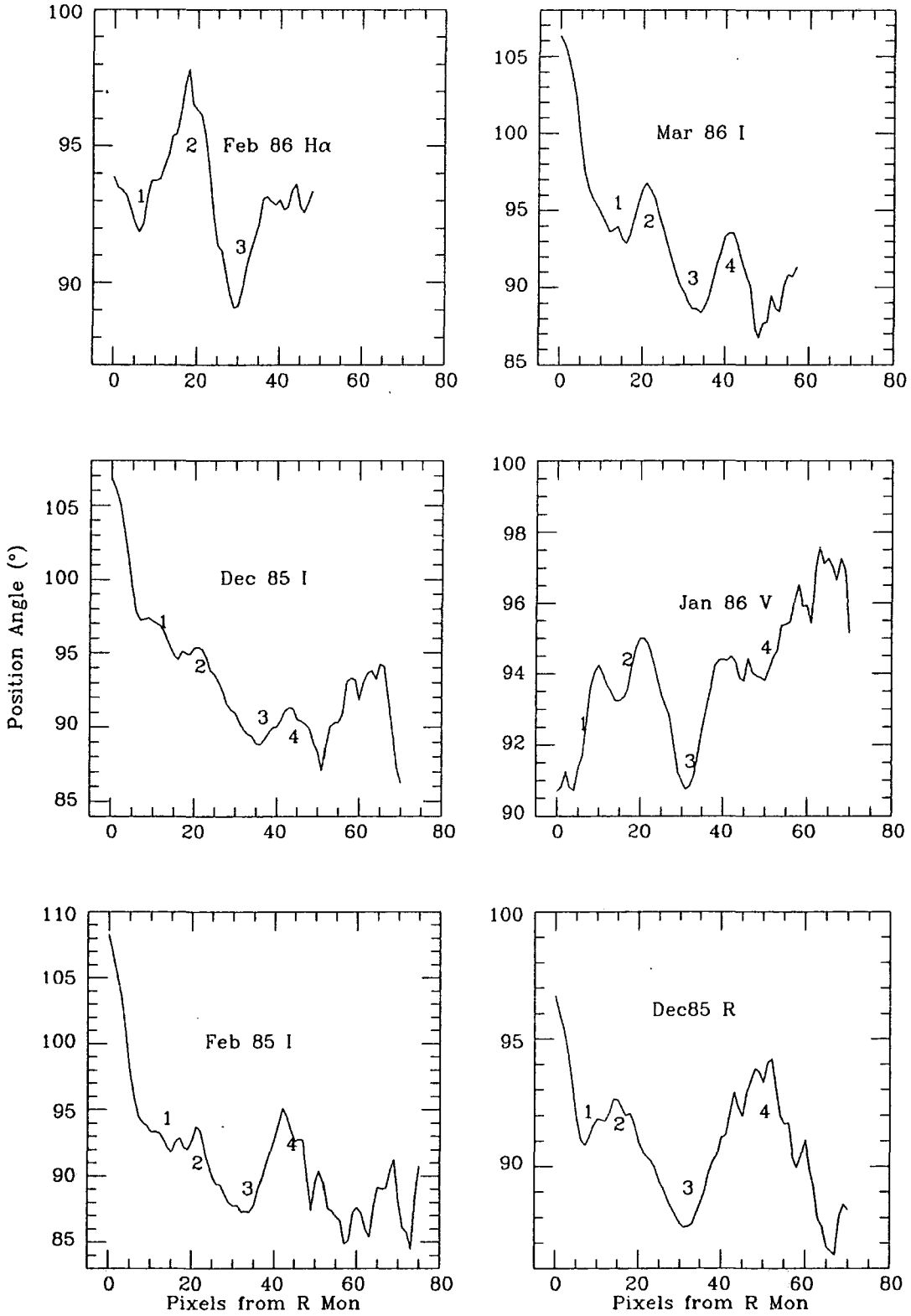


Figure 4.37: Traces of position angle along a line directly north from R Mon, for the datasets shown.

measurements also exhibit periodic variations. Since the $H\alpha$ filter has a band width of only 5 angstroms it does not matter what the power spectrum of the object is, or how it varies from point to point as the $H\alpha$ filter essentially selects out one possible position for the fast axis of the superachromatic halfwave plate. So the variations in position angle are not due to effects produced by the halfwave plate.

The other possible non-geometrical mechanism for producing the variations in the position angle, is the change in position angle of polarisation of R Mon itself with time. Light travel times to the varying parts of the nebula are considerably different, the nebula axis being of the order one light year or so in the figures presented here. Therefore any change in the position angle of polarisation of R Mon would take a finite time to affect different parts of the nebula. If the polarisation of R Mon were changing systematically one might expect variations to exhibit themselves to and fro along the direction perpendicular to the polarisation of R Mon as viewed at present. Clearly there is only one decisive way to test this hypothesis, which is to see the changes in position angle propagating with time. Again the three I datasets are invaluable for testing this hypothesis, covering about the correct timescale to allow the effects to propagate completely across the nebula. In fig 4.37 traces of the position angle of polarisation, directly north from R Mon, are shown for the same datasets as in fig 4.36, again repetitive features are indicated by numbers. The I band datasets are also shown in this figure and clearly show (most clearly between the February 1985 and March 1986) correlations which are almost constant with time. This must rule out variations in the polarisation of R Mon as being the mechanism re-

sponsible for producing the variations in position angle seen along lines perpendicular to the polarisation of R Mon.

It thus seems that the periodic variations in position angle seen along the radius lines perpendicular to the polarisation of R Mon must represent real geometrical fixed effects, which are not due to the polarisation of the source. These effects are therefore most likely to be due to preferential absorption from aligned grains within the nebula. The most likely alignment mechanism is an enhanced Davis-Greenstein mechanism as postulated to explain the alignment of grains within the interstellar medium. This explanation is further favoured by noting that the variations of the position angle are slightly correlated with the R-I colour of the nebula, only really being strongly correlated with feature 3. If the effects noted are due to aligned grains then one would expect some form of correlation with the colour of the nebula, as the induced polarisation should be related to the extinction.

Unfortunately these changes do not allow us to determine the field direction other than to say that it does not lie along the direction running circularly around R Mon, because this would not produce any changes in the position angle. It also cannot lie along the radial direction in the nebula, otherwise this would again rule out any change in position angle (the scattering induced polarisation plus the polarisation due to the source would be perpendicular to field direction, at least in a symmetric nebula face-on). It therefore seems as if the most likely magnetic field configuration is one of a field which escapes helically into the interstellar medium (the field must necessarily reconnect

to the interstellar). Such fields are proposed in both the Pudritz and Norman (1983,86) model and the Shibata and Uchida (1987) model, for accelerating the molecular bipolar outflows from objects such as R Mon.

Another effect (so far uncommented upon) in the traces of polarisation through the nebula, are the variations very close to R Mon, say within 20 pixels (≈ 24 arcsec). This region encompasses the feature designated as 1 in all the position angle traces. This is within the polarisation disk surrounding R Mon. Other secondary effects must also be at play within the disk. It appears that we must return to a scenario which places some magnetic fields within the disk, but their effects must now assume a secondary status compared with their previous standing, as the only source of the polarisation disk. The field direction in the region profiled must be, as in the above argument, somewhere between the perpendicular and parallel directions to the polarisation observed in R Mon. Certainly there is no evidence that the field configuration is toroidal. The field may even run almost perpendicular to the disk, as proposed somewhat speculatively in the section on the $H\alpha$ measurements. Perhaps the best compromise is to have the field helical, but not as wound up as a toroidal field. However, the actual field structure in the disk remains undetermined by this study. Its amount of winding will depend on many parameters of the initial conditions of the cloud from which R Mon condensed ie. the amount of field slip (ambipolar diffusion) and the angular momentum and angular momentum loss efficiency.

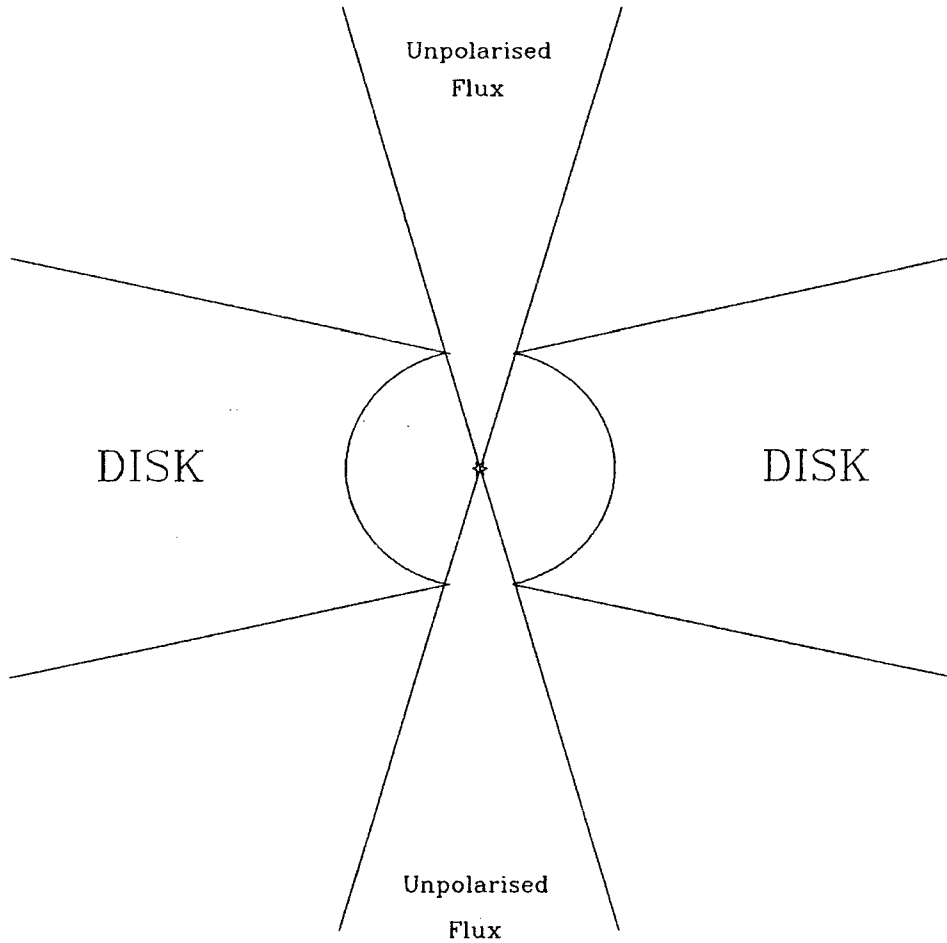


Figure 4.38: Representation of a possible configuration for the inner regions of the disk surrounding R Mon. In this model R Mon is shrouded from the nebula from above and below.

A perhaps more surprising result from the polarisations observed within the nebula is that the flattening of the polarisation pattern does not appear to end with any definity within the area of measurement. This implies that the disk is *thick* at its inner edges, and is at least twice as thick as the inner dimension, possibly even thicker, based upon the model shown in fig 4.19. If the actual disk shape is more rounded on the inner edges and extends above and below the source, the actual disk thickness could be reduced (say as in fig 4.38); in this model R Mon would be “shrouded” from direct view in the nebula.

4.1 Conclusions.

The major conclusion to be drawn from the work outlined in this chapter is that the existence of the anomalous polarisations (disk) across the head of the nebula encompassing the illuminating source R Mon, is mainly due to the intrinsic polarisation of R Mon, and, unlike in previous interpretations of spatial polarisation measurements of the cometary nebula NGC2261, not to a toroidal magnetic field aligning the grains within the disk causing the band of polarisations by preferential absorption. This conclusion is supported by the observations presented here which show that the band of polarisations change orientation on a prohibitively (for the aligned grain method) short timescale. Within this scenario, the properties of the polarisation disk produced by an essentially intrinsically polarised source were analysed, using an expansion of the model first proposed by Elsässer and Staude (1978), together with

the calculations of Notni (1985), for the scattering of polarised light in such a geometry.

Use of the variations of polarisation of R Mon has allowed the estimation of physical parameters associated with the disk surrounding R Mon. The inner size scale of the disk is probably of the order 14 astronomical units, with a thickness of around 30-60 astronomical units at this radius, or the disk may extend above and below R Mon shrouding R Mon from direct view from any direction except on the nebula axis.

A detailed investigation of the small scale deviations of the polarisation vectors in the main nebula body from centrosymmetry shows that it too exhibits variations indicative of an apparently polarised source. Further investigation, however, has revealed the presence of effects which can only be attributed to magnetic field and aligned grain effects. A configuration is suggested to fit the observations, in which the magnetic field has a helical structure in the main nebula body. The field configuration in the disk is now undetermined, and hence it can be maintained that the Shibata and Uchida model for accelerating the energetic bipolar outflows is no longer preferred over the Pudritz and Norman model, at least for NGC2261.

Chapter 5

Concluding Remarks.

The aim of this final chapter is to re-emphasise the main conclusions of the preceding chapters and outline future options and research, which may be undertaken in consequence of the work presented here. Also the results discussed in Chapter 4 will be generally extended in their application to other similar objects.

In Chapter 1, a new detector system incorporating a CCD, which is now used with the Durham Imaging Polarimeter, was described in full, together with its associated software. This chapter was intended, in part, to document this system so that future work with this device can be more easily undertaken. However, the addition of an “automated” polarimeter to the setup is imminent, as is the addition of a blue sensitive coated CCD, so this work will require up-dating by the next generation of workers in polarimetry in Durham, in the not too distant future,

Chapter 2 introduced and explained a new problem inherent in the data produced by the new polarimeter setup. This source of complication is not due to the CCD (which has proven itself again and again during many observations over the period with which the author and co-workers have used it) but to the necessary addition of a superachromatic halfwave plate to the Polarimeter itself. This addition was necessary to enable the polarimeter to function over the very extended wavelength coverage of the CCD detector. The problem with the superachromatic halfwave plate is that, due to its method of operation, the equivalent (effective) optic axis is slightly variable with wavelength. A method for producing “first order” corrections to this variation was described and values for each of the existing filters was derived. The authors experience with these variations in the equivalent optical axis suggests that for most applications (even where good accuracy is require, as in this work) these corrections are perfectly satisfactory.

Also in Chapter 2 the results obtained with the CCD detector were compared with those obtained using an electronographic camera, to check that the new results were reasonable and fairly accurate. This was confirmed, as was the (unsurprising) fact that the CCD together with its filter system, is a much more sensitive arrangement than the equivalent electronographic arrangement. This, in combination with the Chapter 1 finding that the CCD is simpler and considerably quicker to use when observing, makes this a much more useful instrument, especially as it optimises the use of expensive large telescope time, making possible large increases in the effective observing schedule. These statements are borne out by the amount of work which has subsequently

been published, using data taken with this instrument.

If it ever becomes necessary to achieve greater accuracies than have been obtained to date, specifically with respect to the position angle measurements in which a large amount of information about the (secondary) polarisation mechanisms in objects is found, it is possible to remove the variation of the optic axis of the superachromatic halfwave plate by the use of a second, fixed, identical, halfwave plate as outlined in theory in Appendix B.

The interpretation of the results presented in Chapter 4, represents a new direction for explaining the mechanism which produces the anomalous band of polarisation seen across the head of NGC2261/R Mon. This re-interpretation opposes the almost standard explanation which invokes a toroidal magnetic field around the object and consequently aligns the (elongated) dust grains within its confines. This leads to the observed polarisation pattern which is the consequence of preferential absorption of one component of the light in transit through this region. The change in interpretation has been forced by a previously unobserved change in the orientation of the anomalous band of polarisation on a dynamically very short timescale.

The model now favoured for the production of the bands of polarisation, is an expansion of the model of Elsässer and Staude (1978) explaining the polarisation of objects which are partially obscured within the confines of a surrounding disk /torus. The expansion involves the further scattering of the light from the central object, which now ap-

pears polarised to nearly all parts of the nebula, certainly to all the disk. Further application of this model to NGC2261 and R Mon shows that the variations in the anomalous polarisations must be due ^{to} effects within 14 astronomical units of R Mon and that the inner disk must be surprisingly thick, or that it extends well above and below R Mon (ie. R Mon is still shrouded by material).

The model is also successfully applied to the large scale (small) deviations from centrosymmetry which are observed in what appears to be a normal reflection part of the NGC2261 nebula. But on close examination of these variations, it is still necessary to invoke a secondary cause, such as a magnetic field within the nebula. This also appears to be true in part of the anomalous band of polarisations. However, the field geometry is now suggested to be helical rather than toroidal as a best fit to the observations. As a by-product of this interpretation it seems now to be impossible to select a best model to explain the acceleration of the molecular outflow in NGC2261.

Other problems with this model include the non-alignment of the so-called “null points” with the central brightness peak, at certain times, and the increase in the size of the deviations from centrosymmetry in the nebula with increasing wavelength. These points still require further enhancement of the understanding of how polarised light scatters within the nebula to properly explain them.

More generally it seems sensible to attempt to use the model for the polarisation of R Mon and NGC2261 to explain the polarisations

observed in other similar systems. Some points which may apply to other systems are:-

- the anomalous bands of polarisation seen in other objects may also be due to the effects in the polarised light scattering model described here. However, there is no complementary evidence for this interpretation in other objects, but the results found for NGC-2261/R Mon must weaken the argument in favour of a magnetic interpretation in other similar objects.
- The position angle of the bands of anomalous polarisations in other nebulae may only weakly decide the nebula axis, as will the polarisation of the sources (ie. it is usual to suppose that the polarisation of the source and hence the band of polarisations, are perpendicular to the nebula axis and the local magnetic field). This may throw some light on the range of variations observed when trying to correlate these quantities (for instance in the results of Hodapp (1984) and Sato *et al.* (1985)).
- There are some cometary /bipolar nebulae which do not show a band of polarisations (ie. LkH α 208 Shirt, Warren-Smith and Scarrott (1983)). This fact is now naturally explained in terms of the inner “thickness” (or lack of shrouding) of the inner disk. Thin disks would show no anomalous effects due to the model described here, but should show the other effects due to say the true magnetic field geometry. The disk thickness would depend on many factors, such as the status of evolution of the object (it might be expected that as the object and disk evolve the disk dissipates and thins

out), or the initial conditions before the pre-stellar cloud collapses.

- Conversely, in less evolved objects, or objects with different initial conditions, “thick” or shrouded inner areas of the disk would be expected to produce stronger polarisation effects, particularly within the main nebula.

To fully appreciate the model for the NGC2261 nebula outlined in this thesis it would be useful if a rigorous numerical model was made, with perhaps a different set of grain types and a different size distribution. However, to cover the areas outlined above it would have to calculate the variations with wavelength and variations in polarisation as the polarisation of R Mon changes, which all in all would probably make the venture very difficult and time consuming (not mentioning the incorporation of the secondary effects observed). Perhaps a simpler method of verification and extension would be to make similar observations of other nebulae (such as NGC6729, which is similarly classified as variable and has frequently been compared to NGC2261) but again a large commitment of observation time would be required to gain the necessary temporal as well as spectral coverage. So it seems that further confirmation of the ideas outlined in Chapter 4 will be hard to achieve, particularly with respect to extending the observations to other objects, but this challenge cannot be ignored.

An area of interest which has not been expanded upon in Chapter 4 is that of planetary formation. The observation of effects within a radius of 14 astronomical units of a star could easily be associated with

planetary bodies, and one might suggest that the obscuring bodies are protoplanets. If this were true it would put considerable constraints on the actual source of the visible light. It seems unlikely that planetary bodies would accrete onto the protostar, as would be necessary if the protostar is the main source of light. Also non-accretive sources of variations in the light illumination would necessarily have to be above the source, ie. between the source and the polarising regions, planets are unlikely to be found in these high latitudes. It therefore seems that unless some other more pervasive source of illumination is identified, it is unlikely that any of these variations in illumination can be associated with obscuration due to any orbiting planetary objects. However, the inner regions of the disk must be quite empty (compared to the disk) and as such seem the perfect region for planets to have formed /to be forming.

In conclusion the results described in this work have shown that CCD polarimetry is a versatile and accurate tool for probing regions of astronomical interest, particularly regions of recent star-formation. The power of this tool lies in the simplicity of interpretation which can be achieved, but this is only possible when the data under consideration is complete. This seems particularly true if, as in this case, the system can be observed temporally, as well as spectrally. Any changes in the system provide a powerful probe of the mechanisms at work in the system.

Publications.

Draper, P.W., Warren-Smith, R.F., Scarrott, S.M. (1985).

A polarization study of the cometary nebula Parsamyan 21.

M.N.R.A.S. 212:1p.

Draper, P.W., Warren-Smith, R.F., Scarrott, S.M. (1985).

*The source of illumination of the bipolar nebula near
NGC7129.*

M.N.R.A.S. 212:5p.

Draper, P.W., Warren-Smith, R.F., Scarrott, S.M. (1985).

*Illumination of reflection nebulosity in the L1551 dark cloud by
the IR sources IRS5 and L1551NE.*

M.N.R.A.S. 216:7p.

Scarrott, S.M., Warren-Smith, R.F., Draper, P.W., Gledhill, T.M. (1985).

Optical polarimetry of nebulae with emission line jets.

in *Cosmical Gas Dynamics*, Ed. F.D.Khan, VNU Science Press.

p281.

Scarrott, S.M., Warren-Smith, R.F., Draper, P.W., Gledhill, T.M. (1986).

Optical polarimetry of nebulae in regions of star formation.

Can.J.Phys 64:426.

Warren-Smith,R.F.,Draper,P.W.,Scarrott,S.M. (1986).
*Observation of magnetic field structure around newly formed
stars.*

in *Interstellar Magnetic Fields*. eds R.Beck, K.Klein, Pub.
Springer-Verlag,Berlin.

Scarrott,S.M.,Warren-Smith,R.F.,Draper,P.W.,Bruck,M.T.,
Wolstencroft,R.D. (1987).

The Bruck Bipolar: a nebulous star cluster.

M.N.R.A.S. 225:17.

Warren-Smith,R.F.,Draper,P.W.,Scarrott,S.M. (1987).

*Polarimetry of the NGC 2261/R Monocerotis system and the
faint jetlike feature to its southwest.*

Ap.J. 315:500.

Warren-Smith,R.F.,Draper,P.W.,Scarrott,S.M. (1987).

*Evidence from optical polarimetry for spiral structure in the
magnetic field and cloud density around newly-formed stars.*

IAU Symposium 122, *Circumstellar Matter*, p129. eds.

Appenzeller,I., Jordan,C. Pub. Reidel Co.

Warren-Smith,R.F.,Draper,P.W.,Scarrott,S.M. (1987).

*Magnetic fields and star formation: evidence from imaging
polarimetry of the Serpens Reflection Nebula.*

M.N.R.A.S. 227:749.

Appendix A

DORADO.

This appendix contains a listing of all the routines which are available when using the DORADO system, together with a brief description of their functions.

TAPEMOUNT: Initialises the mounting of magnetic tapes, it checks and creates entries in the tape catalogue, and creates a log file for each tape. It also reports what the status of the foreground frame dumping routine was when it last terminated, so that any errors which occurred (see messages section below) during the last dumping session can be rectified. When tape initialisation occurs, the tape number (each tape is defined by a number in the range 1 to 9999) given is checked against all previous entries in the catalogue. If the tape has been used before, an instruction is passed to the frame dumping program to load the tape to the number of frames which have already been dumped, or to a number supplied

by the user. If the magnetic tape is new, the tape number is entered into the tape catalogue, initialising a new entry, and a new tape log file is created. Finally this routine loads the foreground frame dumping program (TAPEDUMP) and re-initialises the error status flags.

TAPECAT: Displays a listing of the catalogue of tapes which have been introduced into the DORADO system. It shows the tape numbers, the number of frames on each tape and the file name of the corresponding tape log: the entry with a "*" next to it is the tape currently in use. This routine also shows the status of the foreground process.

TAPELOG: Displays a listing of the frames that have been dumped onto a particular tape. This routine also shows the status of the foreground process.

TAPESTOP: Forces an exit of the tape dumping process. A message is shown indicating the status of the routine if it has already been terminated.

TAPEQ: Displays a listing of which frames are queued for dumping to tape. Also shows the frame dumping process status.

TAPESUB: Submits a single frame or a range of frames to the frame dumping queue.

EXP,EXPS: Make an exposure. First they read out the CCD to clear any residual charge, then open the electronic shutter for a given number of seconds (note that the number of seconds can be

any real number). Then they read out the CCD to disk frame. Finally they submit an entry to the frame dumping queue so that the frame can be dumped to tape. To aid data security console interrupts are allowed only during the shutter open period (so that, for instance previous frames can be displayed, the disk can be purged to create space during a long exposure), but these exposures then have to be terminated by either the EXPFIN or EXPSTOP routines. EXPS performs these tasks cyclically, without terminating the program, so that the object names and exposure times have only to be entered once.

EXPFIN: Finishes an exposure. It waits for the allotted exposure time to expire, or finishes an exposure immediately if the exposure time has been overrun. If the time is overrun the actual exposure time is calculated and entered into the frame header. It reads out the CCD to disk and finally submits the frame to the frame dumping queue. Note that if this program is run when an exposure was not started by EXP it inquires (as does EXP) as to the exposure time, object etc., and reads out the CCD to disk immediately and then submits an entry to the tape queue. Again interrupts are allowed only during any shutter open period, the exposure can then either be finished with EXPFIN or stopped with EXPSTOP.

EXPSTOP: Stops an exposure immediately, regardless of its exposure state (ie. if any exposure time is left). The actual exposure time is calculated and written to the frame header. The frame is then read to disk and submitted to the frame dumping queue. Note that if this program is run when an exposure was not started

by EXP(S) it inquires (as does EXP(S)) as to the exposure time, object etc., reads out the CCD to disk and submits an entry to the tape queue.

FLIST: Lists the headers of the frames on disk. Frames still to be dumped are indicated by “**” immediately after the frame number.

TESTSHOT: Allows the CCD to be exposed for a number of seconds each time RETURN is pressed, so that single ‘test’ shots may be made. Does NOT store the resultant frames on disk, so the disk does not fill up if you are making a lot of test exposures, ie. during object finding.

CCDCLEAR: Continuously reads out charge from the CCD, displaying the current level of charge after each read out sequence. This routine is intended to be run during the day and for other long periods when the CCD system is not in use. This process keeps the noise level of the CCD low and also retains the CCD in a ready state so that observations can begun immediately.

CCDTEMP: Gives a continuous readout of CCD temperatures (note these are only reliable if the CCD is already fairly cold).

CCDMON: Shows the current values in the CCD and electronics rack monitors.

FDISP: Displays a frame on the image display unit. The frame may be multiplied by an integer constant (or divided if the constant supplied is negative) and have an integer offset applied before being displayed. (The division aspect is useful for displaying images which are wrapped on the image store display; to obtain the full

data range simply divide the image by 16). This routine also allows the displayed image to be binned in the x-direction by any integer. Note that parameters for this program can also be accepted from the command line eg `FDISP/C DF=1999 GA=-16`.

FINDER: Performs a continuous readout of the CCD to the image display, exposing for a given time between each readout. Any range of columns may be read out, so that for instance a single star can be displayed rapidly for focussing. Parameters may be obtained from the command line when using this program (eg. `FINDER/C SH=10`. Note that any exposure times obtained from the command line have to be integer seconds).

FPURGE: Purges a range of frames from disk. A frame must have had its attributes changed from permanent write protected; this change is made by the frame dumping routine after a frame has successfully been written to tape. It also reports if any corruption of the frame index has occurred, if so, the bad entries are removed.

FDEL: Deletes any frame from the disk. Dumped frames are deleted as in `FPURGE`. Frames whose attributes have not been reset from permanent write protected (the sign that they have not been dumped for some reason), are deleted on persistent request. It also reports if any corruption of the frame index has occurred, if so, the bad entries are removed.

SHOP: Opens the CCD shutter.

SHCL: Closes the CCD shutter.

STATSHOW: Displays the current parameter values in the common block /STAT/. This common block contains the value of the next frame to be written to disk, the values of the CCD instruction words which cause the CCD to readout etc., and other important values.

TAPEDEL: Removes all the occurrences in the tape queue of a frame number. This is useful if a frame has been deleted from disk and is still entered in the tape queue. The foreground process will terminate if it cannot find a frame, entered in the frame dumping queue.

TAPELOAD: Reads any frame in FITS format from tape onto disk file.

TAPELIST: Lists the header information from FITS formatted tapes.

(TAPEDUMP): This program is loaded into the foreground of the Nova memory by the TAPEMOUNT routine. It is not intended for other use. It is the routine that writes the frames in the frame dumping queue to magnetic tape, updating the tape log file and the tape catalogue, and removing the entry from the tape queue, as each frame is dumped. It can only be terminated (on request) by the routines TAPEMOUNT and TAPESTOP. If for any other reason this process terminates the symbol FG TERM will appear on the console, this message must not be ignored. Any errors which have occurred can be shown by running either, TAPEMOUNT, TAPESTOP, TAPEQ, TAPELOG, OR TAPECAT. Prompt action

must be taken to correct any such errors. The process can then be reloaded by re-TAPEMOUNTing.

(NEWCAT): This program re-initialises the tape catalogue; any information in the tape catalogue will be lost after this program has been run. It is only intended for the use of programmers and for installing a catalogue in a new directory if required and should not otherwise be used. It may be run by typing in the command DORADO:NEWCAT.

(STATFIX): Resets all the values in the common block /STAT/ to those stored in the backup file STATFIX.DD. However, the frame index is reset to a value supplied by the user. This program should only be used when a serious corruption of the common block has occurred, or if the frame index is in danger of exceeding the value 9999. It may be run by typing DORADO:STATFIX from the OBSERVE(ing) directory; it will NOT run in any other directory unless a STATFIX.DD file has been installed.

MESSAGES: The following messages may be reported by some of the TAPExxx routines.

- *Unidentified fatal error*. The TAPEDUMP program encountered a fatal error while being loaded into the foreground. This should not normally occur.
- *Terminated on request*. Normal process termination. This can only occur if the process is stopped by TAPEMOUNT or TAPESTOP.

- *Tape not on line.* The magnetic tape unit is not on line, put it on!
- *Tape write error (no write-ring?).* Magnetic tape has no write ring in, or for some other reason the tape is not writable to. Put in the write-ring!
- *Error reading data file.* Error encountered reading disk frame, it has probably been deleted from disk, possibly corrupted. Remove it from the tapequeue and re-TAPEMOUNT.
- *Tape full.* Tape is full, re-TAPEMOUNT a new one!
- *Queue handling error (disk full?).* Error occurred while updating the tape queue file (TAPE.QQ). Possibly no disk space left to create a new queue. Create some!

Appendix B

Some Retardance Theory.

The Stokes parameters I', Q', U', V' , of the light transmitted through a perfect analyser, with principal plane at position ϕ are related to the incident light parameters, I, Q, U, V , by the transformation equation :-

$$\begin{pmatrix} I' \\ Q' \\ U' \\ V' \end{pmatrix} = 1/2 \begin{pmatrix} 1 & \cos 2\phi & \sin 2\phi & 0 \\ \cos 2\phi & \cos^2 2\phi & 1/2 \sin 4\phi & 0 \\ \sin 2\phi & 1/2 \sin 4\phi & \sin^2 2\phi & 0 \\ 0 & 0 & 0 & 0 \end{pmatrix} \begin{pmatrix} I \\ Q \\ U \\ V \end{pmatrix} \quad (1)$$

so the light transmitted through a perfect analyser is:-

$$I' = 1/2(I + Q \cos 2\phi + U \sin 2\phi)$$

similarly the equation for a perfect retarder of retardance τ and optic axis at position ψ is:-

$$\begin{pmatrix} I' \\ Q' \\ U' \\ V' \end{pmatrix} = 1/2 \begin{pmatrix} 1 & 0 & 0 & 0 \\ 0 & G + H\cos 4\psi & H\sin 4\psi & -\sin\tau\sin 2\psi \\ 0 & H\sin 4\psi & G - H\cos 4\psi & \sin\tau\cos 2\psi \\ 0 & \sin\tau\sin 2\psi & -\sin\tau\cos 2\psi & \cos\tau \end{pmatrix}$$

$$\begin{pmatrix} I \\ Q \\ U \\ V \end{pmatrix} - (2)$$

where

$$G = 1/2(1 + \cos\tau), H = 1/2(1 - \cos\tau).$$

from equations (1) and (2) we obtain the intensity of light transmitted through a retarder with the optical axis at position ψ followed by an analyser with the principal plane at position $\phi = 0^\circ$ (upper signs) or $\phi = 90^\circ$ (lower signs):-

$$I' = 1/2[I \pm Q(G + H\cos 4\psi) \pm UH\sin 4\psi \mp \sin\tau\sin 2\psi]$$

thus for a halfwave plate $\tau = 180^\circ$, $G=0$, $H=1$, and:-

$$I' = 1/2[I \pm Q\cos 4\psi \pm U\sin 4\psi] - (3)$$

For two halfwave plates followed by an analyser, it can similarly be shown that:-

$$I' = 1/2[I \pm Q\cos 4(\psi_1 - \psi_2) \pm U\sin 4(\psi_1 - \psi_2)] - (4)$$

So we see that from (2) if the retardance varies by only 3° , as it does in a superachromatic halfwave plate, since the equation only involves cosine terms in the G and H factors, the depolarisation is very small. Equation (4) shows how the addition of a second halfwave plate removes the dependency on the absolute position of the equivalent optical axis, since if the halfwave plates are identical the wavelength dependent term is the same, so we have $\psi_1 + \Delta\psi$, and $\psi_2 + \Delta\psi$, and the $\Delta\psi$ cancel.

Appendix C

Durham CCD References.

The following is a list (to the end of 1987) of all the published material which is directly attributable to the success of the CCD detector system.

Draper, P.W., Warren-Smith, R.F., Scarrott, S.M. (1985).

A polarization study of the cometary nebula Parsamyan 21.

M.N.R.A.S. 212:1p.

Draper, P.W., Warren-Smith, R.F., Scarrott, S.M. (1985).

*The source of illumination of the bipolar nebula near
NGC7129.*

M.N.R.A.S. 212:5p.

Warren-Smith, R.F., Gledhill, T.M., Scarrott, S.M. (1985).

*Polarimetric evidence against a collimated flow in the
Horsehead Nebula.*

M.N.R.A.S. 215:75p.

Draper, P.W., Warren-Smith, R.F., Scarrott, S.M. (1985).

*Illumination of reflection nebulosity in the L1551 dark cloud by
the IR sources IRS5 and L1551NE.*

M.N.R.A.S. 216:7p.

Scarrott, S.M., Warren-Smith, R.F., Draper, P.W., Gledhill, T.M. (1985).

Optical polarimetry of nebulae with emission line jets.

in *Cosmical Gas Dynamics*, Ed. F.D.Kahn, VNU Science Press.

p281.

Scarrott, S.M., Warren-Smith, R.F., Draper, P.W., Gledhill, T.M. (1986).

Optical polarimetry of nebulae in regions of star formation.

Can.J.Phys 64:426.

Wolstencroft, R.D., Reipurth, B., Walker, H.W., Warren-Smith, R.F.,

Scarrott, S.M. (1986).

*A bipolar nebula in Orion associated with the IRAS source
05329-0505.*

M.N.R.A.S. 218:1p.

Scarrott, S.M., Brosch, N., Ward-Thompson, D., Warren-Smith, R.F.

(1986).

An optical polarization study of two possible bipolar nebulae.

M.N.R.A.S. 223:505.

Gledhill, T.M., Warren-Smith, R.F., Scarrott, S.M. (1986).

The structure of Haro 6-5.

M.N.R.A.S. 223:867.

Warren-Smith, R.F., Draper, P.W., Scarrott, S.M. (1986).

Observation of magnetic field structure around newly formed stars.

in *Interstellar Magnetic Fields*. eds R.Beck, K.Klein, Pub.

Springer-Verlag, Berlin.

Scarrott, S.M., Ward-Thompson, D., Warren-Smith, R.F. (1986).

Optical polarization studies of galaxies.

in *Interstellar Magnetic Fields*. eds R.Beck, K.Klein, Pub.

Springer-Verlag, Berlin.

Scarrott, S.M., Gledhill, T.M., Warren-Smith, R.F. (1986).

Optical polarization studies of star formation regions.

in *Interstellar Magnetic Fields*. eds R.Beck, K.Klein, Pub.

Springer-Verlag, Berlin.

Scarrott, S.M., Ward-Thompson, D., Warren-Smith, R.F. (1987).

Evidence for a spiral magnetic field configuration in the galaxy M51.

M.N.R.A.S. 224:299.

Scarrott,S.M.,Warren-Smith,R.F.,Draper,P.W.,Bruck,M.T.,

Wolstencroft,R.D. (1987).

The Bruck Bipolar: a nebulous star cluster.

M.N.R.A.S. 225:17.

Warren-Smith,R.F.,Draper,P.W.,Scarrott,S.M. (1987).

Polarimetry of the NGC 2261/R Monocerotis system and the faint jetlike feature to its southwest.

Ap.J. 315:500.

Warren-Smith,R.F.,Draper,P.W.,Scarrott,S.M. (1987).

Evidence from optical polarimetry for spiral structure in the magnetic field and cloud density around newly-formed stars.

IAU Symposium 122, *Circumstellar Matter*, p129. eds.

Appenzeller,I., Jordan,C. Pub. Reidel Co.

Scarrott,S.M.,Gledhill,T.M.,Warren-Smith,R.F. (1987).

Polarimetry of Herbig-Haro objects: I. The HH57 Nebulosity.

M.N.R.A.S. 227:701.

Warren-Smith,R.F.,Draper,P.W.,Scarrott,S.M. (1987).

Magnetic fields and star formation: evidence from imaging polarimetry of the Serpens Reflection Nebula.

M.N.R.A.S. 227:749.

Scarrott,S.M.,Gledhill,T.M.,Warren-Smith,R.F. (1987).

Polarimetry of Herbig-Haro objects: II. The HH24 nebulosity.

M.N.R.A.S. 227:1065.

Scarrott,S.M.,Warren-Smith,R.F.,Gledhill,T.M., Wolstencroft,R.D.

(1987).

Polarimetry of Herbig-Haro objects: III. HH100 in Corona Australis.

M.N.R.A.S. 228:553.

Wolstencroft,R.D.,Warren-Smith,R.F.,Scarrott,S.M. (1987).

The optical counterpart of the FIR source in NGC6334.

M.N.R.A.S. 228:805.

Scarrott,S.M.,Warren-Smith,R.F.,Wolstencroft,R.D., Zinnecker,H.

(1987).

A Polarization study of the Chamaeleon IRN.

M.N.R.A.S. 228:827.

Scarrott,S.M,Warren-Smith,R.F. (1987).

Optical polarization in the jet of 3C273.

M.N.R.A.S. 228:35p.

Gledhill, T.M., Warren-Smith, R.F., Scarrott, S.M. (1987).

Optical imaging and polarization mapping of the nebulosity associated with the PMS star PV Cephei.

M.N.R.A.S. (in press).

Scarrott, S.M., Wolstencroft, R.D. (1987).

An optical polarization study of the Reipurth 50 nebulosity.

M.N.R.A.S. (in press)

Scarrott, S.M. (1987).

Polarimetry of Herbig-Haro objects: IV. The HH34 complex.

M.N.R.A.S. (in press).

References.

- Allen, D.A. 1973. M.N.R.A.S. 161:145
- Appenzeller, I. 1983. Rev.Mex.Astron.Astrofis. 7:151
- Aspin, C., McLean, I.S., Coyne, G.V. 1985. Astron.Astrophys. 149:158
- Aspin, C., McLean, I.S., McCaughrean, M.J. 1985. Astron.Astrophys.
144:220
- Axon, D. 1977. Ph.D. Thesis. University of Durham.
- Bally, J. 1982 Ap.J. 261:558
- Bally, J., Lada, C.J. 1983. Ap.J. 265:824
- Barral, J.F., Cantò, J. 1981 Rev.Mex.Astron.Astrofis. 5:101
- Bartla, W., Menten, K.M. 1985. Ap.J. 298:L19
- Beckwith, S., Zuckerman, B., Skrutskie, M.F., Dyck, H.M. 1984. Ap.J.
287:793
- Beckwith, S., Sargent, A.I., Scoville, N.Z., Masson, G.R., Zuckerman, B.,
Phillips, T.G. 1986. Ap.J. 309:755
- Bieging, J.H. 1984. Ap.J. 286:591
- Bruck, M.T. 1974. M.N.R.A.S. 166:123
- Brugel, E.W., Mundt, R., Bührke, T. 1984. Ap.J. 287:L73
- Cantò, J. 1983 Rev.Mex.Astron.Astrofis. 7:109
- Cantò, J., Rodriguez, L.F. 1980. Ap.J. 239:982
- Cantò, J., Rodriguez, L.F., Barral, J.F., Carral, P. 1981. Ap.J.
244:102
- Cantò, J., Sarmiento, A., Rodriguez, L.F. 1987.
in Star Forming Regions.
eds. M.Peimbert & J.Jugaku.

I.A.U. symposium 115:239

- Chesterman, J.F., Pallister, W.S. 1979. *M.N.R.A.S.* 191:349
- Cohen, M. 1973. *M.N.R.A.S.* 161:105
- Cohen, M., Biegging, J.H., Schwartz, P.R. 1982. *Ap.J.* 253:707
- Cohen, M., Harvey, P.M., Schwartz, R.D. 1985. *Ap.J.* 296:633
- Cudworth, K.M., Herbig, G.H. 1979. *Astron.J.* 84:548
- Cugnon, P. 1985. *Astron. Astrophys.* 152:1
- Cullum, M., Deiries, S., D'Odories, S., Reiß, R., 1985. *Astron. Astrophys.*
153:L1
- Draine, B.T. 1983. *Ap.J.* 270:519
- Draper, P.W., Warren-Smith, R.F., Scarrott, S.M. 1985(a). *M.N.R.A.S.*
212:1P
- Draper, P.W., Warren-Smith, R.F., Scarrott, S.M. 1985(b). *M.N.R.A.S.*
212:5P
- Draper, P.W., Warren-Smith, R.F., Scarrott, S.M. 1985(c). *M.N.R.A.S.*
216:7P
- Elsässer, H., Staude, H.J. 1978. *Astron. Astrophys.* 70:L3
- Finkenzeller, M., Mundt, R. 1984. *Astron. Astrophys. Suppl.* 55:109
- Franco, J., Cox, D.P. 1983 *Ap.J.* 273:243
- Garrison, L.M., Anderson, C.M. 1978 *Ap.J.* 221:601
- Genzet, R., Reid, M.J., Moran, J.M., Downes, P. 1981. *Ap.J.* 244:884
- Gething, M.R., Warren-Smith, R.F., Scarrott, S.M., Bingham, R.G. 1982.
M.N.R.A.S. 198:881
- Gledhill, T.M., Warren-Smith, R.F., Scarrott, S.M. 1986. *M.N.R.A.S.*
223:877
- Greenberg, J.M. 1978. in *Cosmic Dust*.
ed. J.A.M. McDonell. p256. John Wiley and Sons

- Greenstein, J.L. 1948. *Ap.J.* 107:375
- Hall, R.C. 1964. *Ap.J.* 139:759
- Hall, R.C. 1965. *P.A.S.P.* 77:158
- Herbig, G.H. 1960. *Ap.J. Suppl.* 4:337
- Herbig, G.H. 1968. *Ap.J.* 152:439
- Hodapp, K.W. 1984. *Astron. Astrophys.* 141:255
- Hubble, E.P. 1916 *Ap.J.* 44:190
- Imhoff, C.L., Mendoza, V. E.E. 1974. *Rev. Mex. Astron. Astrofis.* 1:25
- Johnson, H.L. 1967 *Science* 157:635
- Johnson, H.L. 1968. in *Nebulae and Interstellar Matter*.
 eds. L.H. Aller and R.M. Middlehurst. p 167.
 Univ of Chicago Press
- Johnson, H.M. 1966. *A.J.* 71:224
- Jones, B.F. *Rev. Mex. Astron. Astrofis.* 7:71
- Jones, B.F., Herbig, G.H. 1982. *A.J.* 87:1223
- Jones, T.J., Dyck, H.M. 1978. *Ap.J.* 220:159
- Joy, A.H. 1945. *Ap.J.* 102:168
- Kaburaki, O., Itoh, M. 1987. *Astron. Astrophys.* 172:191
- Kaifu, N. 1987. in *Star Forming Regions*.
 eds. M. Peimbert & J. Jugaku.
I.A.U. symposium 115:213
- Kaifu, N., Suzuki, S., Hasegawa, T., Morimoto, M., Inatani, J., Nagane, K.,
 Chikada, Y., Kanzawa, J., Akabane, K. 1984. *Astron. Astrophys.*
 134:7
- Kawabe, R., Ogawa, H., Kukui, Y., Takano, T., Fujimoto, Y., Sugitani, K.,
 Fugimoto, M. 1984. *Ap.J.* 282:L73
- Königl, A. 1982. *Ap.J.* 261:115

- Kuhi,L.V. 1964. Ap.J. 140:1409
- Kuhi,L.V. 1978. in *Protostars and Planets*.
 ed. T.Gehrels. p708.
 Tucson Arizona Press
- Kuhi,,L.V. 1983. Rev.Mex.Astron.Astrofis. 7:127
- Lada,C.J. 1985. Ann.Rev.Astron.Astrophys. 23:267
- Lampland,C.O. 1926. Popular Astronomy. 34:621
- Little,L.T.,Dent,W.R.F.,Heaton,B.,Davies,S.R.,White,G.J. 1985.
 M.N.R.A.S. 227:217
- Lorenzetti,D.,Saraceno,P.,Strafella,F. 1983. Ap.J. 264:554
- Low,F.J.,Smith,B.J. 1966. Nature. 212:675
- Mathis,J.S.,Rumpl,W.,Nordsieck,K.H. 1977. Ap.J. 217:425
- Mendoza,V. E.E. 1966 Ap.J. 143:L1010
- Mendoza,V. E.E. 1968 Ap.J. 151:977
- Menten,K.M.,Walmsley,C.M.,Krugel,E.,Ungerechts,H. 1984.
 Astron.Astrophys. 137:108
- Mannion,M.D., 1987 Ph.D. Thesis. University of Durham.
- Mundt,R. 1987. in *Circumstellar Matter*.
 eds. I.Appenzeller and C.Jordan.
I.A.U. symposium 122:147
- Mundt,R.,Bührke,T.,Fried,J.W.,Neckel,T.,Sarcander,M.,Stocke,J.
 1984. Astron.Astrophys. 140:17
- Mundt,R.,Fried,J.W. 1983. Ap.J. 274:L83
- Norman,C.A.,Silk,J. 1979. Ap.J. 228:197
- Norman,C.A.,Silk,J. 1980. Ap.J. 238:158
- Notni,P. 1985. Astron.Nachr. 306:265
- Ohman,Y. 1939. M.N.R.A.S. 99:824

- Pickering, E.C. 1873. in *American Academy of Arts and Sciences*.
 Proceedings. New Series. 9:1
- Plambeck, R.L., Wright, M.C.H., Welch, W.J., Biegging, J.H., Baud, B.,
 Ho, P.T.P., Vogels, N. 1982. Ap.J. 259:617
- Pudritz, R.E. 1985. Ap.J. 293:216
- Pudritz, R.E., Norman, C.A. 1983. Ap.J. 274:677
- Pudritz, R.E., Norman, C.A. 1986. Ap.J. 301:571
- Pudritz, R.E., Silk, J. 1987. Ap.J. 316:213
- Rainey, R., White, G.J., Richardson, K.J., Griffin, M.T., Cronin, N.J.,
 Montero, T.S., Hitton, J. 1987. Astron. Astrophys 179:237
- Rodriguez, L.F. 1987. in *Star Forming Regions*.
 eds. M. Peimbert & J. Jugaku.
I.A.U. symposium 115:213
- Rodriguez, L.F., Cantò, J., Torrelles, J.M., Ho, T.P.T. 1986. Ap.J.
 301:L25
- Sato, S., Nagata, T., Nakajima, T., Nishida, M., Tanaka, M., Yamashita, T.
 1985. Ap.J. 291:708
- Scarrott, S.M., Warren-Smith, R.F. 1988. Preprint. (to be published in
 M.N.R.A.S.)
- Scarrott, S.M., Warren-Smith, R.F., Draper, P.W., Gledhill, T.M. 1986.
 Can. J. Phys. 64:426
- Scarrott, S.M., Warren-Smith, R.F., Pallister, W.S., Axon, D.J.,
 Bingham, R.G. 1983. M.N.R.A.S. 204:1163
- Scarrott, S.M., White, C., Pallister, W.S., Sollinger, A.B., 1977. Nature.
 265:32
- Schmidt, G.D., Miller, J.S. 1979. Ap.J. 234:L191
- Schmidt, G.D., Vrba, F.J. 1975. Ap.J. 201:L33

- Schwartz,R.D. 1983. *Ann.Rev.Astron.Astrophys.* 21:209
- Serkowski,K. 1973. in *Planets Stars and Nebulae Studied With Photopolarimetry.* p 135. ed T.Gehrels.
- Serkowski,K. 1974. in *Methods of Experimental Physics.* 12 part A:361
- Shibata,K.,Uchida,Y. 1987. in *Star Forming Regions.* eds. M.Peimbert & J.Jugaku. *I.A.U. symposium* 115:213
- Shirt,J.V.,Warren-Smith,R.F.,Scarrott,S.M. 1983. *M.N.R.A.S.* 204:1257
- Shu,F.H.,Adams,F.C.,Lizano,S. 1987 *Ann.Rev.Astron.Astrophys.* 25:23
- Smith,B.A.,Terrille,R.J. 1984. *Science.* 226:1421
- Snell,R.L. 1987. in *Star Forming Regions.* eds. M.Peimbert & J.Jugaku. *I.A.U. symposium* 115:213
- Snell,R.L.,Loren,R.B.,Plambeck,R.L. 1980. *Ap.J.* 239:L17
- Snell,R.L.,Scoville,N.Z.,Sanders,D.B.,Erickson,N.R. 1984 *Ap.J.* 284:176
- Snell,R.L.,Bally,J.,Strom,S.E.,Strom,K.M. 1985. *Ap.J.*290:587
- Stockton,A.,Chesley,D.,Chesley,C. 1975. *Ap.J.* 199:406
- Strom,K.M.,Strom,S.E.,Wolff,S.C.,Morgan,J.,Wenz,M. 1986. *Ap.J. Suppl* 62:39
- Strom,K.M.,Strom,S.E.,Kinman,T.D. 1974. *Ap.J.* 191:L93
- Strom,S.E.,Grasdalen,G.L.,Strom,K.M. 1974. *Ap.J.* 191:111
- Strom,S.E.,Strom,K.M.,Grasdalen,G.L.,Capps,R.W.,Thompson,D. 1985. *Astron.J.* 90:2575

- Strom,S.E.,Strom,K.M. 1987. in *Star Forming Regions*.
 eds. M.Peimbert & J.Jugaku.
I.A.U. symposium 115:255
- Torbett,M.V. 1984. *Ap.J.* 278:318
- Thronson,H.A.,Lada,C.J. 1984. *Ap.J.* 284:135
- Torrelles,J.M.,Rodriguez,L.F.,Cantò,J.,Carrall,P.,Marcaide,J.,
 Moran,J.M.,Ho,P.T.P. 1983. *Ap.J.* 274:214
- Torelles,J.M.,Cantò,J.,Rodriguez,L.F.,Ho,P.T.P.,Moran,J.M.
 1985. *Ap.J.* 294:L117
- Uchida,Y.,Kaifu,N.,Shibata,K.,Hayashi,S.S.,Hasegawa,T. 1987.
 in *Star Forming Regions*.
 eds. M.Peimbert & J.Jugaku.
I.A.U. symposium 115:213
- Uchida,Y.,Shibata,K. 1984. *Pub. Astr. Soc. Japan.* 36:105
- Ulrich,.R.K. 1978. in *Protostars and Planets*.
 ed. T.Gehrels. p718. Tucson Arizona Press
- Walmsey,C.M.,Menten,K.M. 1987. *Astron.Astrophys.* 179:231
- Walsh,J.R.,Malin,D.F. 1985. *M.N.R.A.S.* 217:31
- Ward-Thompson,D.,Warren-Smith,R.F.,Scarrott,S.M.,
 Wolstencroft,R.D. 1985. *M.N.R.A.S.* 215:537
- Warren-Smith,R.F.,Draper,P.W.,Scarrott,S.M. 1987(a). *Ap.J.*
 315:500
- Warren-Smith,R.F.,Draper,P.W.,Scarrott,S.M. 1987(b). *M.N.R.A.S.*
 227:749
- Warren-Smith,R.F.,Scarrott,S.M.,Murdin,P.,Bingham,R.G. 1979.
M.N.R.A.S. 187:761
- Warren-Smith,R.F. 1979. Ph.D. Thesis. University of Durham.

- Wells,D.C.,Greisen,E.W.,Harten,R.H. 1981. Astron. Astrophys. Suppl.
44:363
- White,R.L. 1979. Ap.J. 229:954
- Wilking,B.A.,Lebofsky,M.J.,Martin,P.G.,Rieke,G.H.,Kemp,J.C. 1980.
Ap.J.235:905
- Wilson,M.J.,Falle,S.A.E.G.,Innes,D.E. 1987.
in *Circumstellar Matter*.
eds. I.Appenzeller and C.Jordan.
I.A.U. symposium 122:147
- Wright,J.F.,Mackay,C.D., 1981. Proc. Soc. Phot. Instr. Eng.
290:160
- Vrba,F.J.,Strom,S.E.,Strom,K.M. 1975. P.A.S.P. 87:337
- Vrba,F.J.,Strom,S.E.,Strom,K.M. 1976. Astron.J. 81:958
- Zellner,B. 1970 A.J. 75:182
- Zuckerman,B.,Kuiper,T.B.H.,Kuiper,E.N.R. 1976. Ap.J.209:L137

Acknowledgements.

Firstly, I would like to thank my supervisor Dr. S.M. Scarrott for his help and guidance during the period of my studentship. Also I am in debt to Dr. Rodney Warren-Smith for his guidance (particularly in computing) and many fruitful discussions about all subjects. My thanks also go to my contemporaries in the Polarimetry Group in Durham, Derek Ward-Thompson, Tim Gledhill and David Mannion for all measure of support. My gratitude must also be extended to all previous workers in Imaging Polarimetry in Durham for their heritage of knowledge and data.

Also thanks are due to Professor Wolfendale and Professor Bransden the heads of the Department of Physics during my studentship, for the facilities provided in Durham.

My computing has been greatly assisted in all technical areas by Mr. Alan Lotts, manager of the Durham node of STARLINK. Many thanks go to the people involved in maintaining the telescopes and sites that I have visited. The assistance of the staff of the RGO in digitising electronographs during the authors first months is also acknowledged.

My loving thanks go to my wife Jane for help in correcting my frequently tangled English and for moral support and patience.

Finally thanks to my daughter Hannah in return for many extra wakeful hours in which to think; hours which would have otherwise been wasted in blissful sleep.

